UNIVERSITY OF BIRMINGHAM

4D QUANTIFICATIONS OF INTERMETALLICS IN SOLIDIFYING ALUMINIUM ALLOYS

by

ZIHAN SONG

A thesis submitted to the University of Birmingham for the degree of

DOCTOR OF PHILOSOPHY

School of Metallurgy and Materials

College of Engineering and Physical Sciences

University of Birmingham

December 2022

Abstract

High-speed synchrotron X-ray tomography was used to investigate the growth dynamics and mechanisms of faceted intermetallic compounds (IMCs) in aluminium alloys under different solidification conditions (temperature gradients, cooling rates and external magnetic field). Different IMCs in four aluminium alloys are studied including $Al_{13}Fe_4$ in Al-5wt%Fe alloys, Al_2Cu in Al-45wt%Cu alloys, Al_3Ni in Al-10wt%Ni alloy and β-IMCs in W319 (Al-Si-Cu) based alloys.

4D quantifications (3D plus time) were achieved in determining the nucleation rates, nucleation densities, volume fractions and growth velocities of $Al_{13}Fe_4$ IMCs with various faceted morphologies. In both Al-45wt%Cu and Al-10wt%Ni, two stages of the formation processes were identified including the growth of the basic unit and the growth of the faceted dendrite. The transition of various morphologies of the basic unit was observed and the relationship between these morphologies was determined. The growth mechanism of the faceted dendrite was proposed to be self-repeated layer-by-layer stacking of the basic units (such as L-shaped in Al_2Cu or V-shaped in Al_3Ni).

In addition, the work studied the effect of magnetic fields on solidification in Al-45wt%Cu and W319 alloys. A transverse magnetic field of 0.5T was used to control the solidification processes while the sample was rotating. Highly refined Al_2Cu intermetallic compounds were obtained including the in Al-45wt%Cu alloys which were much finer than those without the imposition of the magnetic field. Under the magnetic field, fine α-Al dendrite with smaller primary dendrite arm spacing in W319 alloys was obtained. The macro segregation zone was almost eliminated, while the solid/liquid interface was

altered from tilted to flat. Gradient volume distribution of the secondary β-IMCs was observed.

This work first reveals the growth mechanisms of different faceted IMCs with various morphologies. It also demonstrates that rotating the sample under a transversal magnetic field is a simple yet effective method of controlling the morphologies and volume distribution of crystals via altering the temperature and composition profiles in the melt.

Acknowledgement

I would like to express my deepest appreciation to my supervisor Dr Biao Cai who guided and extensively supported my study. Thank you for the valuable advice and suggestions on both experiments and manuscripts. I am also thankful to my supervisors Professor Hanshan Dong and Professor Ales Leonardis for supporting conferences and providing valuable discussions of my project. Additionally, I would like to thank the UK-EPSRC CDT Grant (No: EP/L016206/1) in Innovative Metal Processing for financial support for my PhD.

I am extremely grateful to the staff from the University of Birmingham and my friends, Dr Leonardo Stella, Dr Lei Tang, Mr Tay Sparks and Miss Wanxuan Teng, Mr Federico Pratissoli, Dr Sheng Li, Dr Stano Imbrogno, Mrs Jie Chen and Miss Amy Jade Newell for helping the experiments and for a cherished time spent together in the lab and social settings.

I am also grateful for the beamtime from B16 and I12 at Diamond Light Source which is vital for this PhD project. Dr Hongchang Wang and Dr Oxana V. Magdysyuk are great acknowledged for their support in experiments.

Finally, I would like to offer my special thanks to my parents, my brother and my sister-in-law for their unwavering support and belief in me.

Scientific contribution

Journals:

1. **Z. Song**, O. V Magdysyuk, L. Tang, T. Sparks, B. Cai, Growth Dynamics of Faceted $Al_{13}Fe_4$ intermetallic Revealed by High-speed Synchrotron X-ray Quantification, J. Alloys Compd. (2021) 158604. https://doi.org/10.1016/j.jallcom.2021.158604.
2. **Z. Song**, O. V Magdysyuk, T. Sparks, Y. Chiu, B. Cai, Revealing growth mechanisms of faceted Al_2Cu intermetallic compounds via high-speed Synchrotron X-ray tomography, Acta Mater. (2022) 117903. https://doi.org/10.1016/j.actamat.2022.117903.
3. **Z. Song**, Elodie Boller, Alexander Rack, Peter D Lee, Biao Cai, Magnetic field-assisted solidification of W319 Al alloy imaged by high-speed synchrotron tomography, J. Alloys Compd. (2022), 168691 https://doi.org/10.1016/j.jallcom.2022.168691.
4. **Zihan Song**, Hongchang Wang, Tay Sparks, Wanxuan Teng, Biao Cai, the influences of cooling rates on the growth mechanisms of Al_3Ni intermetallic compounds revealed by 4D synchrotron X-ray tomography, (In draft).
5. S. Li, B. Cai, R. Duan, L. Tang, **Z. Song**, D. White, O. V. Magdysyuk, M.M. Attallah, Synchrotron Characterisation of Ultra-Fine Grain TiB2/Al-Cu Composite Fabricated by Laser Powder Bed Fusion, Acta Metall. Sin. (English Lett. 35 (2022) 78–92. https://doi.org/10.1007/s40195-021-01317-y.

Conferences and workshops:

1. Zihan SONG, revealing growth mechanisms of faceted Al_2Cu intermetallic compounds via high-speed synchrotron X-ray tomography (Presentation), MS&T, 2022, Pittsburgh, USA.
2. Zihan SONG, revealing growth mechanisms of faceted Al_2Cu intermetallic compounds via high-speed synchrotron X-ray tomography (Poster), 6^{th} Dimensional X-ray Computed Tomography conference, 2022, Manchester, UK.
3. PhD Research Sandpit Workshop, 11-20 January 2021, Henry Royce Institute. (The winning team).
4. Zihan SONG, synchrotron 4D X-ray study of Al_3Fe intermetallics in solidifying Al-Fe alloys, National student conference in Metallic Materials, 2019, Sheffield, UK (Awarded the best external presentation).
5. Zihan SONG,4D quantification of Al_3Fe intermetallics in solidifying Al-Fe alloys (Presentation), Euromat 2019, Stockholm, Sweden.

Table of Contents

List of Definitions/Abbreviations

G_l^m	the molar free energy of the liquid phase
G_s^m	the molar free energy of the solid phase
γ_{SL}	interfacial energy
V	The volume of a spherical particle
A	The surface area of a spherical particle
V^m	The molar volume of a spherical particle
R	The radius of a spherical particle
ΔG^{homo}	Gibbs free energy of homogeneous nucleation
ΔT	Undercooling
ΔS_f^m	The molar entropy of fusion
ρ	density
$S(\theta)$	Shape factor
ΔG^{heter}	The heterogenous nucleation
ΔF	Free energy
k	The Boltzmann's constant
L	Latent heat
T_e	Melting temperature
ξ	Fraction of the total binding energy
α	Jackson's factor
I	Intensity of X-ray
I_0	Intensity of the incoming X-ray
E	Electromotive force

μ	Local velocity
B	The strength of the applied magnetic field
σ	Electrical conductivity
J	Induced electric currents
F	Lorentz force
ρ	density
H	The dimension of the flow
υ	Viscosity
ΔV	Voltage difference
η	Thermoelectric power
ΔT	Temperature difference
f_s	Fraction of solid
M	Magnetic torque
Δx	Anisotropic in the volume magnetic susceptibility
a	The angle between the direction of the magnetic field and the axis of maximum x
μ_0	Magnetic constant
$\overrightarrow{\nabla}.$	Divergence operator
$\vec{V}_L$	The velocity of the fluid
μ_L	Dynamic viscosity of the fluid
∇^2	Laplacian operator
P_L	The pressure of the fluid

List of Figures

List of Tables

Chapter 1: Introduction

1.1 Thesis overview

Solidification is a key technique in a broad range of industrial processes including casting [1], additive manufacturing [2], and welding in assembling structural parts [3]. The morphologies of the solidified microstructures were classified into faceted structure or non-faceted structures [4]. Much research has been focused on the growth behaviours of these patterns which can influence the ultimate properties of the materials [5]. The dendritic structure is a common morphology in hypoeutectic Al alloys, and many characterizations including OM, SEM, in-situ radiography[6], in-situ X-ray tomography[7,8], and numerical simulations [9] have been performed. In hypereutectic Al alloys, intermetallic compounds are generally the primary phases, which have complex crystal structures, presenting anisotropic faceted morphologies, for instance, faceted plate-like $Al_{13}Fe_4$ [10,11], L-shaped Al_2Cu [12], needle-like β-Al_5SiFe [13], and I-like Al_3Ni [14] in Al alloys. However, the dynamic growth mechanisms of these patterns, especially the faceted structures, are still not clear due to the post-mortem characterization methods used. Therefore, it is great of interest to perform *in situ* observation of different intermetallics in Al alloys and reveal growth mechanisms of their growth behaviours.

On the other hand, the effects of these patterns in the context of morphologies, primary and secondary arm spacing upon mechanical properties have attracted great interest [15,16]. One of the key methods to control the microstructures of the phases in aluminium alloys is the use of a magnetic field, which can drastically benefit the properties of materials. Magnetic-assisted solidification has been studied for more than half a century

[17,18]. Today, the use of magnetic fields has become a crucial technique in a broad range of applications, for instance, the eliminations of iron-rich intermetallics and non-metal inclusions [19–21], microstructure refinement [22,23] and semi-conductors[24–26]. However, there has been little quantitative analysis of its dynamic effects on solidification.

4D X-ray imaging technique (3D plus time, CT at high-speed) is a powerful tool to investigate the solidification process of metals and has been used previously to determine the nucleation and growth of intermetallics in Al alloys. For instance, 3D structures and morphology of α-AlFeSi, β/δ-Al_5FeSi have been revealed [13,27–32]. Non-faceted morphologies such as dendrites have been successfully investigated via *in situ* synchrotron X-ray study [7,27,33].

In this project, 4D x-ray synchrotron tomography is used to study faceted crystal growth and magnetic-assisted solidification. This work will generate fresh insight into the dynamic growth of primary dendritic and faceted structures, and explore how the magnetic field influences the microstructures during solidification. Therefore, this work makes a major contribution to research on the growth mechanisms of faceted intermetallic compounds and the physical effects of the magnetic field on solidification.

1.2 Thesis outline

Chapter 2 reviews the relevant literature related to crystal growth including classical and non-classical. It summarizes the applications of the magnetic field in solidification and the research of using X-ray tomography in studying crystals.

Chapter 3 investigates the growth dynamics of faceted $Al_{13}Fe_4$ IMCs with various morphology in terms of their nucleation rates, volume fraction, and growth velocity via in-situ X-ray tomography.

Chapter 4 uses in-situ X-ray tomography to study the growth mechanisms of faceted dendrites such as Al_2Cu IMCs. The influences of a transverse magnetic field on the temperature distribution and morphology of Al_2Cu IMCs are revealed.

Chapter 5 studies the influence of the cooling rates on the morphologies of Al_3Ni IMCs and their growth mechanisms.

Chapter 6 studies the influence of the magnetic field during the vertically upward direction solidification of an Al-Si-Cu-based W319 alloy. It revealed the effects of the magnetic field on primary dendrites refinement, macro-segregation elimination and gradient distribution of β-IMCs.

Chapter 7 contains the conclusions and future work.

Chapter 2 Literature review

2.1 Solidification

Melting and solidification are two common initial processes for most manufacturing techniques including casting, welding, powder metallurgy and additive manufacturing. Understanding the relationship between process, microstructure and properties is vital to controlling the performance of end products [34]. Solidification is a transformation from a non-crystallographic state (liquid) to a crystallographic state of metals or alloys, in which latent heat is liberated during the transformation. From solid to liquid, the heat is conducted through the interface, which results in forming the phase boundary along with the interface. Nucleation, growth, and coarsening are the three main stages of solidification [35]. The nucleation of a new phase can come from the random formation of clusters of atoms beyond the crystal sizes. These clusters will grow in multiple ways including the diffusional transportation of atoms. Finally, small particles can be dissolved while the large ones continue to coarsen to reduce the overall interfacial energies [36,37].

2.1.1 Nucleation

Driving force exits for solidification if a liquid is cooled below its melting temperature. However, the liquid phases might not spontaneously solidify because the liquid can be undercooled or supercooled below the melting temperature without phase transformations occurring. Also, free energy barriers exist for nucleating new solids, until the conditions for nucleating solids, in terms of thermodynamics and kinetics, are achieved. The nucleation theory will be introduced briefly in two aspects including homogeneous nucleation and heterogeneous nucleation [4].

2.1.1.1 Homogeneous nucleation

During solidification, crystalline solids form from the melt. This process starts with the formation of clusters of atoms due to fluctuations. In the classical theory of homogeneous nucleation, the clusters are assumed to appear in the absence of foreign particles. The clusters contain a small number of atoms and sharp interfaces that exist to separate the solid and liquid phases. To simplify the presentation, the clusters are considered as sphere shapes. The sphere that contains a few atoms has a radius of R. By considering both phases are homogenous, the molar free energy of the liquid phase is set as G_l^m. The molar-free energy of the solid phase is treated as G_s^m[38]. The interfacial energy is given by γ_{SL}. Therefore, the Gibbs free energy difference between the system, which contains a spherical particle with volume V and surface area A in contact with the liquid, and the liquid melt is given by equation 2-1:

$$\Delta G^{homo} = V\frac{G_s^m - G_l^m}{V^m} + A\gamma_{SL} \qquad 2\text{-}1$$

Where V^m is the molar volume of the particle. Replacing V and A by the appropriate formula for a sphere with a radius of R, yields

$$\Delta G^{homo} = \frac{4}{3}\pi R^3 \frac{G_s^m - G_l^m}{V^m} + 4\pi R^2 \gamma_{SL} \quad 2\text{-}2$$

To consider that for a small undercooling ΔT, the $G_s^m - G_l^m$ is similar to $-\Delta S_f^m \Delta T$. ΔS_f^m is the molar entropy of fusion. Also $\rho \Delta s_f = \frac{\Delta S_f^m}{V^m}$. Substituting the results, yields

$$\Delta G^{homo} = -\frac{4}{3}\pi R^3 \Delta s_f \Delta T + 4\pi R^2 \gamma_{SL} \quad 2\text{-}3$$

The negative sign in the first term indicates the energy released during solidification that is proportional to cubic R. The second term is the energy associated with the formation of a surface area, which is quadratic in R. Therefore, the size of the particle is critical for it to grow. More details can be found in chapters 2 and 7 of the book [38].

2.1.1.2 Heterogeneous nucleation

However, homogeneous nucleation is rare. In practice, the solidification sites can naturally or especially be introduced to the melt, which can ease the nucleation. In the case that the nucleation occurs on the existing solidification sites such as mould walls, oxides or other foreign particles is considered heterogeneous nucleation. For example, Aluminium oxide particles were identified as nucleation sites for primary Al_3Ti intermetallic compounds in Al-0.4wt%Ti alloys [39]. Al_3Sc particles have a close lattice parameter to pure Al, which has shown a great effect on grain refinement by acting as nucleation sites before the solidification of the α-Al phase in Al alloys [40,41]. Nucleation on the existing particles that have good chemical and structural matching with the nucleus can reduce the interfacial energy. As shown in Figure 2.1, a shape of a sphere cap is formed. Angle θ is given by the interfacial tensions.

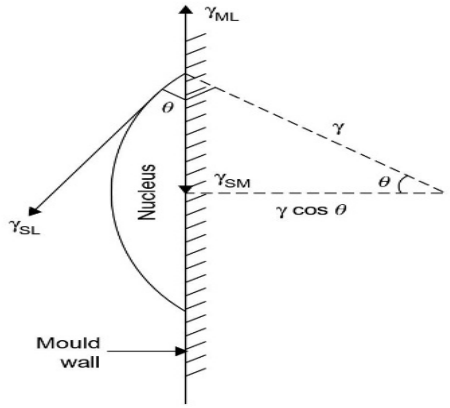

Figure 2.1 Schematic diagram of heterogeneous nucleation, after [42].

$$\Delta G^{heter} = \Delta G^{homo} S(\theta) \quad \text{2-4}$$

$$S(\theta) = \frac{(2 + cos\theta)(1 - cos\theta)^2}{4} \quad \text{2-5}$$

$S(\theta)$ is the shape factor that is less or equal to 1. The work for heterogeneous nucleation is less than homogeneous. No wetting or energy reduction occurs when $\theta = 180°$. While $\theta \rightarrow 0°$, complete wetting and energy tends to be zero. Some energy reduction and wetting when $0° < \theta < 180°$[42].

2.1.2 Classical crystal growth theories

The knowledge of how crystal growth is important in metallurgy, where the properties of end-produce are partly dependent on the morphologies of the crystal during the growth process. A deep understanding of the effects of various factors such as cooling rates, temperature gradient and external fields which can influence crystal growth is an important tool to improve the properties of the materials. For instance, the primary dendrite arm spacing is strongly refined with increasing cooling rates in Al-Cu alloys [43]. Primary Al_3Ti intermetallic compounds were refined under the imposition of ultrasonication, in which morphologies were changed from dendrite to small tablets [44]. The microstructure of Al_2Cu intermetallics in Al-40%Cu alloys can be refined under a strong magnetic field of 12T during directional solidification [22].

The growth of crystals begins once a nucleus is formed via either homogeneous or heterogeneous nucleation. In the classical theory of crystal growth, such growth is limited by the atomic attachment kinetics, capillarity and the diffusion of heat and mass [4,45]. Depending on the morphologies, the crystals are categorized as non-faceted and faceted

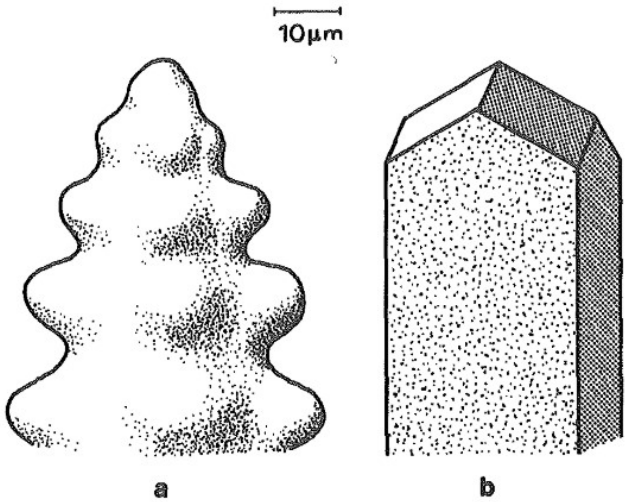

Figure 2.2 non-faceted and faceted morphologies, after [4].

structures [4]. The main difference is whether the tips of the crystal have sharp solid/liquid interfaces or not [4], as shown in Figure 2.2.

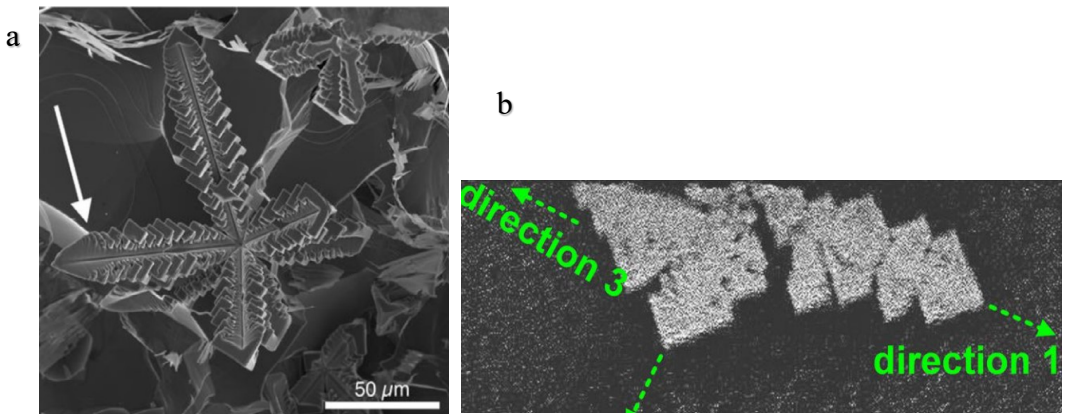

Figure 2.3 (a) SEM image of faceted Al3Sc dendrite, after [48]; (b) X-ray radiography image of faceted Al2Cu dendrite, after [49].

Faceted dendrites can be observed in various alloy systems, such as Cu_6Sn_5 [46], I-AlMnBe phases [47], Al_3Sc in Al-2wt%Sc alloy [48], Al_2Cu in Al-Cu alloys [49]. Figure 2.3 shows the faceted Al_3Sc dendrite and Al_2Cu dendrites. Different to typical non-faceted dendrites with parabolic tips. Here, faceted side branches are observed. However, the origins of the macro-steps on the side branches are still known, as the 4D (3D plus time) information of the faceted dendrites cannot be acquired by using either SEM or in-situ X-ray radiography [49].

Morphological instability, that the solid/liquid interface develops into non-faceted dendritic arms with branching, is considered to the growth mechanism of dendrites [50]. Its growth behaviour was intensively studied by using synchrotron X-ray tomography in the last few years [8,51–54]. However, faceted IMCs have highly anisotropic crystal growth kinetic, morphological instability may not be applicable. Few work has been done

to reveal the growth process of faceted crystals in-situ. The mechanism for the growth process of faceted dendrites has not been clearly elaborated.

2.1.2.1 Atomistic scale

The simplest model to describe the crystal growth process is known as Kossel crystal [55], as shown in Figure 2.4. Periodic arrangements of small blocks were used to represent a

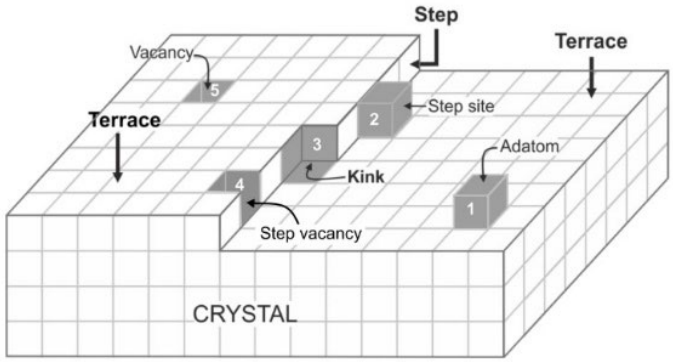

Figure 2.4 Surface of a simple Kossel crystal, after [55].

crystal. The small blocks can be atoms, ions or molecules. According to the model, depending on the number of the nearest neighbours, growth sites will have different binding energies (attachment energies). For instance, if a unit is attached to the top of the terrace (site 1), one bond will be formed. Likewise, the atom attached to site 3 will form three bonds. Higher free energy is gained. The position of site 3 is considered the kink position. The attachment of the atoms at this site is repeatable, as the surface is not qualitatively changed.

2.1.2.2 Step growth

According to Kossel, Stranski and Volmer's model (KSV model), the crystal grows via absorbing atoms layer-by-layer on the surface. During growth, the building units can collide, diffuse, migrate and be absorbed onto the sites, where the energy becomes minimum. The atoms can either migrate over the surface until they get absorbed or detached from the surface. Consequently, the adatoms on the crystal surface migrate towards a step and move along it to a kink site and get incorporated [56]. As mentioned before, attachment at a kink position can not only gain high free energy but also its repeatability plays a key role in crystal growth. This growth process will maintain until the full layer is accomplished. Therefore, the density of the steps can influence the rate of crystal growth.

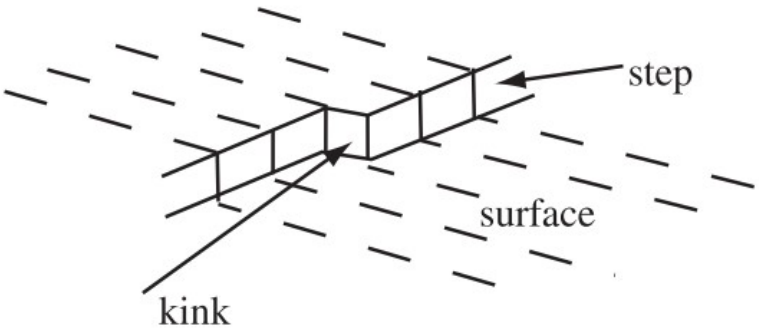

Figure 2.5 Schematic of step growth, effectively treating individual atoms as cubes, after [56].

2.1.2.3 2D nucleation

If there are no steps on an atomically flat surface, a two-dimensional nucleus is required for the crystals to grow. As shown in Figure 2.6, a small monolayer-thick island is of sufficient size for it to add new molecules and then grow into a new layer [55,57].

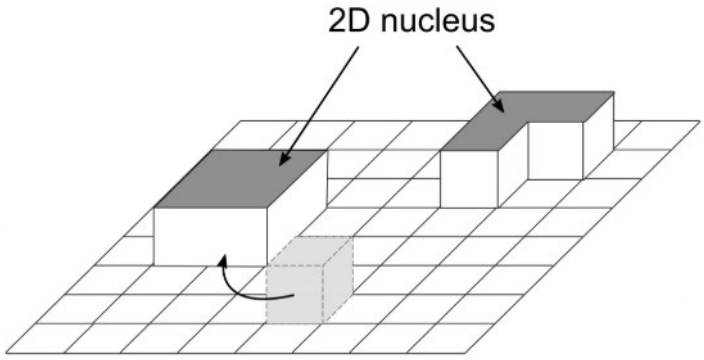

Figure 2.6 2D nucleation growth model, after [55].

2.1.2.4 Spiral growth

In the step growth model, a step was assumed to pre-exist on a crystal surface. One of the major issues of this model is once the available sites from steps or kinks are consumed, no new favourable sites are provided. 2D nucleation was proposed to provide new steps. Burton, Cabrera and Frank [58] proposed a theory, in which dislocations exist in real solids. A single molecular layer step can be present when the screw dislocation intersects

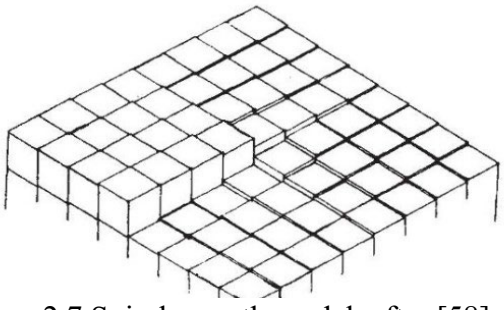

Figure 2.7 Spiral growth model, after [58].

with a surface as shown in Figure 2.7. The screw dislocation can provide a continuous source of steps that become spiral; therefore, such growth is also named spiral growth.

Experimental evidence of spiral growth was reported by several researchers [57]. Griffin, L.J. has observed the unimolecular growth steps on beryl crystals by using a microscope [59]. To increase the contrast of the image, a thin film of silver was deposited on the surface of the crystal. Carborundum. A. Verma [60] observed numerous growth spirals on carborundum crystals with various shapes including circular and hexagonal, as shown in Figure 2.8.

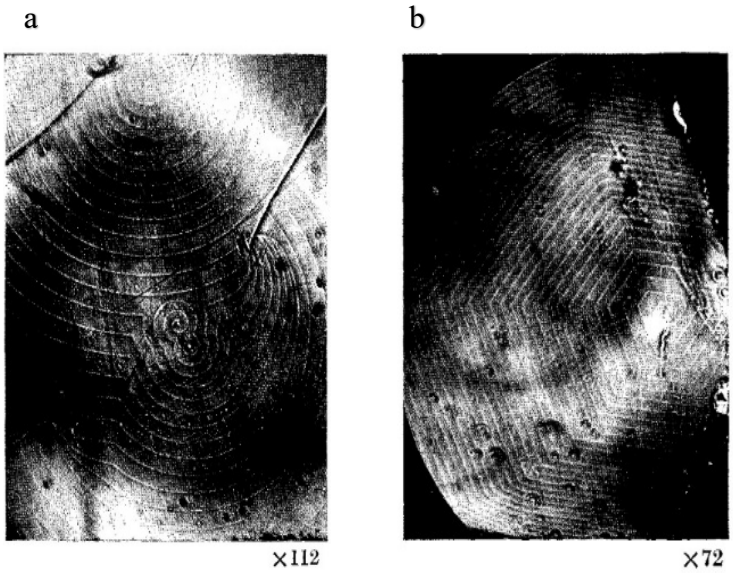

Figure 2.8 Spiral growth with circular (a) and hexagonal (b) shapes, after [60].

The models above have answered the question of why crystals grow at the atomic level. However, the question of why some of the crystals are faceted while others are not on a micro-scale has not been considered. Jackson [61] has proposed the interface morphology theory to explain the morphological difference between various crystals.

2.1.2.5 Jackson's factor

The number of kink sites is vital for growth kinetics. The parameters, that determine the atomistic state of the surface, attract attention. Jackson [61] calculated the change in free energy by adding extra molecules at the one-layer interface. The states of surface roughness can be represented by the fraction x of the total number N of possible sites. An expression is obtained as shown in equation 2-6:

$$\frac{\Delta F}{NkT_E} = \alpha x(1-x) + xlnx + (1-x)ln\,(1-x) \qquad 2\text{-}6$$

$$\alpha = \frac{L}{kT_e}\xi \qquad 2\text{-}7$$

Where ΔF is the free energy, k is the Boltzmann's constant, L is the latent heat, T_e is the melting temperature, ξ is the fraction of the total binding energy, which is always less than unity. Figure 2.9 is frequently used to represent the relationship between the occupied fraction of surface sites and the free energy of an interface [62]. Parameter α divides the curves into the ones ($\alpha < 2$) with lowest free energy at 0.5 (occupied fraction of surface sites) and the ones ($\alpha > 2$) with lowest free energy nearby 0 or 1. Therefore, it was well used to predict the surface to be atomically smooth (faceted in macro-scale) or rough (non-faceted in macro-scale). For instance, the entropy of fusion ΔS_f ($\frac{L}{kT_e}$) of Al_3Fe intermetallic compound is 4.6. Faceted structures were observed at slow cooling rates such as 0.1 K/s or 1.2 K/s [63,64]. The dimensionless entropy of the fusion of Cu_6Sn_5 intermetallic compound was calculated to be 2 hence the morphologies were predicted to be the transition between faceted and non-faceted. By increasing the cooling rate, faceted

hexagonal rods transferred into non-faceted dendritic shapes. The increased interface velocity limits the time for solute to diffuse, which can increase the driving force (solute undercooling). The solid liquid interface may undergo roughening transition at atomic level, resulting in non-faceted dendrites [46].

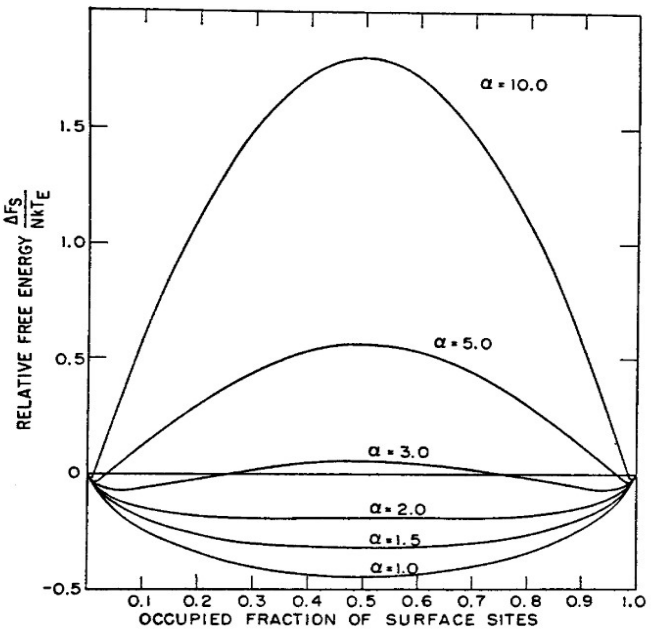

Figure 2.9 free energy vs occupied fraction of surface sites. After [62].

2.1.2.6 Twin-related re-entrant edge

Twin-related re-entrant edge growth mechanism has been used to explain the growth of faceted Silicon [65–67], and Germanium [68]. The schematic image of this mechanism is shown in Figure 2.10 [67]. The crystal is formed by one twin and is bounded by planes {111}. One re-entrant corner is formed with an angle of 141°, which allows the crystal to grow rapidly. In this case, the rapid growth will cease once the re-entrant corner is fulfilled. This mechanism has also been used to explain the growth process of faceted dendrites when multiple twinning planes are formed [69]. However, the formation process of the re-entrant corner was not observed, which is perhaps due to the limited temporal and spatial resolution of the in-situ 2D imaging method [67].

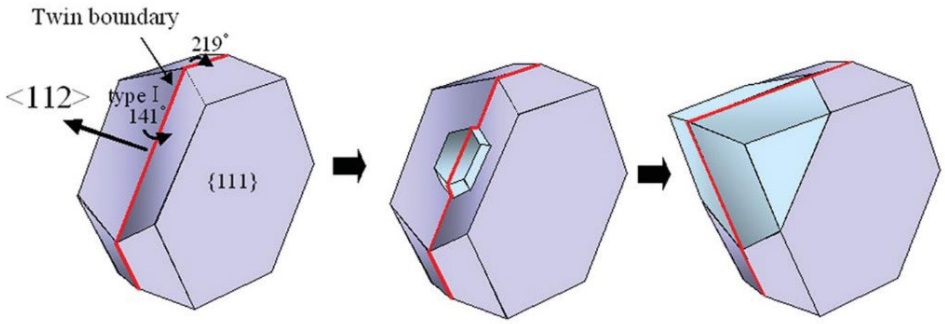

Figure 2.10 Growth of faceted crystal with one twin, after [67].

2.1.2.7 Interface instability

The evolution of non-faceted patterns such as dendrites is studied extensively, as it is the main morphologies of solidified metals and alloys. One of the earliest experimental studies of the growth process of the dendritic pattern was by Losert, W. et al., [70]. As shown in Figure 2.11, when the solidification starts rapidly, the solid/liquid interface becomes unstable. Depending on the cooling conditions, it can transfer into cellular, cells and dendritic array. The physical origin of this instability was studied by Rutter, J. W. and Chalmers, B. et al, [71,72]. It was considered 'constitutional supercooling'. Because the solubility of the elements in the melt is higher than that in the solid. The rejected solute can accumulate ahead of the solid/liquid interface.

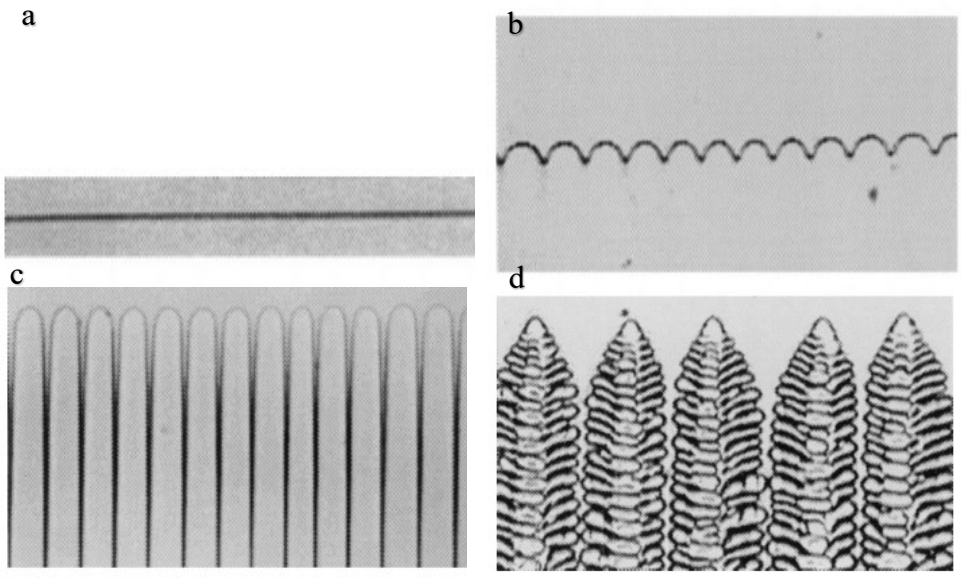

Figure 2.11 Interface of succinonitrile and coumarin 152 binary alloys during directional solidification with increasing growth rates. (a) Planar, (b) cellular, (c) deep cells, (d) dendrites, after [70].

2.1.3 Non-classical crystal growth

2.1.3.1 Atomistic scale

In the classical crystal growth theory, the growth of crystals is due to the attachment of new atoms from the melt to the surface. In Burton, Cabrera and Frank's theory, screw dislocation can provide a continuous source of steps. However, the origin of the screw dislocation was not answered as nanocrystals are normally defect-free [73]. R. Lee Penn et al., [74] have used high-resolution transmission electron microscopy to observe the growth process of titania (TiO_2). Chains of particles were observed. In Figure 2.12, five nano-crystalline are attached to a crystallographic surface to form a single crystal. In this case, the growth of crystals is proposed to be the attachment of nanocrystals rather than atoms. An oriented particle attachment mechanism was proposed.

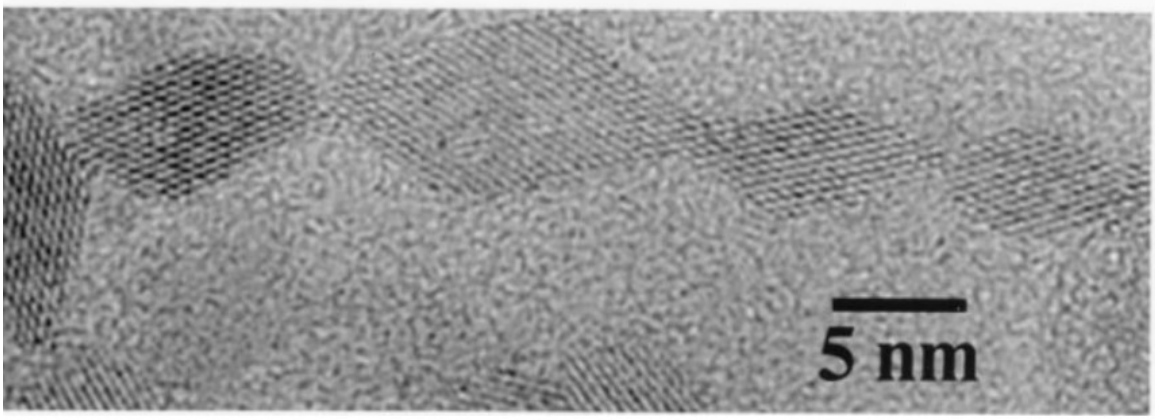

Figure 2.12 single crystal formed by primary crystallines, after [74].

In-situ TEM was developed in recent years, which allows researchers to observe the attachment behaviour of the nanocrystals during the growth process. Li et al., [75] have reported direct observation of the oriented particle attachment growth mechanism. when particles approached, they rotated until achieving a perfect crystallographic alignment. In some cases, the lattice planes near the boundary are slightly mismatched, dislocations can be generated [75–77].

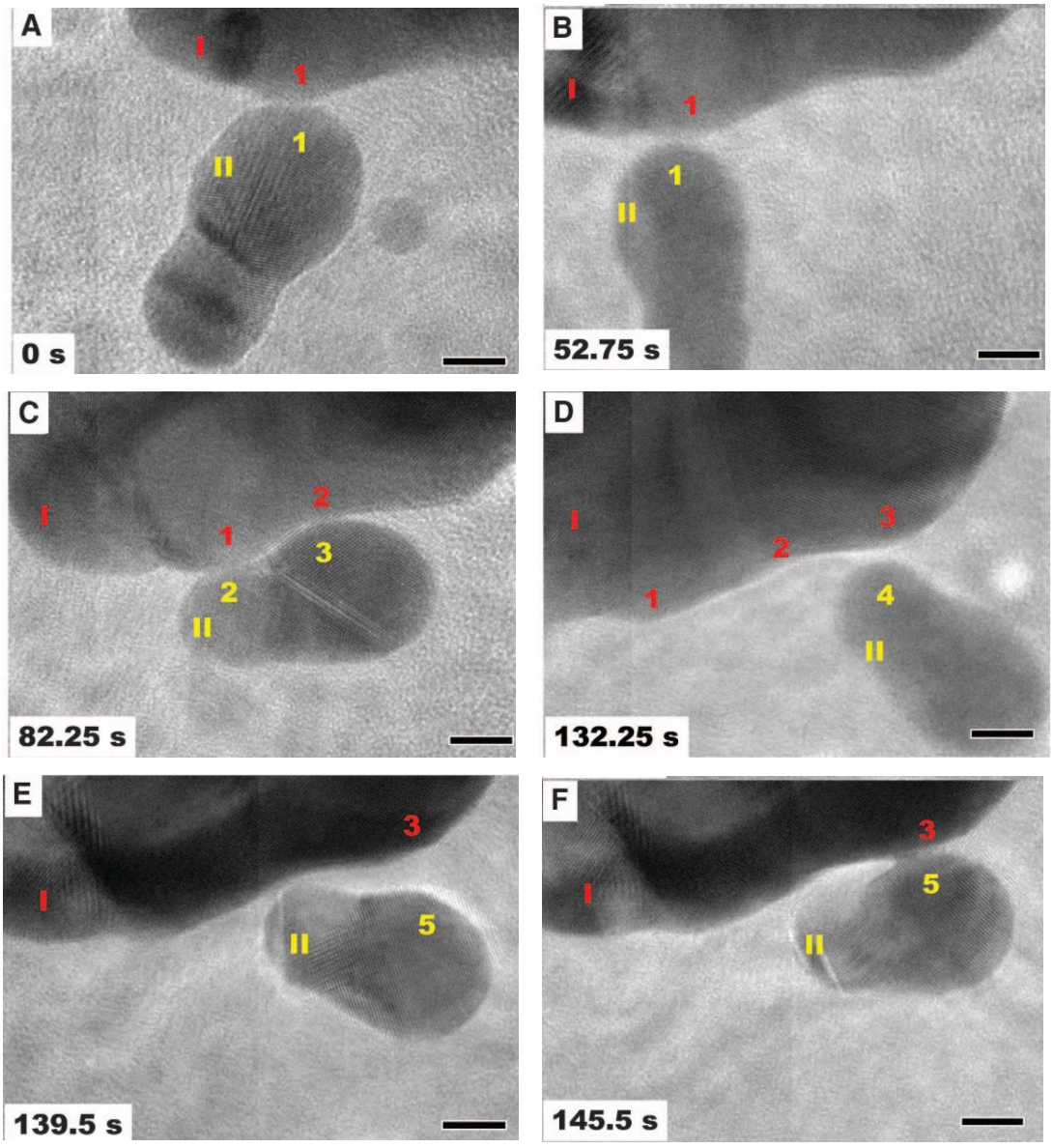

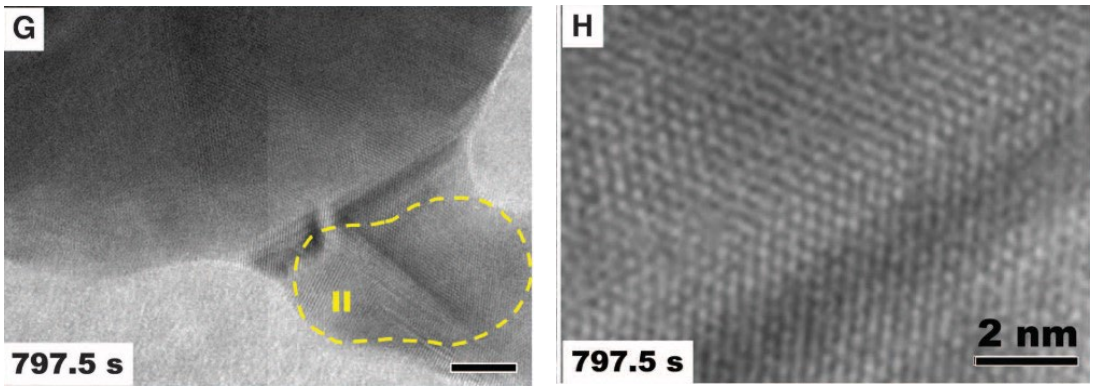

Figure 2.13 images of the attachment process(A-G) scale bars are 5nm, （H）interface in (G) showing twin structure, after [75].

Figure 2.13 shows the direct observation of the oriented particle attachment process of iron oxide nanoparticles under a high-resolution TEM *in situ*. Particles I and II have made several contacts and transient before growing together. Starts from points 1-1, particle II then rotated to contact with particle I at points 1-2 and 2-3. It continued to change its orientation until two particles meet at points 3-5. They finally attached and grew together either sharing the same crystallographic orientation or forming twinning in Figure 2.13-H.

Figure 2.14 [78] shows the schematic diagram of the classical (monomer-by-monomer) and non-classical crystal growth (subunit-by-subunit). The novel non-classical crystal growth mechanism has been widely observed in many natural and synthetic materials under TEM. For example, amorphous precursor (dense liquid droplets) appears first in calcium carbonate ($CaCO_{3)}$ [79,80], crystalline particles grow by the accretion of primary nano-particles in faceted magnetites [81], nearly oriented attachment of crystallites in zeolite [82] and oriented attachment of nanocrystals in TiO_2 nanowires [83] Ag [84] and Au [85]. For example, TiO_2 However, the existence of the non-classical crystal growth mechanism in solidification is rarely studied, due to the complexity of such experiments.

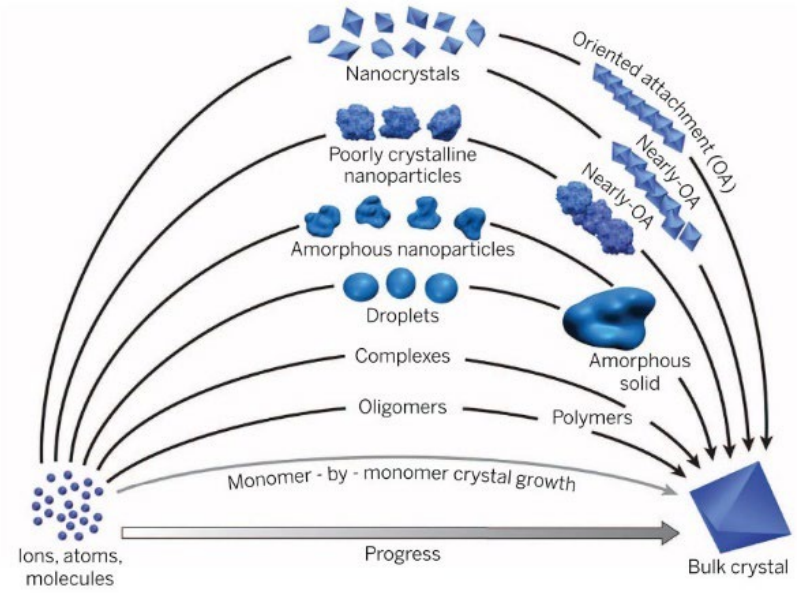

Figure 2.14 Pathway of crystal growth, after [78].

2.2 Solidification under magnetic field

2.2.1 Physical principles of magnetic-assisted solidification

Magnetic stirring has been implemented in Japan and by European steelmakers since the 1970s [86]. In continuous casting, it was reported to improve the surface quality, and structures, and reduce inclusion content and segregation [87,88]. Today, the applications of the magnetic field, such as electromagnetic stirring and brake, have extended to various purposes such as the elimination of iron-intermetallics, and microstructure refinement in Al alloys and semiconductors. Especially in manufacturing Al alloys, one of the key methods to control the microstructures in aluminium alloys is the use of magnets, which can drastically benefit the properties of the material [89].

Depending on the direction of the magnetic field, three categories are assigned. For instance, the transverse magnetic field is when the direction of the magnetic field is perpendicular to the growth direction of the crystals. For the axial magnetic field, the directions of both the magnetic fields and the growth direction of the samples were the same. And an alternative magnetic field is when the direction of the magnetic field is changing while the sample is cooling.

The physical principle of this technique is based on magnetohydrodynamics, which is the fluid dynamics of electrically conducting fluids under the magnetic field [90]. For magnetic field-assisted solidification, the influence of a magnetic field includes microstructure alignment [91–95], convection damping [96], and thermoelectric-magneto-hydrodynamic (TEMHD) [97].

2.2.2 Under a static transverse/axial magnetic field

2.2.2.1 Convection damping and thermoelectric-magneto-hydrodynamic (TEMHD)

Convection damping or named as electromagnetic braking effect uses the interaction of flowing melts with the applied magnetic field, which can produce forces [96]. During the solidification process of metals, when a liquid metal that is an electro-conducting fluid, crosses magnetic field lines, the change of flux can generate local electromotive force as shown in equation 2-8. Then induced electric currents can arise as shown in equation 2-9. The interaction between the induced electric currents and d.c magnetic field can generate Lorentz force as presented in equation 2-10 [96].

$$E = \mu \times B \tag{2-8}$$

$$J = \sigma(u \times B) \tag{2-9}$$

$$F = J \times B = \sigma(u \times B)B \tag{2-10}$$

$$Ha = \sqrt{\frac{\sigma}{\rho \upsilon}} BH \tag{2-11}$$

Where u is the local velocity, B is the applied magnetic field, σ is the electrical conductivity, F is the breaking Lorentz force, ρ is the density, H is the dimension of the flow, υ is the viscosity.

Hartmann number is a typical value to determine the importance of the EMD effect as shown in equation 2-11. The impacts of electromagnetic damping are in a broad range, for instance, it can suppress melt turbulence and braking motions. However, this induced braking force is not able to stop the liquid flow completely, because the force is proportional to the fluid velocity.

During solidification, the temperature gradient is almost impossible to avoid. Once the magnetic field is positioned, temperature gradients will be coupled to produce thermoelectric magnetohydrodynamic (TEMHD) effects including, the Peltier effect, the Thomson effect and the Seebeck effect [97]. Peltier (temperature difference can be created between the junctions) and Thomson effects (absorption of heat when the electric current passes through a material with temperature difference) can be negligible at a high-temperature solidification process. The Seebeck effect will be considered in Figure 2.15 and Figure 2.16. In the condition of solidification, if two media, such as two phases, of different thermoelectric power are connected and if there are temperature gradients exist between two junctions (interfaces), then a voltage can be induced [98]. As shown in Figure 2.15. There will be a current flowing in the dendrite as shown in Figure 2.16 [98]. Assuming uniform currents exist in idealized dendrites, the electrical current density can be summarised in equation 2-13 [98].

$$\Delta V = (\eta_S - \eta_l)\Delta T \qquad 2\text{-}12$$

$$J_{TE} = \frac{\sigma_S \sigma_l^2}{(\sigma_S - \sigma_l)^2} f_s (\eta_S - \eta_l)\Delta T \qquad 2\text{-}13$$

Where η is the thermoelectric power. S refers to the solid phase. L refers to the liquid phase. σ the electrical conductivity. f_s is the fraction of solid. ΔT is the temperature difference.

Therefore, under the magnetic field, mutual effects between the induced thermoelectric current and the magnetic field can generate Lorentz force $J_{TE} \times B$, producing flows in the melt.

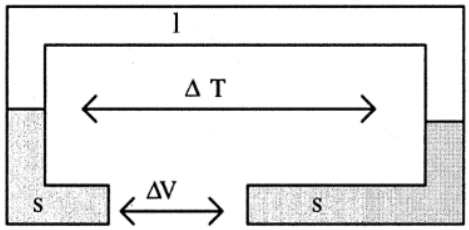

Figure 2.15 Seebeck effect, after [98].

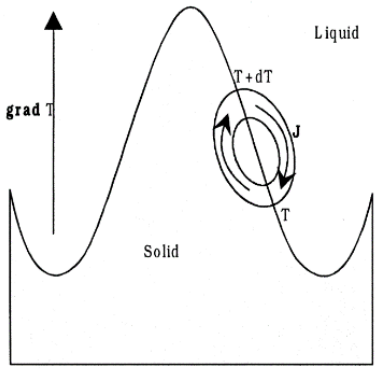

Figure 2.16 short-circuited at the interface, after [98].

Back in 1965, to eliminate the growth-striae in the growth of single-crystal of metals and semiconductors due to temperature fluctuations, Hurle [99] applied a 1k Guass (0.1 T) steady transverse magnetic field on the molten gallium under a temperature fluctuation of 2℃. The temperature fluctuations were entirely damped out in Figure 2.17. The magnetic field was applied from time point A and then was removed from time point B. The results suggested that the applied transverse magnetic field can remove the growth striae due to temperature fluctuations.

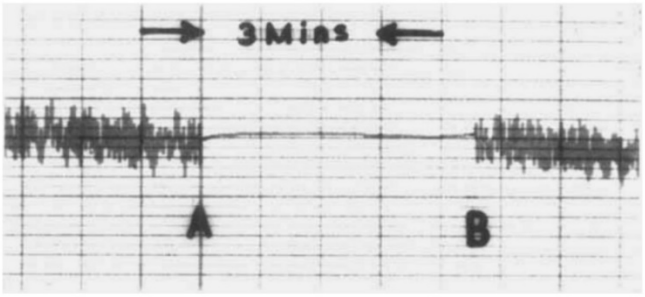

Figure 2.17 Effect of the steady transverse magnetic field on the oscillations, after [99].

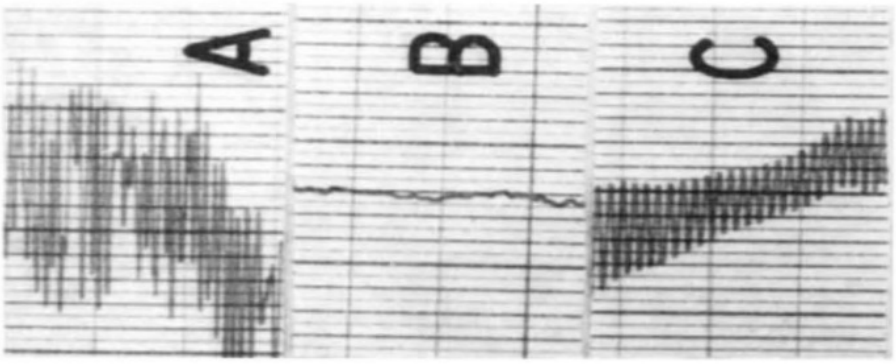

Figure 2.18 Thermocouple records: Magnetic field in A =0, in B, 2.5kG, in C 1.96kG, after [17].

Later, the experiment was expanded to molten tellurium-doped indium antimonide [17]. As shown in Figure 2.18, in zone A, the thermocouple recorded temperature fluctuations of 5℃. Over-stability was considered to be the cause of the temperature oscillations. while in zone B, the fluctuations were removed under a magnetic field of 2.5kG (0.25T). The field was steadily decreased in zone C where the magnetic field is in the strength of 1.96kG (0.196T). The solidified sample was then etched, and no striations were observed under the magnetic field of 2.5kG (0.25T).

Striae were formed in the sinusoidal oscillation's manners under the magnetic field of 1.96kG (0.196T) as shown in the right-hand side of Figure 2.19. This experiment further confirmed that the transverse magnetic field can suppress the temperature fluctuation of the molten metals.

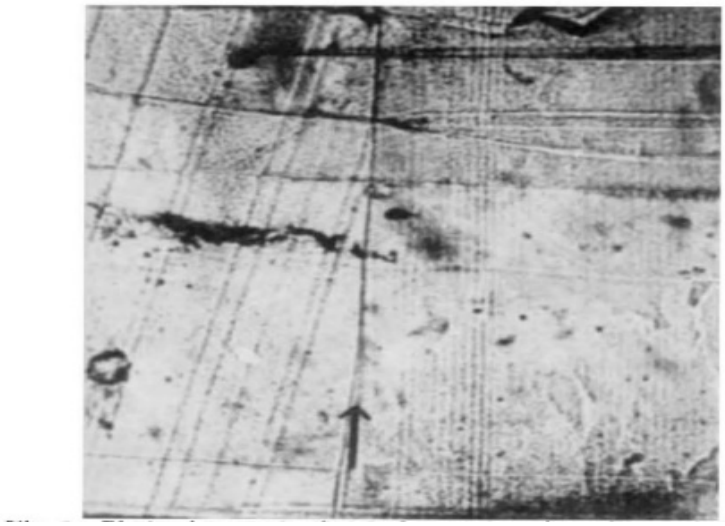

Figure 2.19 Etched crystal section, left of the arrow was growth H =0, right with H = 1.96kG, (X44), after [17].

In the same year, researchers from MIT [100] implemented a horizontal crystal growth furnace as shown in Figure 2.20.

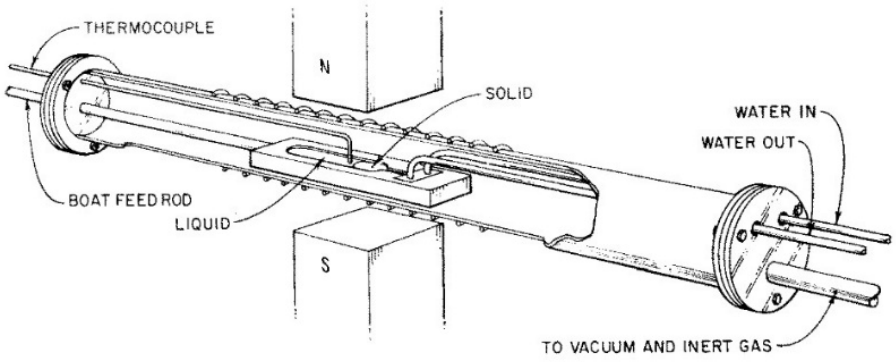

Figure 2.20 Sketch of the apparatus, after [100].

The vertical magnetic field has the strength of 1.75 Kg (0.175T). Tellurium-doped indium antimonide was solidified at a rate of 3 cm/h and a temperature gradient of 33 ℃/cm. Temperature fluctuations of 5℃ were recorded without the magnetic field as shown in the left side of Figure 2.21-a. Solute bands were observed in the left side of Figure 2.21-b, due to the turbulent thermal convection ahead of the solid/liquid interface. Once the magnetic field is on, both temperature fluctuations and the solute bands were eliminated.

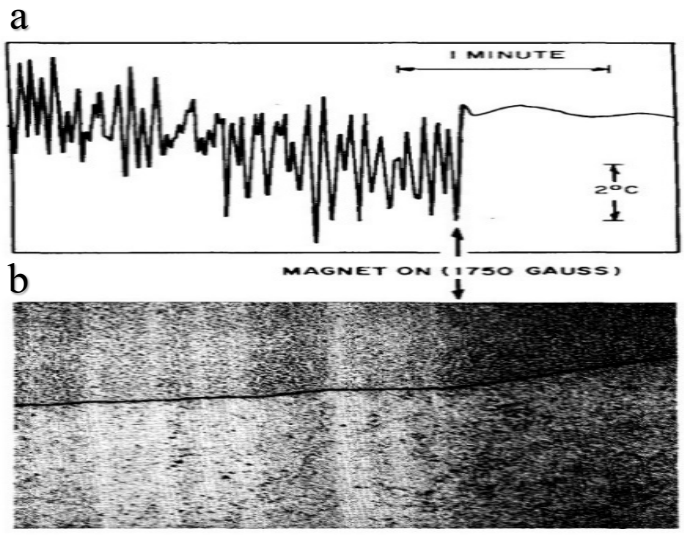

Figure 2.21 Early portion of the run, X135, after [100].

In metallurgy, Youdelis et al.,[101] investigated the influence of a transverse magnetic field of 3.4T on the directional solidification of Al-Cu (0.5 %-4.5 %) alloys. It was found that the effective distribution coefficient was reduced by the application of the magnetic field and the normal segregation was increased at a higher cooling rate of 0.5 inches per hour.

Zhu et al., [102] reported the enrichment of solute Cu in front of the solid/liquid interface and the dendrites refinement in directionally solidified Al-4.5wt%Cu alloys with the transverse weak magnetic field ($\leq 0.3T$), also tilted solid/liquid interface was observed,

which are attributed to the effect of TEMHD. The same phenomenon was also revealed in Al-0.85wt%Cu hypoeutectic alloys [103]. More researchers [104,105] found that unidirectional thermal electrical magnetic convection generates near the liquid/solid interface in Fe-Ni and Pb-Bi alloys, which may reduce the dendrite spacing.

Wang et al., [22] observed the structure refinement of Al_2Cu under an axial magnetic field (6T and 12T) in Al-40%Cu hypereutectic alloy, in which the thermal gradient has the same direction as an applied axial magnetic field. 3D simulations were performed to demonstrate that torque was produced on Al_2Cu due to the TEMHD effect, which may lead to a fragmented Al_2Cu column.

2.2.2.2 Microstructure alignment

Besides convection damping and thermoelectric magnetohydrodynamic (TEMHD) effects, a strong magnetic field also has a significant influence in aligning the microstructures. A crystal with magneto crystalline anisotropic can be magnetized, resulting in inducing a magnetic torque M as shown in equation 2-14 [106].

$$M = |\Delta x| B^2 V \sin(2a)/2\mu_0 \qquad 2\text{-}14$$

Where M is the magnetic torque, Δx is the anisotropy in the volume magnetic susceptibility,

B is the strength of the magnetic field, V is the crystal volume, a is the angle between the direction of the magnetic field and the axis of maximum x, μ_0 is the magnetic constant. Therefore, the easy magnetization axis will rotate towards the direction of the magnetic field. For instance, the easy magnetization axis of Al_3Ni and Al_2Cu is in the <001> direction [106]. By increasing the strength of the magnetic field from 0T to 12T, the preferred growth orientation of primary Al_3Ni IMCs has changed from random directions to being perpendicular to the direction of the applied magnetic field. From EBSD, it shows <001> crystal direction of Al_3Ni IMCs was oriented along the direction of the magnetic field as presented in Figure 2.22 [106]. In this case, no obvious structure alignment was observed when the strength of the magnetic field is weak (less than 1T). Ref [107] has reported the tendency of the alignment behaviour of primary Al_3Zr IMCs is increased by increasing the strength of the magnetic field from 0T to 12T. A noticeable influence was observed when the applied magnetic field is higher than 2T. <110> direction of Al_3Zr is oriented to the direction of the magnetic field.

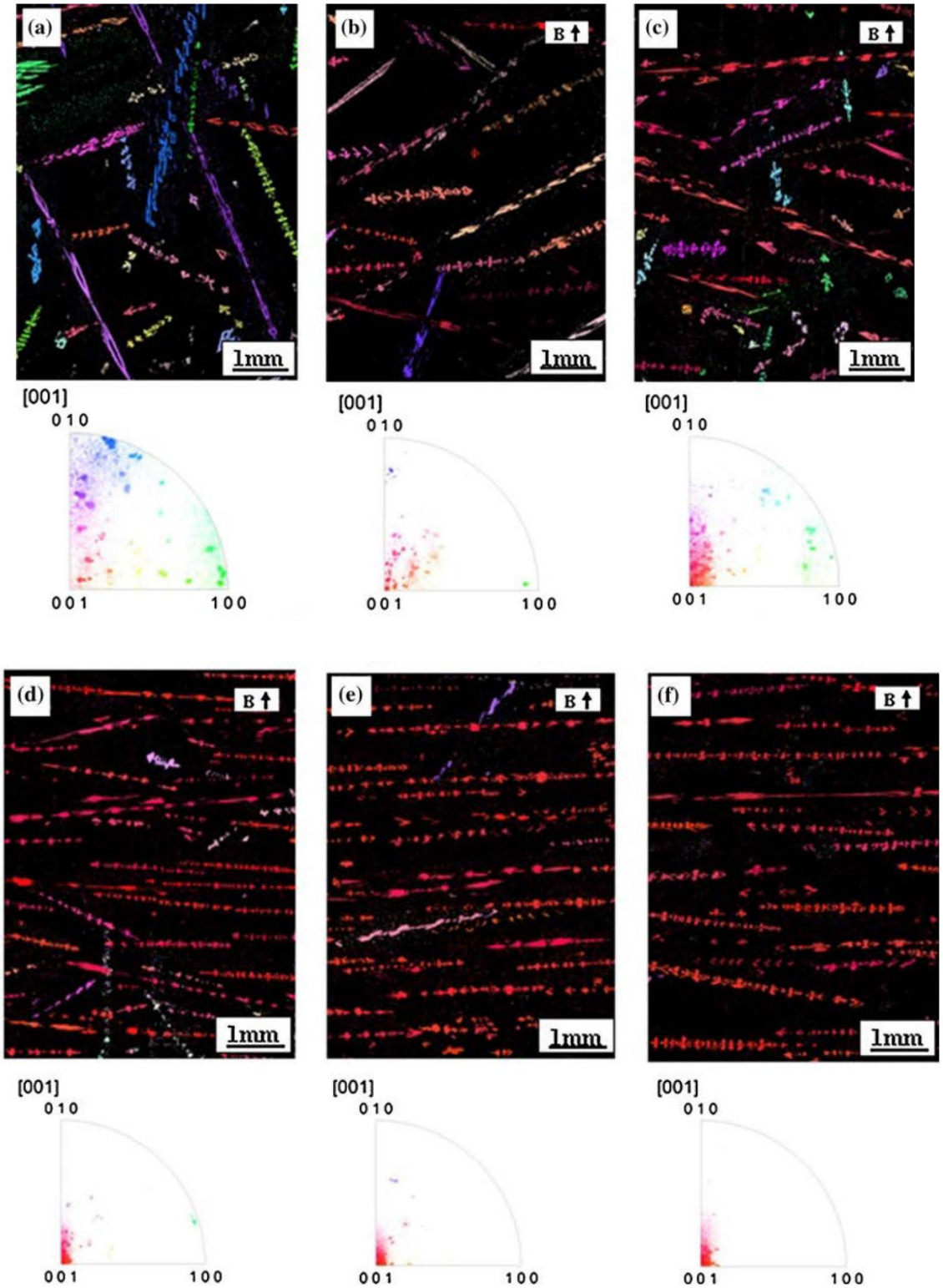

Figure 2.22 EBSD maps and pole figures of Al_3Ni under magnetic field of (a) 0T, (b) 0.8T, (c) 0.9T, (d) 1.0T, (e) 1.5T, (f)12T, after [106].

Li et al. [108] have reported the microstructure alignment phenomenon in Al-Ni alloys by applying a high-strength axial magnetic field up to 12T. As shown in Figure 2.23-a and b. Al_3Ni grew in the direction of <010> with the magnetic field under a cooling rate of 5 $\mu m/s$. However, As the intermetallic compound has magneto-crystalline anisotropy, the easy magnetization axis for the Al_3Ni phase is the <001> direction. Once the magnetic field is imposed, a layer-like Al_3Ni phase is formed perpendicularly to the direction of the magnetic field. For Al_2Cu intermetallic compounds, the preferred growth direction and the easy magnetization direction are the same [108].

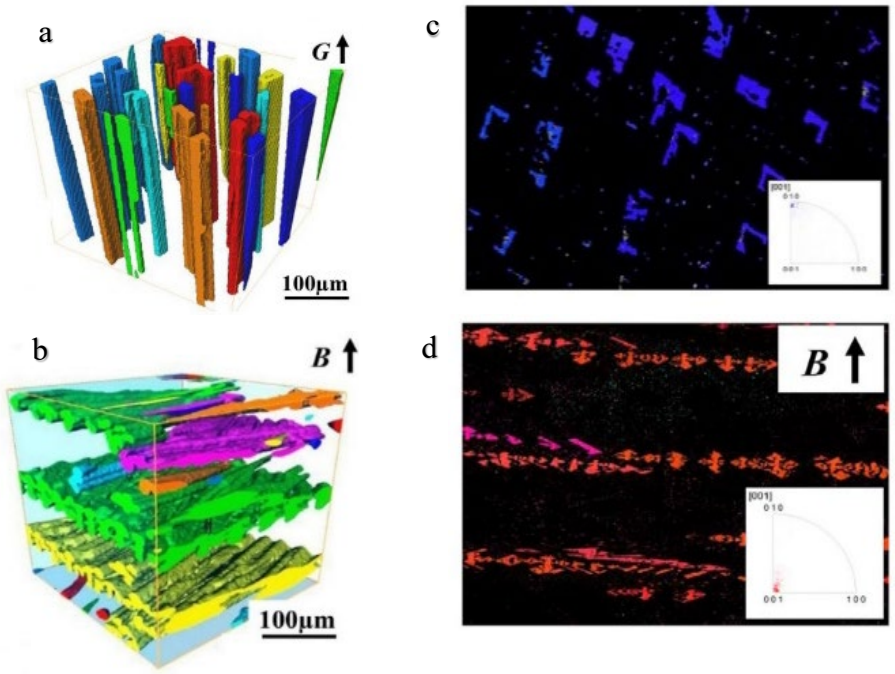

Figure 2.23 Al-12 wt%Ni alloys solidified without(a) and with (b) a 12 T magnetic field; EBSD map fo Al-12 wt%Ni alloys solidified without(c) and with (d) a 12 T magnetic field, after [108].

A strong axial magnetic field of 10 T has enlarged the primary dendrite spacing in Al-4.5wt%Cu alloys [109], The preferred growth orientation of primary α-Al dendrites was altered from <100> direction (without magnetic field) to its easy magnetization direction <111> direction (under strong axial magnetic field). Consequently, the preferred growth

direction is tilted from the directional solidification direction, resulting in larger primary dendrite arm spacing.

2.2.3 Under a rotating magnetic field

The disadvantage of the Uni-directional magnetic field either transverse or axial is the macro-segregation can be worse, as the generated force is also in one specific direction. The solute may migrate from one side of the sample to the other side of the sample. Axial macro segregation was reported under a transverse magnetic field of 0.1T and 0.5T in Al-40 wt.%Cu, Al-12 wt.%Ni alloys and Al-21 wt.%Si alloys [110]. Under a rotating magnetic field, the generated flows from both convection damping and thermoelectric-magneto-hydrodynamic (TEMHD) are multi-directional. In the paper from Mikolajczak, P. et al., [111], Al-Si-Fe alloys were directionally solidified with a temperature gradient of $3\,K/mm$ and a cooling rate of $0.04\,mm/s$. Maximum 6mT with a frequency of 50Hz rotating magnetic field was yielded from three pairs of coils during solidification. The length of β-Al_5FeSi was reduced by 20% in the dendritic region while the number of β-Al_5FeSi was increased. Under a rotating magnetic field up to 30.66 mT [112], the grain size of solidified Sn-3.5%Pb alloys was reduced from 186 μm without a magnetic field to 65 μm. Figure 2.24 shows microstructures are significantly refined with the enhancement of the intensity of the rotating magnetic field. The effect of a rotating magnetic field during solidifying aluminium alloys A356 has been studied [113]. It revealed that the microstructure of the primary phase has been modified from dendritic to globulitic structures. Primary dendritic arm spacing of the primary α-Al phase in Al-6Si-4Cu alloy was reduced under a rotating magnetic field of 0.016T [114]. However, due to the complexity of the apparatus and only limited information that can be acquired from

OM and SEM, how the microstructure was altered by the imposition of a rotating magnetic field, was rarely studied.

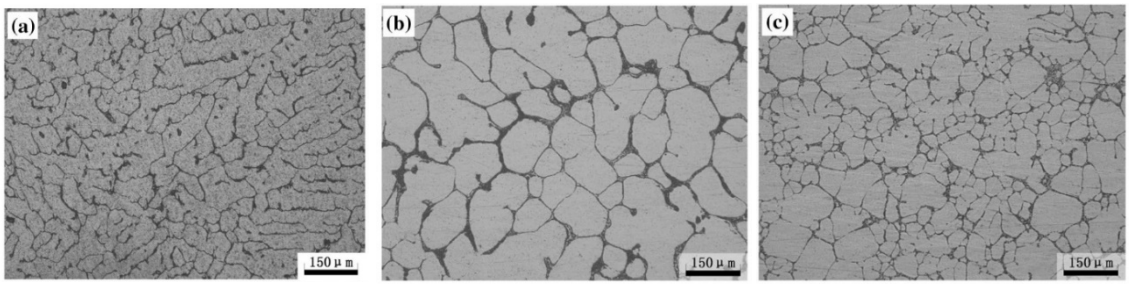

Figure 2.24 Microstructures of Sn-3.5%Pb alloy without a rotating magnetic field (a) 0 V and with a rotating magnetic field of (b) around 17mT (c) 30.66 mT, after [113].

2.3 X-ray imaging study on solidification

2.3.1 Principle of X-ray tomography

X-rays were discovered by Wilhelm Conrad Röntgen in 1895, who was awarded the Noble Prize in Physics after 6 years. Later, William D. Coolidge invented vacuum tubes to produce X-rays [115]. Since then, the brightness and spatial resolution of the X-rays were marginally improved until the arrival of the synchrotron light source. In the UK, the third-generation synchrotron source named Diamond Light Source has been used for both academic and industrial research, which can produce high-intensity X-rays. Figure 2.25 presents the schematic diagram of the experiment hall at beamline I12, Diamond Light Source [116]. Users can bring their laboratory instrumentation to use on the sample stage at a restricted dimension.

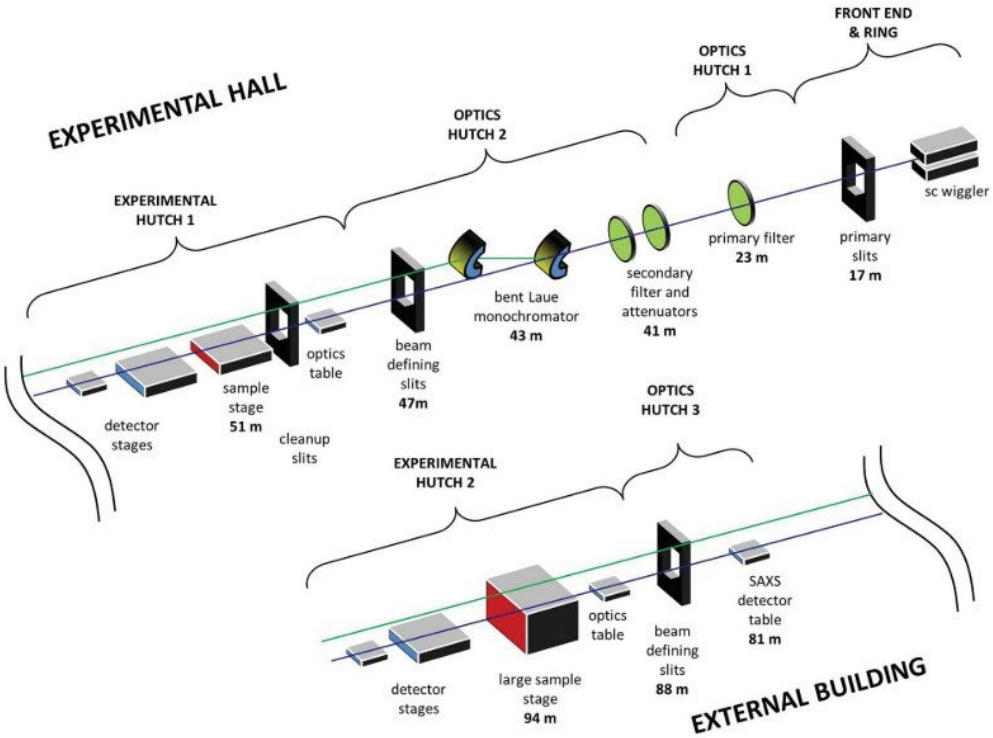

Figure 2.25 The schematic diagram of beamline I12, Diamond Light Source, after [116].

CCD or COMS sensors are used to record the images. X-rays first enter the optics module either 1,2,3 or 4 depending on the required field of view and voxel size. The scintillator will then generate a visible-light image whose path will be folded twice by mirrors. Finally, the visible light image is recorded by sensors. The schematic diagram of the imaging camera is shown in Figure 2.26.

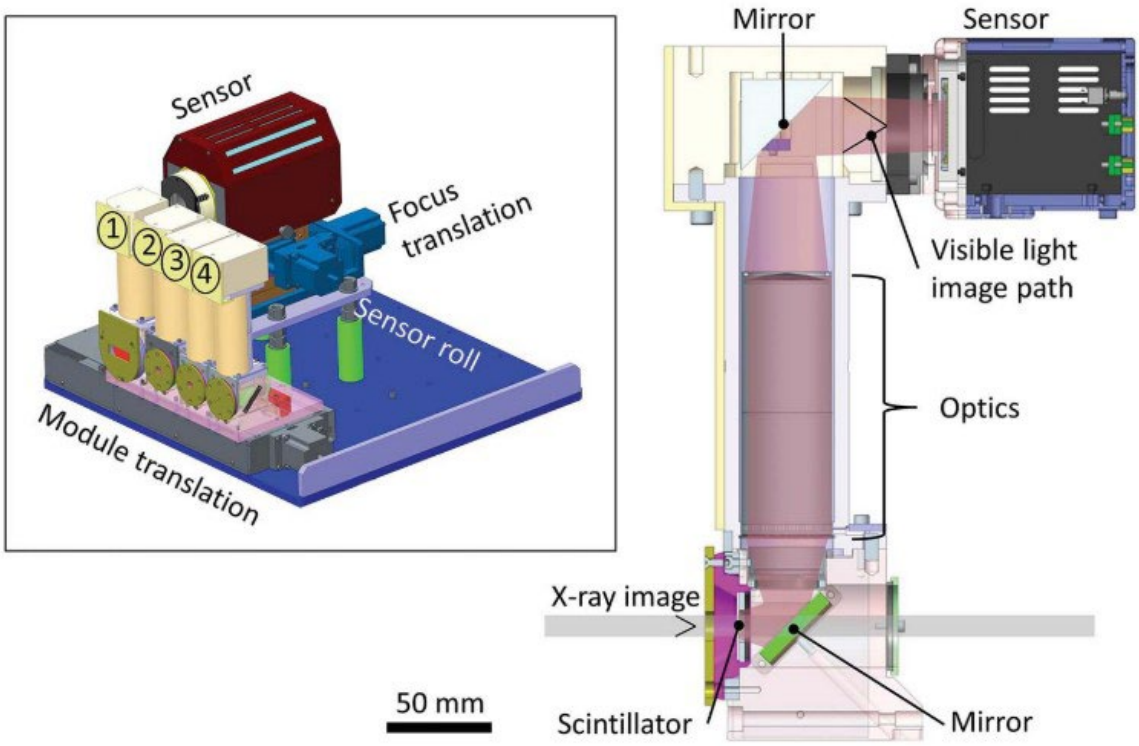

Figure 2.26 Schematic diagram of I12 imaging camera, after [116].

Absorption contrast is frequently used to distinguish different phases. According to equation 2-15, after passing through an object with thickness d, the intensity I of the monochromatic X-ray is characterized by the absorption coefficient u which includes coherent Rayleigh and incoherent Compton scattering and photoelectric attenuation [117]. I_0 is the intensity of the incoming X-ray.

$$I(y,z) = I_0 exp\left(-\int_0^d u(x,y,z)dx\right) \quad \text{2-15}$$

Synchrotron X-ray tomography is used to take hundreds of radiographs, while the specimen is rotating at 180 ° for a period of time. The radiographs were then retrieved to 3D structures by using specific methods such as filtered back projection [118]. As a result, the density or material-related absorption synchrotron X-ray tomography allows researchers to resolve and observe different phases of an object with the spatial resolution of a few micro-metres within a minute [119,120]. Compared with other methods, for instance, OM, SEM, and focused ion beam tomography, it also has advantages in non-destructive analysis and allows in-situ 3D study. Recent developments of the synchrotron x-ray techniques provide vast improvements in the quality of X-ray imaging, which lead to an increase in the impact of these techniques in materials research, especially in solidification science [121–123].

2.3.2 Non-faceted structures-α-Al phase

One of the earliest in-situ 3D tomography investigations on solidification was by N.Limodin et al., in 2007 [51]. It focused on revealing the coarsening process of Al-15.8wt%Cu alloys. In 2009, the same group investigated both the growth and coarsening process of solidifying Al-10wt%Cu alloys [8] at a constant cooling rate of $3K/min$. The scan was captured every minute with a pixel size of 2.8 μm. Two coarsening mechanisms were identified. As shown in Figure 2.27, small secondary arms were remelting to the benefit of the larger neighbour arms. Inter-arm spacing was filled via coalescing of the adjacent arms. However, the initial growth process of the dendrite was not captured in this study, perhaps due to the scanning speed was not fast enough.

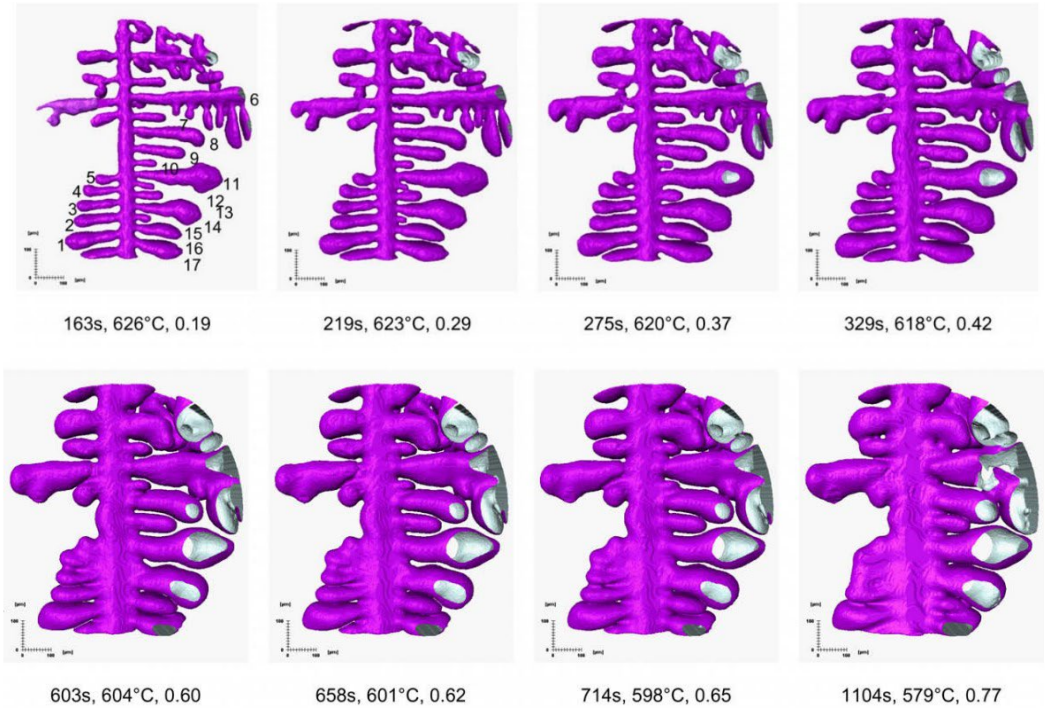

Figure 2.27 Evolution of a dendrite with solidification time, after [8].

With the improved both spatial and temporal resolution of the synchrotron X-ray tomography to 0.65 μm and 1.8 seconds, respectively, Gibbs, J. W. et al from Northwestern University, USA [52] investigated the 3D morphologies of growing dendrites in Al-24wt% Cu alloys. Tip splitting was observed. As shown in Figure 2.28, an initial flat secondary arm in Figure 2.28-a split into two narrower arms in Figure 2.28-b. The edge of the secondary arms may experience morphological instability which can lead to tip splitting.

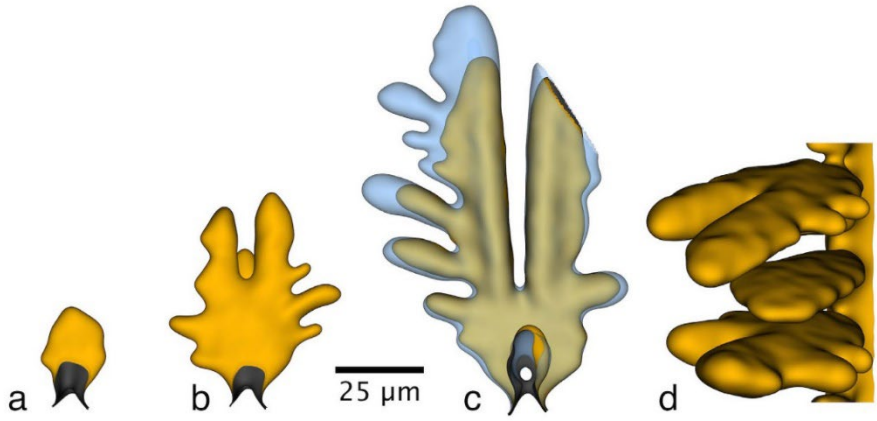

Figure 2.28 Evolution of tip splitting of a secondary dendrite arm at (a) 7.2s, (b) 9.0, (c) 10.8 and 14.4s (in blue), (d) multiple branches, after [52].

More detailed studies of dendrite growth were published by B.Cai et al, in 2016 [83]. Al-15wt%Cu was chosen due to high absorption between the primary phase and melt. As shown in Figure 2.29, Protrusions were observed at the corners of the cell, which then split into two tips due to morphological interface instabilities. One of the new tips was

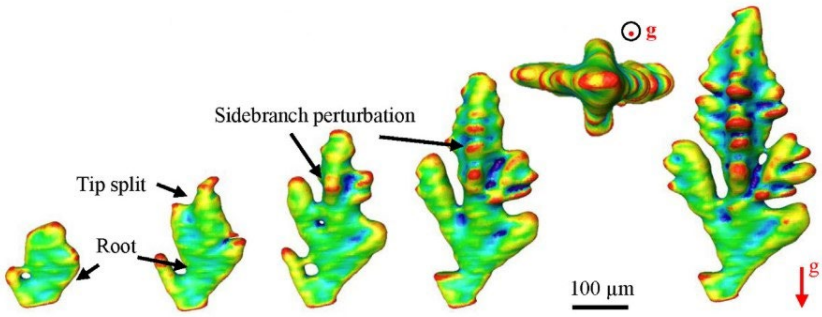

Figure 2.29 Initial growth of dendritic structure, after [83].

then branched to form a primary arm, at the same time, side-branching perturbations were also formed.

2.3.3 Faceted structures-Intermetallic compounds

2.3.3.1 Iron-rich intermetallic compounds in aluminium alloys

In the automotive industries, the demand for the average amount of aluminium alloys has doubled [124]. For instance, in the parts of the powertrain, chassis and suspension and car body. At the same time, the recycling of the materials has been considered by automotive manufacturers as well, because there are several environmental benefits to recycling aluminium alloys. For instance, 95% of greenhouse gas emissions can be reduced by using recycled aluminium parts, since the greenhouse gases are generated in the manufacturing process (upgrading and purification of bauxite, electricity consumption and CO_2 emissions in the electrolysis process) of primary aluminium [125,126].

However, most of the recycled aluminium alloys contain a mixture of productions from wide applications, for instance, engine cylinder heads of automotive are made from various alloys depending on the preferences of the industries. The majority of the alloys fall in the Al-Si, Al-Si-Mg and Al-Si-Cu-Mg systems [127]. As for casting parts, the mixture of alloys may not be an issue; however, in the process of shredding and sorting, it can be a challenge. Primarily, for high-performance alloys in terms of high toughness and ductility, the compositions of alloys are strictly controlled. One of the main impurities in recycled aluminium alloys is iron, which comes from during the manufacturing process (melting, casting) using ferrous equipment or containers. It can form secondary phases in the aluminium alloys, due to low solid solubility in an equilibrium state in aluminium[128]. For instance, $Al_{13}Fe_4$, Al_6Fe, α-AlFeSi, and β-Al_5FeSi, these phases are

detrimental to the performance of recycled aluminium alloys in terms of machinability [129], castabilities[130,131] and mechanical properties [132,133].

The evolution of faceted β-Al_5FeSi IMCs in solidifying Al-Si-Cu-based alloys (Al-8wt%Si-4wt%Cu-0.8wt%Fe) was investigated by S.Terzi et al, in 2010 [30]. It revealed the β-Al_5FeSi IMCs have plate-like shapes with complex branches and are nucleated at the oxidized surface as shown in Figure 2.30. However, as the temporal resolution was around 57 seconds, whether the origin of the branches come from the growth process of the existing structure or due to impingement of different IMCs was not observed.

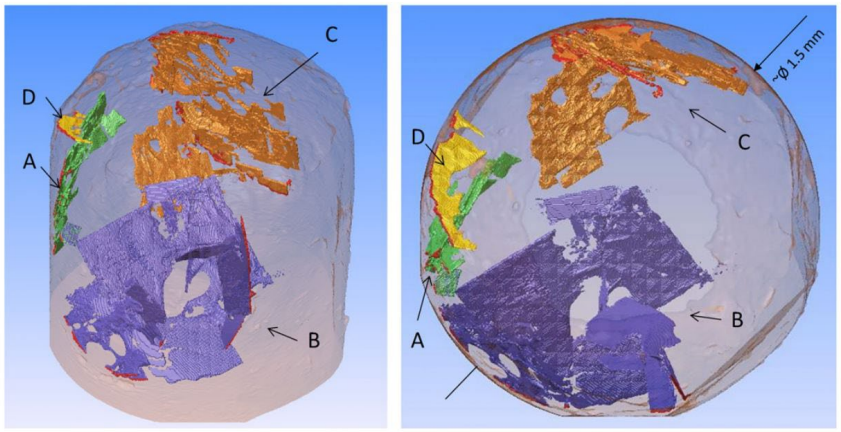

Figure 2.30 Reconstructed sample volume of β-plates at temperature T=573°C, oblique and top-down, after [30].

The initial nucleation and growth stages of β-Al_5FeSi IMCs are systemically investigated by using high-speed (temporal resolution of 12 seconds) synchrotron X-ray tomography in 2014 [27]. Four types of nucleation sites were identified including surface oxide, on/near primary dendrite, on existing IMCs and the skin of pores. The evolution of β-Al_5FeSi IMCs with various shapes was successfully captured. As shown in Figure 2.31-a, the β-IMCs grew rapidly in the lateral direction. In the second case, when the β-IMCs

contact with the primary phase, they can wrap around the dendrite and create complex shapes in Figure 2.31-b.

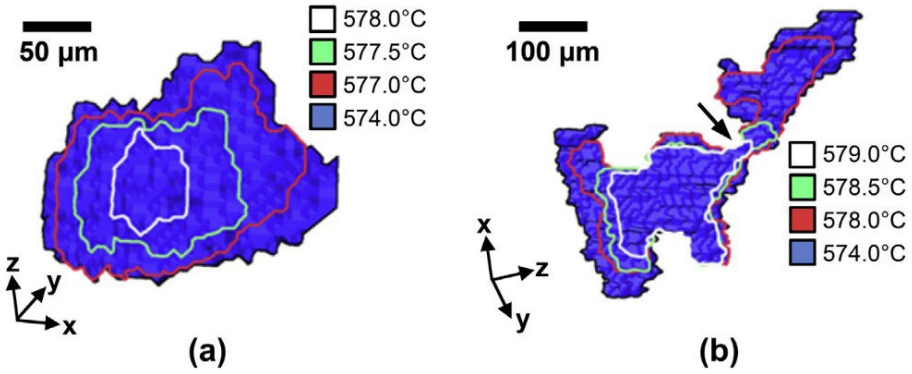

Figure 2.31 Growth process of B-phase during solidification, after [27].

Furthermore, intermetallic-intermetallic interactions were observed. Two individual IMCs grew towards and impinged into each other, resulting in the formation of complex shapes, which perhaps can be used to explain the origin of the complex branches in Figure 2.32.

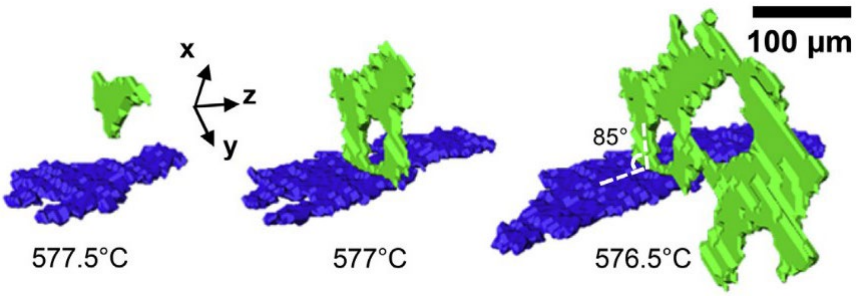

Figure 2.32 Intermetallic-intermetallic interaction: impingement, after [27].

Later, the coupled study of both synchrotron X-ray tomography and numerical simulation was performed to study the influence of IMCs on the permeability of solidifying Al-Si-Cu alloys [134]. However, the growth mechanisms of faceted IMCs were not investigated. One of the main reasons perhaps is due to the limited thickness of β-Al_5FeSi (around 20

μm [27]), its faceted angles cannot be captured by synchrotron X-ray tomography. The crystallographic orientation and its preferable growth orientations were not revealed.

2.4 Summary

In conclusion, as illustrated in the literature, high-speed X-ray tomography (recording tomograms in seconds or less) has advanced our understanding of the dynamic nucleation, growth and fragmentation of non-faceted dendrite [6,7,135], allowing us to verify existing growth mechanisms of non-faceted dendritic structure in aluminium alloys. To further explore the growth mechanisms of faceted structures such as plate-like $Al_{13}Fe_4$ (Chapter 3), and faceted dendritic structure of Al_2Cu and Al_3Ni IMCs (Chapter 4 and Chapter 5), it is critical to reveal and quantify the growth process of various intermetallic compounds in Aluminium alloys by the state-of-art synchrotron X-ray tomography in 4D (3D plus time).

Secondly, some attention has been paid to the influences of transverse and axial magnetic fields on macro-segregation and primary dendrite spacing in binary Al alloys during solidification. However, there is a lack of knowledge on the influence of the rotating magnetic field in solidifying aluminium alloys, in terms of macro-segregation, primary dendrite spacing (Chapter 4), the size distribution of secondary phase in more complex Al alloys systems (Chapter 6). Previous research has used OM, SEM, x-ray radiography, and computed tomography to investigate the microstructures of the solidified phases under the magnetic field [94,102,143,144,111,136–142], which is not able to reveal the dynamic formation process of different phases during solidification. Coupled magnetic-assisted solidification and 4D (3D plus time) X-ray synchrotron tomography allows

acquiring the volume distribution, morphologies transformation, growth speeds, nucleation rates, and growth orientations during solidification processes under a rotating magnetic field (Chapter 4 and Chapter 6), offering a deeper understanding of the mechanisms behind magnetic field-assisted solidification.

The research starts from studying a simple binary alloy under one cooling condition ($Al_{13}Fe_4$ in Chapter 3), it was then extended into studying the IMCs under different solidification conditions (various cooling rates, temperature gradients and external magnetic field) (Al_2Cu and Al_3Ni in Chapter 4 and 5). Finally, the complex solidification behaviour in commercial alloys was investigated (W319 in Chapter 6).

The criterion in selecting materials includes the density, size of the IMCs, melting temperatures of the alloys and morphologies. The ideal candidates should have a large density difference to aluminium melt, large volumes such as a few hundred micrometres, relatively low melting temperatures (due to the limitation of the furnace) and peculiar morphologies. Therefore, a series of binary alloys including Al-10%Mn, Al-5%Ti, Al-45%Cu, Al-5%Fe, and Al-10%Ni were selected. However, some of the experimental results were not successful due to the loss of the beam source during the experiments or because the crystal was not fully melted. The results of three binary alloys (Al-5%Fe, Al-45%Cu, Al-10%Ni) are presented in this thesis.

The scientific concerns or industrial applications of each material will be presented in the introduction sections of each chapter. For example, due to the difficulty of removing Fe and its low solubility in recycled Al alloys, iron intermetallics (such as α-Al(FeMnCr)Si, β-Al_5FeSi and $Al_{13}Fe_4$) form, which are detrimental to their mechanical and corrosion resistance performance. However, the branches of α-Al(FeMnCr)Si phase and plate-

shaped β intermetallics are very thin and as a result, their detailed 3D morphology has not been resolved clearly by high-speed synchrotron X-ray tomography. $Al_{13}Fe_4$ is known to form various shapes with large sizes (few-hundred micrometres) during solidification. Their faceted angles and growth processes can then potentially be captured by synchrotron X-ray tomography. Under slow cooling rates, Al_2Cu and Al_3Ni have peculiar, faceted dendrites, which growth mechanisms have not been studied in the literature. The sizes of such IMCs are large enough to be revealed by using X-ray tomography. The influences of magnetic field and cooling rates are revealed in this study. Finally, the investigation was extended into a more complex alloy system W319 (Al-Si-Cu based), in this case, the influence of the magnetic field has been studied in detail.

Chapter 3: Growth Dynamics of Faceted $Al_{13}Fe_4$ Intermetallic Revealed by High-speed Synchrotron X-ray Quantification*

* This chapter has been published in Journal of Alloys and Compunds.

Z. Song[a], O. V Magdysyuk[b], L. Tang[a], T. Sparks[a], B. Cai[a], Growth Dynamics of Faceted Al13Fe4 intermetallic Revealed by High-speed Synchrotron X-ray Quantification, J. Alloys Compd. (2021) 158604. https://doi.org/10.1016/j.jallcom.2021.158604.

a.School of Metallurgy and Materials, University of Birmingham, Birmingham, UK

b.Diamond Light Source Ltd, Harwell Science and Innovation Campus, Didcot, UK

Acknowledge of Collaborative Work:

Zihan Song: Writing-Original draft, Methodology, Validation, Investigation; Oxana V. Magdysyuk: Investigation; Lei Tang: Validation, Investigation; Tay Sparks: Writing - Review; Biao Cai: Writing - Review & Editing, Conceptualization, Supervision, Funding acquisition.

3.1 Introduction

During the solidification of metallic alloys, intermetallic compounds can form with complex crystal structures that commonly show anisotropic faceted morphologies, which significantly influence the mechanical and functional properties of the materials [145–147]. Therefore, faceted intermetallics have been extensively studied, and there is renewed interest in developing intermetallic materials for engineering applications [148–150]. Additionally, faceted crystals can form during a wide range of chemical and physical processes, ranging from electrochemical reactions [151], and the freezing of water [152,153] to the crystallization of magmas [154]. Thus, new insights into faceted crystal growth could have significant impacts on a range of subjects encompassing materials science, chemistry and geology.

Aluminium (Al) alloys are used in many applications ranging from mobile phones to cars and aeroplanes. During the solidification of Al alloys, many faceted intermetallics such as β-Al_5FeSi, $Al_{13}Fe_4$ (or named as Al_3Fe), Al_6Mn and Al_3Ni can form [10,130,155–157]. Due to the difficulty of removing Fe from Al alloys and the low solubility of Fe in Al, Fe-enriched intermetallics are common in many Al alloys, which are detrimental to the mechanical and corrosion resistance performance [132,158,159]. This has become a more serious issue in recycled Al alloys as Fe accumulates within the alloy during recycling. Continuous research efforts have been focused on understanding Fe-rich intermetallic formation during Al alloy solidification, such as α and β phase in Al-Si or Al-Si-Cu based alloys [30,160] and $Al_{13}Fe_4$ in Al-Fe alloys [92,161,162].

Many previous studies used post-mortem characterization methods (such as electron and optical microscopies or X-ray tomography) to determine the faceted morphology of the

intermetallic compounds (e.g. Al_8Mn_5 and $Al_{13}Fe_4$) in Al or Mg-Al alloys [65,163,164] which could not reveal the dynamic formation processes. In situ X-ray radiography was used to capture the formation and evolution of α-Al(FeMnCr)Si [31,165] and β-Al_5FeSi [29] intermetallic phases in iron-containing Al-Si/Al-Si-Cu alloys, which allows the growth dynamics to be determined, but provides limited information regarding on their 3D morphology. High-speed synchrotron tomographic imaging, which capture tomograms in seconds or sub-seconds [166], enables time-resolved characterization of Fe-enriched intermetallics in 3D (termed as 4D imaging [7,13,167–169]). Much research focused on the β-Al_5FeSi phase [27,30,167], as it plays an important role in the mechanical performance of Al-Si based Al alloys. However, the plate-shaped β intermetallics are very thin [170] and as a result of its 3D morphology has not been resolved clearly by high-speed synchrotron X-ray tomography which usually has relatively low spatial resolutions (a few μm [32,116]). $Al_{13}Fe_4$ intermetallic in Al-Fe alloys, on the other hand, could grow into large faceted morphology [171], potentially resolvable by high-speed synchrotron tomography. We are interested in $Al_{13}Fe_4$ phase as currently in situ observation of $Al_{13}Fe_4$ formation has not been reported and this phase is known to form various shapes during solidification [172] while the exact mechanisms for the shape variation have not been clearly understood, meaning in situ observation of $Al_{13}Fe_4$ formation is of significant interest.

In the present study, high-speed synchrotron tomography was performed to investigate the nucleation and growth dynamics of $Al_{13}Fe_4$ intermetallics during Al-5wt%Fe alloy solidification. Quantifications of the synchrotron tomography provide details of the formation process of the intermetallic and establish a link between the morphology and the crystal structure, yielding new insights into faceted crystal growth mechanisms.

3.2 Materials and Methods

3.2.1 Sample preparation

An Al-5wt% Fe alloy was prepared from Al-20wt% Fe master alloys and pure (higher than 99.9%) aluminium. The materials were melted in a graphite crucible using electrical resistance heating and held for half an hour to ensure all materials were fully melted. The alloys were then cast into a preheated mild-steel mould. Finally, cylindrical specimens with 1.8 mm diameter and 100 mm length were machined from the as-cast alloy via wire electrical discharge machining.

The in situ solidification experiment was performed at I12 beamline at the Diamond Light Source, Oxford with 55 keV monochromatic X-ray beam [116]. Module 3 out of four optical modules coupled with a PCO.edge camera (PCO AG, Germany) was used, providing pixel sizes of 3.24×3.24 μm^2. Images are cropped to 1080×1394 pixels, resulting in a frame rate of 200 frames per second. During solidification, high-speed tomographic scans were captured as the sample was continuously rotated. Each tomogram required a collection time of 5 seconds and was composed of 1000 projections (radiograph), collected over a range of $180°$. Another 5 seconds waiting time was required for downloading the tomogram between two consecutive scans.

A bespoke temperature gradient furnace [13,166] was used to perform the solidification experiment, as shown in Figure 3.1. During the experiment, the samples were placed in a 2 mm inner diameter alumina tube. The experiment procedure includes first heating up the specimen gradually up to 790℃ and holding for 10 minutes to ensure fully temperature homogenization. Both the top and bottom heater was run at the same

temperature hence, no temperature difference was applied to the specimen. The specimen was then cooled at a constant rate of $0.1℃/s$ until fully solidified.

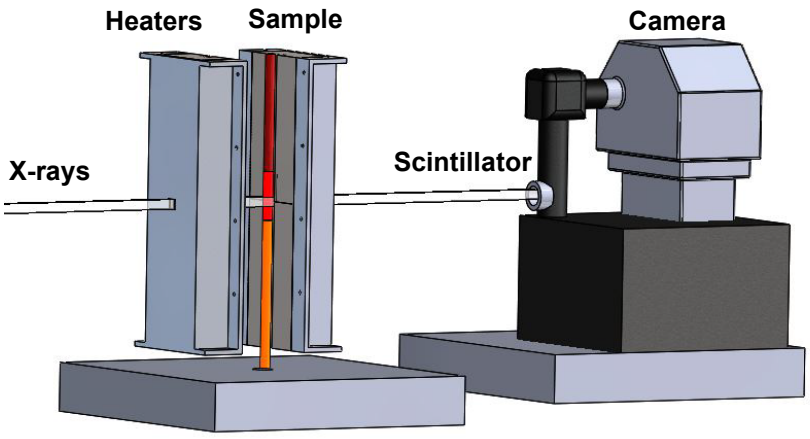

Figure 3.1 Schematic of the experiment apparatus

3.2.2 Tomographic data processing

The collected tomograms were first reconstructed using the Savu package [118,173]. 3D anisotropic diffusion was applied to reduce the noise [33], followed by image segmentation in Avizo 9.2 (FEI VSG, France). To quantify the intermetallics, particle tracking and principal component analysis methods were used [13,174].

3.2.3 Deep etching and SEM characterization

A deep etching technique was used to reveal the 3D morphology of $Al_{13}Fe_4$ intermetallic by eliminating the aluminium matrix. 5% NaOH solution as an etchant was used to etch the sample for 1 hour. The sample used for deep etching was melted and cooled at a rate of $0.1\,℃/s$ in differential scanning calorimetry (NETZSCH DSC 404C). The microstructures of $Al_{13}Fe_4$ particles were characterised by scanning electron microscopy (SEM-HITACHI TM3030 PLUS).

3.2.4 ToposPro and KrystalShaper

A unit cell of $Al_{13}Fe_4$ intermetallic was created from ToposPro [175] and KrystalShaper (JCrystalSoft, 2018) to demonstrate the crystal structure and shape.

3.3 Results and Discussion

3.3.1 Overall observation

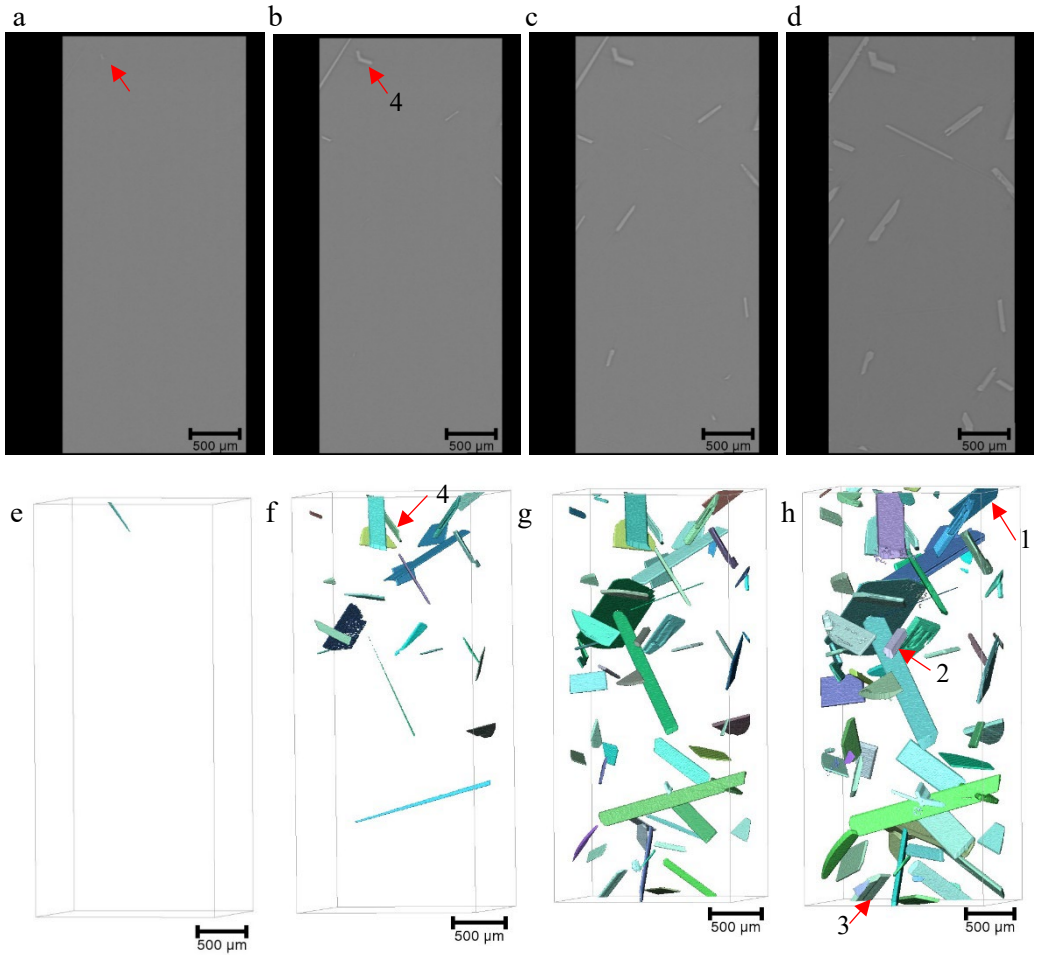

Figure 3.2 (a-d) 2D slices extracted from the tomography at t, t+40 s, t+100 s, t+400 s; (e-h) 3D rendered volume of intermetallic at t ,t+40 s,t+100 s,t+400 s.; numbers 1-4 indicate four morphologies: plate-like (1), hexagonal tabular (2), stair-like (3) and V-shape (4).

High-speed synchrotron X-ray tomography allows the in-situ observation of the solidification process of the $Al_{13}Fe_4$ intermetallic. A set of vertical slices are shown in Figure 3.2a-d, which illustrates the microstructure evolution in solidifying Al-5wt.%Fe

alloy at t, t+40 s, t+100 s, t+400 s. (where t is the time when the first $Al_{13}Fe_4$ intermetallic appeared in the field of view). The $Al_{13}Fe_4$ intermetallics appeared to be much brighter than the aluminium liquid because the iron-rich intermetallics have higher X-ray attenuation than the liquid. This also allows the $Al_{13}Fe_4$ to be easily segmented from the aluminium liquid. Figure 3.2e-h represent the corresponding 3D rendered images of the intermetallics after image segmentation (see also the supplementary movie 1). The intermetallics are mostly plate-like shapes. The first intermetallic was observed in Figure 3.2-e, at 781 ± 1℃. This solidification starting temperature was determined from the binary Al-Fe phase diagram. Below this temperature, $Al_{13}Fe_4$ intermetallics continued to grow and new intermetallics nucleated rapidly. As shown in Figure 3.2-f, after a fall in temperature of 4℃ from Figure 3.2-e, many more intermetallics have nucleated. The number and size of intermetallics increase rapidly in the first 100 s to 771℃, as shown in Figure 3.2-g. The formation of new intermetallics ceased at 741℃, with the total number of intermetallics formed being 62.

3.3.2 Nucleation of the intermetallics

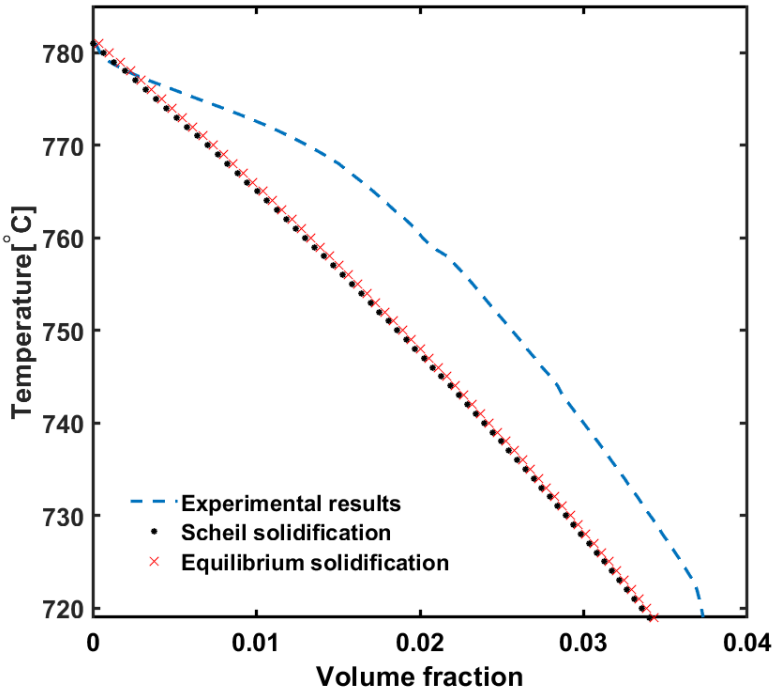

Figure 3.3 Volume fraction as a function of temperature.

In addition to the qualitative observation of the overall solidification behaviour of the Al-5wt%Fe alloy, we can also quantify the evolution of the $Al_{13}Fe_4$ intermetallics. Figure 3.3 plots the volume fraction of $Al_{13}Fe_4$ intermetallic as a function of temperature from both experimental results and the Scheil and equilibrium solidification model. The density of the liquid was considered between 2.42 and 2.44 g/cm^3, while the density of $Al_{13}Fe_4$ are in the range of 3.72-3.74 g/cm^3.It shows that the experimentally determined values deviated from the both models, indicating that the cooling profile may not be linear.

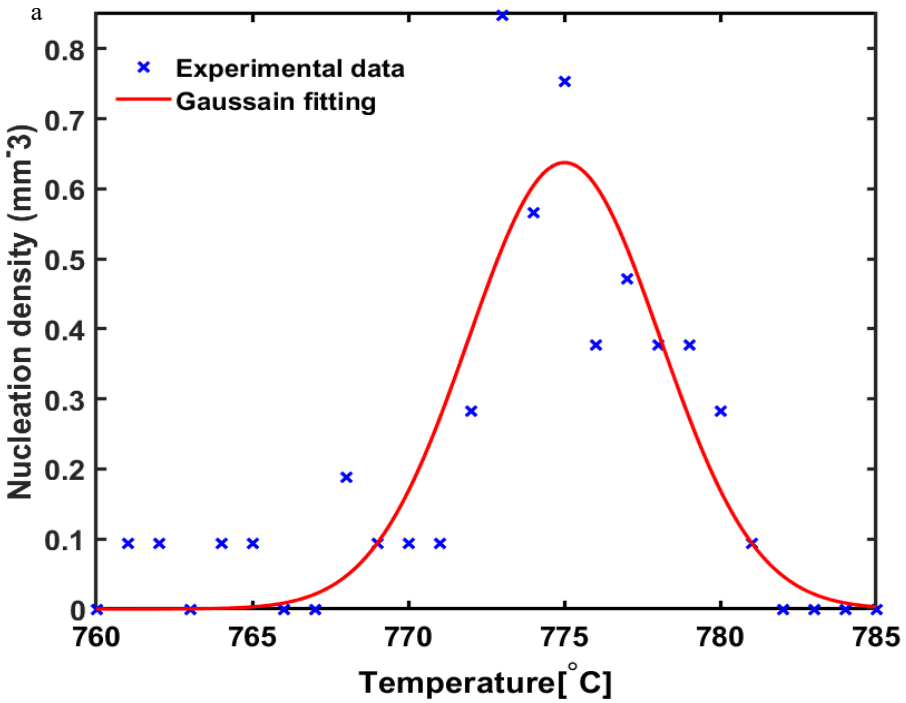

Figure 3.4 (a) nucleation density as a function of temperature.

Figure 3.4 shows a histogram of the nucleation density of the intermetallic (the number of nucleation sites divided by the volume of the sample) as a function of nucleation temperature. As discussed earlier, the first crystal nucleated at 781℃. The intermetallics mainly (more than 90%) nucleated in the temperature range from 781℃ to 764℃. The curve shows the nucleation density reaches its maximum at around 775℃, followed by a decline with the increasing of undercooling. A Gaussian distribution (3-1) can be used to fit the nucleation density as a function of nucleation undercooling. The nucleation density/rate is related to the number of stable nuclei and frequency of attachment. Both factors are dependent on temperature (below the melting temperature). The number of stable nuclei is anti-proportional to the temperature while the frequency of attachment is proportional to the temperature. The nucleation rate is proportional to the product of both factors, resulting in Gaussian distribution. The nucleation undercooling was

approximated according to the difference between the predicted nucleation temperature and the observed nucleation temperature inferred from the tomography.

$$n = n_{max}\, exp\left(-\frac{(\Delta T_N - \Delta T_M)^2}{{\Delta T_\sigma}^2}\right) \quad 3\text{-}1$$

Where n is the nucleation density at a specific nucleation undercooling, ΔT_N is the nucleation undercooling. ΔT_M is the mean value of the Gaussian distribution of nucleation undercooling (6 ℃). ΔT_σ is the deviation of the Gaussian distribution (4.3℃). n_{max} is the maximum nucleation density ($0.637\ mm^{-3}$) with 95% confidence bounds. The decline of the number of nucleation sites at a higher degree of nucleation undercooling can be explained by the solute depletion in the melt due to the growth of intermetallic particles.

The nucleation sites of the intermetallic can also be identified. In a prior study [30,176], it was found that Fe-rich intermetallics were promoted to nucleate at the surface of inclusion and the primary phase, as well as the outer oxide layer of the specimen. In this experiment, two different nucleation sites were identified.

As shown in Figure 3.5, most of the $Al_{13}Fe_4$ intermetallics connected to the sample surface (58 out of 62). The surface of the specimen is most likely covered with aluminium oxide [27]. The oxide layer exhibited high potency for the nucleation of $Al_{13}Fe_4$ phases. Another possibility is that the surface of the sample was first undercooled, which can then trigger heterogeneous nucleation of $Al_{13}Fe_4$ in the melt near the surface. The rapid growth of these $Al_{13}Fe_4$ crystals can release a significant amount of latent heat, which may suppress nucleation in its nearby regions. Nucleation also occurred at the tip of existing intermetallics, as shown in Figure 3.5-c1 to Figure 3.5-c6. Once nucleated, the crystal

grew rapidly. In this case, the existing intermetallic can be considered as inclusions that provide high potential for nucleation.

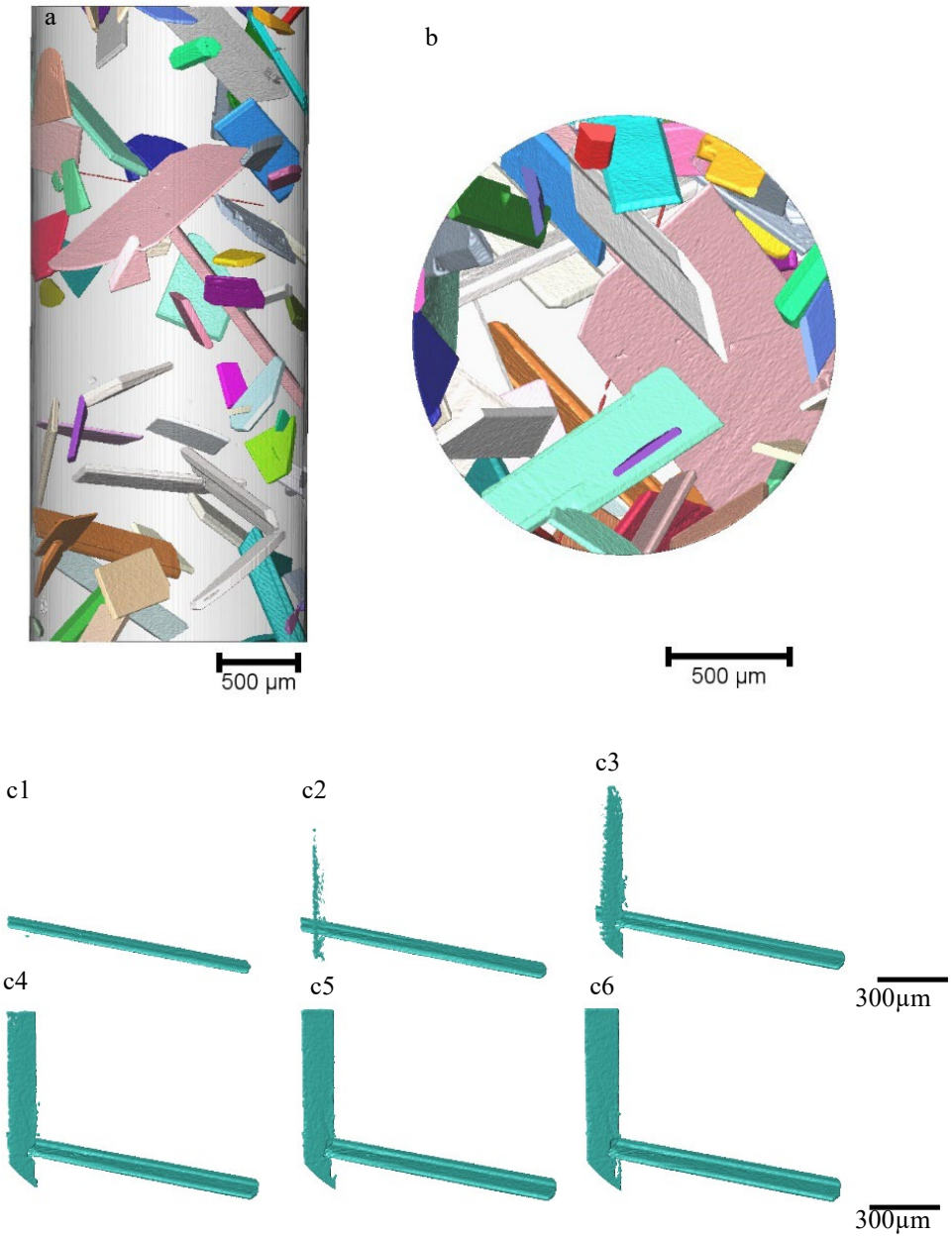

Figure 3.5 3D rendered intermetallics to show the nucleation on oxide surface (a) side view and (b) top view; (c1-c6) self-nucleation at t0 +20 s to t0 +70 s.

3.3.3 Growth of the intermetallics

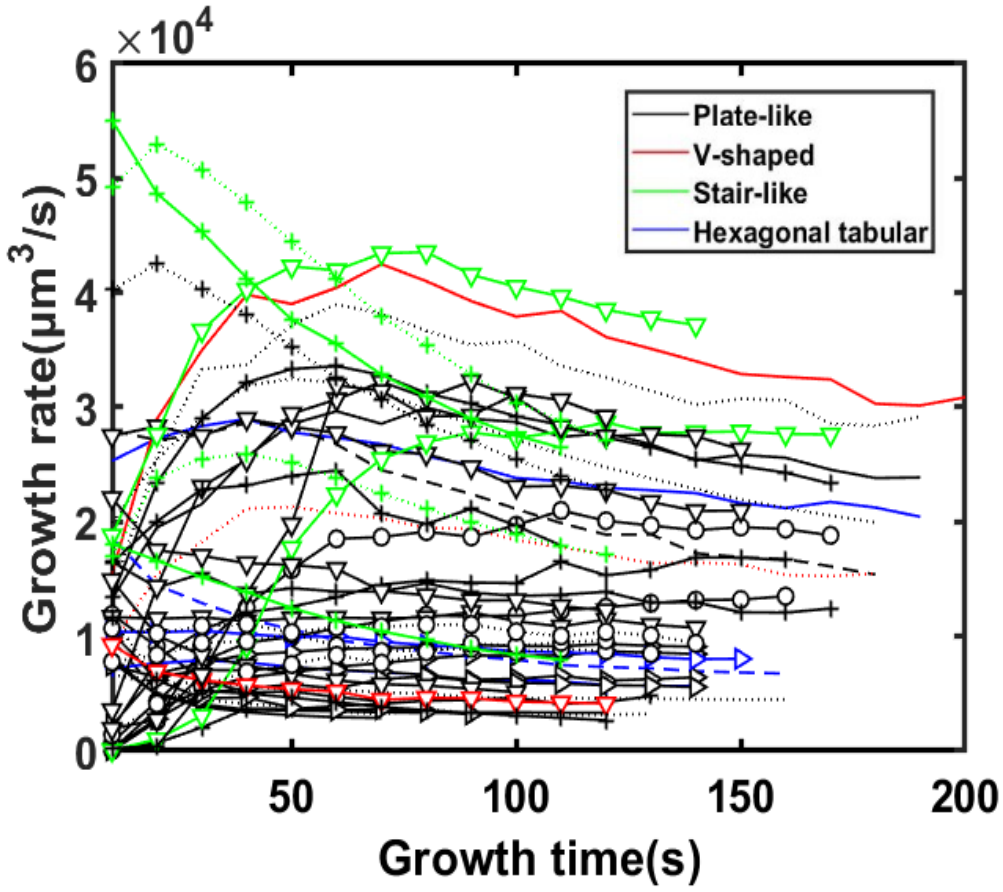

Figure 3.6 Growth rates of each intermetallic from t to t+200 s

After nucleation, individual particles were tracked using a particle tracking method [13], allowing the quantification of individual intermetallic growth. Figure 3.6 shows the growth velocities of different patterns as a function of the growth time. The growth velocities of impinged intermetallics are not included. 50 intermetallics were chosen. The curves can be divided into two main types. The first type is that the particle growth rates increase at the initial stage of solidification (the first 50 seconds), then slow down slightly approaching constant values. The second type is that the particles have the highest growth rates initially, then the rates slowed down continuously as the temperature decreasing.

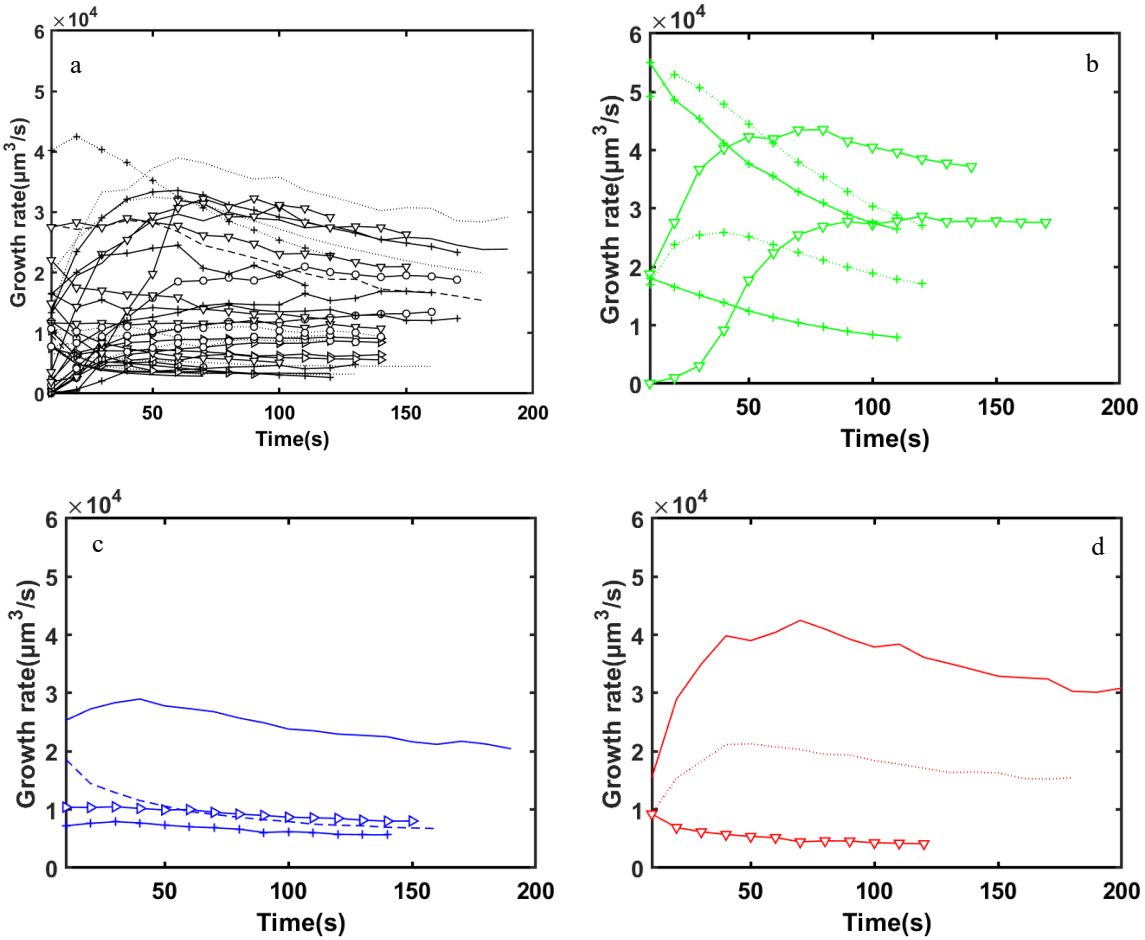

Figure 3.7 Growth rates of each intermetallic from t to t+200 s, (a) plate-like; (b) Stair-shaped; (c) Hexagonal tabular; (d) V-shaped.

Four colours were also used to represent four types of intermetallics (plate-like, stair-like hexagonal tabular and V-shaped), there seem no correlation between the growth velocities and the morphologies.

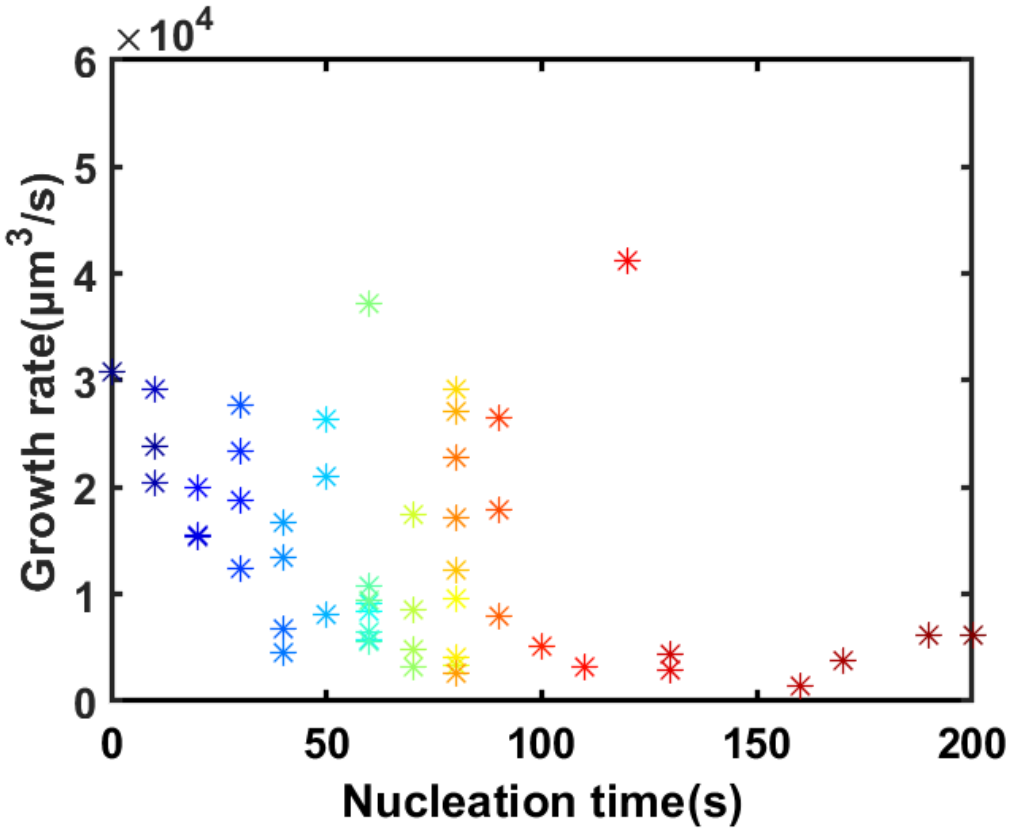

Figure 3.8 Overall growth rate of intermetallics as a function of its nucleation time

Figure 3.8 demonstrates the overall growth rate of intermetallics as a function of its nucleation time (t_n). t_n is the nucleation time of the particle n. As can be seen, the growth rates of most of the intermetallics are inversely proportional to the nucleation time. The first intermetallic has a growth rate of $3\times 10^4\ \mu m^3/s$. The overall growth rate dropped by 80% to 6000 $\mu m^3/s$ in 200 s. This might be because of the depletion of solutes which restricted the growth at the later stage of solidification [177].

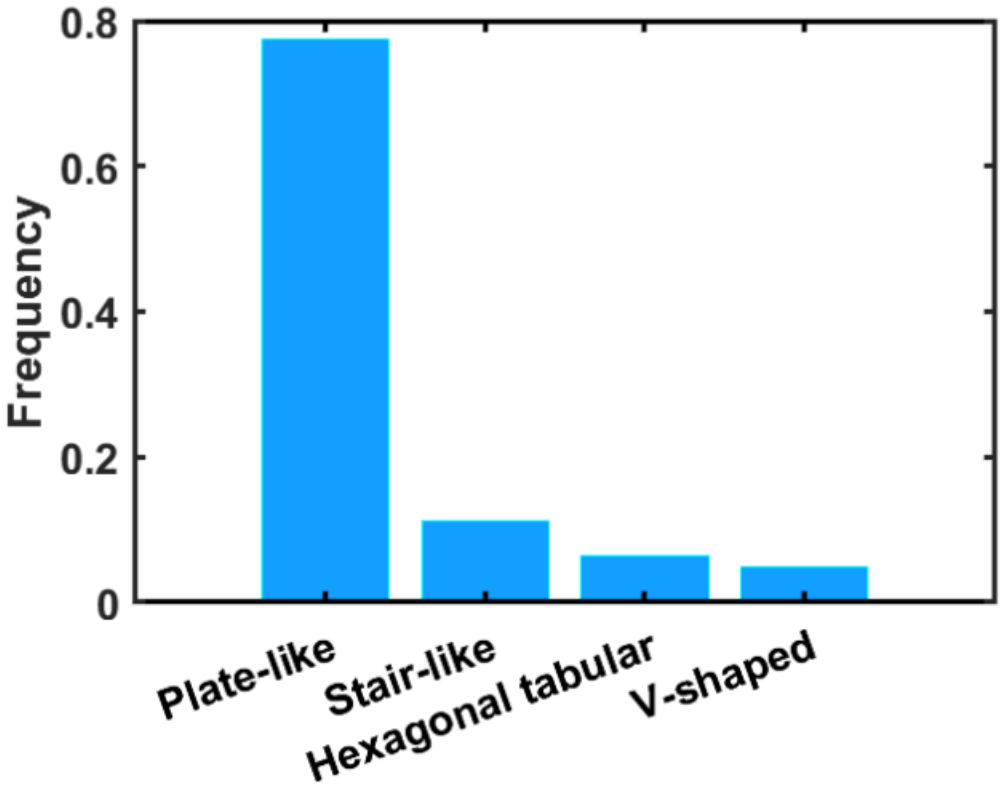

Figure 3.9 Frequency of various morphologies

The intermetallic was shown to grow into different faceted morphologies (Figure 3.2). Here, four main shapes were observed, which are plate-like, hexagonal tabular, stair-like and V-shaped. Figure 3.9 demonstrates the percentage of each morphology. Plate-like patterns have a frequency of 78%. Only a few intermetallics are classified into stair-like, hexagonal tabular and V-shaped structures in the percentage of 11%, 6% and 5%, respectively. The formation process of those different shape of crystals are discussed in the next section.

3.3.3.1 Morphologies and crystal structure

The melting entropy can be used to predict the crystallisation behaviour. The intermetallics that have high dimensionless entropy of more than 2 (entropy of fusion ΔS_F =3.65) can form faceted phases [65]. Otherwise, they tend to form non-faceted structures. The entropy of fusion ΔS_F of $Al_{13}Fe_4$ is 4.6 [64]; hence the faceted structure was formed. The morphology of a crystal strongly relates to its crystal structure. The crystal structure of $Al_{13}Fe_4$ particles is monoclinic C2/m (a=1.549nm, b=0.808nm, c= 1.248nm, α=γ=90°, β=107.7°) [163,178]. A unit cell and the simulated shape of the $Al_{13}Fe_4$ are shown in Figure 3.10-a to Figure 3.10-c. According to the crystal growth theory [4], the high-index planes have higher rates of accepting atoms and grow faster. These planes will disappear, and the crystal will be bounded by low-index planes that grow slowly. The low index planes of $Al_{13}Fe_4$ include (100), (001), (20$\bar{1}$) and (110). The corresponding d-spacing and interplane angles are listed in Table 1. Previous studies have shown that the preferred extension direction of $Al_{13}Fe_4$ was suggested to be <010> or <011> [162]. The morphology evolution and growth rate quantification of each pattern from the four groups are demonstrated in Figure 3.11-10.

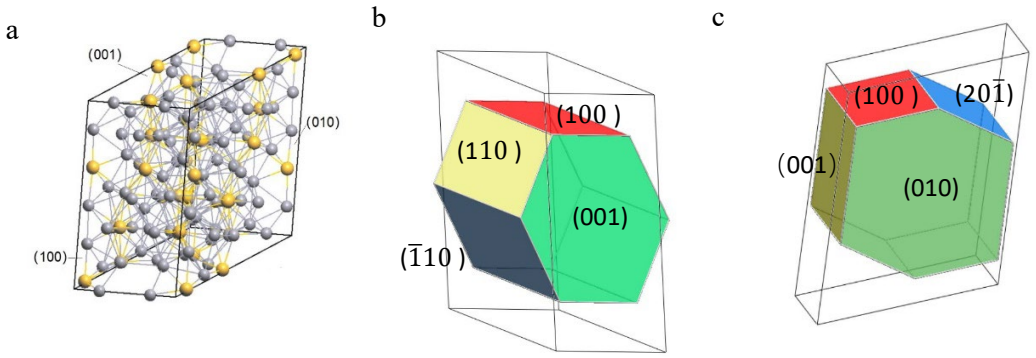

Figure 3.10 (a) Unit cell; (b) simulated planes of the plate-like $Al_{13}Fe_4$ intermetallic; (c) simulated planes of the hexagonal tabular $Al_{13}Fe_4$ intermetallic.

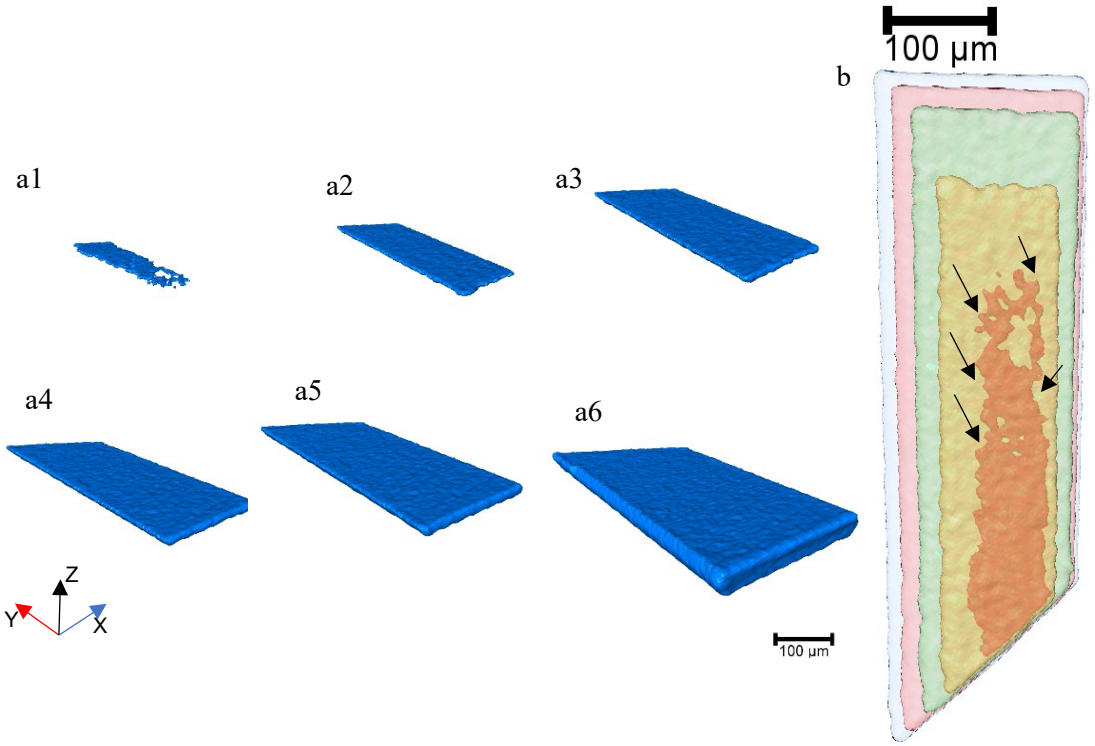

Figure 3.11 (a1-a4) 3D rendered volume of plate-like $Al_{13}Fe_4$ at t1, t1+10 s, t1+20 s, t1+30 s, t1+ 40 s , t1+180 s; (b) Transparent image of plate-like $Al_{13}Fe_4$ at t1, t1+10 s, t1+20 s, t1+30 s, t1+ 40 s.

The majority of the observed particles are plate-like. One example (number 1 marked in Figure 3.2) is shown in Figure 3.11 a1-a6 at t_1, t_1+10 s, t_1+20 s, t_1+30 s, t_1+40 s, t_1+180 s, clearly showing the growth anisotropy. t_1 is the first time when the plate-like pattern appears in the selected field of view. Figure 3.11-b presents the evolution of the plate-like pattern in the first 40 seconds overlapped together. The first particle is in the shape of a thin plate in Figure 3.11-a1. A series of re-entrant corners were formed along the edges of the plate, as pointed out by the black arrows in Figure 3.11-b. This repeated formation of re-entrant corners may contribute to the anisotropic growth and results in plate-like intermetallics with high aspect ratios. This growth behaviour of $Al_{13}Fe_4$ was also observed by an in-situ radiographic observation [10].

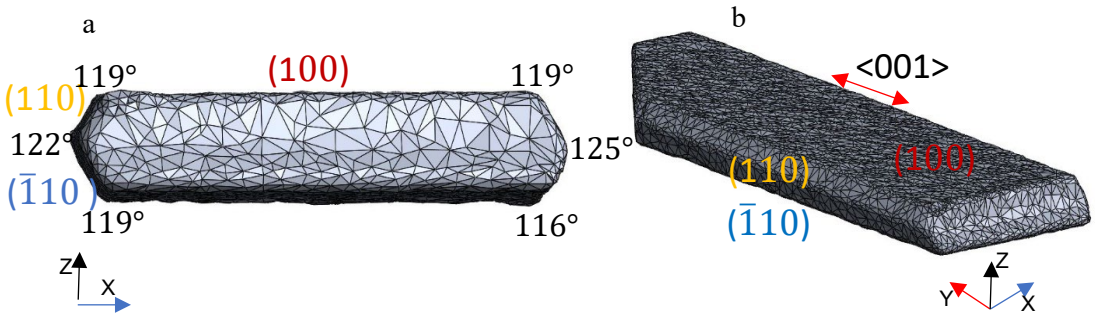

Figure 3.12 Meshed plate-like intermetallic and the angles between different facets:(a) front view; (b) side view.

Table 3-1 d-spacing and interplane angles of Al13Fe4 intermetallic

Planes	(001)	(20$\bar{1}$)	(110)	($\bar{1}$10)	**d-spacing(nm)**
(100)	107.69°	143.89°	118.7°	-	1.476
(001)	-	108.42°	98.39°	-	1.188
(20$\bar{1}$)	-	-	112.82°	-	0.735
(110)	-	-	-	122.62°	0.709

Figure 3.12 shows the meshed intermetallics and the angles between different facets were measured. Figure 3.12-a shows the front view of one plate-like crystal. All of the six proximal angles of this crystal are around 120°. According to Table 3-1, the angles between (100) and ($\bar{1}$10) planes, between (110) and ($\bar{1}$10) planes are both around 120°. This allows us to index the bounding facets to be (100), (110) and ($\bar{1}$10) as shown in Figure 3.12-a. The extension direction of this crystal is <001> as shown in Figure 3.12-b. The simulated crystal shape (Figure 3.10-b) bounded by those planes is similar to Figure 3.12-b.

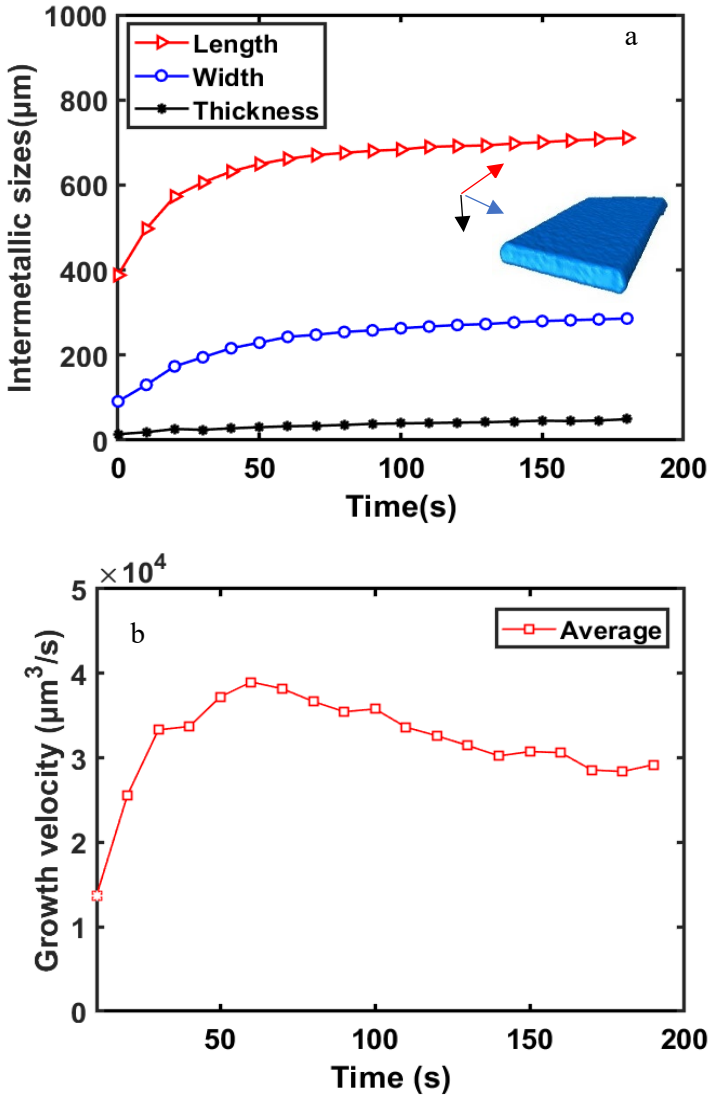

Figure 3.13 (a) Growth of plate-like particle in three dimensions;
(b) Growth velocity of the plate-like particle.

We then used the principal component analysis [13,174] to calculate the dimensions of the plate-like particles. The length, width and thickness of plate-shaped particles are the first, second and third principal components. Figure 3.13-a presents the size evolution of one plate-like intermetallic in three directions as a function of temperature. Red, blue and black arrows indicate the measured direction of length, width and thickness, respectively. At t_1, the plate-like structure has 388 μm in length, 91 μm in width and 14 μm in thickness.

It appears that the crystal grew rapidly at the early stage of crystallization especially at the length and width directions in the first 60 seconds. Then the growth rate slows down but continued to grow to 710 μm in length, 286 μm in width, and 49 μm in thickness in 180 s. This demonstrates the growth anisotropy of the $Al_{13}Fe_4$ crystal. It grew much faster in length and width than in thickness, which is most likely caused by the slow attachment of atoms on the flat faceted plane [179]. The quantified 3D dimensions of plate-like patterns can be used to verify the numerical modelling.

The average growth velocities of the plate-like intermetallics are presented in Figure 3.13-b. The average growth rate is the particle volume divided by its solidification time, while the instantaneous growth rate is the increased volume over 10 s divided by the interval (10 s). The selected plate-like particle has a growth rate of $1.4 \times 10^4\ um^3/s$ in the first 10 s, it then increased until a maximum value of $3.9 \times 10^4\ um^3/s$ in 60 s. Finally, it approached to a constant average growth rate of around $3 \times 10^4\ um^3/s$ in 190 s.

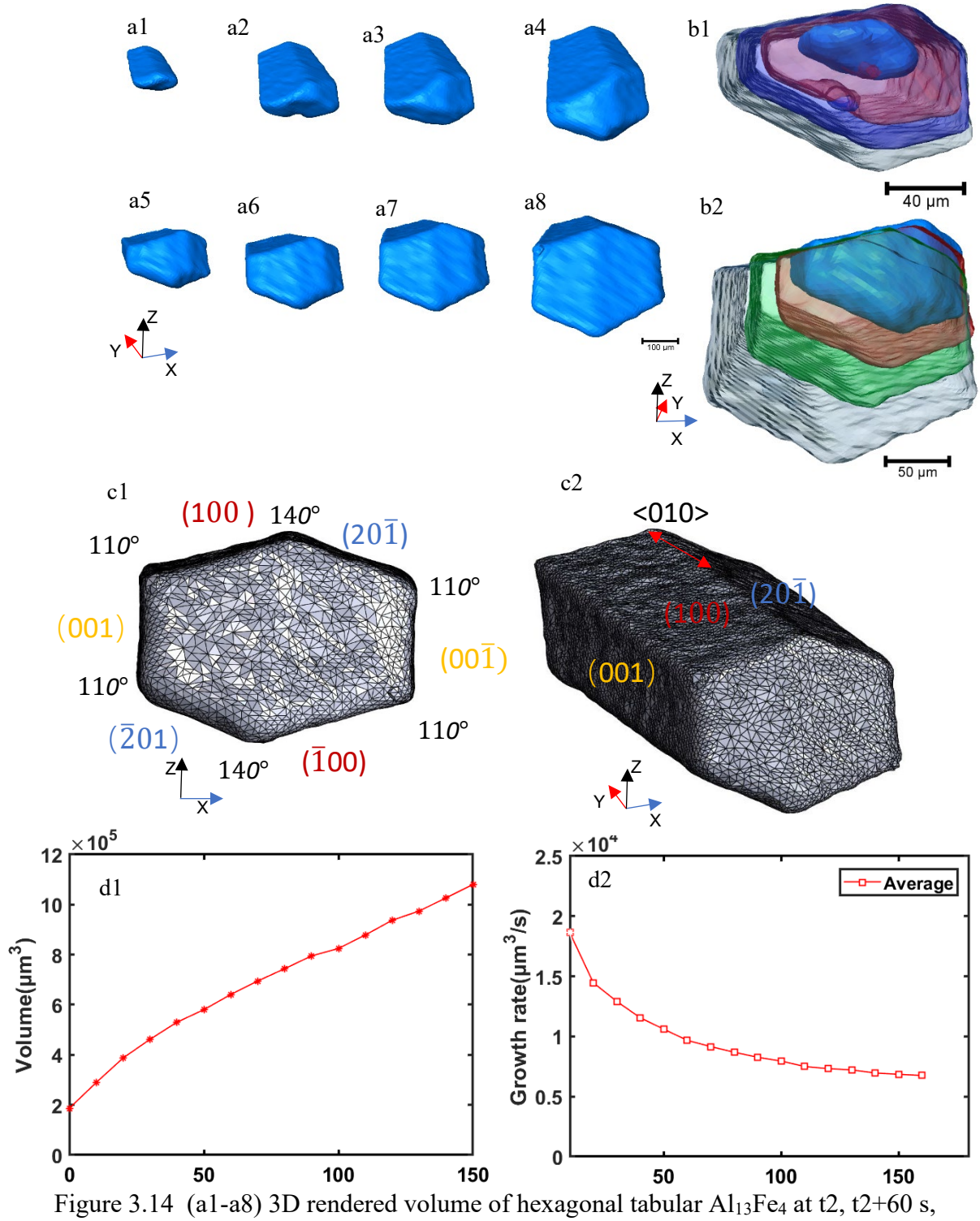

Figure 3.14 (a1-a8) 3D rendered volume of hexagonal tabular $Al_{13}Fe_4$ at t2, t2+60 s, t2+110 s, t2+160 s, t2+220 s, t2+ 330 s , t2+ 440 s t2+610 s; (b) Transparent images (c) Meshed hexagonal tabular intermetallic and the angles between different facets; (d1)Volume change of the particle as a function of time (d2) Growth velocity of the hexagonal tabular particle.

Figure 3.14-a presents the growth process of hexagonal tabular (number 2 marked in Figure 3.2) $Al_{13}Fe_4$ intermetallics. The intersection angles between the facets are different from the crystal in Figure 3.13. Figure 3.14-b shows the front view of the corresponding transparent images from Figure 3.14-a, which provide a clear formation process of the crystal pattern. The first particle in Figure 3.14-a1 has a hexagonal tabular shape rather than a thin plate as in Figure 3.13-a. It first extended in y-direction towards liquid. It then coarsened in z-direction while the shape of the crystal was maintained. The crystal grew into a hexagon with almost equal edge length, different from the one in Figure 3.13. The measured angles between facets are about 110° and 140°, as shown in Figure 3.14-c1. According to Table 1, the angle between (100) and (001) planes is 107°, while the angle between (100) and $(20\bar{1})$ is 143°. Hence, we can index the bounding facets to be (100), (001) and $(20\bar{1})$ as shown in Figure 3.14-c1. The extension direction for this crystal was subsequently identified to be <010>. The simulated crystal shape bounded by these planes is shown in Figure 3.10-c, which closely resembles the shape of the hexagonal tabular crystal in Figure 3.14-c. The volume change of the particle during growth was quantified as shown in Figure 3.14-d1, the first pattern that was observed by tomography has the volume of $1.8 \times 10^5 \mu m^3$. After 150 seconds, the volume is increased to $10.8 \times 10^5 \mu m^3$. Figure 3.14-d2 present the average growth velocities. The particle has the highest average growth rate of $1.8\ \mu m^3/s$ in the beginning, it then slowed down to a value of $0.7\ \mu m^3/s$. This growth behaviour may be due to slow atom attachment on all highly ordered faceted planes.

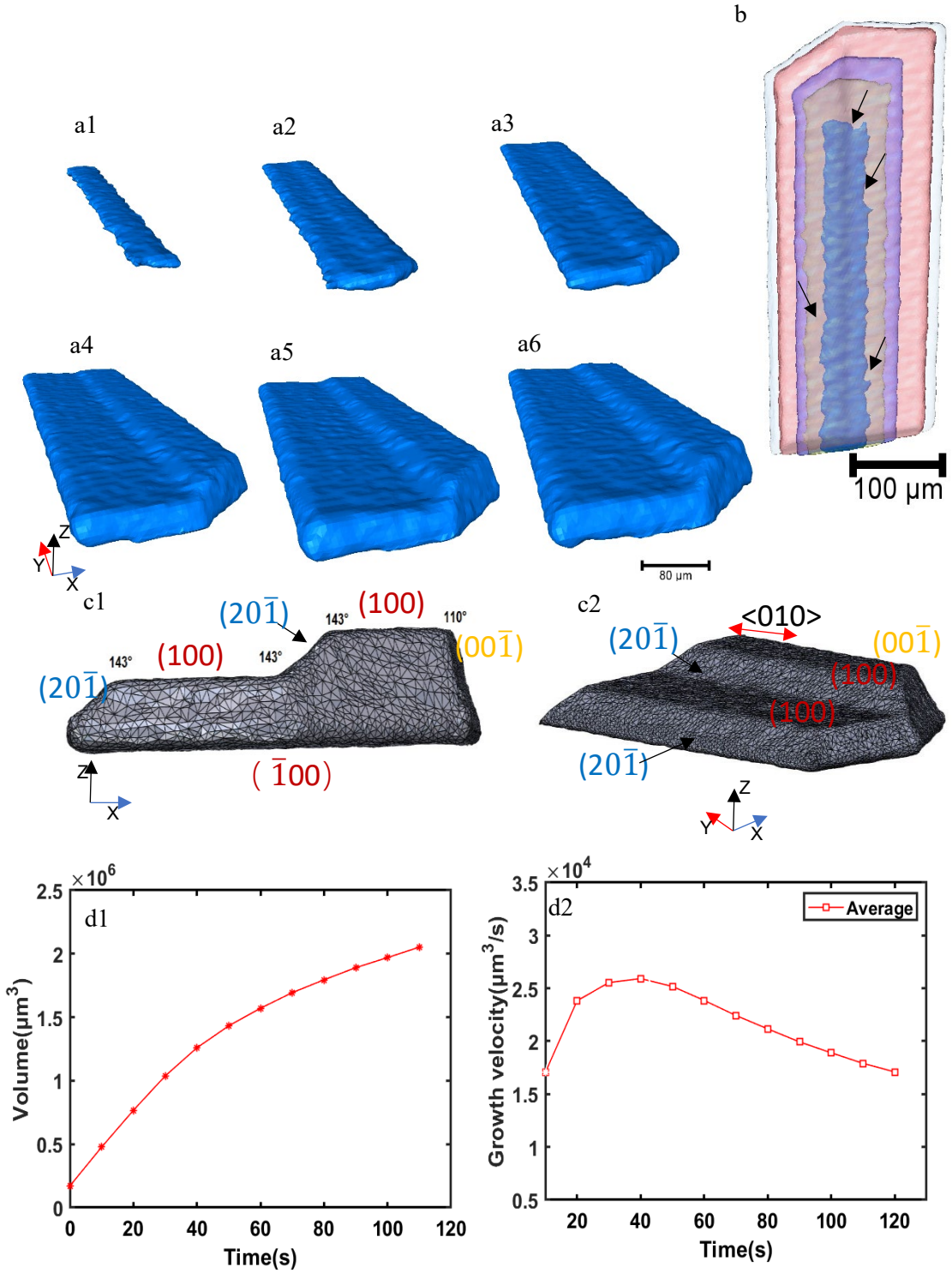

Figure 3.15 (a) 3D rendered volume of stair-like $Al_{13}Fe_4$ at t3, t3+10 s, t3+20 s, t3+60 s, t3+100 s , t3+110 s; (b) Transparent image of stair-like Al13Fe4 t3, t3+10 s, t3+20 s, t3+ 100 s , t3+110 s; (c) Meshed stair-like intermetallic and the angles between different facets; (d1)Volume change of the stair-like particle as a function of time (d2) Growth velocity of the stair-like particle.

Another morphology is stair-like (number 3 marked in Figure 3.2), as shown in Figure 3.15-a and Figure 3.15-b. It can be seen that initially, a plate-like crystal form (Figure 3.15-a_1 and a_2). Multiple re-entrants were also observed in Figure 3.15-b. Later, part of the crystal on the flat surface started to thicken at a faster rate than the rest of the plate, forming a stair (Figure 3.15-a_3 to a_6). Figure 3.15-c1 and Figure 3.15-c2 show the facets of the meshed stepped intermetallic. Similarly, we first measured the angles between different facets as shown in Figure 3.15-c1. Then according to Table 3-1, we indexed the bounding planes. Stairs were frequently observed on the (001) facet of β-AlFeSi intermetallics in solidified Al-Si-Mg-Fe alloys, which were caused by the presences of lattice faults [179]. A similar mechanism can be used to explain the stair-like $Al_{13}Fe_4$ intermetallic formation: during $Al_{13}Fe_4$ growth, a fault could form on the (100) plane, resulting in low energy sites for atoms to deposit, forming a stair on top of the (100) facet. The volume of this pattern increased to $2.05 \times 10^6 \mu m^3$ in 110 s from $1.7 \times 10^5 \mu m^3$ in Figure 3.15-d1. The quantification of the average growth velocities is presented in Figure 3.15-d2. The average growth velocity increased from $1.7 \times 10^4\ \mu m^3/s$ to $2.5 \times 10^4\ \mu m^3/s$ in the first 40 s, it then reduced to $1.7 \times 10^4\ \mu m^3/s$.

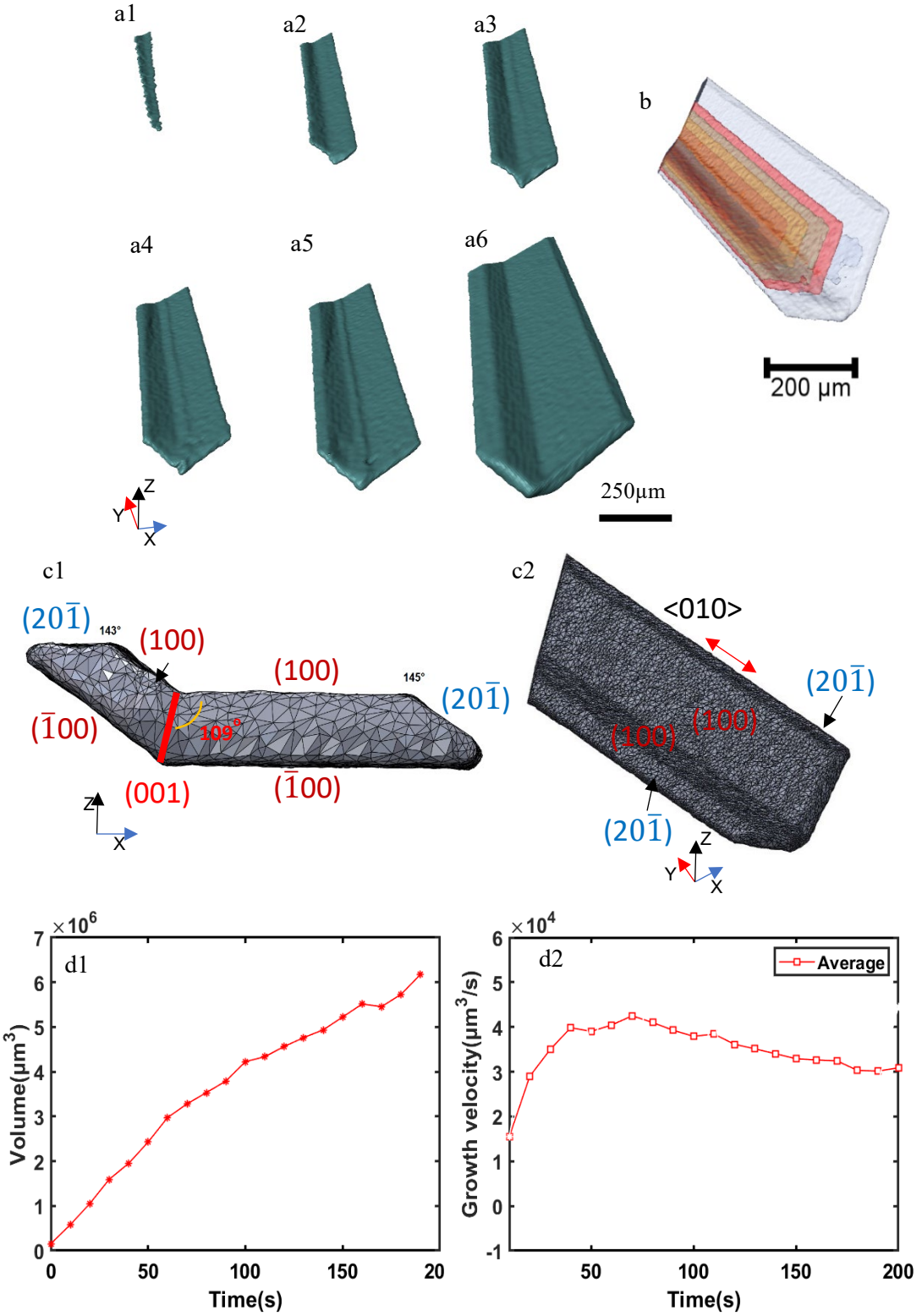

Figure 3.16 (a) 3D rendered volume of V-shaped $Al_{13}Fe_4$ at t4, t4+10 s, t4+20 s, t4+30 s, t4+40 s , t4+190 s; (b) Transparent image of V-shaped $Al_{13}Fe_4$ t4, t4+10 s, t4+20 s, t4+30 s, t4+ 40 s , t4+190 s; (c) Meshed V-shaped intermetallic and the angles between different facets; (d1)Volume change of V-shaped particle as a function of time (d2) Growth velocity of the V-shaped particle.

The last morphology is V-shaped (number 4 marked in Figure 3.2) in Figure 3.16-a and b, which have the lowest quantities. Only three intermetallics out of 62 were V-shaped. Figure 3.16-c1 and Figure 3.16-c2 show the front view and side view of a V-shaped particle. Li et al [162] observed a $Al_{13}Fe_4$ particle by SEM with similar morphology (called as bended particle in their study), and suggested that it is a twinned particle. For $Al_{13}Fe_4$ crystal, (001) plane was proposed to be the possible twinning plane [10,162,180]. Here, the V-like structure can be considered as twins connected by two plate-like patterns which share a common plane. Here to identify and index the facets of the bended crystal, we also measured the angles between different facets, as shown in Figure 3.16-c1. We started with two angles around 140° in Figure 3.16-c1. Since the interplane angle between (100) and $(20\bar{1})$ is 143.9°, the bound facets of the angles were indexed to be (100) and $(20\bar{1})$. According to the shape of the crystal, we can identify a twinning plane marked by a red line. The measured angle between the red line and the top flat facet is about 109°. From Table 3-1, We know the angle between (100) and (001) is 107.7°. Hence, the twinning plane in the red line is highly likely to be (001) as suggested by Li et al [162].

The growth mechanism of the V-shaped intermetallic is proposed to be as follows. First, an $Al_{13}Fe_4$ intermetallic was nucleated and grew into a small plate-like particle extending in <010> direction. This compound has a tendency to twin, and so a stacking fault relates to (001) plane may occur. The intermetallic was then extended in the reflected direction of the (001) twinning plane. Finally, the V-shaped intermetallic was bound by low index faces (100), (001) and $(20\bar{1})$.

The intermetallic grew to $6.18 \times 10^6 \mu m^3$ in 190s in Figure 3.16-d1 continually. The average growth rate first increased then decreased. As shown in Figure 3.16-d2, it has a

growth velocity of $1.5 \times 10^4\ \mu m^3/s$ in the first 10 seconds, it then increased until a maximum value of $4.2 \times 10^4\ \mu m^3/s$ in 70 seconds. Finally, the average growth rate reduced to around $3 \times 10^4\ \mu m^3/s$.

3.3.4 Crystal-crystal interactions

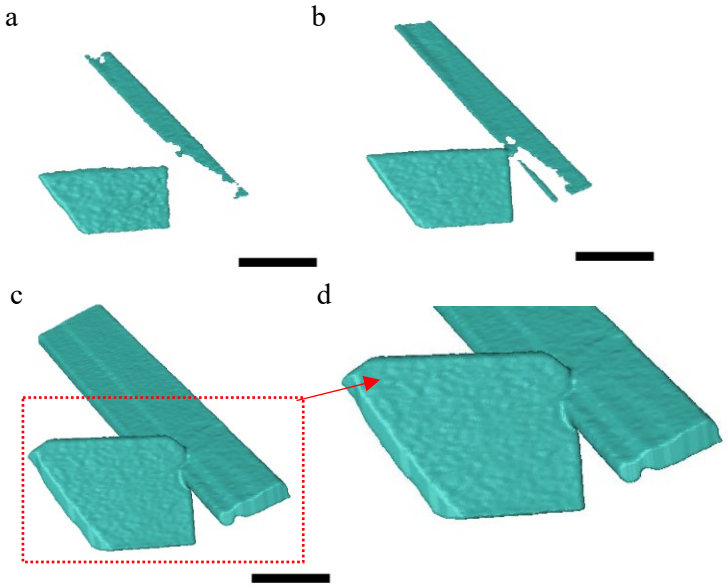

Figure 3.17 (a-c) Impingement growth mechanism at t5 +10 s, t5 +20 s, t5 +190 s; scale bar:200µm (d) Enlarged view

Interactions between intermetallics during growth, mainly impingement, have also been observed, as depicted in Figure 3.17-a to d. When two or more intermetallics grow towards each other, they will impinge and insert into one another. Before impingement (Figure 3.17-a), the two crystals are both platelet-like. Figure 3.17-b and Figure 3.17-c show that the two crystals grew into each other at an angle. One of the crystals on the right-hand side, after impingement, became stair-like crystal (Figure 3.17-c and Figure 3.17-d), indicating that crystal-crystal interactions may alter the shape of the intermetallics, for instance, from plate-like to stairs. However, even faster tomographic scans are required to reveal this phenomenon in more detail.

3.3.5 Internal defect formation

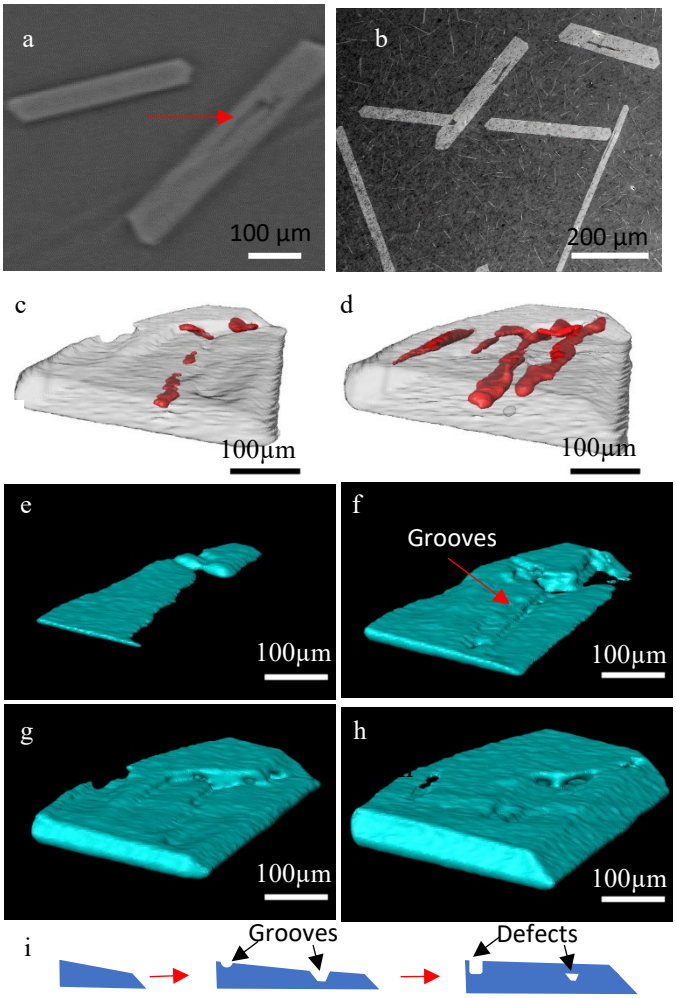

Figure 3.18 (a) and (b) 2D slices of the Al13Fe4 particle; (c) and (d) internal defects at t6 +160 s, t6 +560 s. scale bar:100µm (e-h) morphology of the crystal with internal defects at t6+30 s, t6 +90 s, t6 +160 s, t6 +560 s; (i) Schematic diagram of the defects formation process.

An orthogonal cross-section slice extracted from the tomography shows internal defects (dark region, pointed by a red arrow) in the $Al_{13}Fe_4$ crystals (bright region) as displayed in Figure 3.18-a. This kind of defects was also confirmed by SEM characterization (in Figure 3.18-b). Figure 3.18-c and Figure 3.18-d show the morphology of the internal defects in 3D (red coloured), which were connected to the crystal surface and appears to be hole-like. The shape of the crystal was rendered as transparent. The hole-like defects were not porosities but filled with aluminium melt since they have the same image

contrast as the melt. in Figure 3.18-e to in Figure 3.18-h demonstrate the surface morphology of a crystal with internal defects in 3D at t_6+30 s, t_6+90 s, t_6+160 s and t_6+560 s. At the early stage of crystal formation, some irregularities appeared on the supposedly flat surface, which became grooves as shown in in Figure 3.18-f. The grooves appear to be engulfed later on during solidification, leading to the formation of internal defects/holes. The process was schematically shown in in Figure 3.18-i. Similar defects or holes in faceted Ge crystals were also observed by Shahani et al.,[181] in Al-Ge alloys, and their formation was attributed twinning and plate branching. The surface defects of faceted Al_5FeSi intermetallics observed in Al-Si alloys [30] was attributed to the physical interaction of the intermetallics with aluminium dendrites.

3.3.6 Potential growth hypothesis

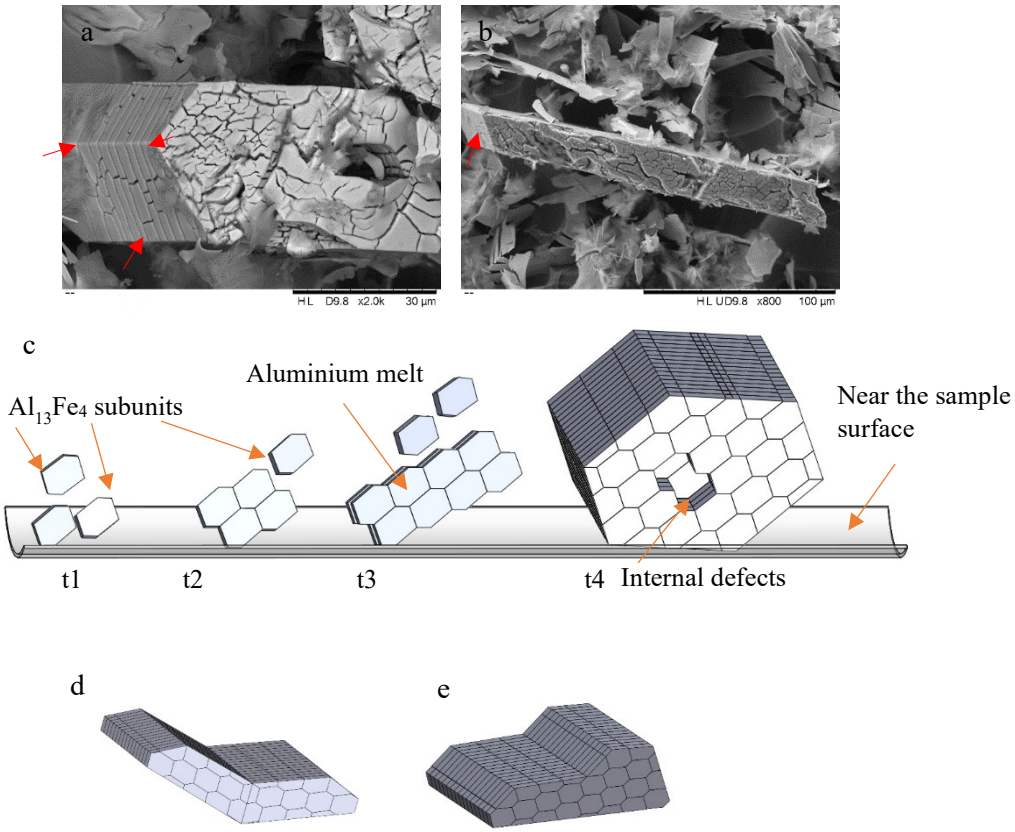

Figure 3.19 (a-b) SEM images of Al13Fe4 intermetallics after deep etching; (c) Schematic diagram of the formation mechanism of Al13Fe4, where t1-t4 are at different stages of solidification processes; (d) V-shaped structure; (e) Stair-like structure.

Figure 3.19-a and Figure 3.19-b reveal the SEM images of deeply etched $Al_{13}Fe_4$ particles. During the etching process, aluminium acts as an anode, and the $Al_{13}Fe_4$ particles act as a cathode [182]. After deep etching, the aluminium matrix surrounding the iron intermetallics were dissolved, revealing $Al_{13}Fe_4$ blocks. The hexagonal tabular (Figure 3.19-a) and plate-shaped particles (Figure 3.19-b) were observed. There are also many cracks on the surface of the deep-etched particles and a large hole, although we cannot confirm whether the cracks and hole were formed during crystal growth or as a result of

deep-etching. On the side facets, the cracks seem to be organized (pointed by red arrows), dividing the crystal facets into many sub-units.

Here, we propose a hypothesis that the growth behaviour of $Al_{13}Fe_4$ intermetallic may be the oriented particle attachment [45]. There also is more widespread acceptance that crystals form through the assembly of building subunits/blocks [81,82], an alternative pathway for crystallisation. During the nucleation stage, precursors nucleated and grew into small crystal subunits (Figure 3.19 c-t1). As the temperature reduced, new subunits could form in the nearby region and attached together (The directed covalent bonding may tend to rotate the subunits towards the same crystallographic direction as the existing structure) to form a large crystal. Then this large one will coarsen as more subunits are attached (Figure 3.19 c-t2 and t3). Some faults might form during this process, leading to a change of the attached order and the formation of internal defects (Figure 3.19 c- t4) and various shapes (Figure 3.19 -d and 13-e). Similar mechanisms were proposed to describe the formation of faceted Al_2Cu intermetallics in Al-Cu alloy [183]. However, we do not have direct evidence to confirm this hypothesis in this study except that the SEM images (Figure 3.19 -a and Figure 3.19 -b) of deep etched samples shows that the crystals are cracked into regular subunits. A recent study by in situ X-ray radiography shows that the growth of $Al_{13}Fe_4$ is by repeated attachment of $Al_{13}Fe_4$ sub-platelets to its corners [10], which could be understood as oriented particle attachment. To prove or disprove this hypothesis, we need to carry out extensively more research, including (1) nano-scale in situ TEM [80] or X-ray tomography [184] to observe the nucleation process of intermetallics which the aim to identify the subunits; and (2) even fast micro-scale tomography (sub-second) [135] to visualize the particle attachment process if it happens.

3.4 Summary

In summary, the formation of $Al_{13}Fe_4$ intermetallic in a solidifying Al-5wt% Fe alloy was quantified via 4D synchrotron X-ray imaging. The in-situ solidification under a slow cooling rate ($0.1℃/s$) was performed at scan intervals of 10 s, which allows us to observe the rapid nucleation and growth of faceted $Al_{13}Fe_4$ intermetallic. The work demonstrates that high-speed synchrotron X-ray tomography can be a useful tool to reveal the dynamic of faceted crystal growth. The following conclusions can be made:

1. Regarding the nucleation of $Al_{13}Fe_4$, the intermetallics (more than 95%) prevalently nucleated near the melt surface and the rest nucleated on the intermetallics formed earlier. The number of nucleation sites or nucleation density as a function of the temperature follows a Gaussian distribution, providing a sufficient equation for numerical modelling of intermetallic growth.
2. Individually faceted intermetallics were classified and quantitated. Four types of intermetallics were found based on different morphologies, which are plate-like, hexagonal tabular , stair-like and V-shaped. The variation in morphologies was explained by the crystal structure and twinning of the particle. Both volume change and growth velocity of the formation processes were provided.
3. The processes by which hole-like defects form, on the surface and inside the faceted $Al_{13}Fe_4$ intermetallic, were observed.
4. A potential hypothesis of oriented particle attachment was proposed to describe the faceted crystal growth and internal defect formation. However,

even faster tomography with higher resolution is required to observe the attachment process in solidifying $Al_{13}Fe_4$ intermetallics.

Chapter 4: Revealing growth mechanisms of faceted Al_2Cu intermetallic compounds via high-speed Synchrotron X-ray tomography*

* This chapter has been published in Acta Materialia.

Zihan Song[a], Oxana V. Magdysyuk[b], Tay Sparks[a], Yu-Lung Chiu[a], Biao Cai[a], Growth Dynamics of Faceted Al13Fe4 intermetallic Revealed by High-speed Synchrotron X-ray Quantification, Acta Materialia. (2022) 117903, https://doi.org/10.1016/j.actamat.2022.117903.

a.School of Metallurgy and Materials, University of Birmingham, Birmingham, UK

b.Diamond Light Source Ltd, Harwell Science and Innovation Campus, Didcot, UK

Acknowledge of Collaborative Work:

Zihan Song: Writing-Original draft, Methodology, Validation, Investigation; Oxana V. Magdysyuk: Investigation; Tay Sparks: Investigation, Yu-Lung Chiu: Validation, Biao Cai: Writing-Review & Editing, Conceptualization, Investigation, Supervision, Funding acquisition.

4.1 Introduction

Understanding microstructure formation is key in a broad range of solidification processes ranging from casting to welding [3,50,185]. The morphologies of solidified microstructures were classified into faceted and non-faceted patterns [186]. Growth mechanisms of non-faceted patterns, including cellular and dendrites, have been extensively advanced thanks to our new capabilities in experimental techniques (e.g. in situ X-ray radiography [187] and tomography [7,8,188]) and numerical simulations [189]. However, faceted patterns, which many intermetallic compounds (IMCs) grow into, have received much less attention. Regardless, faceted IMCs are of significance, impacting both the mechanical and functional properties of materials. For instance, in aluminium alloys, many faceted particles including plate-like $Al_{13}Fe_4$ [10,190], I-shaped Al_3Ni [191], polyhedron Al_6Mn [156] and Al_2Cu [192], could form, all of which play an important role on the mechanical and corrosion properties of Al alloys [193,194].

One interesting phenomenon regarding faceted crystals is the formation of faceted dendrites observed in various alloy systems, such as Cu_6Sn_5 in Sn-4.2Cu alloy [46], I-AlMnBe phases in Al-6Mn-2.5Be alloy [47] and Al_3Sc in Al-2wt%Sc alloy [48]. Regarding the dendritic growth mechanism, the classic view is a morphological instability of the solid-liquid interface that develops into dendritic shapes with branches along preferred crystallographic directions [50]. However, these mechanisms may not be applicable to faceted crystals due to their highly anisotropic crystal growth kinetics. Previous studies proposed a twin-related re-entrant edge mechanism to explain the growth of faceted Silicon [65,66], Germanium [68] and $Al_{13}Fe_4$ intermetallic [10], all with plate-lets morphologies. However, whether this mechanism can be applied to faceted dendrites is still unknown and many crystals do not form twins during formation. Al_2Cu is a typical

intermetallic formed in Al-Cu based alloys. It has body centre tetragonal crystal structures (a = b = 0.6063nm, c = 0.4872nm) [195]. Previous studies have shown that it can grow into L-shape, hollow-rectangular and dendritic shape [49,110,183,196]. We also observed L-shape, and dendritic Al_2Cu patterns in an Al-45wt%Cu sample melt and solidified in a differential scanning calorimetry (see the supplementary figure s1). However, not much work has been done to understand the transitions between these growth patterns, and the mechanism for the formation of dendritic Al_2Cu has not been clearly elaborated.

The morphologies of IMCs are influenced by external growth conditions [197], including temperature gradients, cooling profiles and magnetic fields. In recent decades, magnetic fields have been proposed as an efficient method to alter the solidification microstructures. The mechanisms are mainly based on magneto-hydrodynamics (MHD), which includes magnetic damping, magnetic stirring and thermoelectric magnetohydrodynamics. Under a static magnetic field, magnetic damping is the interaction between the applied magnetic field and fluid flows, which can generate Lorentz force to slow down the fluid flows [96]. The interaction between the thermoelectric currents (due to Seebeck effect) and applied magnetic field can also produce Lorentz force but generate flows [22,98,198,199]. This effect is contrary to magnetic damping. For an alternating magnetic fields, magnetic stirring [200] can be induced that may cause temperature and concentration fluctuation in the melt. Recent work shows that MHD effects can be controlled in various solidification settings, from driving solute segregation via thermoelectric effect, to solute mixing and microstructure refinement via magnetic stirring [201]. Magnetic fields have also been shown to influence the growth morphology of Al_2Cu intermetallic. Under a high axial magnetic field (up to 12 T), Li et al. demonstrated that the Al_2Cu crystals were oriented with the <001>-crystal direction along the magnetic field [202]. Wang et al. revealed the

structure refinement of Al_2Cu phase during directional solidification under a high (12T) magnetic field [22]. Li et al.[110] shows that a significant axial macro segregation of the primary Al_2Cu was formed under a static transverse magnetic field during directional solidification. However, the effect of sample rotation under magnetic fields on Al_2Cu crystal formation has rarely been studied.

High-speed X-ray tomography (recording tomograms in seconds or less) has advanced our understanding of nucleation, growth and coarsening of non-faceted crystals during alloy solidification [7,135,203], and recently, it has been applied to study faceted Si [204] and $Al_{13}Fe_4$ particles [190] in Al alloys. Here we used high-speed synchrotron X-ray tomography to study the growth of faceted Al_2Cu crystals under various solidification conditions including upwards and downwards solidification, and rotational solidification under magnetic fields. This work generates fresh insights into the growth mechanisms of faceted crystals, also discusses how the thermo-solute flow, including magnet field-driven flow, influences the microstructures during solidification.

4.2 Materials and Methods

4.2.1 Sample preparation

The Al-45wt% Cu master alloy was used in this study. Cylindrical specimens with a diameter of 1.8 mm and length of 100 mm were machined via a wire electrical discharge machining.

4.2.2 In-situ synchrotron x-ray tomography

A bespoke temperature gradient stage [201] in Figure 4.1 was used to control the melting and solidification of the Al-45wt%Cu sample, which can be coupled with high-speed synchrotron tomography to capture solidification processes in situ and in real-time. As shown in ref [201], two heaters were used to allow a temperature gradient applied to the sample, allowing directional solidification. The samples were heated up until fully melted under an applied vertical temperature gradient, then held for another 10 min to achieve a steady state condition. The solidification experiments were carried out via cooling both heaters at a constant predefined cooling rate (CR) while keeping the temperature gradient (TG). A transverse static magnetic field with a strength of B=0.5 T using a permanent magnetic yoke can also be applied to the sample [201]. The distribution of the magnetic flux density surrounding the sample is in around 0.5 T (supplementary figure s3). Six experiments were performed with different solidification conditions as shown in Table 4-1. A positive temperature gradient (TG) means that the top furnace is hotter than the bottom one, which allows upwards solidification, whereas a negative TG means the bottom furnace is hotter, allowing downwards solidification.

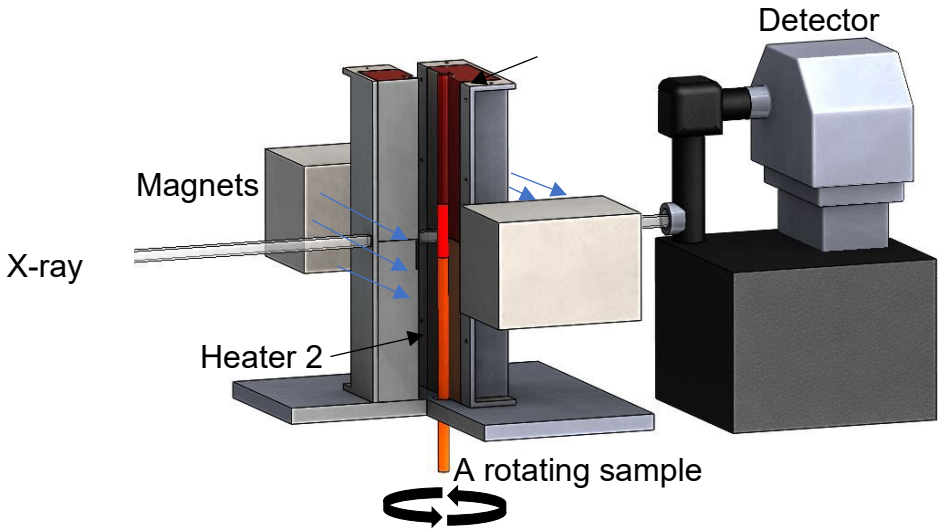

Figure 4.1 The schematic diagram of this experiment.

Table 4-1 Solidification conditions

Sample	CR	TG	B=0.5 T
A	0.05 ℃/s	0℃/mm	No
B	0.05 ℃/s	-4℃/mm	No
C	0.05 ℃/s	7℃/mm	No
D	0.05℃ /s	0℃/mm	Yes
E	0.02 ℃/s	7℃/mm	Yes
F	0.05 ℃/s	7℃/mm	Yes

The in situ solidification experiment was performed at I12 beamline, Diamond Light Source[116] using a 53 keV monochromatic X-ray beam. During the solidification process, a high-speed camera (PCO.edge) was set to obtain the tomograms in 5 seconds over 180° every 10 seconds, while the sample was rotating continuously. The images were cropped to 1600×1600 pixels. Each tomography consisted of 1000 projections. Savu system [205] was used to reconstruct the tomograms. The reconstructed volume has a voxel size of 3.24 μm^3.

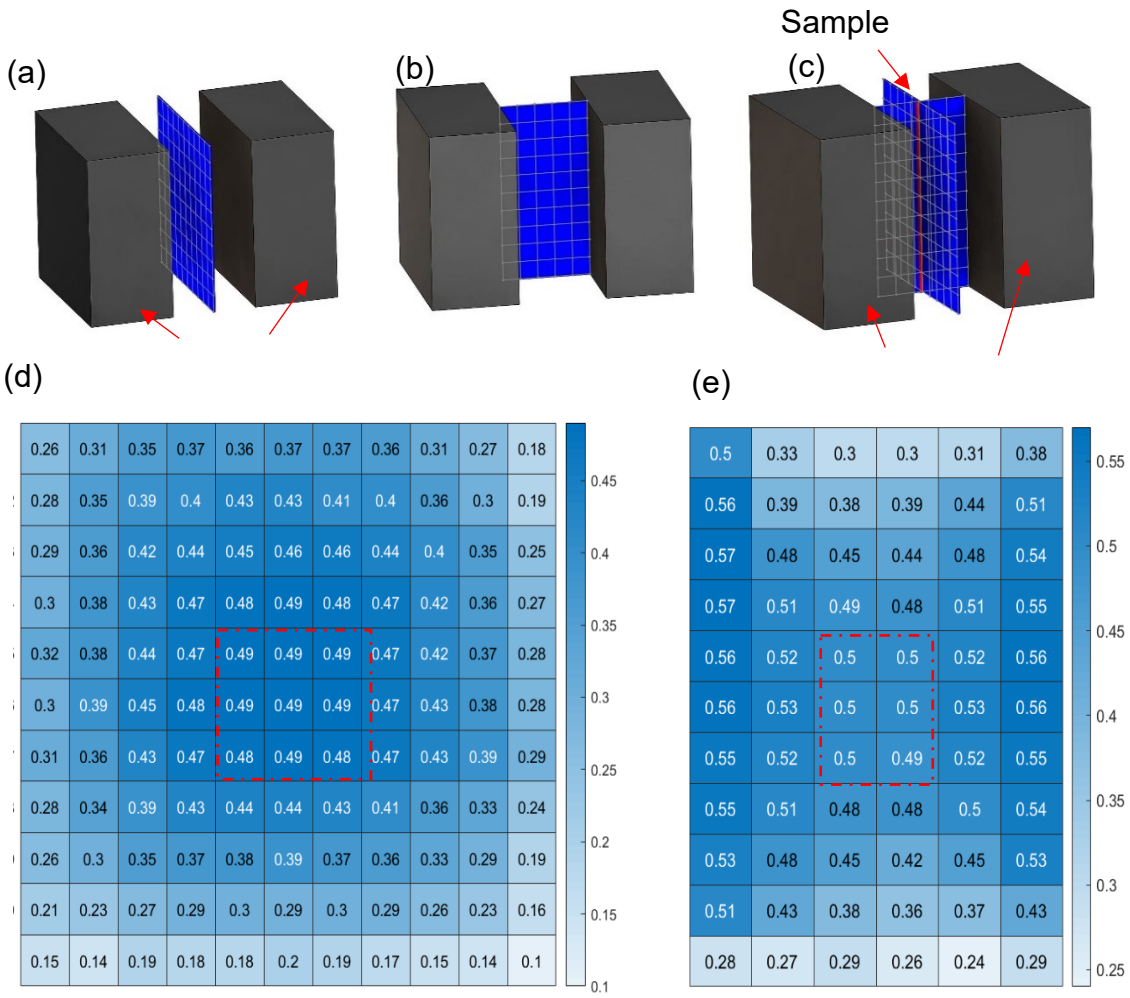

Figure 4.2 The schematic diagram of measured points between two magnets (a) perpendicular to the magnetic field, (b) parallel to the magnetic field; (c) the position of the sample; (d) The distribution of magnetic flux density of measured points in (a); (e) The distribution of magnetic flux density of measured points in (b).

Figure 4.2 shows the measured points and the distribution of magnetic flux density. A piece of paper was placed in the middle of the magnets that is perpendicular to the magnetic field as shown in Figure 4.2-a, 11 points were drawn in each row and column with an interval distance of 10mm. A handheld magnetic field gauss meter (GM04, Hirst Magnetics) was used to measure the magnetic flux density of the 121 points. The corresponding values are shown in Figure 4.2-d. Similarly, another piece of paper was placed in the middle of the magnets that is parallel to the magnetic field. 6 points in each row and 11 points in each column were drawn and measured, whose values are shown in Figure 4.2-e. Figure 4.2-c shows the position of the sample during tomographic scans. The surrounding magnetic flux density of the sample that was scanned is in the range of 0.48-0.50T.

4.2.3 Image processing

The 3D images were analysed by Avizo 2020.1 (ThermoFisher Scientific, USA). To segment the Al_2Cu crystals, a 3D anisotropic diffusion filter, followed by interactive thresholding was used. The thresholding values were chosen based on the Otsu's method [206] from Image J.

Figure 4.3 demonstrates the 2D images at sequences of image treatment, which are raw data (a), after de-noising (b), after thresholding process(c). Thanks to the large density difference between the Al matrix and Al_2Cu, the raw data has a good contrast difference between the two phases, providing a sharp interface. Figure 4.3-d plots the distribution of grey values between the Al matrix and Al_2Cu, indicating a large contrast difference. After de-noising, the contrast between the two phases is more diverse as presented in Figure 4.3-e. Finally, Thresholding values, which are based on Ostu's method from ImageJ, was chosen, as a result, the Al_2Cu phase was effectively segmented (Figure 4.3-c).

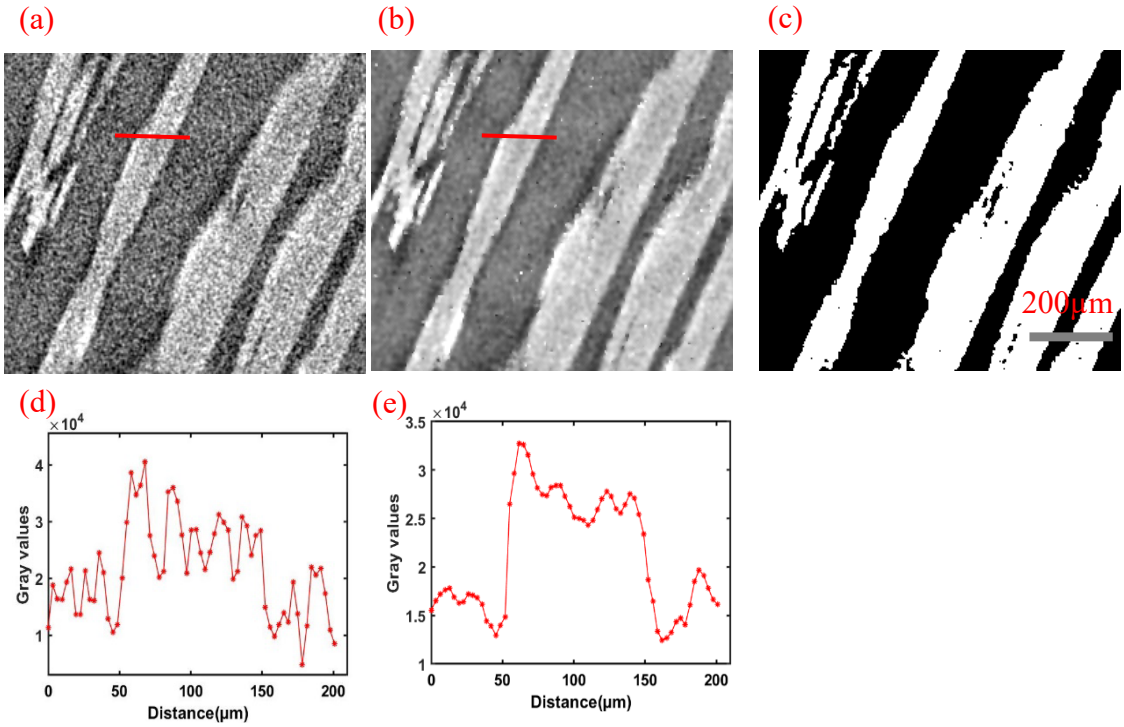

Figure 4.3 Image processing of Al_2Cu phase from synchrotron x-ray experiment (a) raw image (b) denoised image; (c) segmented Al2Cu phase; (d) Gray values of the region pointed by a red line in a; (e) Gray values after de-noising of the region pointed by the red line in(b).

4.2.4 SEM characterization and EBSD analysis

A sample of Al-45%Cu alloy (30 mm long, 1.8 mm diameter) was solidified inside a ceramic tube at a cooling rate of 0.05 ℃/s without temperature gradients and magnetic fields. The solidified specimen was then sectioned parallel to its longitudinal direction, which was ground using SiC papers in the sequences of #1200, #2500, #4000 on Struers Labopol-5. It was then polished using 'MD-Dac' cloth (Struers) with 3 μm liquid diamond suspension and finally using 'MD-chem' cloth with 0.04μm OPU (colloidal silica suspension).

The microstructural observation was carried out by using Tescan MIRA 3 SEM, equipped with an Oxford Instruments EBSD detector controlled by the AZtec software. The EBSD data was acquired at an accelerating voltage of 20 kV, a working distance of 15.8 mm, a tilt angle of 70 ° and a step size of 1.6μm in a square scan area of 1270 μm × 507 μm. The obtained data were interpreted by HKL Channel-5 Tango software to index the grain orientations.

After EBSD analysis, the sample was scanned by Synchrotron X-ray tomography at I12 beamline, Diamond Light Source, Oxford, to reveal the angles between the sectioned surface and the growth orientation of the dendrites. The raw images have 2560×2560×2150 pixels with a voxel size of $1.3\mu m^3$. The 3D images were analysed by Avizo 2020.1 (ThermoFisher Scientific, USA).

4.3 Results and discussion

4.3.1 Overall microstructural evolution

4.3.1.1 Solidification without magnetic fields

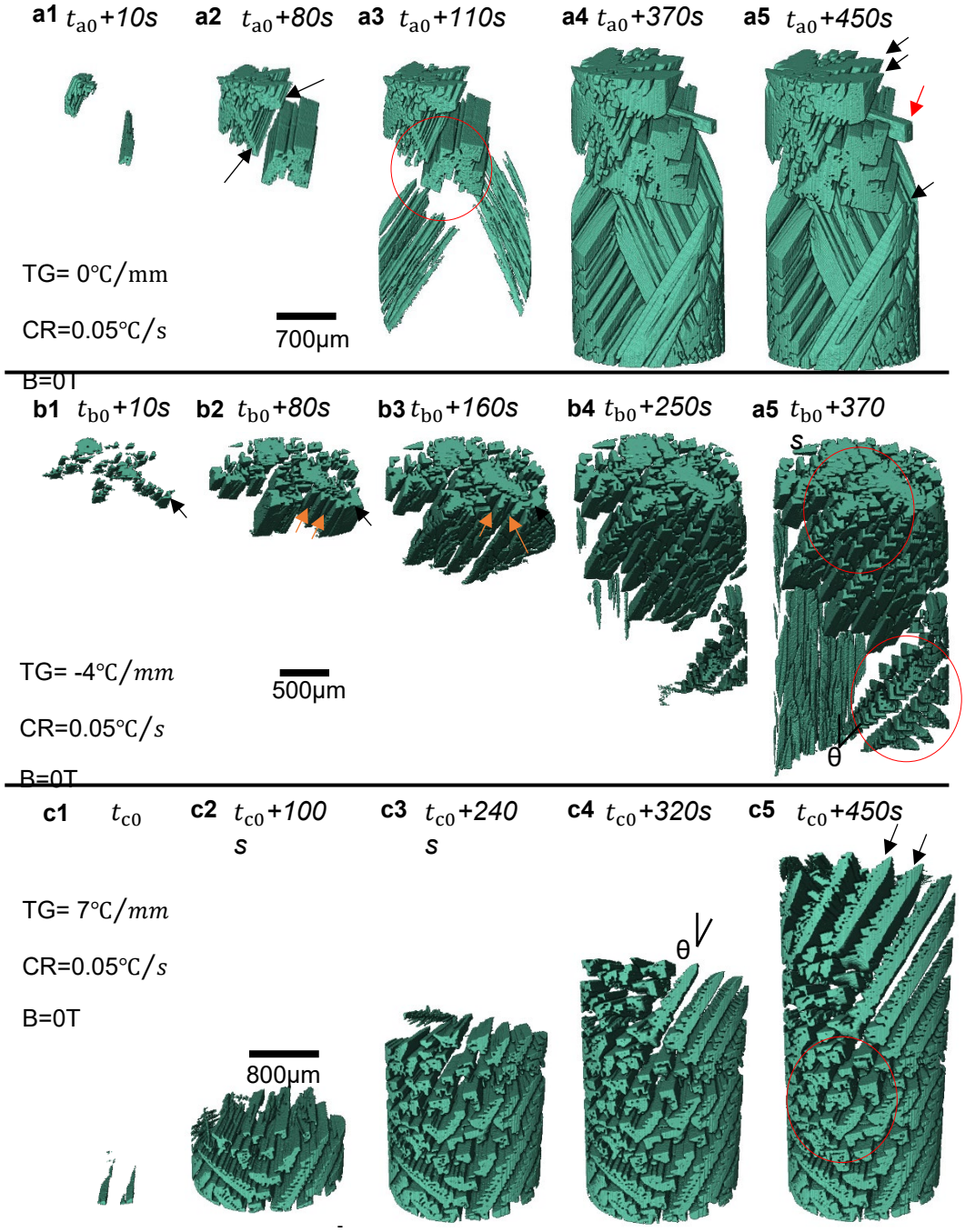

Figure 4.4 3D rendered volume of Al2Cu phase at different timestamp under solidification (a) conditions of A (CR=0.05℃⁄s, TG= 0℃⁄mm and B=0T); (b) condition B (CR=0.05℃⁄s, TG= -4 ℃⁄mm and B=0T); (c) condition C (CR=0.05℃⁄s, TG= 7℃⁄mm and B=0T).

Figure 4.4-a shows the volume rendered Al_2Cu phase after segmentation at different timestamps solidified under condition A (CR=0.05 ℃/s, TG= 0℃/mm, B= 0T). t_{a0} is the first time when the IMCs appeared in the field of view (FOV). The IMCs nucleated at the sample surface (Figure 4.4-a1). It grew horizontally towards the other side of the sample, then into a dendritic shape (Figure 4.4-a2). Later, more crystals formed and grew in different directions to fill the space (from Figure 4.4-a3 to a5). A few different morphologies were identified. One is the equiaxed-prism, which has a quasi-equiaxed cross-section plane while a prism structure in the through-thickness direction (marked by the red circle in Figure 4.4-a3). L-shaped patterns were formed near the edge of the sample (indicated by black arrows in Figure 4.4-a5). L-shaped particles refer to the long rod-like particle whose cross-section perpendicular to the growth direction is L-shaped. A hollow-rectangular pattern (marked by the red arrow) was observed which impinged into the equiaxed-prism structure in Figure 4.4-a5. The hollow-rectangular particles refer to the elongated particle whose cross-section is hollow-rectangular.

The downwardly solidifying microstructure under condition B (CR=0.05 ℃/s, TG= -4℃/mm, B= 0T) is shown in Figure 4.4-b. Here, multiple highly ordered L-shaped Al_2Cu were formed on the upper side of the FOV (Figure 4.4-b1), which then grew downwards, into faceted dendritic structures with secondary arms (pointed by orange arrows in Figure 4.4-b2 and b3). Another two new dendrites with the same orientation were formed in the middle region (marked by the red circle). Most of the primary dendrites tilted by about 40° from the vertical direction. However, in the left region of the sample, at the later stage of solidification, a cluster of L-shaped patterns grew downwards almost parallel to the vertical direction.

Figure 4.4-c shows the upward growth (growth rate of 7.7±0.3 μm/s) of Al_2Cu from the experiment C (CR=0.05 ℃/s, TG= 7℃/mm, B= 0T). The growth rate was calculated based on stabilized overall growth rates of Al_2Cu intermetallic compounds in the vertical direction (see the supplementary note). Two distinctive morphologies were observed: L-shaped (within the red circle in Figure 4.4-c5) and dendrites. The columnar faceted dendritic patterns (e.g. marked by the black arrows) have plate-shaped primary stems and small secondary arms with faceted planes and sharp corners. Around 11 dendrites, parallel to each other, tilted by about 30° from the vertical direction, were found. The dendrites observed are asymmetric. One side of the dendrite has multiple secondary branches, while the other side is almost flat.

4.3.1.2 Solidification under magnetic fields

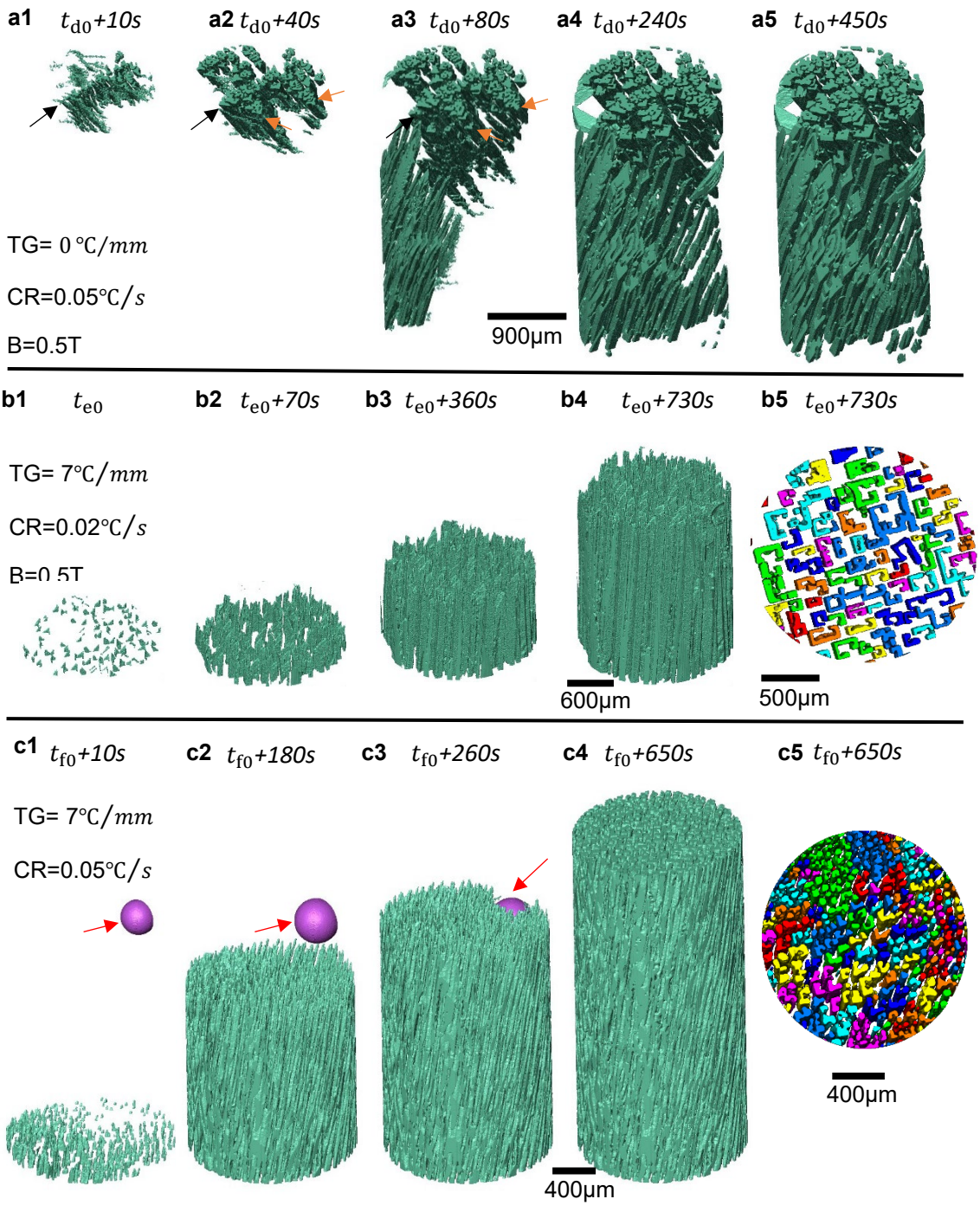

Figure 4.5 3D rendered volume of Al2Cu phase at different timestamp under solidification condition D (CR=0.05 ℃/s,TG= 0℃/mm and B=0.5T); (b) condition E (CR=0.02℃/s,TG= 7℃/mm and B=0.5T); (c) condition F (CR=0.05℃/s,TG= 7℃/mm and B=0.5T).

Three more experiments were performed to study the influence of the 0.5 T magnetic field on the morphology of Al_2Cu IMCs. A static transverse magnetic field (B=0.5T) was imposed while the sample was rotating for recording X-ray tomograms.

The formation of Al_2Cu under condition D (CR=0.05 ℃/s, TG= 0℃/mm, B= 0.5T) is shown in Figure 4.5-a. The Al_2Cu compounds appeared first at the top region of the FOV (Figure 4.5-a1), leading to the formation of a cluster of faceted dendrites Figure 4.5--a2). The growth direction of L-shaped patterns was no longer orientated to the transverse direction (Figure 4.5-a3), different from condition A under similar solidification condition but without the imposed magnetic field.

Figure 4.5-b shows the upwards growth of Al_2Cu under solidification condition E (CR=0.02 ℃/s, TG= 7℃/mm, B= 0.5T). Multiple L-shape, U shape and hollow-rectangular patterns (Figure 4.5-b2 to 3-b3) grew almost parallel to the vertical direction (z). The stabilized growth rate is about 3.5±0.2 μm/s. No faceted dendritic patterns were observed. The well-aligned growth of the IMCs along the vertical direction (z), which were different from sample C, indicates the heat flow in the melt had been modulated because of the imposition of the magnetic field. This also indicates there was no longer a horizontal temperature distribution under condition E. Furthermore, the size of the intermetallic of sample E ($9.5 \times 10^3 \pm 650$ μm^2 in area was 20 times smaller than that of sample C ($2.07\times 10^5 \pm 34000$ μm^2), and the primary pattern spacing was reduced. To calculate the primary dendrite arm spacing [207], we used:

$$\lambda = c\sqrt{\frac{A}{N}} \quad (1)$$

Where λ is the distance between each pattern, c is the coefficient that depends on its microstructure, 0.5 is chosen for a random array of points, and A is the selected area, and N is the number of patterns in the selected area. The primary pattern spacing is calculated to be 142.7 μm.

The growth process of Al_2Cu under solidification condition F (CR=0.05 ℃/s, TG= 7 ℃/mm, B= 0.5T) is displayed in Figure 4.5-c. Many fine L or U shape Al_2Cu intermetallic compounds grew upwards at a rate of about 9.9 ± 0.1 μm/s figure 3-c1), well-aligned along the z-direction with a slight tilt. A few non-faceted long cylinder-like intermetallic compounds were observed as well (Figure 4.5-c5) at the later stage of the solidification. Levelled solid/liquid front can be observed as shown in Figure 4.5-c2 and c3. The primary pattern spacing reduced from 142.7μm (sample E) to 88.4 μm (sample F), as the number of IMCs increased from 99 to 224. A spherical pore was also observed (purple coloured in Figure 4.5-c1, c2 and c3). Due to phase-contrast effect [208], the fringes at the edges of the pore were bright and have similar contrast as Al_2Cu. The pore was formed during the cooling process in the melt, which highly likely came from hydrogen [209] that tended to escape from the solution and form bubbles during solidification.

4.3.1.3 Heat flows and the effects of the magnetic field

It is known that the heat flow has a strong influence on the growth orientations of Al_2Cu intermetallic [12]. Hence the growth direction of Al_2Cu observed allows us to determine the heat flow direction of the sample during the experiments.

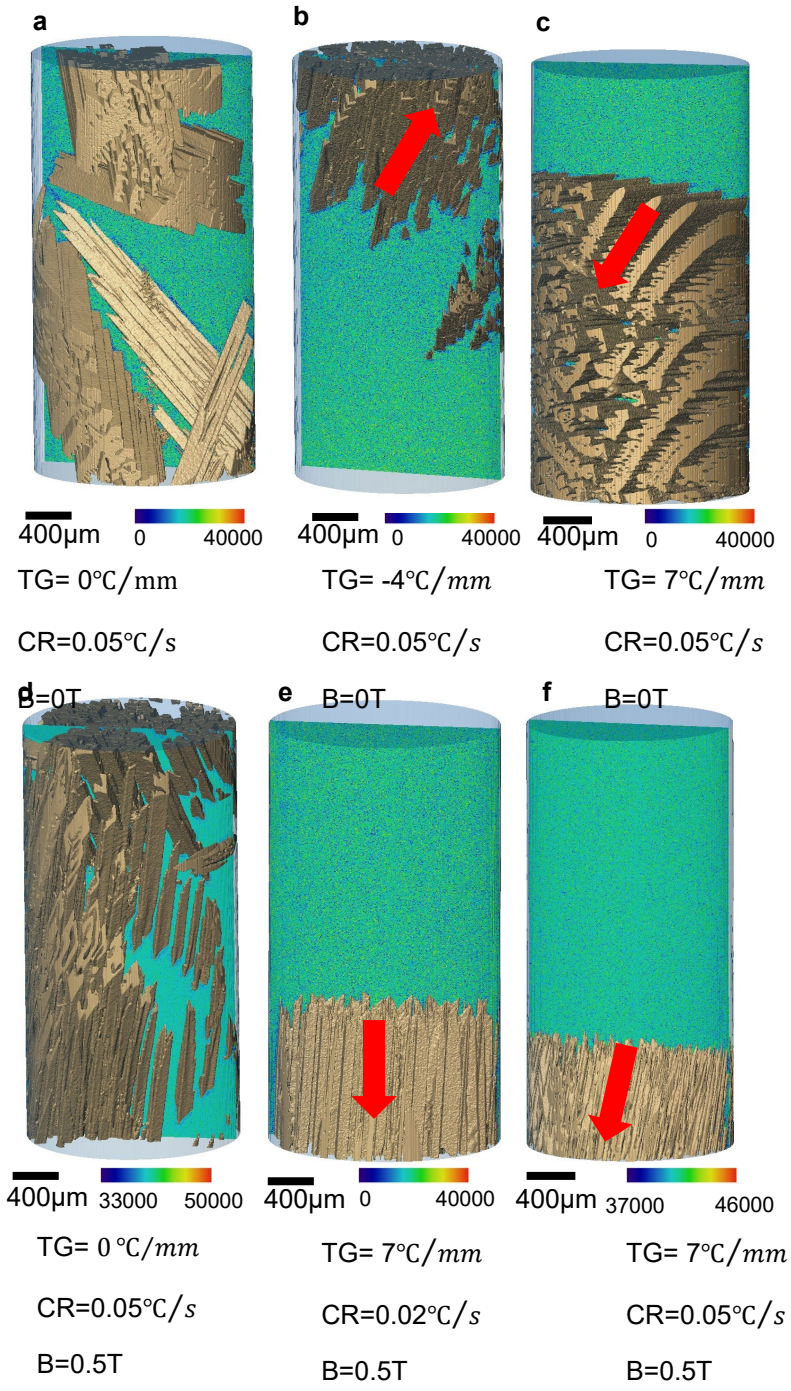

Figure 4.6 Composition distributions in six experiments.

Under solidification condition A, B and C, the orientation of the faceted dendrites is controlled by a heat flow resulted from the combination of vertical and horizontal temperature gradients. For sample A, which did not apply vertical temperature gradient but has a horizontal temperature gradient, a prism with an equiaxed shape formed, elongated along the horizontal temperature gradient, as shown in Figure 4.6-a. There were a few randomly oriented crystals, indicating that the heat flow is rather complicated and non-directional. For sample B, which has a vertical temperature gradient of -4℃/mm, the crystals grew downwards, titled about 40° from the vertical direction, as shown in Figure 4.6-b. For sample C, when applying a vertical temperature gradient of 7℃/mm, the crystals grew upwards, tilted about 30° respecting to the vertical direction in Figure 4.6-c. The tilted growth of crystals suggests that the heat flow deviated from the vertical direction. Possible heat flow directions are indicated by the red arrows in Figure 4.6-b and Figure 4.6-c for the two samples.

It is also noted that sample A, B and C were rotated. Here, we used the grey values of the tomograms to indicate and map the composition distribution as shown in Figure 4.6 a-c. No macro-segregation was observed, which suggests that sample rotation did not cause solute segregation in the melt during solidification. A previous study [210] shows that when using the accelerated crucible rotation technique to spin up the melt from static to a high rotation speed such as 2π rad/s, the flows were stirred by produced a shearing of the solution. In our experiments, after the sample was accelerated from static to a slower rotation speed of $\omega = \pi/5$ rad/s, it was held and rotating at this speed for another 10 minutes to achieve a steady-state condition before cooling. Therefore, the accelerated effect can be neglected.

The temperature gradient and cooling rate between sample C (CR=0.05 ℃/s ,TG= 7℃/mm and B=0T) and F (CR=0.05℃/s,TG= 7℃/mm and B=0.5T) are the same. But sample F was rotated in a magnetic field of 0.5 T during solidification, while sample C was not. Al_2Cu crystals formed in sample F were all basic unit shapes – fine, elongated and aligned well along the vertical direction, significant different from sample C (tilted, coarse plate-like columnar dendrites). This indicates that the heat flow direction in sample F was along the vertical direction (indicated by the red arrow in Figure 4.6-f) and there was no horizontal heat flow. It is likely that when rotating the melted Al-45wt%Cu in a static transversal magnetic field, a rotational flow on the horizontal plane could have been induced that homogenized the horizontal temperature gradient. A rotational flow or even swirling flow has already been proven to be induced under similar conditions numerically in our previous work [201].

The elimination of horizontal temperature gradients shows that an additional rotational flow might be induced in the transverse plane that homogenized the temperature. The question is what drives the flow. Our previous work [201] have shown that when rotating the directional solidifying samples inside a magnetic field, it can cause both electromagnetic stirring (EMS) and thermoelectric (TE) magnetic convection, both of which can induce flows in the mushy zone and the liquid zone. The strength of EMS is mainly determined by the sample rotation speed and magnetic field strength, both of which are the same for samples D, E and F. Therefore, if EMS was the controlling mechanism that drove the flow, the microstructure modification would be the same for D, E, and F samples. However, in our experiments, the substantial refinement of Al_2Cu was only observed in sample E and F when a temperature gradient was applied, but not in sample D. TE magnetic convection, on the other hand, is strongly related to the

temperature gradient as TE currents=$S\nabla T$ (where S is the Seebeck coefficient and ∇T is the temperature gradient). This indicates that TE magnetic convection might prevail in the sample E and F as the controlling mechanism that drives the flow. This peculiar flow might also push the solute out of the mushy zone, likely resulting in a homogenised solute layer above the solid-liquid interface absent of segregation [201]. Li et al. [110] carried out directional solidification experiments on Al-40wt%Cu alloys under a static transverse magnetic field of 0.5 T (noted their samples were not rotated). They found out that an axial macro segregation zone was formed, attributed to the TE magnetic convection [110]. Their work shows that TE magnetic convection can cause the redistribution of solutes. In Figure 4.6-e and f, macro-segregation was absent suggesting that rotating the sample within the 0.5 T magnetic field did not cause solute segregation.

It is less clear about what has caused the significant structure refinement. Wang et al. [22] showed that dislocations formed in Al_2Cu in directionally solidified Al-40wt%Cu under a 12 T magnetic field. They suggested that TEMF in solid Al_2Cu led to the dislocation multiplication and dendrite fragmentation during solidification, which is the main mechanism they proposed for the refinement of the structures. However, the effect of solute redistribution due to the very strong magnetic field on Al_2Cu refinement was not discussed. Cai et al. [201] showed that via simulation, on an Al-Si-Cu alloy, EMS and TEMHD combined flows in the melt can be controlled in a way to significantly refine microstructures during direction solidification. In this study, we suspect that the stirring flow caused by rotating the sample under a transversal magnetic field drive the solute from the mushy region, leading to the depletion of solute there and a decrease of the dendrite spacing. The next step would be to perform numerical simulations on hypereutectic Al-Cu alloys as in ref [201] to determine the flow conditions.

Experimentally, it would be necessary to develop methods to measure the magnetic field-driven flow as well.

4.3.2 Morphologies of Al_2Cu IMCs

From the six experiments, it can be shown that most of Al_2Cu crystals have a rod-like shape with L, U and hollow-rectangular cross-section, which we categorized as basic units. A few crystals have faceted dendritic patterns. To further investigate the development of these morphologies during solidification, we obtained some representatives of the compounds, as shown from Figure 4.7 to Figure 4.16.

4.3.3 Basic units

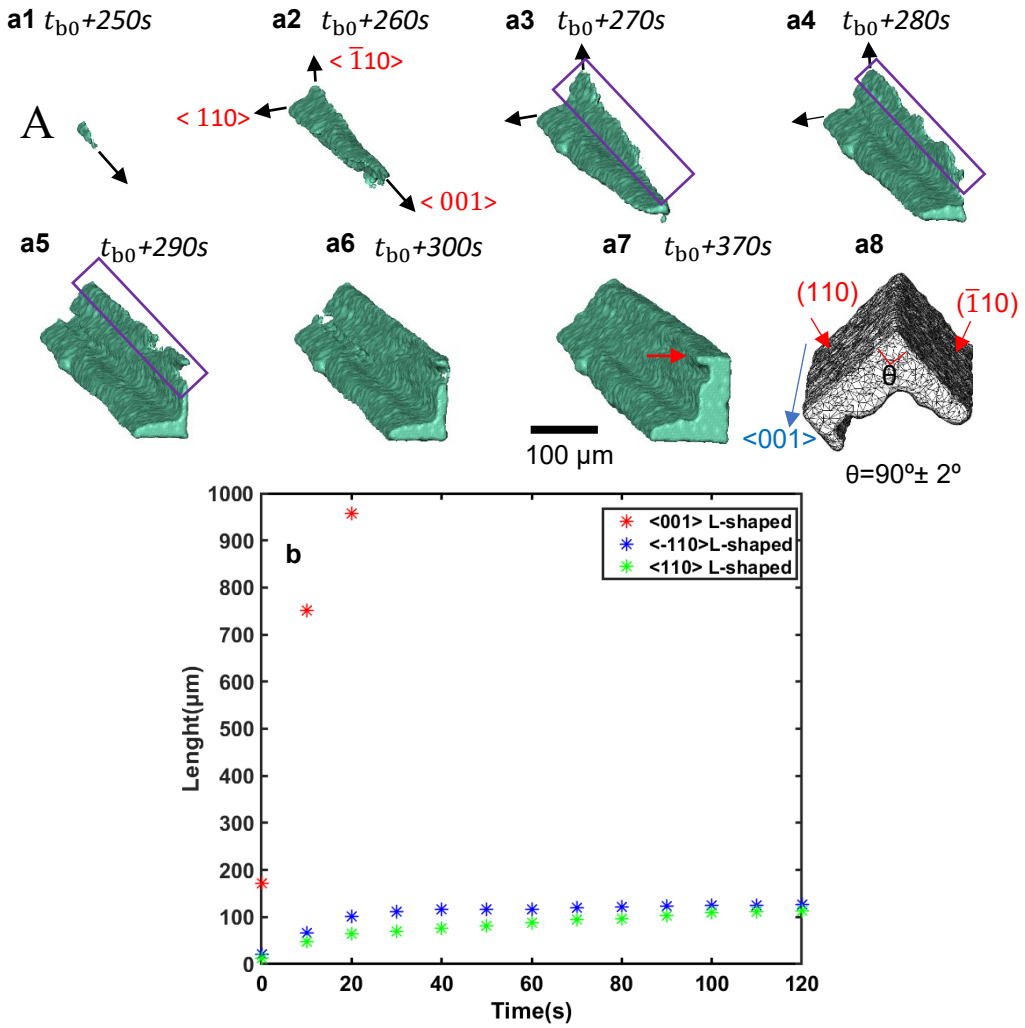

Figure 4.7 (a1-a7) Selected L-shaped pattern from solidification condition B (CR=0.05℃/s,TG= -4 ℃/mm and B=0T); (a8) angles between different facets of L-shaped pattern; (b) Growth length according to its crystallographic directions from (a8).

Figure 4.7 presents the growth of one L-shaped pattern from t_{b0} +250s to t_{b0} +370s extracted from sample B. A small rod-like pattern (Figure 4.7-a1) first appeared. Then it grew longer and formed two branches perpendicular to each other within 10 s (and Figure 4.7-a2). The growth directions of the branches are marked by the black arrows. After another 10 s, the rod became longer, and the branches grew thick too (Figure 4.7-a3).

The branches extended further in Figure 4.7-a4 and Figure 4.7-a5, forming the L-shaped pattern. It continued to thicken at the later stage of solidification while the overall L shape was maintained. A fin (pointed by the red arrow in Figure 4.7-a7) formed on one of the branches, oriented perpendicular to that branch.

Table 4-2 Crystallographic properties of the main lattice planes of Al_2Cu

Plane	d_{hkl} (nm)	Al2Cu molecular attachment energy $\times 10^{18}$ J	Angle with <001> direction
110	0.429	0.579	0°
020	0.303	0.803	0°
002	0.244	0.993	90°
211	0.237	0.964	29.098°
112	0.212	1.090	60.395°
130	0.192	1.133	0°
022	0.190	1.153	51.216°

The bounding facets of Al_2Cu intermetallic in an Al-Cu alloy are {110} planes, as these planes require the lowest attachment energy (Table 4-2)[12,183]. Al_2Cu phase also has a strong crystalline anisotropy and a preferred growth direction along <001> [183].

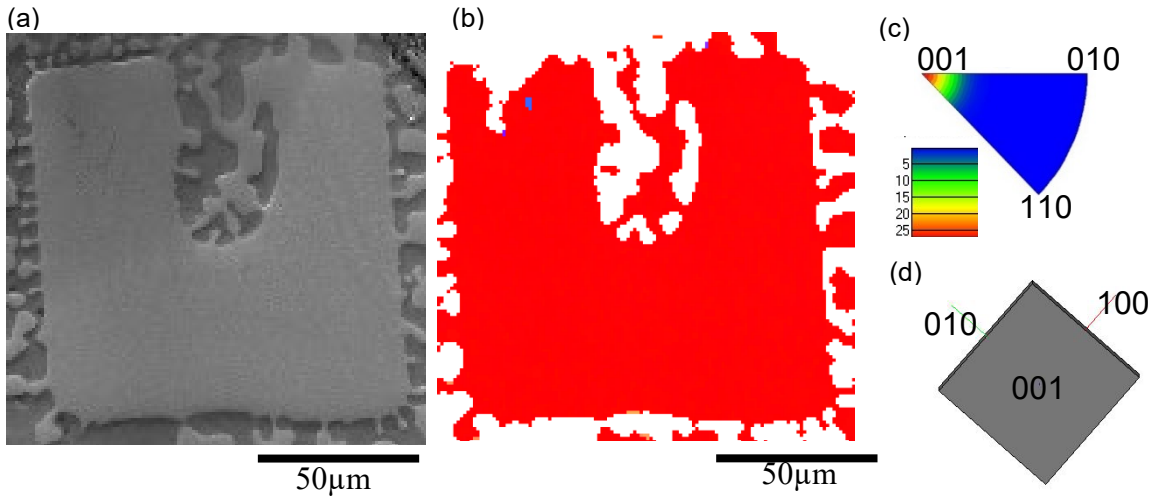

Figure 4.8 SEM image of the sectioned surface; (b) EBSD map; (c) Inversed pole figure (IPF); (d) acquired 3D crystal orientation.

EBSD analysis of the basic unit was also performed which reveals the preferred growth direction is <001> (Figure 4.7-a8). A sample of Al-45%Cu alloy was solidified at a cooling rate of 0.5 ℃/min without temperature gradient magnetic fields applied. The obtained specimen was then sectioned parallel to the transverse direction of the ceramic tube, which was ground and polished following the same steps as the previous sample. EBSD analysis was performed by the same machine (accelerating voltage of 20 kV, a working distance of 16.58 mm, a tilt angle of 70 ° and a step size of 1.6µm in a square scan area of 219.2 µm × 811.2 µm). The microstructure of the solidified sample is shown in Figure 4.8-a, which is in the shape of U-shaped (the basic-unit). EBSD map of Al_2Cu intermetallic compounds is shown Figure 4.8-b (inversed pole figure map). The IPF and acquired crystal orientation (Euler1 = 3.7º, Euler2 = 1.1º, Euler3 = 45.0º; [HKL] = [001]) are presented in Figure 4.8-c and d, respectively. It reveals that the analysed surface of the U-shaped Al_2Cu intermetallic is on plane (001).

The angle between the adjacent facets of the bounding wall of the basic L unit patterns was measured to be 90°±2°. This suggests that the facets are {110} of Al_2Cu. Hence the bounding planes {110} and growth direction <001> of the selected L shaped crystal can be indexed (Figure 4.7-a8). The growth length as a function of time according to its crystallographic direction are quantified and plotted in Figure 4.8-b. In <001> direction, the intermetallic reached a high growth rate of 39.2 $\mu m/s$ in the first 20 seconds, while the branches grew slowly at a rate of 3.0 $\mu m/s$ in the direction of <-110> and 1.9 $\mu m/s$ in the direction of <110> in the first 30 seconds. They then barely grew once the L-shaped was formed.

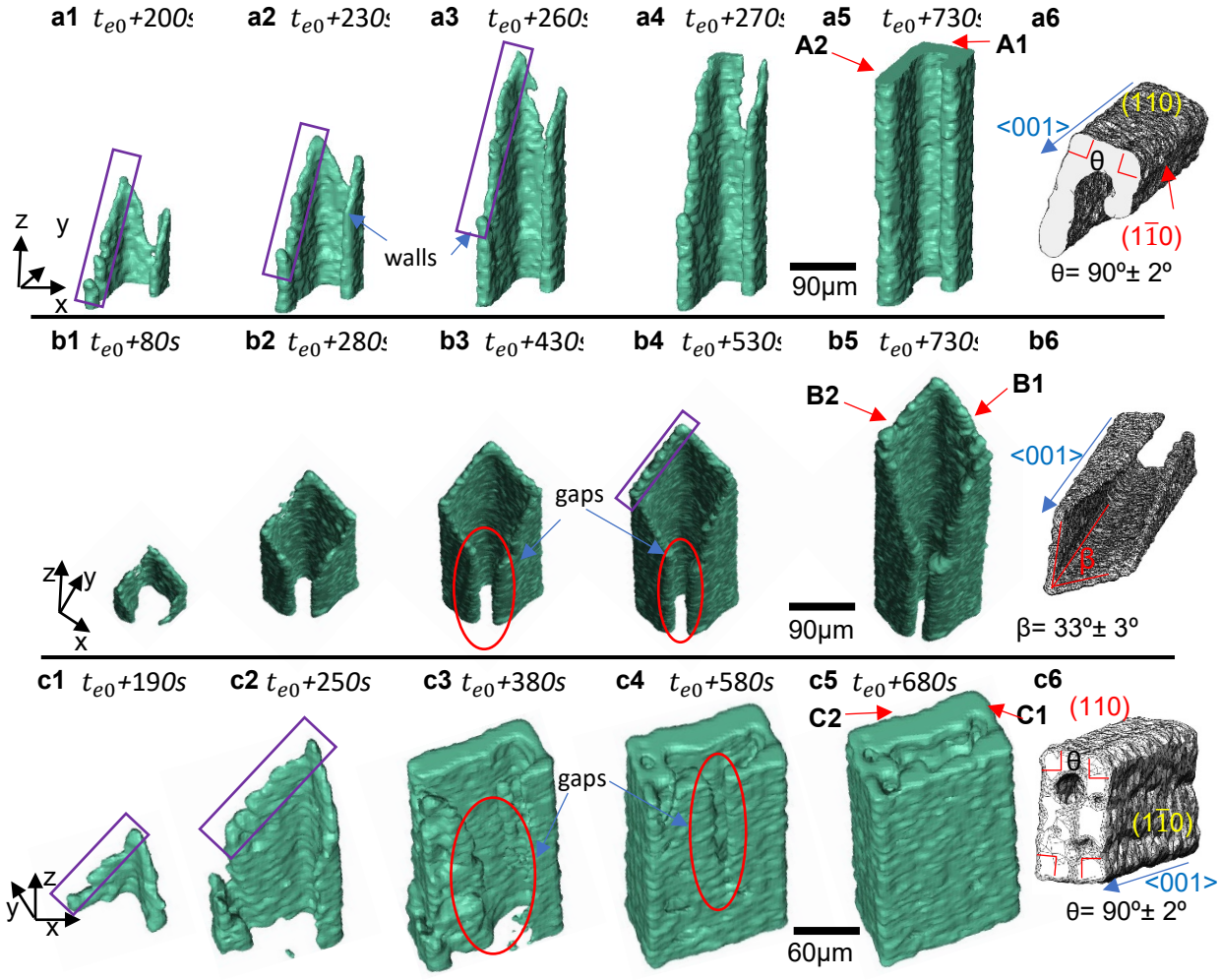

Figure 4.9 Formation process of selected (a1-a5) U-shaped pattern; (b1-b5) nearly hollow-rectangular and (c1-c5) hollow-rectangular pattern; (a6, b6 and c6) bounding facets and growth directions of Al_2Cu crystals.

The growth process of U-shaped Al_2Cu intermetallic compound, extracted from experiment E is shown in Figure 4.9-a. This crystal grew to be very long, so only a part of the crystals was cropped to show in the figures. The crystal had cuspidal growth fronts (Figure 4.9-a1 and a2). The gap between the side walls became smaller due to the thickening of the side walls Figure 4.9-a4 and Figure 4.9-a5). The bounding facets of this crystal are also {110} planes and indexed as shown in Figure 4.9-a6.

The growth processes of two hollow-rectangular Al_2Cu IMCs are shown in Figure 4.9-b and Figure 4.9-c. The crystals grew along <001> at a growth rate of about 3.3 $\mu m/s$ to an elongated rectangular shape with a central rectangular hole The growth fronts of both crystals were also cuspidal (Figure 4.9-b2 to b5 and Figure 4.9-c2), with bounding facets forming an angle of 33°±3° with the <001> growth direction (Figure 4.9-b6). The crystal in Figure 4.9-b grew into a nearly hollow-rectangular shape but still had a gap on one of its walls. The crystal in figure 6-c transited from an L-shaped pattern (Figure 4.9-c2) to U-shaped (Figure 4.9-c3) and finally a hollow-rectangular structure (Figure 4.9-c5). The closure of the gap on the wall (Figure 4.9-c3 to c5) led to the final hollow rectangular shape. The intermetallic compounds have a higher average tip growth rate (9.9 ± 0.1 μm/s) in experiment F under the same cooling rate and temperature gradient than when the magnetic field is absent in sample C. The average growth rate in sample E (lower cooling rate of 0.02℃/s) is around 3.5±0.2 μm/s.

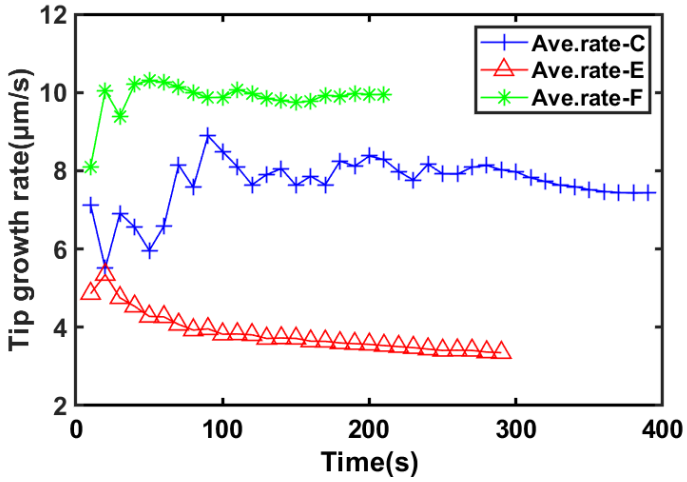

Figure 4.10 (a) Average tip growth rates of the overall crystal array from experiments C, E and F as a function of each growth time.

4.3.4 Dendrites

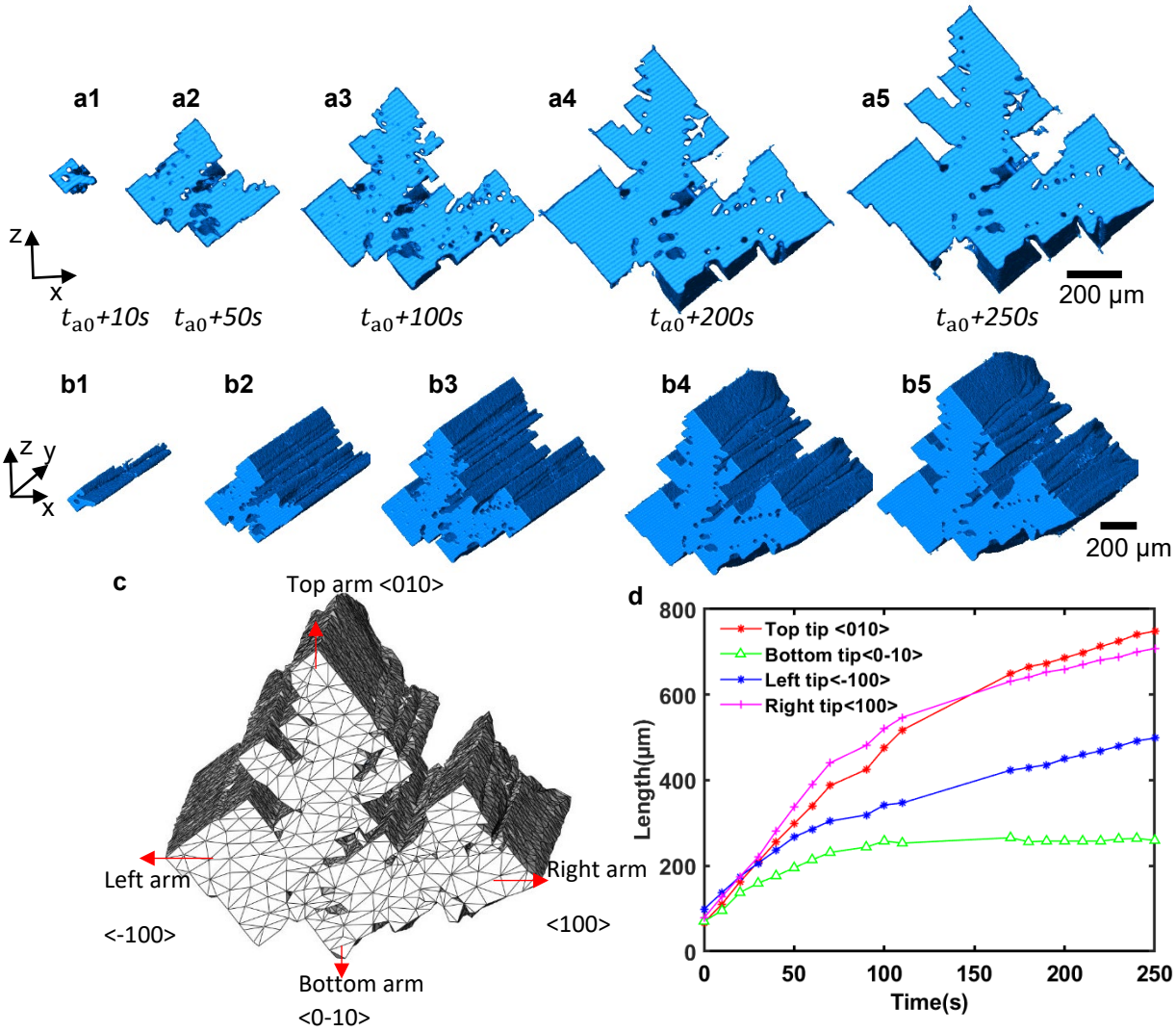

Figure 4.11 Selected dendrite pattern from figure 4.4-a solidification condition A (CR=0.05℃/*s*,TG= 0℃/*mm* and B=0T); (a) Front view of faceted equiaxed-prism structure at different time without temperature gradient; (b) Side view of faceted equiaxed-prism structure

Figure 4.11 shows the growth process of the equiaxed-prism Al_2Cu IMC, extracted from sample A (Figure 4.4-a). The crystal grew into equiaxed-like shape in the x-z plane (Figure 4.11-a), whereas it grew as a prism in y-direction (Figure 4.11-b). This is different from typical equiaxed patterns that proceed equally in all directions [211]. Here, a rectangular-shape basic unit first appeared (Figure 4.11-b1). Then it extended along its

four corners (Figure 4.11-a2), forming four arms around the core, three of which were dendritic shape. The growth of the left and bottom arms was constrained (Figure 4.11-c) due to the limited space available for growth. Only the top and right tips were able to grow into large size as shown in Figure 4.11-a3 to a5. The meshed 3D volume of the equiaxed-prism structure (Figure 4.11-c) shows that the angles between bounding adjacent faceted planes are all around 90º. Different from the dendrite arms in typical non-faceted dendrites, which form parabolic tips [5,7,8], the arm of the Al_2Cu dendrite is flat with sharp corners (Figure 4.11-c). Figure 4.11-d presents the length of the four dendrite arms as a function of time. The length of the crystal arms increased almost linearly in the first 70 seconds. The growth speed slows down afterwards. The bottom tip almost stopped to grow as there was no more available space nearby. The other three arms continued to grow and the left-arm reached a length of 500μm, while the right and top arms have the greatest dimensions of around 750μm.

EBSD analysis was implemented to determine the crystallographic planes of the faceted dendritic structure of one post-solidification sample which shows the tip growth planes are {100} or {010}.

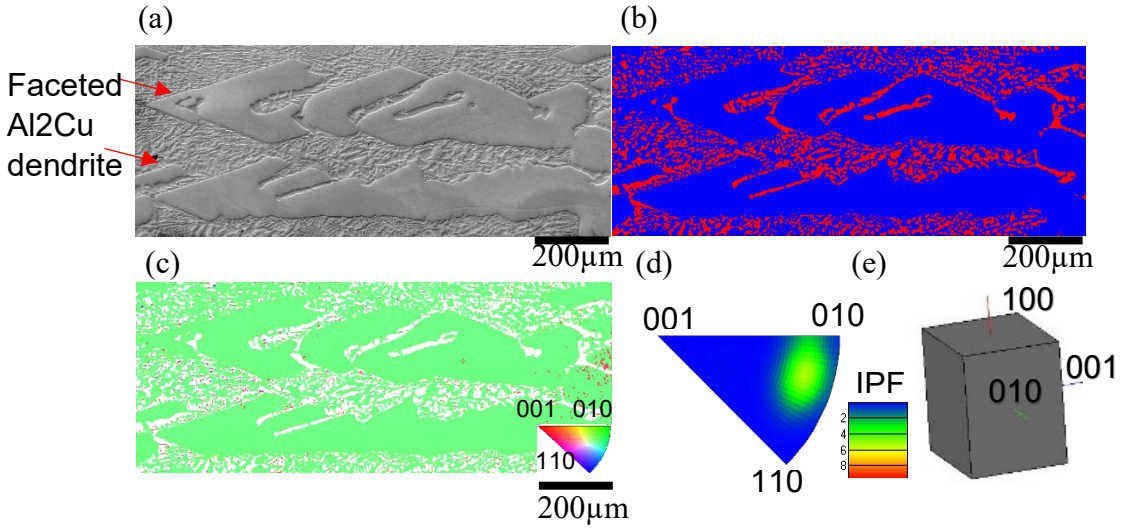

Figure 4.12 (a) SEM image of the sectioned surface; (b) phase map; (c) EBSD map; (d) Inversed pole figure (IPF); (e) acquired 3D crystal orientation.

The microstructural observation was carried out by Tescan MIRA 3 SEM, equipped with an Oxford Instruments EBSD detector controlled by the AZtec software. The EBSD data was acquired at an accelerating voltage of 20 kV, a working distance of 15.8 mm, a tilt angle of 70 ° and a step size of 1.6 µm in a square scan area of 1270 µm × 507 µm. The obtained data were interpreted by HKL Channel-5 Tango software to index the grain orientations. The microstructure of the solidified sample is shown in Figure 4.12-a. EBSD map of Al_2Cu intermetallic compounds (including fine eutectic Al_2Cu and faceted Al_2Cu dendrites) is shown in Figure 4.12--b (phase map) and Figure 4.12--c (inversed pole figure-IPF map). The IPF and acquired crystal orientation (Euler1 = 99.0º, Euler2 = 107.3º, Euler3 = 15.8º; [HKL] = [13$\bar{1}$]) are presented in Figure 4.12--d and e, respectively. It reveals that the analysed surface of the Al_2Cu is on (13$\bar{1}$) plane.

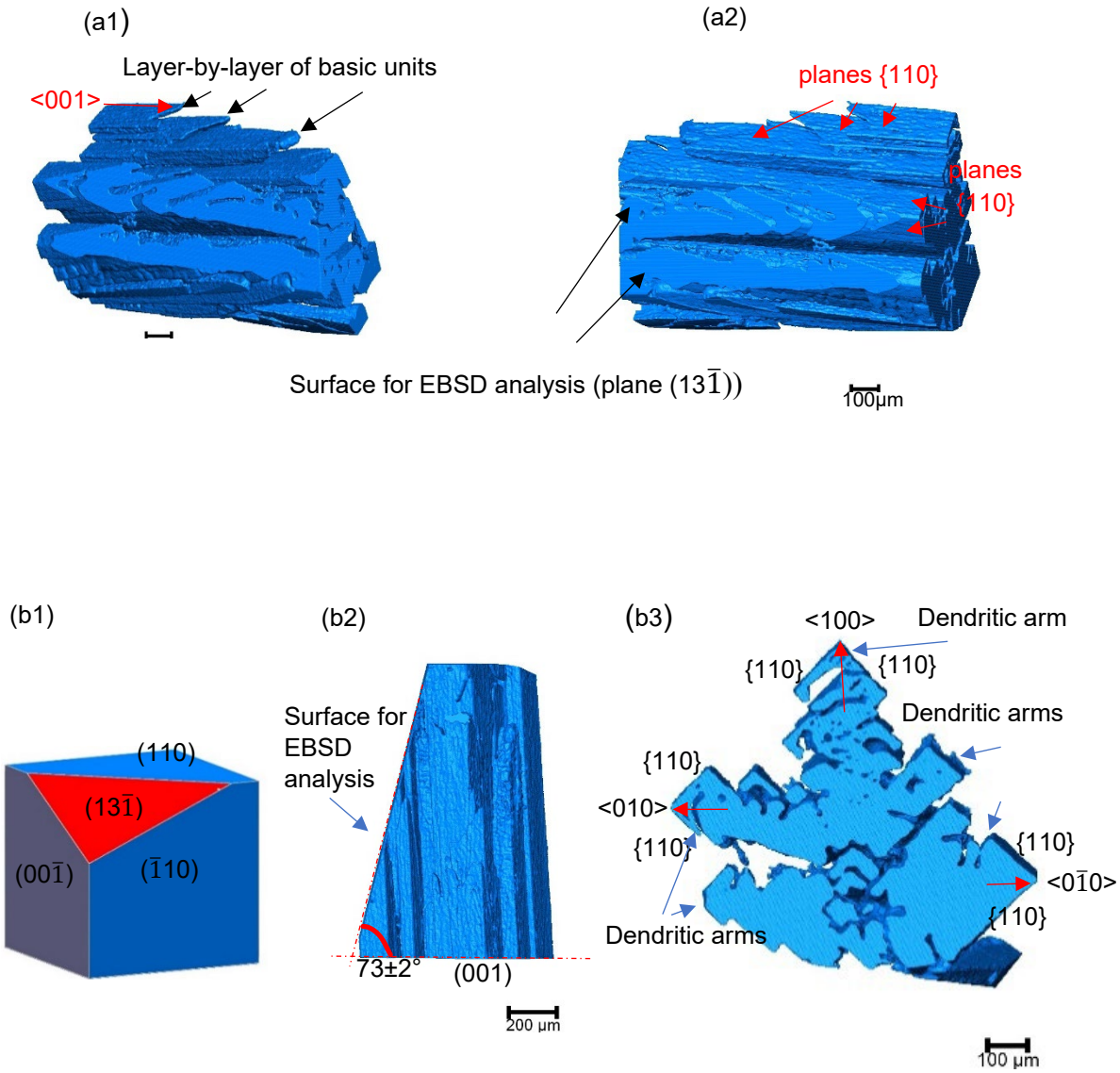

Figure 4.13 (a) 3D volumes of the faceted dendrites (a1) left side view; (a2) right side view; (b1) calculated shape of the crystal; (b2) the measured angle between the surface of EBSD analysis and (001) plane; (b3) the growth directions of primary and secondary dendritic arms and its bounding planes.

After EBSD analysis, the sample was scanned by Synchrotron X-ray tomography at I12 beamline, Diamond Light Source, Oxford, to reveal the angles between the sectioned surface and the growth orientation of the dendrites. The raw images have

2560×2560×2150 pixels with a voxel size of $1.3\mu m^3$. The 3D images were analysed by Avizo 2020.1 (ThermoFisher Scientific, USA).

The mapped 2D Al_2Cu dendrites in the SEM image (Figure 4.12-a) were part of the secondary arms of a large dendritic structure, which were not parallel to its growth direction. Layered basic units can also be observed (pointed by black arrows). The 3D structures were then meshed and imported into Solidworks (Dassault Systemes, France) to measure various interplanar angles. Based on the known crystallographic planes of the basic units of Al_2Cu (grow in <001> direction and bounded by {110} planes), the bounding planes and growth direction of the layers of the dendrite were identified and indexed as shown in Figure 4.13-a1 and a2.

According to KrystalShaper (JCrystalSoft), the bounding planes around $(13\bar{1})$ plane are (110), $(\bar{1}10)$, and $(00\bar{1})$ as shown in Figure 4.13-b1.Angles between the surface of EBSD analysis ($(13\bar{1})$ plane) and these planes ((110), $(\bar{1}10)$, and $(00\bar{1})$ were calculated. The values were then compared with measured angles from the 3D dendrite structures. As shown in Table 4-3, the differences between all the calculated and measured angles are less than 3º. One example of the measurement is shown in Figure 4.13-b2. Additionally, we also measured the angles between the growth plane of the primary dendrite arm and plane $(13\bar{1})$, which is 74±2º. This is very close to the calculated angle (72.9º) between planes (100) and $(13\bar{1})$. The measured angle between the growth plane of the secondary arm and $(13\bar{1})$ is 26±2º, similar to the calculated angle (28.0º) between plane (010) and $(13\bar{1})$. Therefore, for faceted Al_2Cu dendritic structure, the tip growth orientation of the layers (the basic units) is in <001> direction, which then grew layer-by-layer in the direction of <100> or <010> to form the faceted dendritic arms, while the surfaces are bounded by planes {110} as shown in Figure 4.13-b3.

Table 4-3 Interplanar angles

Planes		$(00\bar{1})$	(110)	$(\bar{1}10)$	Growth plane (primary arm)	(100)	Growth plane (Secondary arm)	(010)
Surface for EBSD analysis (13-1)	Measured interplanar angles	73±2º	31±2º	66±2º	74±2º	-	26±2º	-
	Calculated interplanar angles	68.5º	33.7º	65.4º	-	72.9º	-	28.0º

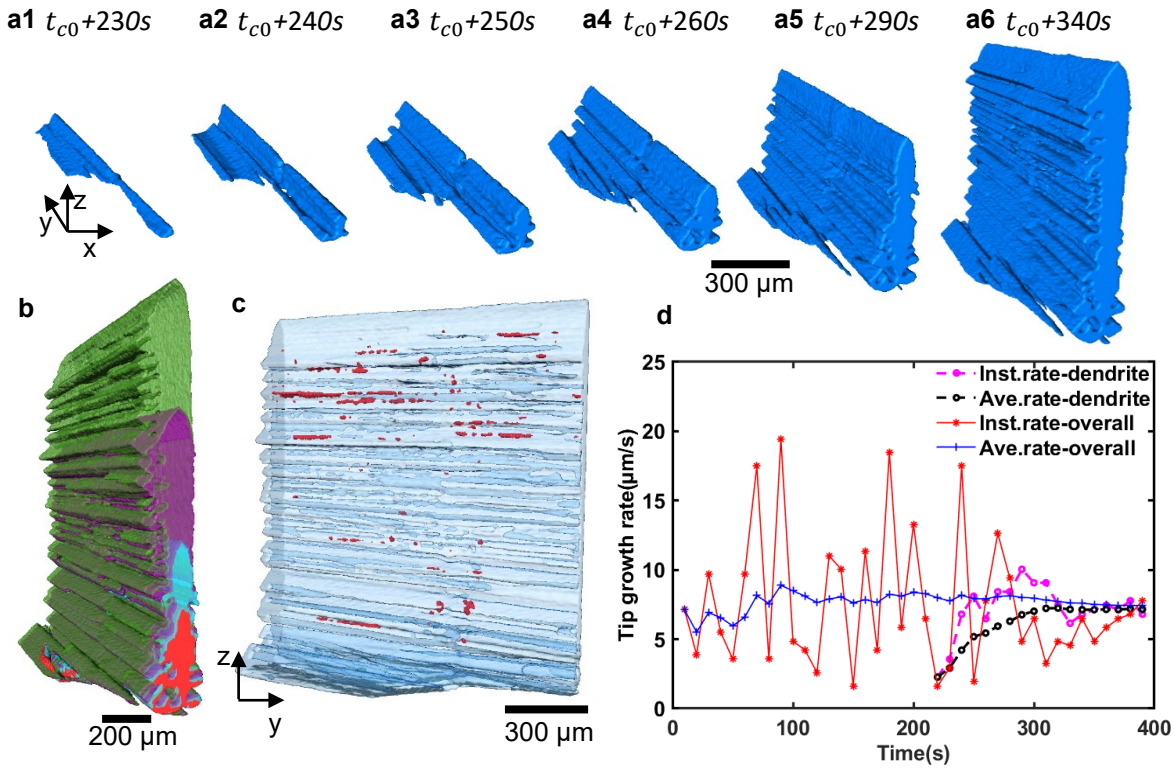

Figure 4.14 Selected columnar dendrite from Fig. 4.4-c under solidification condition C (CR = 0.05 C/s,TG = 7 C/mm and B = 0T); (a1-a6) Volume rendering of a single dendrite with solidification time; (b) Transparent overlapped view of the dendrite at t_c0 + 270 s, t_c0 + 290 s, t_c0 + 340 s,t_c0 + 390 s; (c) Internal defects at t_c0 + 390s front view; (d) Average and instantaneous tip growth rates of the overall crystal array and the single dendrite of figure a.

Figure 4.14-a1 to a6 show the growth of a single large columnar dendrite from t_{c0}+230s to t_{c0}+340s, extracted from sample C (Figure 4.4-c). Figure 8-b shows the overlapped images of the same dendrite at different time points. The growth started from a faceted crystal tip (Figure 4.14-a1), which grew in horizontal y-direction until it reached the sample surface. It then extended in z-direction (Figure 4.14-a2), while secondary arms appeared in x-direction (Figure 4.14-a3). Additionally, gaps and internal holes (which are filled with melt during solidification) occurred at the interfaces between neighbouring secondary arms (Figure 4.14-c, red colour). Figure 4.14-d shows the instantaneous and average growth rates of the whole sample C (Figure 4.14-c) and the selected asymmetric

dendrite. The positions of the dendrite tips were first measured in all tomograms. The instantaneous growth rate is the difference of dendrite tip positions between two consecutive tomograms divided by the time interval (10 s). The average rate is the tip position of the dendrites divided by the total solidification time. The instantaneous tip growth rate of the whole sample is fluctuating in a periodical manner, whereas the average growth rate kept at around 7.7 ± 0.3 μm/s, which is because a constant temperature gradient and cooling rate were applied. The instantaneous growth rate of the selected dendrite is also fluctuating. The average growth rate of the dendrite increased from about 2.2 μm/s to a plateau of 7.2 μm/s within 100 s, indicating that there is a change of growth conditions locally as the dendrite grew. The average tip growth rates of Al_2Cu IMC from experiment E and F are also quantified and shown in supplementary note figure s6.

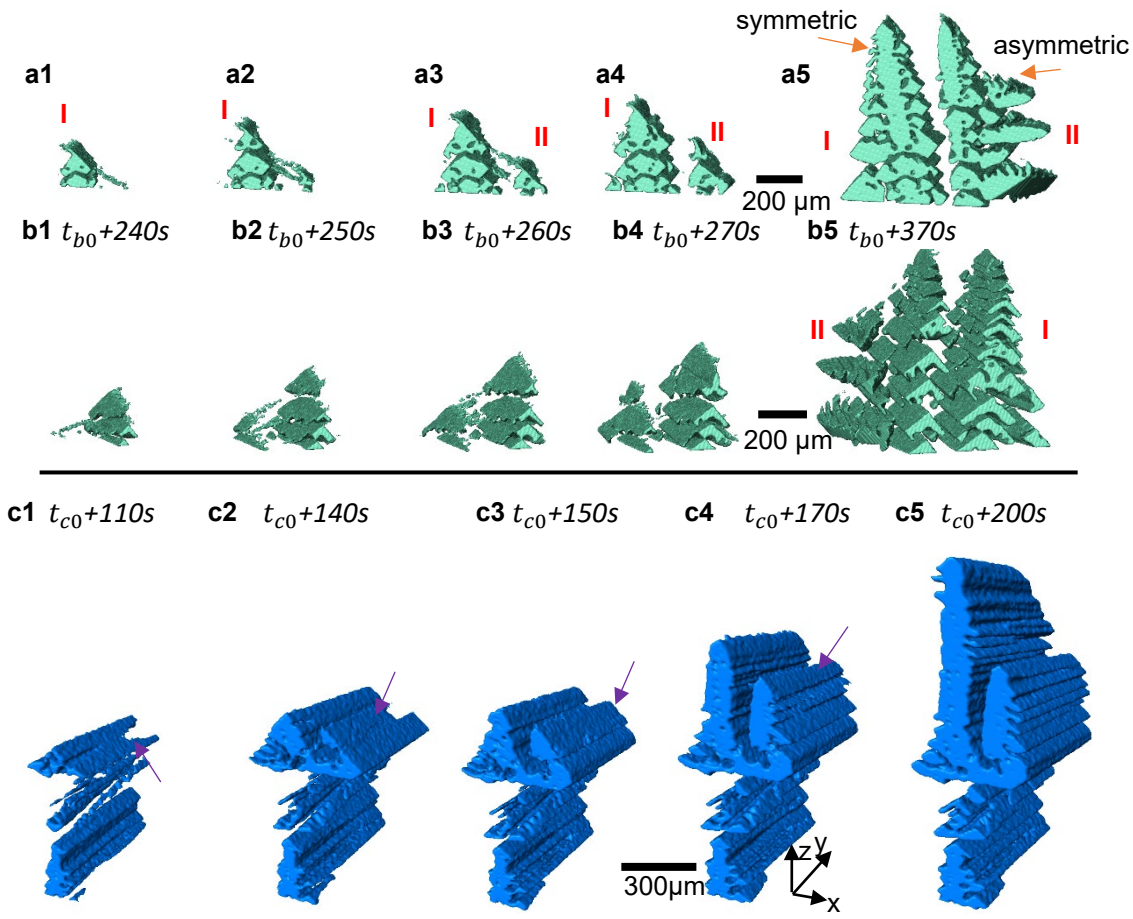

Figure 4.15 Selected pattern from figure 4.4-b under solidification condition B (CR=0.05℃/*s*,TG= -4 ℃/*mm* and B=0T): (a1-b5) showing the growth of a symmetric and asymmetric faceted dendrites; (a1-a5) front view, (b1-b5) back view; Selected pattern from figure 2-c

The formation of a symmetric dendrite (I) and an asymmetric dendrite (II) from sample B are shown in Figure 4.15-a (front view) and Figure 4.15-b (rear view). Dendrite I appeared before the dendrite II. The secondary arms of the dendrite I were branching in both directions perpendicular to the primary arm, forming a symmetric dendrite. Tertiary arms can also be found at later stage of solidification. However, the secondary arms of the dendrite II branched only on one side, forming an asymmetric dendrite. The formation of asymmetric dendrites is common when two or multiple dendrites grow together and compete for space and solute to grow. This has also been observed in non-faceted

dendrites [7]. What is also noticeable is that it seems both dendrites were composed of many L-shaped elongated basic units, which is clearly demonstrated in the rear view (Figure 4.15-b). We also observed a tertiary arm grew into a new primary dendrite (Figure 4.14-c). As shown in figure Figure 4.15-c1, a secondary branch formed first (marked by the purple arrow). Then a tertiary arm formed on the top of the secondary branch (Figure 4.15-c2 and c3), growing upwards into a well-developed asymmetric dendrite (Figure 4.15-c5).

4.3.5 Coalescence and coarsening

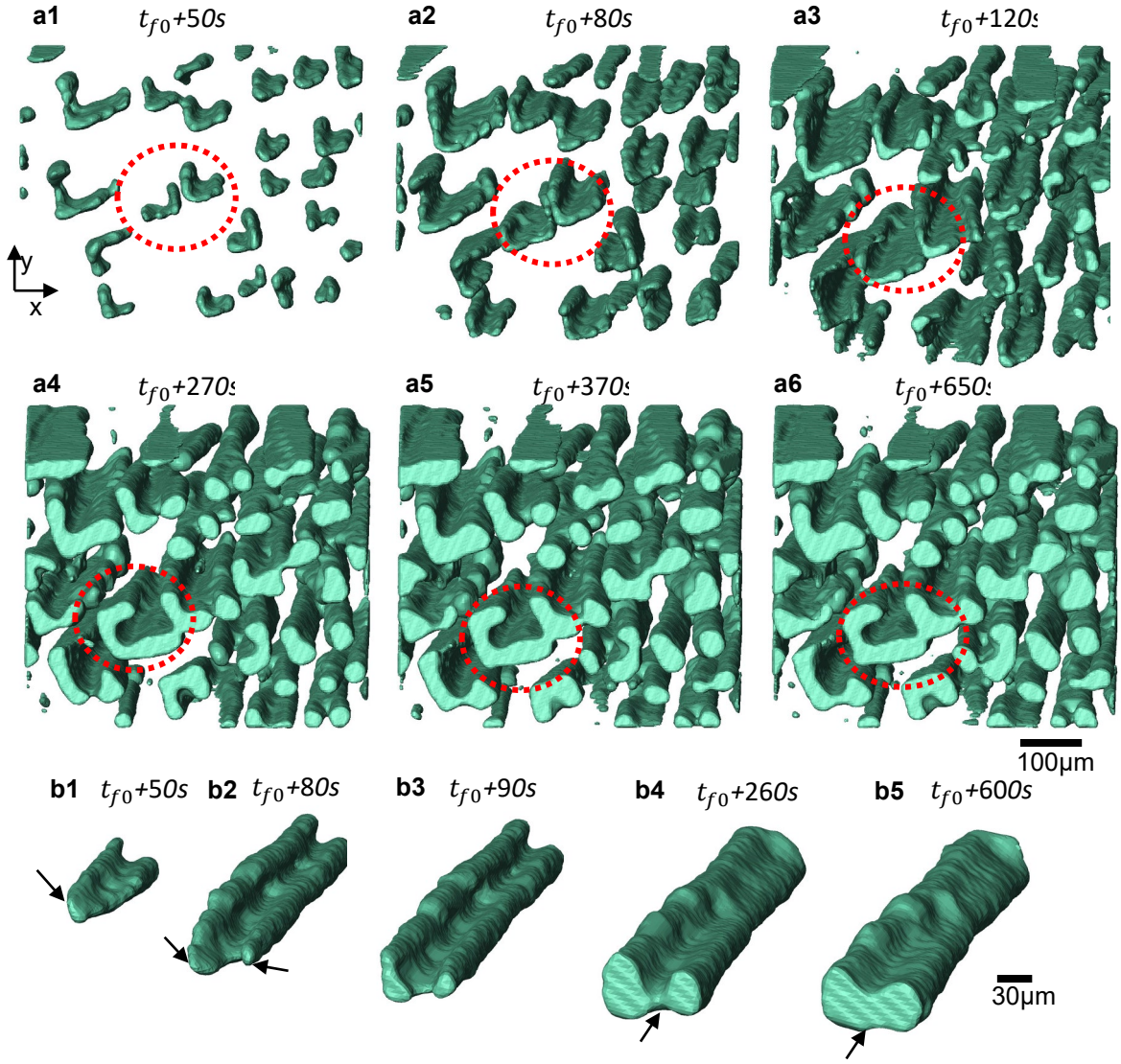

Figure 4.16 (a) Formation process of a selected region; (b) faceted to non-faceted transition of Al2Cu intermetallic compounds cluster; from figure 4.5-c under solidification condition F (CR=0.05℃ / s,TG= 7℃ / mm and B=0.5T).

The coalescing behaviours of nearby IMCs can be observed in Figure 4.16-a. As highlighted by the red circle in Figure 4.16-a1, two L-shape patterns were initially separated. As the solidification proceeded, the walls of the two crystals coarsened and coalesced to form a thicker single wall as shown in Figure 4.16-a2 to a6, highly likely sharing a common crystallographic plane.

Figure 4.16-a also shows that several IMCs transformed from faceted shapes to non-faceted rod-like structures, one of which was extracted and shown in Figure 4.16-b. Here, the transition is related to the processes of growth and coarsening or Ostwald ripening of Al_2Cu at the later stage of solidification. A faceted L-shaped pattern was first formed, similar to the one in figure 5. However, the concave of the L-shaped pattern, as pointed by black arrows from Figure 4.16-b4 to b5, was further filled during the coarsening stage. The driving force of this process is to reduce the total surface free energy [212].

4.3.6 Growth mechanism of Al_2Cu

Jackson [62] proposed a model for the prediction of faceted or non-faceted morphologies based on the interface roughness on an atomic scale as given in equation (1):

$$\alpha = \frac{L}{KT_M}\,\xi \tag{1}$$

where α is the Jackson roughing factor, L is the latent heat or enthalpy of fusion, K is the Boltzmann's constant ($8.31\,JK^{-1}mol^{-1}$), and T_M is the melting temperature. ξ is the orientation factor that is close to unity for the most closely packed plane[62]. The surface of the crystal will be smooth if the α value is higher than 2 and grow into faceted structure, while a rough interface and non-faceted structure are expected if it is smaller than 2 [213] [62,213]. A CALPHAD method is used to calculate the melting point and the latent heat of Al_2Cu intermetallic compounds. The calculation is performed by Thermo-Calc [46], which gives the latent heat of $15188\,J/mol$ and the melting point of $865K$.As the faceted structures are expected to be bounded by the slowest growing planes which are the most closely packed, ξ is treated as closing to unity. Jackson roughing factor for Al_2Cu is around 2.11.

hence faceted patterns are expected for Al_2Cu. Governed by the interface attachment kinetics, stepwise lateral growth, where the solid/liquid front advances by lateral motion of the growth steps has been proposed to be the growth mechanism of faceted IMCs such as Al_3Sc [48] and Cu_6Sn_5 [46] at small undercooling. Rough interfaces have been observed from the early growth stages of Al_2Cu, such as figure 5 a-1 to a-4 and in figure 6 (marked by purple rectangles), which might be evidence of lateral steps.

According to the classic theory of crystallization, the growth of crystal proceeds due to the attachment of atoms from the melt to the surface [45]. Recently, oriented particle attachment via nano-precursor attachment has been proposed as an alternative pathway for crystallization [45,78]. The reduction of total energy is the driving force for crystal growth via oriented particle attachment [214], which comes from the interatomic interactions in the attaching particles, as well as the surface energy of the attaching surfaces [214]. Oriented particle attachment mechanism was proposed in ref [183] to describe the growth mechanism of Al_2Cu. The bonding of Al_2Cu includes Al-Al and Al-Cu covalent bonds [215], which is different from the less directional metallic bonds in α-Al. Hence Al_2Cu intermetallic might grow via oriented particle attachment, rather than classic crystallization. Our work did not provide direct evidence to support this hypothesis. This is because the resolution of the tomography (3.24 μm^3 voxel size) used does not allow us to observe the attachment of precursors which are usually in nano-size. Hence nano-scale imaging techniques such as in situ TEM [80,216] would be a useful tool to be applied to confirm this hypothesis.

Various final morphologies of Al_2Cu (L-shaped, E-shaped, and rectangle) have already been observed in previous studies [12,108,196]. However, the relationship and transitions between these growth patterns have not been experimentally identified. Here, we have shown a clear transition from an L-shaped pattern to U-shaped, and finally to a hollow-rectangular pattern (figure 6-b and 6-c). This suggests that L-shapes and U-shapes might be intermediate stages for Al_2Cu growth, whereas the hollow rectangular shapes are the final stage. The transition stages for the basic unit patterns of the Al_2Cu phase is schematically shown in Figure 4.17-a.

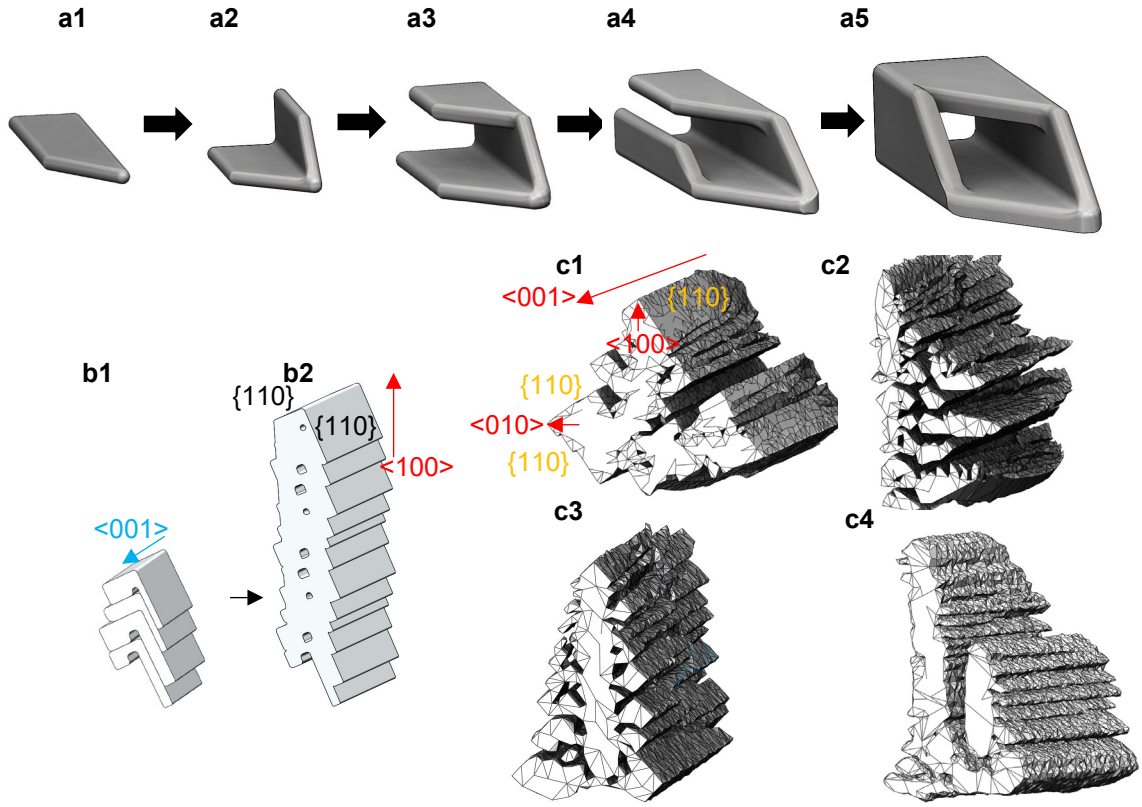

Figure 4.17 (a) the schematic diagram of the formation process of basic units; (b1-b2) Schematic diagram of self-repeating layer-by-layer growth mode of Al2Cu phase; (c1) an equiaxed-prism structure; (c2) an asymmetric faceted dendrite; (c3) a symmetric faceted dendrite; (c4) a faceted dendrite with a tertiary arm.

Two types of faceted dendrites were observed, namely prism-equiaxed and columnar plate shaped. As shown in Figure 4.14, the growth of the faceted dendrites seems to be through a self-repeated stacking of L-shaped patterns layer-by-layer. The process is schematically shown in Figure 4.17-b. An elongated L shaped particle formed possibly along <001> direction first due to a horizontal temperature gradient, then new L shaped particles stacked on top of it. As the process repeated and more particles stacked layer-by-layer, a columnar dendrite arm grew upwards. Figure 4.14 and Figure 4.15 show this process clearly, especially in Figure 4.15-b. The fact that the concave side of the 'L' always stacked on the convex side indicates that the process is controlled by the

crystallographic anisotropy of the Al_2Cu crystal, which minimizes the formation energy and occupies the least space. For the formation of the prism-equiaxed dendrite (Figure 4.11-b), an elongated rectangular-shape core (Figure 4.11-b1) formed first. L-shaped patterns then attached on the four tips of the core layer-by-layer repeatedly, forming four secondary arms. The final shape of the equiaxed-prism structure is also controlled by space and solute contents available for growth. The classical growth mechanism for dendrites formation states that a morphological instability of the planar solid-liquid interface [4,7], resulted into tip splitting, side-branch protrusions and parabolic tips, which is usually applied to non-faceted dendrites [7] as well as some faceted dendrites [19]. However, this mechanism is not suitable to explain the formation of the faceted dendritic structures of Al_2Cu according to our experimental observation (e.g. no protrusions were observed during dendrite growth, the tip shape is not parabolic, and the growth direction of the dendrite tip is not the preferred <001> direction). Self-repeated stacking of basic units that leads to faceted dendrite formation could be widely applicable for a range of faceted crystals, such as Cu_6Sn_5 [46], I-AlMnBe [47] and Al_3Sc [48]. But more experimental work and simulation are needed to further validate and confirm this faceted dendrite formation mechanism.

4.4 Summary

In this study, the growth dynamics and mechanisms of the faceted Al_2Cu intermetallic compounds were investigated using high-speed synchrotron X-ray tomography during solidification of Al-45wt%Cu alloy. This work offers a new perspective to understand intermetallic growth during solidification and open the windows for developing new approaches to control, and new models to predict, intermetallic compounds for a wide range of alloys. The following key conclusions can be made.

1. A variety of faceted patterns were found, which can be classified into two distinctive categories: basic unit shapes and dendrites.
2. The basic unit growth patterns of Al_2Cu are elongated rod-like with an L-shaped, U-shaped, or hollow-rectangular cross-section. A transition process from L-shape to U-shape, and finally to hollow-rectangular shape was observed.
3. Faceted dendritic patterns of Al_2Cu include equiaxed-prism and columnar dendrites (symmetric and asymmetric). The 4D visualization of the growth process of the faceted dendrites suggests that the growth mechanism of the Al_2Cu faceted dendrites is self-repeated layer-by-layer stacking of faceted basic units (such as L-shaped or hollow rectangular patterns), which is different from the interface instability induced dendrite formation.
4. For upward directional solidification of Al-45wt%Cu, when rotating the solidifying sample in a transversal 0.5 T magnetic field, fine and regulated crystal arrays were obtained, much finer than that solidified without the magnetic field. This is attributed to a rotational stirring flow that regulated the heat flow and homogenized the solute distribution. The morphology of faceted Al_2Cu was directly influenced by the thermal profile in the sample. The applied static

magnetic field has an indirect impact via promoting fluid flows to change the temperature gradients while the sample was rotating.

Chapter 5: Influences of cooling rates on the growth mechanism of Al_3Ni intermetallic compounds revealed by 4D synchrotron X-ray tomography

5.1 Introduction

The mass of automobiles is one of the main factors that influence the vehicle's fuel consumption. A 100kg mass reduction can save fuel up to 10%. Therefore, lightweight materials become popular in the automotive industry [124]. Al alloys and Mg alloys are widely used in automotive and aerospace industries thanks to their good strength, and corrosion resistance with low density. The combination of these two alloys can significantly reduce the weight of automobiles.

To eliminate or reduce the Mg-Al intermetallic reaction layer [217], recently, the Ni interlayer has been introduced in various welding techniques including diffusion bonding [218–220], resistance spot welding [221,222], hybrid laser-friction stir welding [223] and laser-arc-adhesive hybrid welding [224]. Less brittle intermetallics such as Al_3Ni can be formed. However, its growth behaviour and morphologies can influence the bonding strength of the Al-Ni interface. For instance, previous studies have shown that the faceted Al_3Ni with sharp edges can reduce the fracture toughness of the Al-Ni interface, while the Al_3Ni IMCs with rough and cellular may improve it. Therefore, it is vital to investigate the growth mechanisms of the Al_3Ni IMCs with various morphologies under different solidification conditions.

Previous studies have used in-situ X-ray radiography to reveal the growth process of Al_3Ni IMCs [191,225–227]. However, the formation process of the complex morphologies of the Al_3Ni IMCs such as faceted hollow-prism structure, layered-

structure were not captured. The proposed growth mechanisms may not accurately explain the growth behaviours, based on interpreting the results from solidified samples.

Here we have used in-situ synchrotron X-ray tomography to investigate the growth dynamics of Al_3Ni intermetallic compounds and the influences of the cooling rates (ranging from extremely slow (0.5℃/min) to high (24℃/min)). The growth mechanisms of Al_3Ni IMCs with different morphologies were discussed in the combination of 4D imaging results and EBSD analysis. This work provides direct evidence of the correlation between the cooling rates and the growth mechanisms of Al_3Ni IMCs.

5.2 Materials and Methods

5.2.1 Sample preparation

Cylindrical specimens with 2.0 mm diameter and 100 mm length were machined from an Al-10wt% Ni master alloy via wire electrical discharge machining.

5.2.2 Bespoke medium temperature furnace design (MTF)

Each beamline in synchrotron facilities has its dedicated layout. For instance, the position of the beam, the height of the rotating stage and the available spacing for integrating users' equipment are designative in different beamlines. To perform experiments at B16, Diamond light source, Oxford, a new bespoke medium temperature furnace (MTF) was designed and manufactured as shown in Figure 5.1. The furnace includes three parts. A heating core that is made from ceramics and is surrounded by resistance heating wire (80% Nickel/ 20% Chromium alloys from OMEGA) will provide a heating source for the samples. Thermal insulation is used to minimise heat loss. An aluminium cover case (printed by selective laser melting) is used to assemble and integrate all parts.

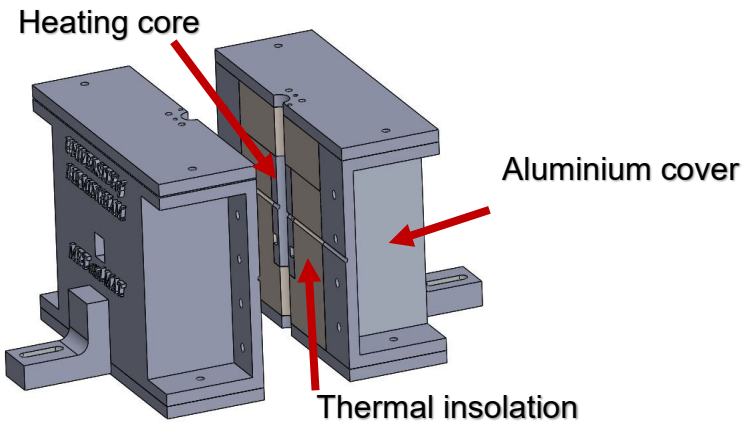

Figure 5.1 Schematic diagram of MTF

5.2.3 Finite element analysis of the temperature distribution via Abaqus

To ensure the surface temperature stays in a safe range (less than 40℃) for surrounding equipment while the central core has a high temperature to melt the sample (up to 900℃), a heat transfer simulation is performed via Abaqus (Dassault Systemes). Table 5-1 shows the properties of the materials used in the simulation.

Table 5-1 The properties of materials

Parts	Materials	Density $(g \cdot mm^{-3})$	Thermal conductivity $(mJ \cdot s^{-1} \cdot mm^{-1} \cdot ℃)$	Specific heat $(mJ \cdot g^{-1} \cdot ℃^{-1})$
Heating core	80% Nickel/ 20% Chromium	8.3E-3	12	880
Thermal insolation	MONOLUX	9.5E-4	0.23	1003
Aluminium shell	Aluminium	2.7E-3	205	910

5.2.3.1 Loading and boundary conditions

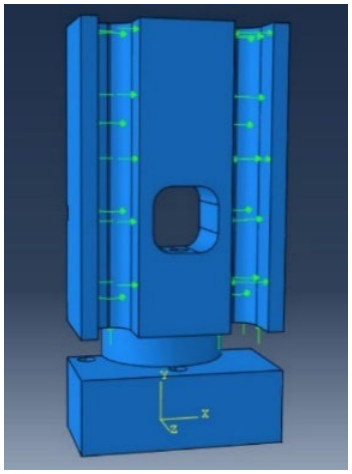

Figure 5.2 loading conditions

The internal channels of the heating cores are covered by the resistance heating wires, which are connected to a temperature controller (Control Unit CU2319 from Severn Thermal Solutions). The surfaces that are contacted with the heating wires are pointed by the green arrows in Figure 5.2. Three steps are considered to simulate the heating process. First, the initial temperatures for all parts and the environment were set at room temperature of 25℃. The heating core was then heated up by the surface heat flux in the magnitude of 24 mW/mm^2 for 1800 seconds, which will be the same heating parameters as in the experiment. Mesh element shape Quad and Technique Free is selected. A 4-node linear heat transfer quadrilateral (DC2D4) in Family Heat Transfer is chosen. The temperature distribution is shown in Figure 5.3. At this stage, only thermal conduction from the heating core to the aluminium shell is considered. It shows the maximum temperature is 893℃ and the surface temperature of the outer shell is 25℃.

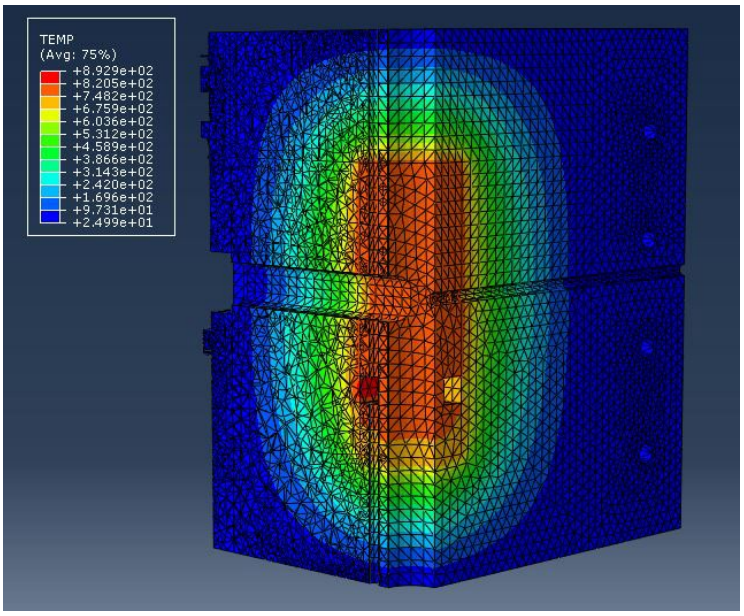

Figure 5.3 Temperature distribution of MTF after heating for 30 minutes.

In the second step, the holding period is simulated. During the experiment, samples will be held at a constant temperature for another 600-1800 seconds to ensure the samples are fully melting. Therefore, it is necessary to lower the surface heat flux in the simulation. In the next step, the heating flux is modified to 21 mw/mm^2 for another 1800 seconds. The modified heat distribution is shown in Figure 5.4. The central temperature is around 909℃. The surface temperature is lower than 40℃ in Figure 5.5, which is safe for the participants to change the samples during the experiment. The assembled furnace system at B16 beamline, the Dimond Light Source is shown in Figure 5.6.

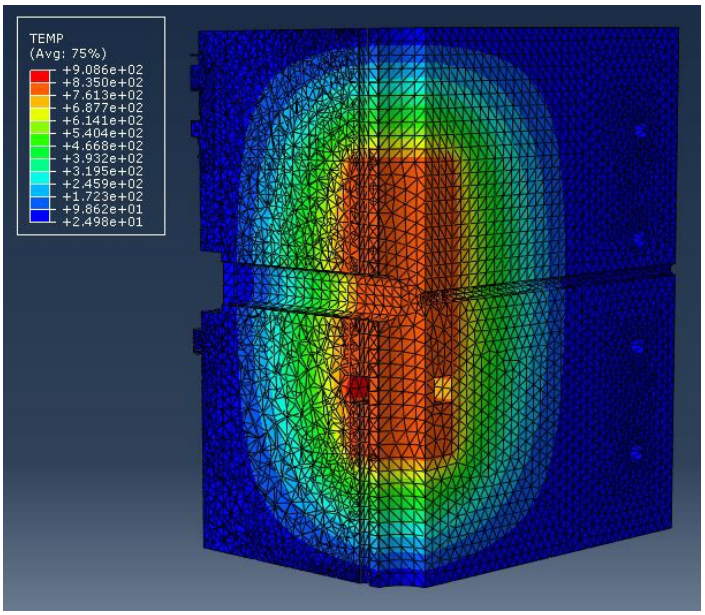

Figure 5.4 Temperature distribution of MTF after heating for 30 minutes and holding for extra 30 minutes.

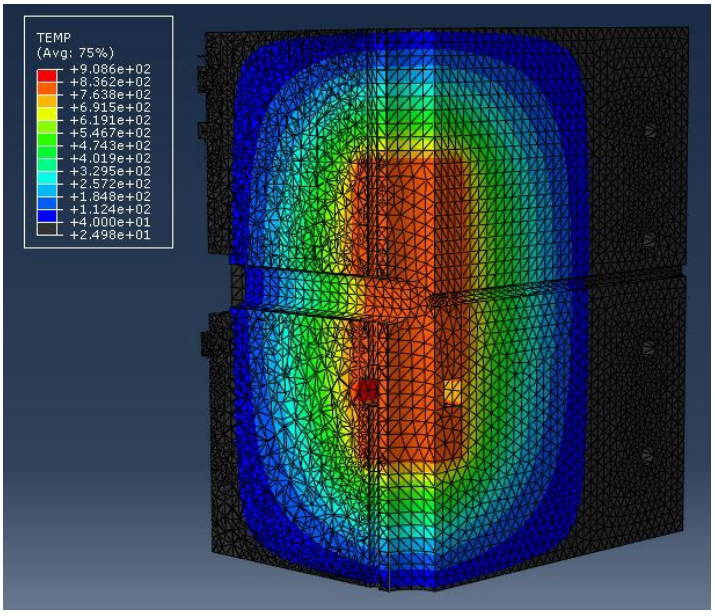

Figure 5.5 Temperature distribution of MTF higher than 40 ℃.

Figure 5.6 Assembled furnace at B16, Diamond Light Source.

During the experiment, the samples were placed in an alumina tube with an inner diameter of 2 mm. The experiment procedure includes first heating up the specimen gradually up to the melting temperature and holding it for 10 minutes to ensure full-temperature homogenization. The specimen was then cooled at different cooling rates as shown in Table 5-2 until fully solidified.

5.2.4 Real temperature distribution

Due to the inherent structure of the heating core, the top side of the heating core has less amount of resistance heating wires. Vertical temperature gradients cannot be avoided. Temperature distribution around the sample was measured by using a thermal camera (thermoIMAGER TIM 160, Micro-epsilon, USA) that has a temperature measuring range from -20℃ to 900 ℃. The camera was set at the same horizon as the window of the furnace as shown in Figure 5.7 The distance between the camera and the furnace was adjusted until the focus was on the ceramic tube.

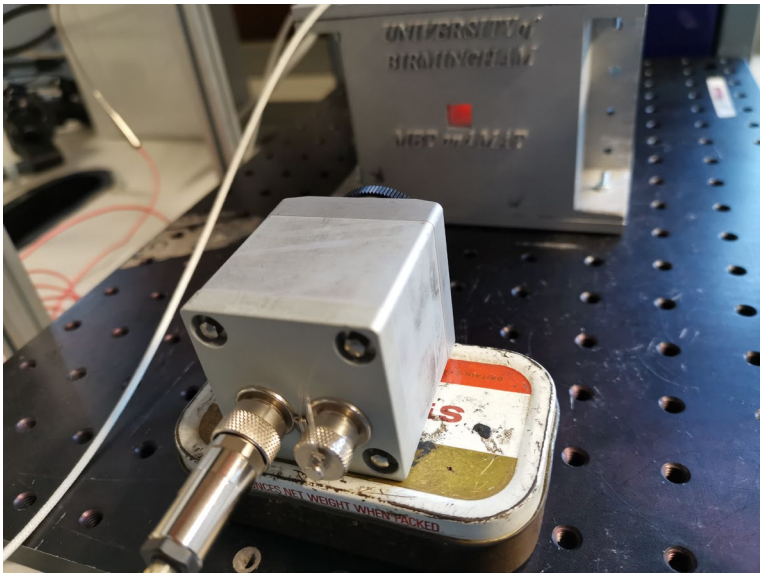

Figure 5.7 Temperature measurement setup.

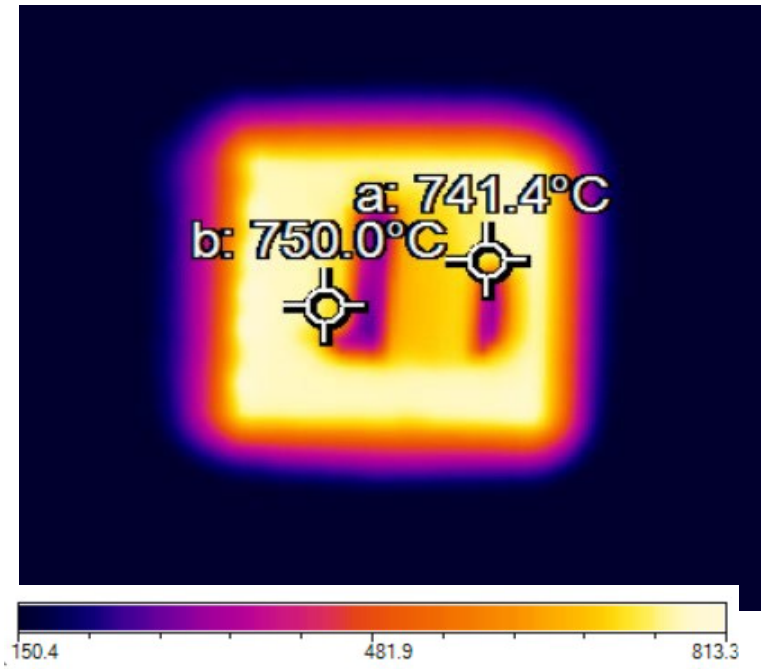

Figure 5.8 Temperature distribution around the sample.

Two type-N thermocouples were inserted nearby the surface of the ceramic tubes, which were then used to calibrate the temperatures by altering the values of emissivity of the materials in the camera system. The tips of the thermocouples are points a and b as shown in Figure 5.8. The vertical distance between these two points is 14.8 mm. The temperature difference is 8.6 ℃. Therefore, the vertical temperature gradient around the surface of the ceramic tube is about 0.6 ℃ $/mm$.

5.2.5 In-situ experiments

The in-situ X-ray tomography experiments were performed at the B16 beamline at the Diamond Light Source, Oxford. 35 keV white X-ray beam was used. High-Resolution X-ray Microscope with a PCO4000 CCD camera was used, providing a voxel size of 1.9 μm^3 (experiment A) and 2.5 μm^3 (experiment B). During solidification, high-speed tomographic scans were performed as the sample was continuously rotated. The collection time of each tomogram and the number of tomograms is presented in Table 5-2.

Table 5-2 experimental conditions:

	Cooling rates	Voxel size	Field of view	No. projections	Scanning speeds	No. Scan
A1	$0.5℃/min$	$1.9\mu m^3$	1350×1350	600	12s	210
B1	$3℃/min$	$2.5\mu m^3$	1600×1600	1000	20s	50
A2	$12℃/min$	$1.9\mu m^3$	1350×1350	600	12s	30
B2	$24℃/min$	$2.5\mu m^3$	1600×1600	1000	10s	50

5.2.6 SEM characterization and EBSD analysis

Solidified samples A1 ($0.5℃/\mathrm{min}$) and A2 ($12℃/min$) were analysed by using EBSD. The solidified samples were then sectioned and ground using SiC papers in the sequences of #1200, #2500, and #4000 on Struers Labopol-5. The samples were then polished using 'MD-Dac' cloth (Struers) with 3 µm liquid diamond suspension and finally using 'MD-chem' cloth with 0.04µm OPU (colloidal silica suspension). The parameters were tested successfully in polishing Al_2Cu IMCs in ref [228] .

The microstructural observations were carried out by Tescan MIRA 3 SEM, equipped with an Oxford Instruments EBSD detector controlled by the Aztec software. The parameters are shown in Table 5-3. Crystal orientations of Al_3Ni IMCs were indexed by using HKL Channel-5 Tango software.

Table 5-3 Parameters for EBSD analysis:

	Working distance (μm)	Step size (μm)	Scan area (μm^2)
A1	15.441	4.0	452×56
A2	16.085	2.5	295×477.5

5.2.7 Lab-based CT scanning of solidified samples

After EBSD analysis, the sample was scanned by using a lab-based CT (SkyScan2211, Bruker), to reveal the angles between the sectioned surface and the preferred growth orientation of the Al_3Ni crystals. The raw images have 4032× 4032 ×2361 pixels with a voxel size of 3.2 μm^3 for sample A1, which were then cropped into a sub-volume of 515× 451 ×905 pixels. The 3D images were analysed by Avizo 2021.2 (ThermoFisher Scientific, USA). The parameters of the CT scan are shown in Table 5-4.

Table 5-4 Scanning parameters of the Lab-based CT

Source of voltage	110 kV
Current	200 μA
CCD Filter	0.5 mm Al
Voxel size	3.2μm

5.2.8 Tomographic data processing

The collected tomograms from B16, Diamond Light Source were reconstructed using the Savu package [118,173]. 3D anisotropic diffusion was applied to reduce the noise [33], followed by image segmentation using Avizo 2021.2 (Thermo Fisher, US) [190].

5.3 Results and discussion

5.3.1 Overall microstructural evolution

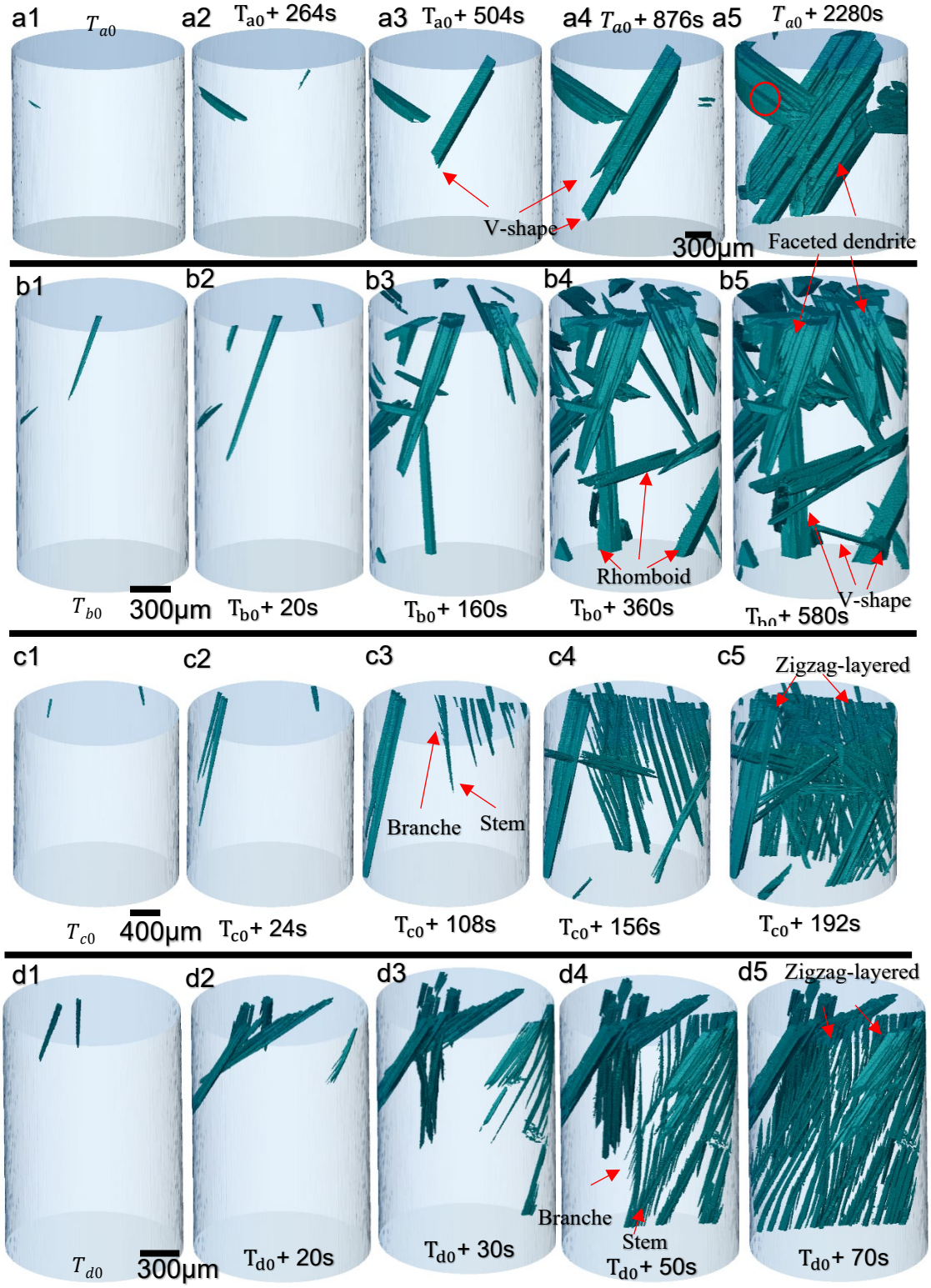

Figure 5.9 Growth process of Al3Ni IMC under different cooling rates of (a) 0.5℃/s; (b) 3℃/s; (c)12℃/s; (d)24℃/s.

Figure 5.9 presents the growth process of Al_3Ni intermetallic compounds under four different cooling rates, ranging from a very slow cooling rate of $0.5℃/min$ and up to a fat cooling rate of $24℃/min$. The light blue cylinder is the shape of the sample. Figure 5.9-a shows the 3D morphologies of Al_3Ni IMCs under a slow cooling rate of $0.5℃/min$. The tomographic images were captured every 12 seconds. The intermetallic compounds first nucleated and grew on the oxidized surface of the sample [190]. After 264 seconds in Figure 5.9 -a2, the second intermetallic compound appeared in the field of view with a needle-like tip, which grew downwards with a slightly tilted angle. One of the reasons that the IMCs grew towards the bottom of the sample is perhaps due to the temperature inhomogeneity of the furnace. A vertical temperature gradient exists as verified from both numerical simulation in Figure 5.4-a and real temperature distribution measurement in Figure 5.5. The vertical temperature gradient next the surface of the ceramic tube is around $0.6\ ℃\ /mm$. Lower temperature exists at the top region of the sample before and during solidification. Two more intermetallic compounds nucleated at the surface of the sample (circled in red) and then coalesced into a single dendrite from Figure 5.9 -a6 to a7. Finally, large trucks of faceted dendrites were formed.

In Figure 5.9-b, the cooling rate was increased from 0.5 to $3℃/min$. Faceted IMCs also nucleated and grew from both the top regions and side walls of the sample. The increased cooling rate has promoted the nucleation of IMCs. The total number of IMCs increased from 4 to 49. Rhomboid structures were observed at the bottom of the sample, such morphology was reported in refs [137,225] whereas faceted dendrites can be observed at the top of the field of view. Different to typical dendrites that have parabolic tips, the growth tips of both faceted dendrites and rhomboid structures clearly show V-shaped.

By further increasing the cooling rate to $12\,℃/min$ and $24\,℃/min$. A peculiar morphology is observed in Figure 5.9-c and d. Rod-like IMCs first appeared in the field of view, which then grew rapidly towards to bottom of the sample. Instead of forming large, faceted dendrites under the slow cooling rate. Protrusions are formed at the side plane of the primary stem (pointed by the red arrow), which then became multiple parallel branches (secondary). Finally, fine tertiary branches are formed from the secondary branch, forming a thin zigzag layered structure. Three main morphologies of Al_3Ni IMCs are categorized from the experiments including rhomboid, faceted dendrites, and zigzag layered structures. Representatives of each morphology are shown in the next sections.

5.3.2 Individual patterns

5.3.2.1 EBSD and CT of Al_3Ni IMCs from sample A1 and A2.

X-ray tomographic analysis can inform us the growth orientation of crystals if the bounding planes and interplanar angles of the crystal morphology can be easily identified as demonstrated in $Al_{13}Fe_4$ [190]. In this work, Al_3Ni formed complicated morphologies as shown in Figure 5.9, making it difficult to identify its preferred growth direction. A combined EBSD, and X-ray tomography approach developed in a previous work on Al2Cu was adopted [228]. Solidified samples from the synchrotron experiments were sectioned and EBSD was used to determine the orientation of the exposed plane of the Al_3Ni crystals. The sectioned specimens were scanned afterwards with lab-based CT scanner to obtain the 3D morphology of the Al_3Ni crystals. The EBSD image was matched with the 3D CT images.

EBSD maps of one region of the A1(0.5℃/min) and A2(120.5℃/min) sample are shown in Figure 5.10-a and b, respectively. Al_3Ni IMCs has an orthogonal crystal structure (a = 0.6598nm, b = 0.7352nm, c = 0.4801nm) [137]. One Al_3Ni IMC with dendritic shape is captured. Figure 5.10-a present the acquired crystal orientation of the faceted dendritic Al_3Ni (Euler1 = 62.1º, Euler2 = 88.2º, Euler3 = 50.3º; [HKL] = $[6\bar{5}2]$). It reveals that the analysed surface of the Al_3Ni is on the $(6\bar{5}2)$ plane. Similarly, the IPF and acquired crystal orientation of the zigzag-layered structure of Al_3Ni is shown in Figure 5.10-b (Euler1 = 62.1º, Euler2 = 88.2º, Euler3 = 50.3º; [HKL] = [430]). The analysed surface of the Al_3Ni is on the (430) plane.

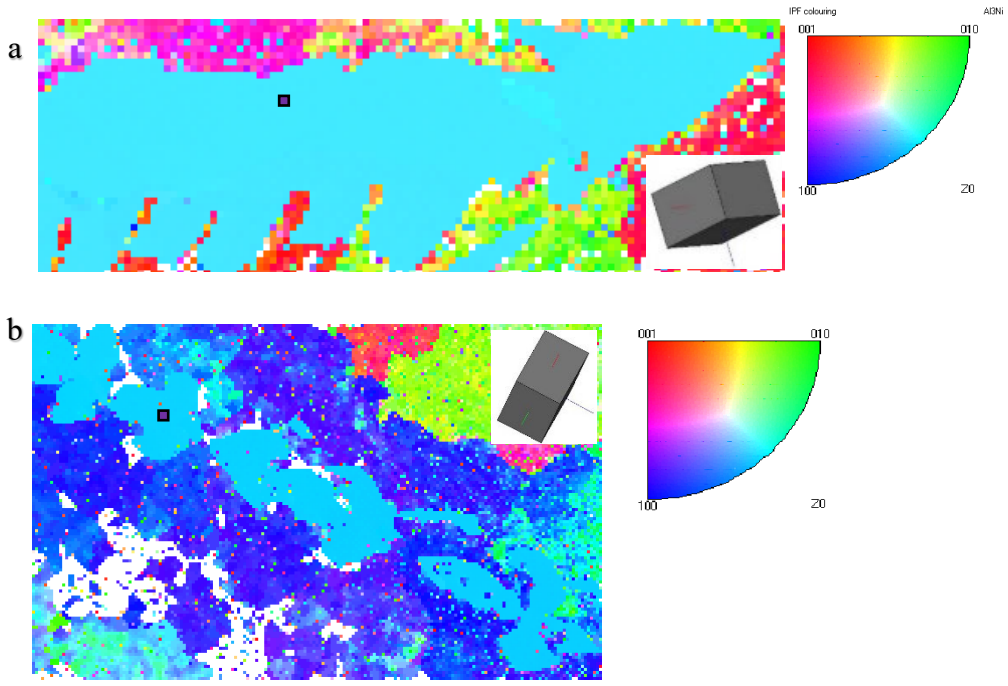

Figure 5.10 EBSD analysis of solidified sample A1(a) and A2 (b).

However, as the EBSD analysis is based on a 2D section from a complicated 3D dendritic structure, results from EBSD cannot accurately determine the preferable growth orientation of the faceted dendrites. The sectioned sample was then removed from Bakelite and scanned by a lab-based CT. The full 3D structure of the solidified faceted dendrite and zigzag-layered structure are shown in Figure 5.11. We were able to identify the dendrite and the sectioned plane, and then match the EBSD map onto the plane. It shows that the sectioned surface for the EBSD of the Al_3Ni dendrites was not parallel to its growth direction. As shown in literature, Al_3Ni crystals grow in <010> direction and bounded by {101} planes [14,106,108,229–232]. The angle between the sectioned surface and the preferable growth direction (red arrow) was found to be 138°$\pm$ 2°. The angle between the sectioned surface and the preferable growth plane (perpendicular to red arrow) was found to be 48°$\pm$ 2°. The angle between the $(6\bar{5}2)$ plane and plane (010)

or $(0\bar{1}0)$ is 124° or 56°, which shows that the preferable growth direction is highly likely in the direction of <010>. The calculated interplanar angle of plane (101) and $(10\bar{1})$ is 72º, which is consistent with the measured interplanar angle 73±2º in Figure 5.11-a. Based on this, we were able to identify and index the bounding planes (101). By using the same method to analysis sample A2, it confirmed that the multiple parallel branches of Al_3Ni share the same crystallographic orientation. The measured angles between the interplane of the faceted structure are around 74º, indicating the bounding planes are also{101}. The measured angle between the preferred growth direction (in black arrow) of the zigzag-layered structure and the sectioned EBSD plane is 40º± 2º. The measured angle between the preferred growth plane (perpendicular to the black arrow) and the sectioned EBSD plane is 50º± 2º. The calculated interplanar between (430) and (010) is 56º. Therefore, the preferred growth orientation is found to be <010> directions as shown in Figure 5.11-b.

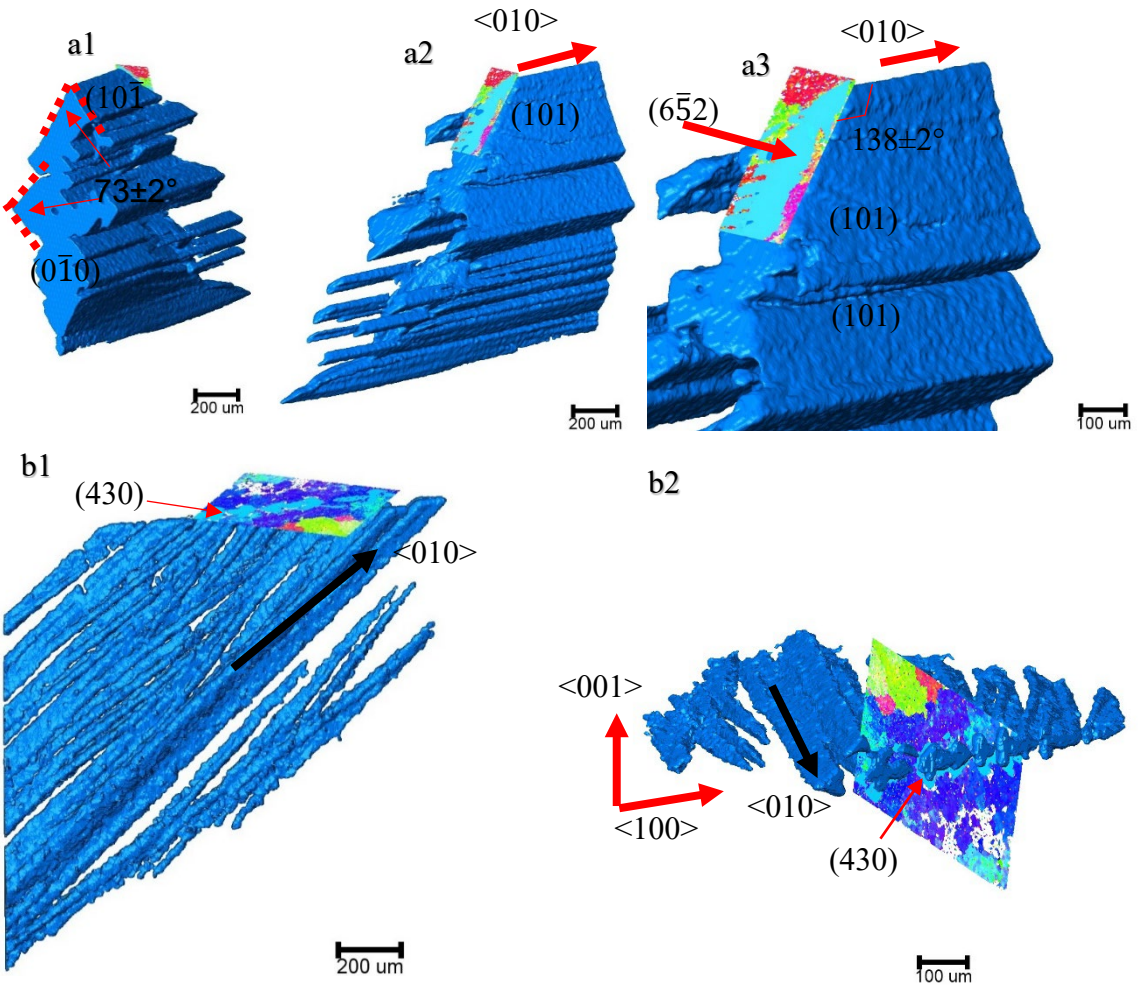

Figure 5.11 CT of faceted dendrite in the solidified sample A1: (a1) front view; (a2) back view; (a3) enlarged view. CT of zigzag-layered structure in the solidified sample A2: (b1) front view; (b2) side view.

5.3.2.2 Stage I- hollow rhomboid

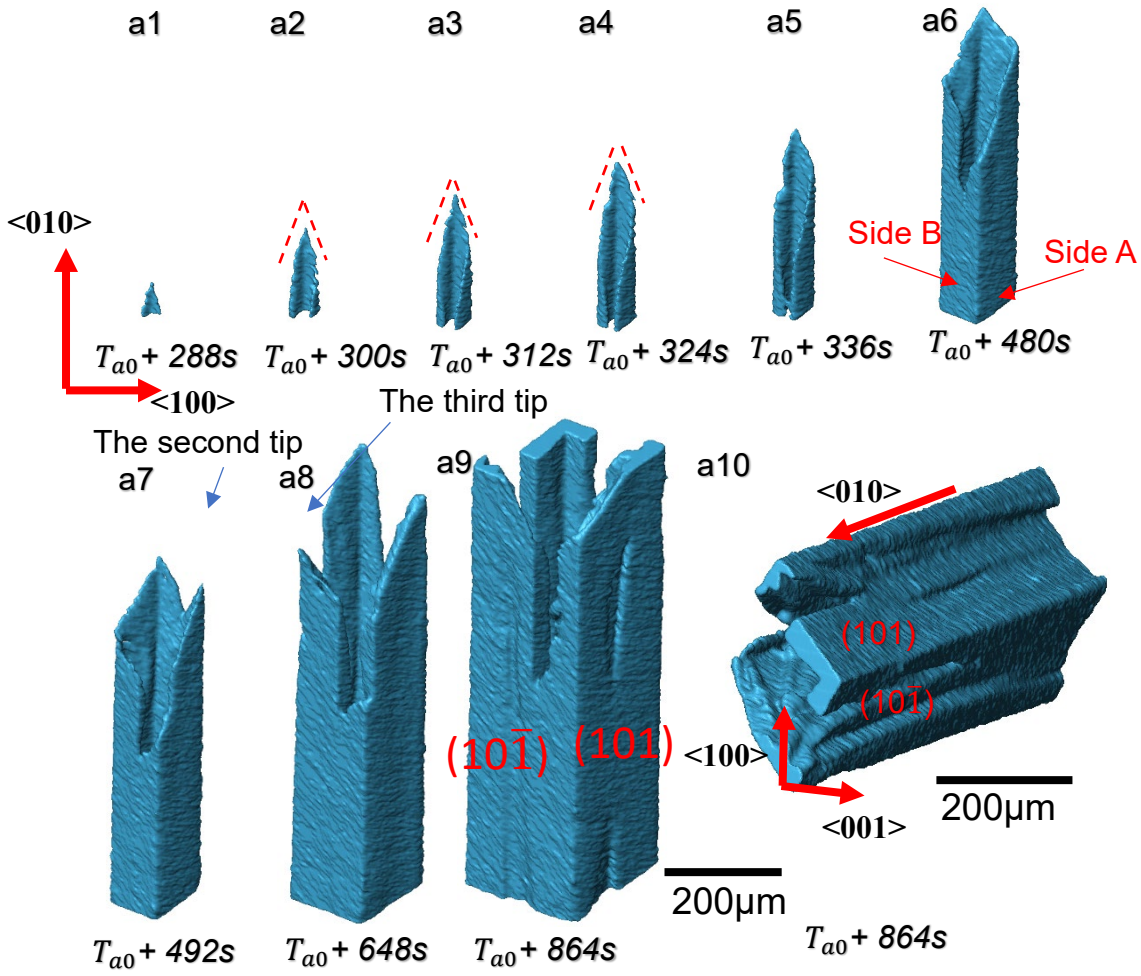

Figure 5.12 Growth process of faceted dendrite under 0.5℃/s at stage I.

By the particle tracking method developed at [190], a single-faceted Al_3Ni dendrite was extracted from the forest of Al_3Ni crystals in sample A1 (CR = 0.5℃/min), which clearly shows a two stage growth process (Stage I-Figure 5.12, showing the formation of a hollow rhomboid structure, whereas stage II – Figure 5.13, showing the growth of the dendrite). In the beginning, a small tip with two side walls was formed in Figure 5.12-a1. The inter-planer angles between the side walls are in the range of 74º to 76 º. In the cross-section area viewed from the top, it has a V-shape. A third wall appeared in the field of view in

the next 12 seconds in Figure 5.12-a2, which has inclined solid/liquid interface as indicated by the red dash lines. The same growth behaviour was also observed in the fourth sidewalls from Figure 5.12-a4 to a5. Once all side walls were fully grown, a central hole was formed.

In stage I, the average tip growth speed in the direction of <010> was 6.5 $\mu m/s$ in the first 12 seconds, which then decreased to 3.1 $\mu m/s$ in 96 seconds. Finally, it has a stable average growth rate of around 1.5 $\mu m/s$ until reaching the surface of the sample. In the direction of {101}, the average growth speeds are much slower. For side A, the average growth rate is reduced from 0.8 $\mu m/s$ to 0.3 $\mu m/s$ in 420 seconds, while it was reduced from 0.7 $\mu m/s$ to 0.2 $\mu m/s$ for side B. Two more sharp tips were formed at the edge of the side walls, which grew upwards until reaching the surface of the sample. Its cross-section area has a rhombus shape with a central hole.

The growth mechanism of faceted hollow rhomboid Al_3Ni IMCs was considered based on the classic Burton-Cabrera-Frank (BCF) theory [137,191], in which the crystal grows along the screw-dislocation line and is governed by the step-growth mechanism. The hollow core was developed perhaps because the strain energy exceeds the surface energy required to create a new face [137,191]. In BCF theory, the crystal continues to grow perpetually 'up a spiral staircase'[58]. However, from our results, the crystal starts to grow from a rod-like tip in the direction of <010> at the rate of 3.1 $\mu m/s$, which then branches in the direction of <101> at a slower rate of 0.2-0.3 $\mu m/s$. Such growth behaviour is significantly different to spiral growth in that crystal grows along a dislocation core.

Furthermore, holes due to dislocation were observed in nano-materials at the scale of nano-metres [233,234]. In Al_3Ni IMCs, the diameter of the central hole is up to a few hundred micrometres in Figure 5.12-a. The required surface energy to create a new inner surface with a diameter of hundreds of micrometres is highly unlikely to be overcome by the dislocation strain energy from the nanoscale. The origin of the hole is more likely due to the anisotropic growth of different planes. The anisotropic growth rate and direction are related to its atomic structures, and covalent bonding [235,236]. The size of the hollow rhomboid can be influenced by the available solute and cooling rate. New tips were observed during the growth of the sidewall pointed by blue arrows in Figure 5.12, perhaps due to the local temperature fluctuation at the solid/liquid interface that promotes their growth velocities. Such growth behaviour was also observed in Al_2Cu basic units [237].

5.3.2.3 Stage II-faceted dendrite

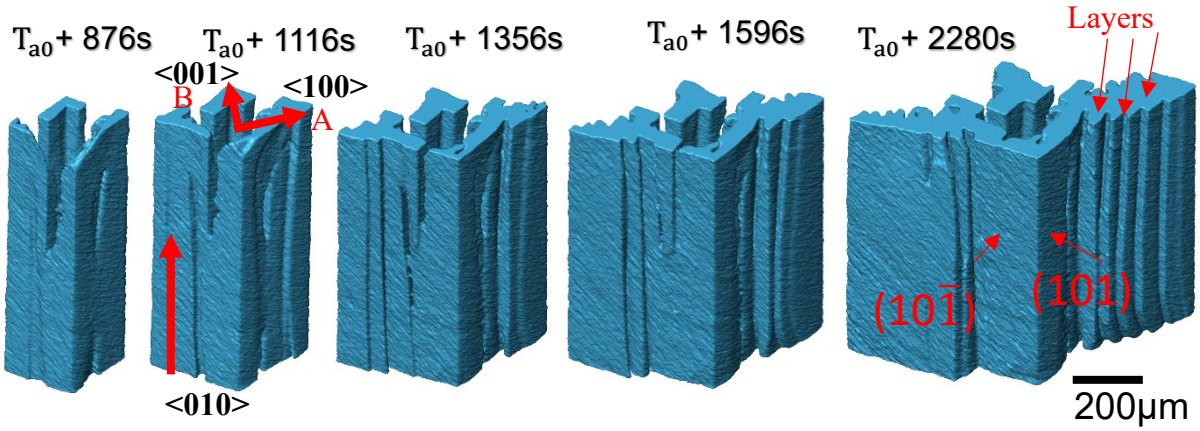

Figure 5.13 Growth process of a faceted dendrite under $0.5℃/s$ at stage II.

Once the front tips reached the surface of the sample, stage II is initiated. The IMCs begin to grow in the diagonal directions of the rhomboid shape. Here they are named as the secondary growth directions. The secondary growth directions are orthogonal to each other. According to its crystallographic relationship, the secondary growth is in the directions of <100> and <001>. New layers (the basic unit in V-shaped) were formed on the side planes in the direction of <100> and <001> layer-by-layer. Finally, a faceted dendrite with a central hole was formed. The diagonal direction A of the bounding plane with the smaller inter-planer angle (74°) is in the direction of <100>, the other diagonal direction B is in <001>. The average growth speed in <100> direction is 0.43 $\mu m/s$ which is almost as double in the other direction $0.21\mu m/s$ in 1032 seconds. Various final morphologies of Al_3Ni (V-shaped, hollow rhomboid and faceted dendrite) have already been observed in previous studies from CT of solidified sample or in-situ radiography [14,191,225]. However, the relationship and transitions between these growth patterns have not been experimentally identified. Here, a clear transition from a V-shaped pattern

to hollow-rhomboid, and finally to a faceted dendrites is observed. This suggests that V-shaped and hollow-rhomboid might be intermediate stages for Al_3Ni growth.

5.3.2.4 Zigzag-layered structure

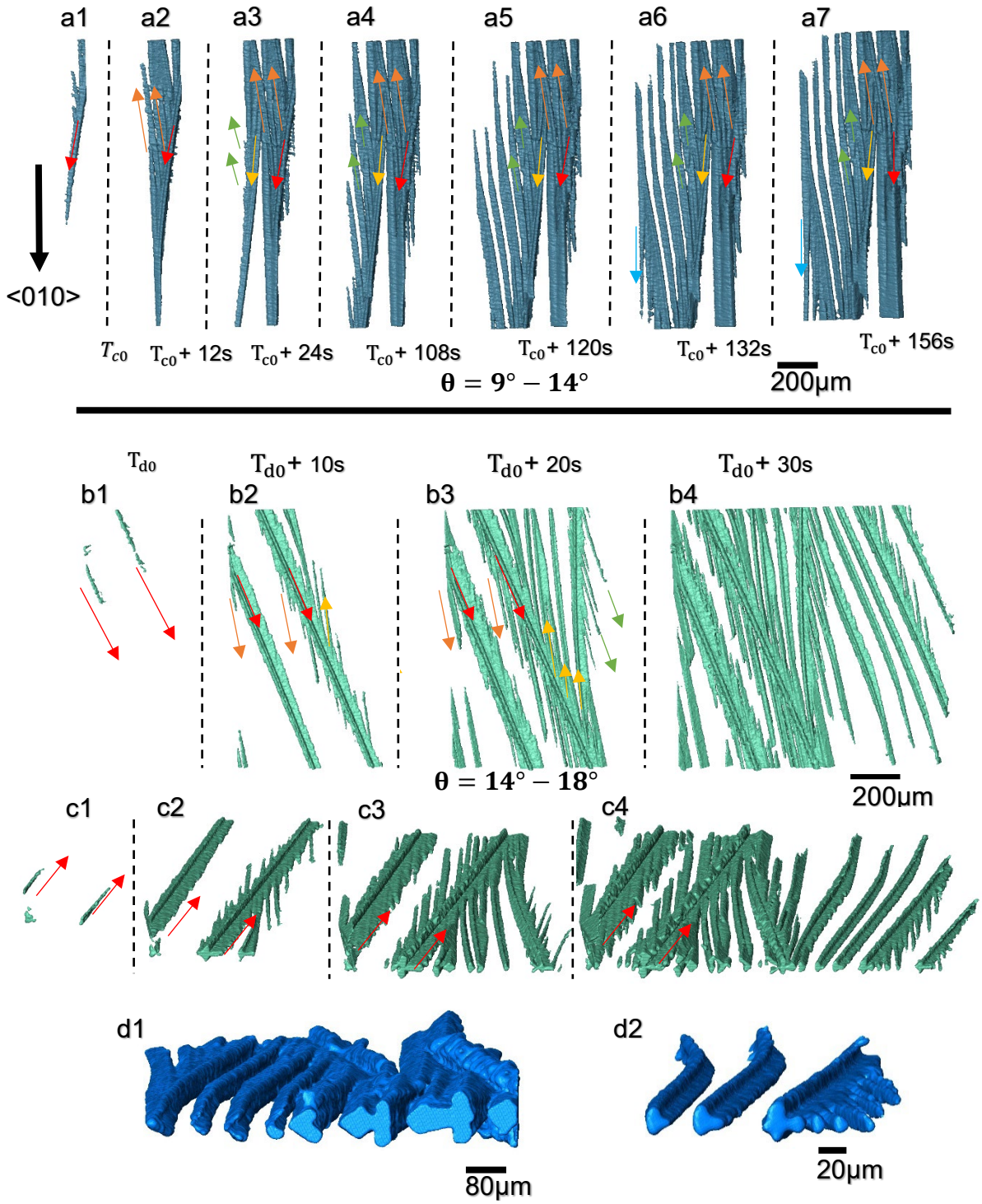

Figure 5.14 Growth process of zigzag layered Al3Ni intermetallic compounds at the cooling rates of 12℃/min (a); and 24℃/min (b) front view; (c) side view; (d1) enlarged side view of (a7); (d2) enlarged side view of (c4).

Figure 5.14-a shows the chosen representative of Al_3Ni IMCs at a high cooling rate of 12 $℃/min$. New morphologies and growth behaviours were observed. Rod-like patterns were first presented in the selected field of view, which grow towards the bottom of the sample as shown in Figure 5.14-a1 (in the direction of the red arrows) which formed the primary stem. Protrusions can already be found at the left side of the stem in Figure 5.14-a2 and the protrusions grew into secondary arms (in the direction of the orange arrows) in Figure 5.14-a3. Later, new protrusions forms on the side plane of the secondary arm, which then grew into the tertiary arms (in green arrows). Finally, by repeating the same protrusion formation and branching behaviours, a zigzag layered structure is formed. The direction of the branches (3rd and 5th branching) either share almost the same growth orientation as the main stem in the direction of <010> or they form an obtuse angle in the range of 9º -14º (2nd and 4th branching) with the growth direction of the main stem (<010>).

Figure 5.14-b presents the growth process of the zigzag-layered structure at the cooling rate of 24 $℃/min$. Two rod-like patterns appeared in the selected field of view, which grow towards the bottom of the sample. Different to Figure 5.14-a2 that protrusions only form on one side of the main stem, in Figure 5.14-b2, protrusions formed in both side of the primary stem. At the left side of the stem, branches grew towards the bottom of the sample (in the direction of orange arrows), while at the other side of the stem, they grew towards the opposite direction forming multiple parallel branches as the secondary arms sample (in the direction of yellow arrows). The angles between the main stem and the secondary arms are in the range of 14° - 18°. By self-repeating the same growth behaviours, a zigzag layered structure was formed. This morphology has been reported in ref [108,137] via 2D in situ radiography.

5.3.3 Influence of cooling rates on Al_3Ni IMCs

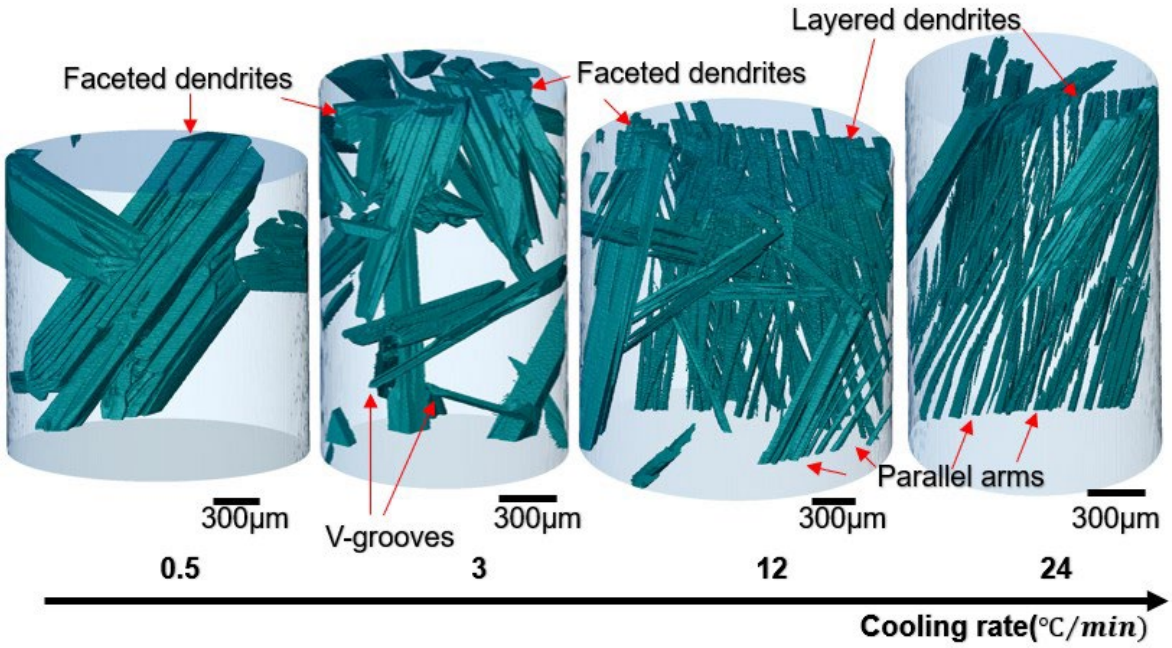

Figure 5.15 3D structures Al_3Ni IMCs under different cooling rates.

Under the slow cooling rates of 0.5℃/min and 3℃/min, the morphology of Al_3Ni IMCs is mainly influenced by their crystal structure and thermodynamic properties [63]. Under sufficient time, it first grew into basic units with a V-shape or hollow-rhombus shape with a preferred growth orientation of <010> and bounding planes of {101}. It then grows layer-by-layer in the direction of <100> and <001> to form a faceted dendrite. This growth mechanism of the faceted dendrites has been observed and proposed in faceted Al_2Cu dendrites [228]. At high cooling rates, Al_3Ni IMCs started with a long stem with a rod-like shape in a preferred growth direction of <010>. Some of the tips of the stem are in a V-shape, which shows a similar growth mode to the basic unit but with a much thinner sidewall. Different to layer-by-layer growth mode the faceted dendrites, and protrusions were formed at the edge of the sidewalls. Jackson's factor for Al_3Ni is 2.1 [238] suggesting it is close to the transition between an atomically smooth (faceted) and rough (non-faceted) interface. Increasing the cooling rate, it can trigger interface or kinetic

roughening [46,239]. High cooling rates can influence the process of heat removal from the front of the solidified structure. It can also reduce the time for the solute to redistribute ahead of the solid/liquid interface resulting in large solute undercooling [63]. For instance, Bäcerud [240,241] studied the undercooling of Al-Cu binary alloys under different cooling rates. It shows the undercooling has been increased from 1 K to almost 5 K in Al-5wt%Cu alloys by increasing the cooling rate from around 0.3 to 4.8 K/s. The increased undercooling can result in an unstable interface. Interface instability was observed in Al_3Sc and Al_6Mn IMCs under high cooling rates and non-faceted dendrites were formed [156,242]. This promotes the formation of protrusions on the existing structure and subsequently grows towards the solute-rich regions to form multiple well-aligned secondary arms. The edges of the secondary arms can also be the initiation sites of the protrusions, which results in ternary arms. By repeating the same growth behaviour, a zigzag layered structure is formed. The tips of the zig-zag structure are in the shapes of both faceted (V-shaped) and non-faceted in Figure 5.14-d1. Under the high cooling rates, no holes or only small holes were observed in the main stem of the zigzag layered structures as expected, because the formation of the central hole was considered due to the anisotropic growth in <010> and <101> directions during stage I (the formation of hollow rhomboid structures). Under the high cooling rate, the time was perhaps not sufficient for the basic units (V-shaped) to grow into faceted rhomboid shapes, thus a central hole was not observed. Non-faceted tips were also observed under the high cooling rates in Figure 5.14-d. It suggests the solid/liquid interface undergoes kinetic roughing that governed by diffusion and curvature as the driving force is increased [46,243].

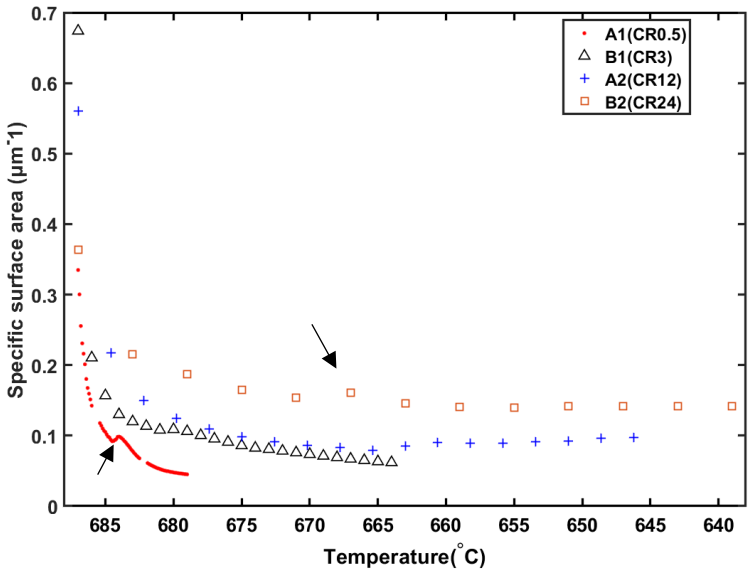

Figure 5.16 Specific surface area as a function of temperature under different cooling rates.

The specific surface areas (surface areas divided by volumes) of the IMCs under different cooling rates were quantified as shown in Figure 5.16. Each sample has the largest specific surface area at the beginning of the crystal growth. It is then reduced rapidly until reaching a steady-state during the growth process [54]. During solidification, the specific surface area can be increased when new nucleation occurs as pointed out by black arrows in Figure 5.16. Sample A1 (CR = 0.5 ℃/min) has the lowest specific area of 0.0478 μm^{-1}at the steady state with large trunk of faceted dendritic structures. By increasing the cooling rate from 0.5 ℃/min to 3 ℃/min, around 680℃, the specific surface area was increased to 0.109 μm^{-1}, as the number of IMCs was increased from 4 to 49. In this sample (A2), we have observed mostly hollow-rhombus and faceted dendritic structures. With further increased cooling rates in sample A2 (CR = 12 ℃/min) and B2 (CR = 24 ℃/min), higher specific surface areas of 0.124 μm^{-1} and 0.187 μm^{-1} were achieved,

respectively. The morphologies of Al_3Ni IMCs were changed from faceted dendrites to zigzag-layered structures. The growth mechanisms were altered from self-repeated layer-by-layer growth mode to zig-zag branching.

5.4 Summary

High-speed synchrotron X-ray tomography has been used to investigate the growth dynamics of Al_3Ni IMCs and the influences of cooling rates on the morphologies of Al_3Ni IMCs. The growth mechanisms of the Al_3Ni IMCs with various morphologies have been studied. The following key points can be made:

- A bespoke medium temperature furnace (MTF) was designed, simulated, and made for the in-situ synchrotron X-ray tomographic experiments at beamline B16, Diamond Light Source.
- Four samples were solidified under different cooling rates from $0.5℃/min$ up to $24℃/min$. Under slowing cooling rates of $0.5℃/min$ and $3℃/min$, V-shaped, hollow-rhomboid and faceted dendrites were observed. Zigzag-layered structures were observed under high cooling rate of $12℃/min$ and $24℃/min$.
- The V-shaped and hollow rhomboid structure are the intermediate stage of the faceted Al_3Ni IMCs, which can continue to grow into faceted dendritic structures.
- The anisotropic tip growth rates in the direction <010> and <101> can be the cause of central holes in hollow-rhomboid or faceted dendrites.
- Layer-by-layer growth mechanism that was observed in faceted Al_2Cu dendrites is still applicable to the faceted Al_3Ni dendrites with different preferable growth directions and bounding planes.

- The zigzag branching growth mechanism was proposed to be the growth of a zigzag layered structure of Al_3Ni IMCs at high cooling rates of 12℃$/min$ and 24℃$/min$.
- By increasing the cooling rate from 0.5℃$/min$ up to 24℃$/min$, the morphology of the IMCs has been changed from faceted dendrite to zigzag-layered structures while the specific surface area has been increased from 0.0478 $\mu m^{-1}$to 0.187 μm^{-1}.

Chapter 6: Magnetic field-assisted solidification of W319 Al alloy imaged by high-speed synchrotron tomography*

* This chapter has been published in Journal of Alloys and Compunds.

Zihan Song[a], Elodie Boller[b], Alexander Rack[b], Peter D Lee[c], Biao Cai[a], Magnetic field-assisted solidification of W319 Al alloy qualified by high-speed synchrotron tomography, J. Alloys Compd. (2022) 168691. https://doi.org/10.1016/j.jallcom.2022.168691.

a. School of Metallurgy and Materials, University of Birmingham, B15 2TT, UK
b. ESRF-The European Synchrotron, 71 Avenue des Martyrs, 380 0 0 Grenoble, France
c. Mechanical Engineering, University College London, London, WC1E 7JE, UK

Acknowledge of Collaborative Work:

Zihan Song: Writing-Original draft, Methodology, Validation, Investigation; Elodie Boller: Investigation; Alexander Rack: Investigation; Peter D Lee: Validation, Writing-Review & Editing; Biao Cai: Writing-Review & Editing, Conceptualization, Investigation, Supervision, Funding acquisition.

6.1 Introduction

Compared with the primary aluminium production from bauxite core, secondary aluminium ingots produced from recycled aluminium scrap, including end-of-life automotive and used beverage cans, can save up to 95% of the energy [244]. However, impurities such as Iron and Silicon accumulate during the recycling process [245]. Iron is expensive to remove. Further, iron has a very low solid solubility (max 0.05 wt%) in aluminium [246] and can form hard and brittle Fe-rich intermetallic compounds (IMCs) such as $Al_{13}Fe_4$ [10,247] and β-Al_5FeSi [248]. Their morphologies, sizes and distribution, if not controlled, can negatively impact alloy castability [130] and reduce the final component's mechanical and corrosion properties [132,249]. IMCs in aluminium alloys can be controlled by both their crystal structures and solidification conditions such as cooling rates, temperature gradients and external fields (e.g. mechanical shearing, ultrasonic processing, or magnetic stirring) [89,237,250–252].

Synchrotron X-ray radiography has been widely used to reveal the growth process of various IMCs in Al alloys during solidification, for instance, α-Al(FeMnCr)Si in Al-Si-Cu alloys [31] and $Al_{13}Fe_4$ in Al-3%Fe alloys [10,11]. Recently, high-speed synchrotron X-ray tomography has been developed allowing us to unravel the microstructures in 4D (3D plus time) [7,13,30,134,190,253], and the approach was applied to study Fe-rich intermetallics in Al alloys. Terzi et al. [30] reported the growth of irregular α-Al/β-Al_5FeSi eutectic. Cai et al. [13] studied the coupled growth of primary α-Al and secondary β-phase in W319 alloy, which found that the growth rates and sizes of β-phase were restricted by the available inter-primary dendritic space. Puncreobutr et al. [134] illustrated the secondary β-phase has great effects on blocking liquid flows and decreasing the permeability of the semi-solid Al-Si-Cu alloys. Cao et al. [253] have revealed the

growth process of the primary Fe-rich IMCs with and without a weak magnetic field (0.07 T) of Al-Si-Fe alloy.

Magnetic fields have been widely used in altering the fluid flows during solidification processes [110,142,201,254–256], making use of physical effects including electromagnetic damping [257,258], electromagnetic stirring [23,259] and thermoelectric magnetohydrodynamic [199,260]. Previous studies showed that when applying a rotating magnetic field, both the temperature and solute distribution can be homogenized during solidification, leading to structure refinement of the primary α-Al phase [114,201]. However, several questions remain unanswered. In Al-Si-Cu based alloys, as the β-intermetallic is the secondary phase following the primary α-Al phase [13], will the growth behaviours of β-IMCs be influenced by the application of magnetic fields? Will the modified morphologies of the solidification microstructure influence the permeability in the mushy zone? In view of these questions, the present study aims to reveal the growth dynamics of both the primary α-Al phase and secondary β-IMC during solidification of W319 (Al-Si-Cu based) alloys under a constant transversal magnetic field of 0.5 T while the sample is rotating via high-speed synchrotron tomography. Then we calculated the absolute permeability of the solidified structures using image-based simulation with and without the presence of the β-intermetallic compounds under different solidification conditions. The results can be used to validate simulation models, especially the growth behaviours of secondary IMCs during the casting of aluminium alloys. It also demonstrates that a magnetic field can be used to control the distribution of iron-rich intermetallics.

6.2 Materials and Methods

The Al-Si-Cu alloy W319 (Al-5.50Si-3.40Cu-0.87Fe-0.27Mg, in weight per cent) was provided by Ford Motor Company. The alloy is frequently used such as in engine blocks and cylinder heads [261]. Cylindrical specimens with diameters of 1.8 mm and lengths of 100 mm were cut via wire electrical discharge machining. Each sample was placed into an alumina tube with a 2 mm inner diameter and 3 mm outer diameter. A bespoke temperature gradient furnace (MagDS) [13,166] was used to perform the solidification experiment. MagDS furnace consists of a small bespoke temperature gradient stage and a magnet yoke**,** which was used to control the solidification conditions (cooling rates (CR), temperature gradients (TG) and the strength of the magnetic field (B)). Two experiments were performed. In the first experiment, the sample was heated up until melting. The specimen was then held at the melting state for 20 minutes before it was cooled at a constant rate (CR) of $0.1℃/s$ until fully solidified [201]. A temperature gradient (TG) $2.5℃/mm$ was applied to the specimen (the top part was set at a higher temperature). In the second experiment, the magnet yoke was installed to the furnace, which was able to produce a transverse magnetic field of B = 0.5T. The solidification experiment was carried out using the same heating and cooling conditions. Thereby, solidification condition I is B = 0 T, CR = $0.1℃/s$, TG=$2.5℃/mm$, whereas solidification condition II is B = 0.5 T, CR = $0.1℃/s$, TG=$2.5℃/mm$. In both conditions, the samples were rotating continuously during cooling for tomography.

The in situ solidification experiment was performed at ID19 beamline of the European Synchrotron Radiation Facility (ESRF), with a 31 keV pink X-ray beam [116]. A high-resolution high-speed detector (PCO.dimax) was used, achieving a pixel size of 2.2 μm,

and a field of view (FOV) of 2.2 × 2.2 mm^2. During solidification, rapid tomographic images were acquired when the sample was rotating at a speed of π (rad/s) continuously. Each tomogram required a collection time of 1 second and was composed of 1000 projections (radiography), collected over 180°. Another 15 seconds of waiting time were consumed for downloading the tomograms between two consecutive scans.

For absorption contrast-based synchrotron X-ray tomography, the phases with higher density (higher absorption coefficients) have higher grey values [27,119], allowing the distributions of density/composition before and during solidification to be mapped. Using this concept, 2D vertical slices with an artificial colour map based on 16-bit unit images were ploted. In this work, the regions with low attenuation values are shown in blue and green (e.g. in Fig.1-a), which normally mean a higher concentration of light elements such as Al and Si in this experiment. Conversely, yellow to red regions should contain heavier elements such as Fe and Cu, which strongly attenuate the X-rays.

Avizo 2020.1 (Thermo Fisher, U.S.) was used to segment and quantify the phases and perform the absolute permeability simulation. For the primary α-Al phase, 3D anisotropic diffusion was chosen to reduce the noises [33], followed by the function of interactive thresholding whose values were based on the Ostu method implemented in ImageJ [206]. To segment the secondary β-Al_5FeSi IMCs, 3D anisotropic diffusion and morphological Laplacian filters were employed.

Figure 6.1 shows the 2D images at sequences of image processing, including a raw image (a), after de-noising (b) and after the thresholding process(c). Figure 6.1-d plots the distribution of grey values between the liquid and α-Al phase, indicating a good contrast difference. After de-noising, the contrast between the two phases is more diverse as presented in Figure 6.1-e. Finally, the thresholding values that are based on Otsu's method from ImageJ were chosen. The α-Al phase was effectively segmented (Figure 6.1-c).

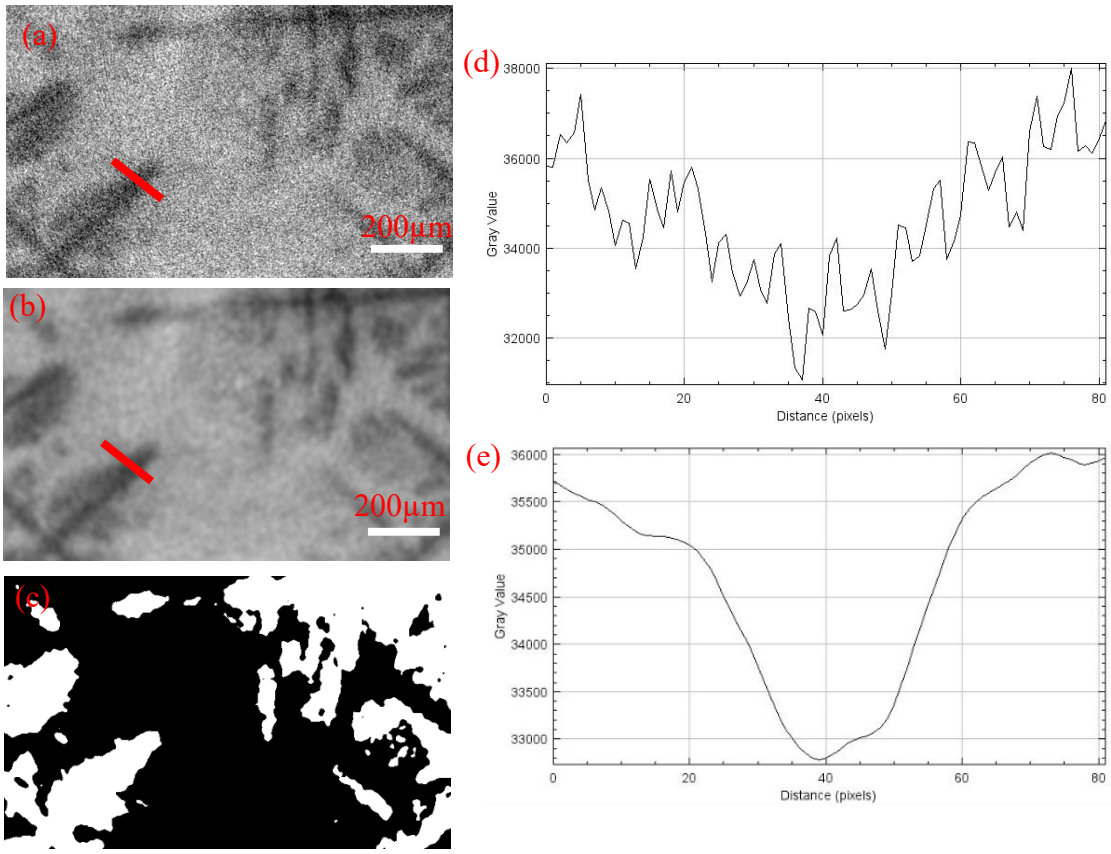

Figure 6.1 Image processing of α-Al phase in W319 alloys (a) raw image (b) denoised image; (c) segmented α-Al phase; (d) Gray values of the region crossed by the red line in figure s1-a; (e) Gray values of the region crossed by the red line in b.

Figure 6.2 demonstrates the 2D images at sequences of image processing. There are three main steps. Figure 6.2-a shows the raw image, which was then de-noised as shown in Figure 6.2 -b. β-phase intermetallic compounds present in bright needle shapes in 2D. The edges of the needle shapes were detected by using the Morphological Laplacian module in Figure 6.2 -c. A good contrast difference between the β-phase and the other regions was achieved. Finally, the intermetallic compounds were segmented (Figure 6.2 -d). In calculating the volume fraction of β-IMCs, we have altered the segmentation values ($\pm$ 10 from the target value) between Figure 6.2 -c and Figure 6.2 -d. The volume fraction of β-IMCs under the magnetic field at T = 272 seconds is in the range of 0.0228-0.246. Its calculated volume fraction is 0.238 based on the target value. Therefore, an uncertainty of $\pm$0.001 is considered.

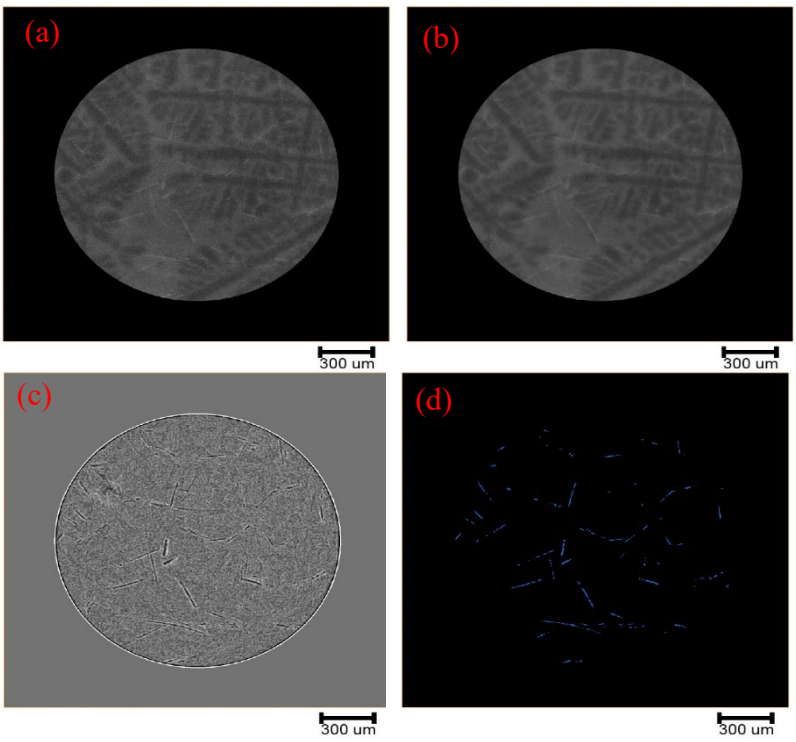

Figure 6.2 Image processing of β-phase in W319 alloys (a) raw image (b) denoised image; (c) detected edges by using Morphological Laplacian module; (d) segmented β-phase.

Absolute permeability was calculated by solving the Stokes equations as shown below using the Avizo XlabSuite Extension toolbox [262].

$$\vec{\nabla}.\vec{V}_L = 0 \quad (6\text{-}1)$$

$$\mu_L \nabla^2 \vec{V}_L - \vec{\nabla} P_L = \vec{0} \quad (6\text{-}2)$$

Where $\vec{V}_L$ is the velocity of the fluid, μ_L is the dynamic viscosity of the fluid, $\vec{\nabla}.$ is the divergence operator, $\vec{\nabla}$ is the gradient operator, ∇^2 is the Laplacian operator and P_L is the pressure of the fluid.

8 groups of tomographic data from each experiment were chosen. Sub-volumes of 882× 882× 882 μm^3 from the botton centre of the FOV were cropped out for the simulation. Inlet flow along the vertical direction provided the permeability of fluid to flow parallel to the primary dendritic arms as the dendrites were aligned with the vertical direction of the samples. The flow simulations were set with the input pressure of 1.3 bar and the output pressure of atmospheric pressure by default. The fluid viscosity was set to be 0.001 Pa.s [134,248].

6.3 Results and discussion

6.3.1 α-Al phase

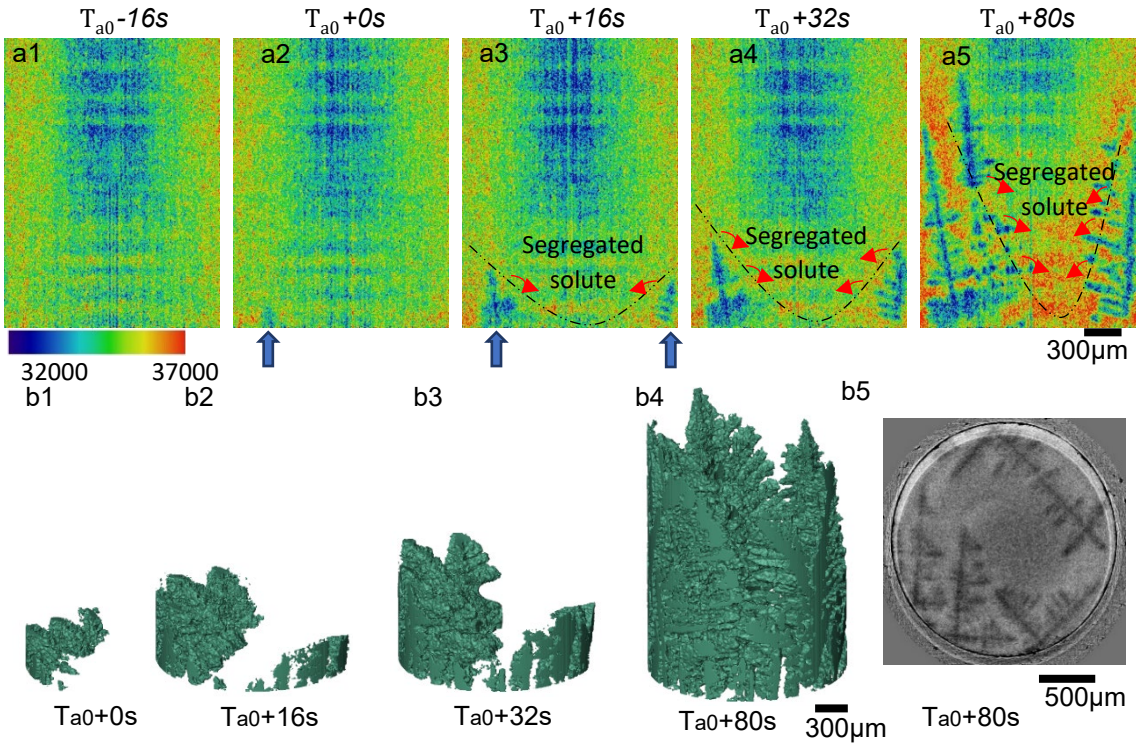

Figure 6.3 (a) 2D vertical slices of α-Al phase at different timestamps (B= 0T, TG= 2.5 ℃/mm, CR= 0.1℃/s); (b1-b4) 3D volumes of α-Al phase at different timestamps; (b5) a horizontal slice at the height of 1.1mm.

Figure 6.3 shows the growth process of the primary α-Al phase without a magnetic field in the first 80 seconds. Figure 6.3-a1 is the slice captured 16 seconds before the dendrites were observed within the FOV. The periphery of the sample shows higher image contrast, indicating heavier elements were driven to the periphery to form the macro-segregation zone, possibly due to the centripetal force resulting from the sample rotation during the holding period (20 minutes). As a positive vertical temperature gradient (TG) of 2.5℃/mm was applied during cooling (a lower temperature at the bottom of the FOV), columnar dendrites appeared at the bottom of the FOV and grew upwards. The dendrites

grew from the left side of the sample first (Figure 6.3-a2 and Figure 6.3-b1). 16 seconds later, a few more dendrites appeared on the bottom right side. These dendrites then branched toward the centre region of the FOV (Figure 6.3-a3 and b2). Well-developed large dendritic trunks with both secondary and tertiary arms formed after 80 s (Figure 6.3-a5 and Figure 6.3-b4). As shown in Figure 6.3-a5, there is a large region (27.8% cross-section area fraction based on Figure 6.3-b5) free of dendrite in the middle of the sample, resulting in a very uneven, concave solid-liquid interface and macro-segregation of Cu, reducing the solidification temperature in this region. The angle between the solid/liquid interface and the horizontal direction is around 70º.

During solidification, solute elements such as Cu, Fe and Si would be ejected into the melt. Due to the gravity effect [166], heavy elements (Cu and Fe) accumulated in the free space in the middle and bottom of the sample, leading to a macro-segregation zone that shows in yellow and red (high grey values) in Figure 6.3-a5. This solute accumulation restricted dendrites from growing into this region, as observed in Figure 6.3-a3 and Figure 6.3-b2, leading to the formation of a curved solid/liquid interface. This curved interface became more severe as more Cu and Fe atoms are ejected into the central region of the sample (Figure 6.3-a4 and a5). The secondary arms of existing dendrites branch into this zone at the later stage of solidification after the temperature has decreased further, forming well-developed dendritic structures (Figure 6.3-b4 and b5).

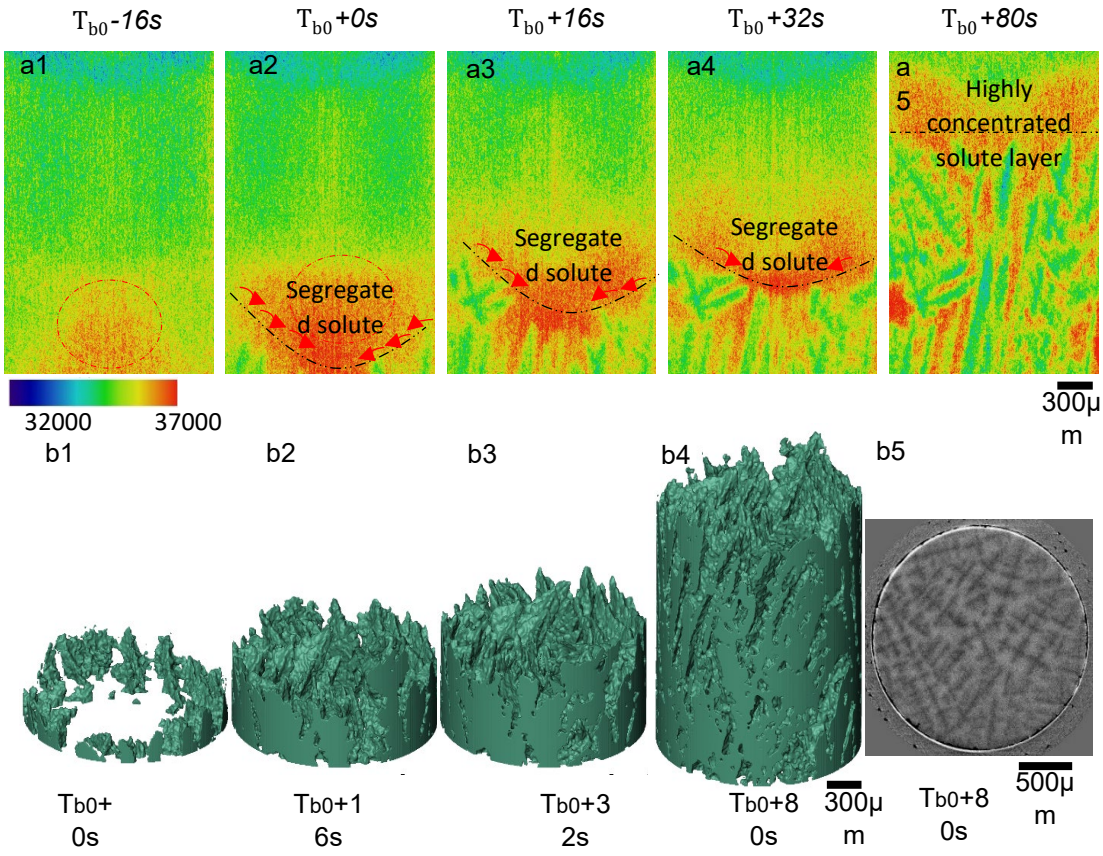

Figure 6.4 (a) 2D vertical slices of α-Al phase at different timestamps (B= 0.5T, TG= 2.5℃ / *mm*, CR= 0.1℃ / *s*); (b1-b4) 3D volumes of α-Al phase at different timestamps; (b5) a horizontal slice at height of 1.1mm.

For solidification condition II with the application of a transversal 0.5 T magnetic field, Cu and Fe elements were shown to be concentrated at the bottom centre of the FOV before solidification (Figure 6.4--a1, red circle). This segregation was eased, as solidification progressed (Figure 6.4-a2 to a4). The solid/liquid interface (black dashed line) was initially a curved one (Figure 6.4-a2) but gradually transitioned to be flat within 64 s as the solidification continued. Multiple dendrites were formed peripherally as shown in Figure 6.4-b1. They grew upwards slightly tilted from the vertical direction. For the dendrites formed around the surface of the sample, their growth orientation was tilted in the range of 0º-20º from the vertical direction. However, the dendrites in the central zone tend to grow in a clockwise direction with tilted angles ranging from 30º to 40º. This

might be due to the re-distribution of the solute from the macro-segregation zone to the outer layers of the sample, forming a small horizontal solute/temperature gradient. The combination of vertical and horizontal temperature gradients promotes dendrites to grow upwards with tilted angles.

The horizontal cross-sections (Figure 6.3-b5 and Figure 6.3-b5) show a significant difference in dendrite sizes formed between the two different solidification conditions. Quantification of the primary dendritic arm spacing can be obtained by equation 6-3 [207]:

$$\lambda = c\sqrt{\frac{A}{n}} \qquad 6\text{-}3$$

Where c is 0.5 for a random array of points, A is the cross-section area, which is 4.54 mm^2 (Figure 6.3-b5) and 4.72 mm^2 (Figure 6.4-b5), respectively; n is the number of dendrites, which are 6 (Figure 6.3-b5) and 60 (Figure 6.4-b5) for the two conditions. Therefore, the primary dendrite arm spacing (PDAS) solidified without and with a magnetic field is 435 μm and 140 μm, respectively.

6.3.2 β-Al5FeSi IMCs

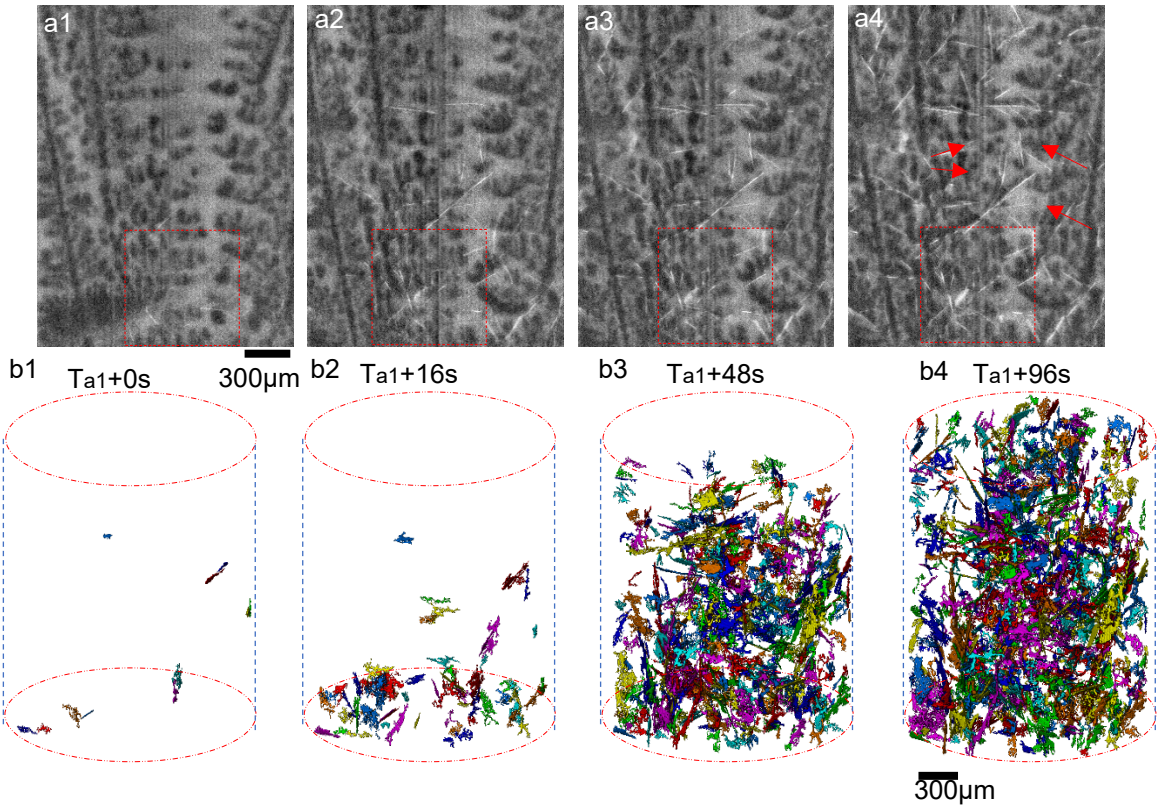

Figure 6.5 (a) 2D vertical slices of β -phase at different timestamps (B= 0T, TG= 2.5℃/*mm*, CR= 0.1 ℃/*s*); (b) 3D volumes of β-phase at different timestamps; Cropped region (882× 882× 882 μm^3) from figure 2-a at different timestamps.

Figure 6.5-a shows the growth process of the β-Al_5FeSi IMCs at different timestamps under solidification condition I. t_{a1} is the time when β-Al_5FeSi IMCs first appeared in the FOV. The bright and thin-plate structure in Figure 6.5-a2 is β-Al_5FeSi, which is the secondary phase after the primary α-Al phase formed in W319 alloys [13]. The light grey regions between the primary α-Al dendrites are liquid, whereas the dark grey is the α-Al phase. 3D volume rendering of IMCs after segmentation is shown in Fig.3-b and video 3 at each corresponding time. The plate-shaped IMCs nucleated and grew first within the bottom of the FOV in Figure 6.5-a1 and Figure 6.5-b1. More IMCs nucleated at the top region (from Figure 6.5-b2 to b4) at the later stage of the solidification. A small volume

(882× 882× 882 μm^3) was cropped out at the bottom of the FOV (red square in Figure 6.5-a1) to provide better visualization of IMCs, as presented in Figure 6.6. The IMCs (in red) nucleated at the inter-dendritic space of primary α-Al phases (in green). β-Al_5FeSi has very high lateral growth rates and low thickening rates, leading to impingement at the later stage of solidification. It also shows that the intermetallic compounds grew within the available spacing between the arms of the dendrites. Figure 6.6-b presents the 3D volume of β-Al_5FeSi while the primary α-Al phase is transparent. The IMCs grew vertically towards the direction of the applied temperature gradient. Few IMCs grew horizontally.

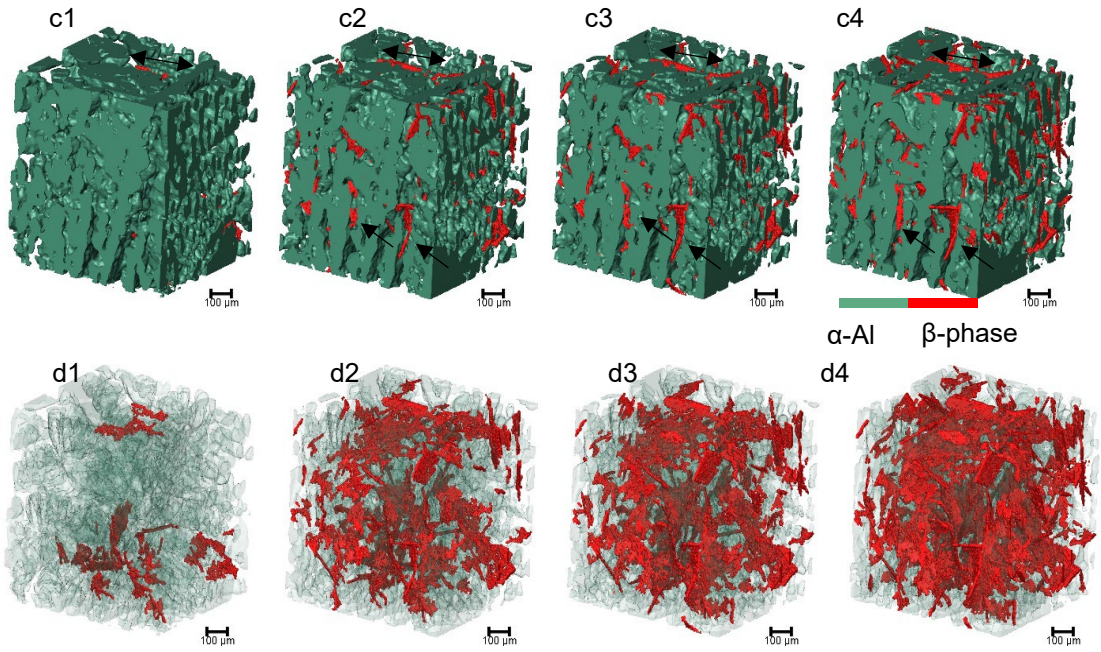

Figure 6.6 (c) 3D volumes (d) 3D volume with transparent α-Al phase.

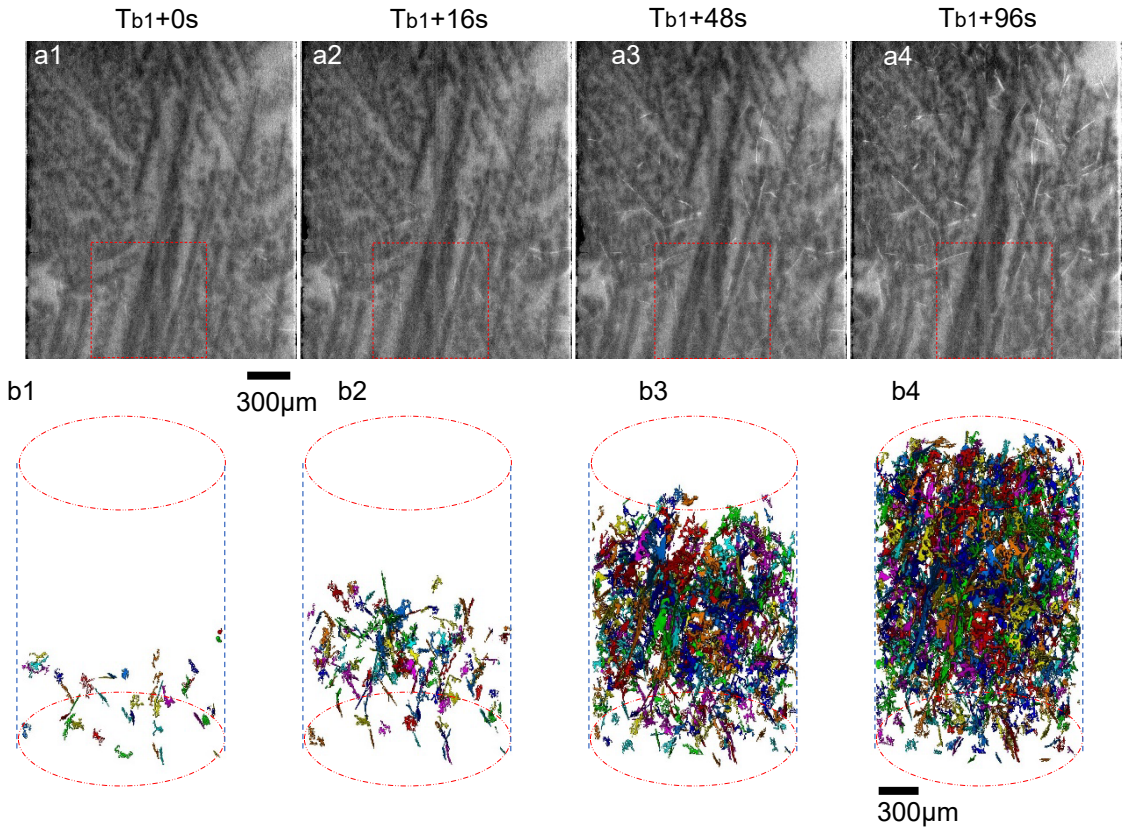

Figure 6.7 (a) 2D vertical slices of β-phase at different timestamps (B= 0.5T, TG= 2.5℃/*mm*, CR= 0.1℃/*s*); (b) 3D volumes of β-phase at different timestamps; Cropped region(882× 882× 882 μm^3) from figure 3-a at different timestamps.

2D vertical slices and 3D rendered volumes of β-Al_5FeSi at different timestamps under the magnetic field (solidification condition II) are shown in Figure 6.7. t_{b1} is the time when β-Al_5FeSi IMCs first appeared in the FOV. Under the magnetic field, IMCs also nucleated at the bottom of the FOV and grew upwards (from Figure 6.7-b1 to Figure 6.7-b4). A small region was also cropped with the same volume as Figure 6.6-c for clearer visualisation, shown in Figure 6.8. Most of the IMCs grew vertically.

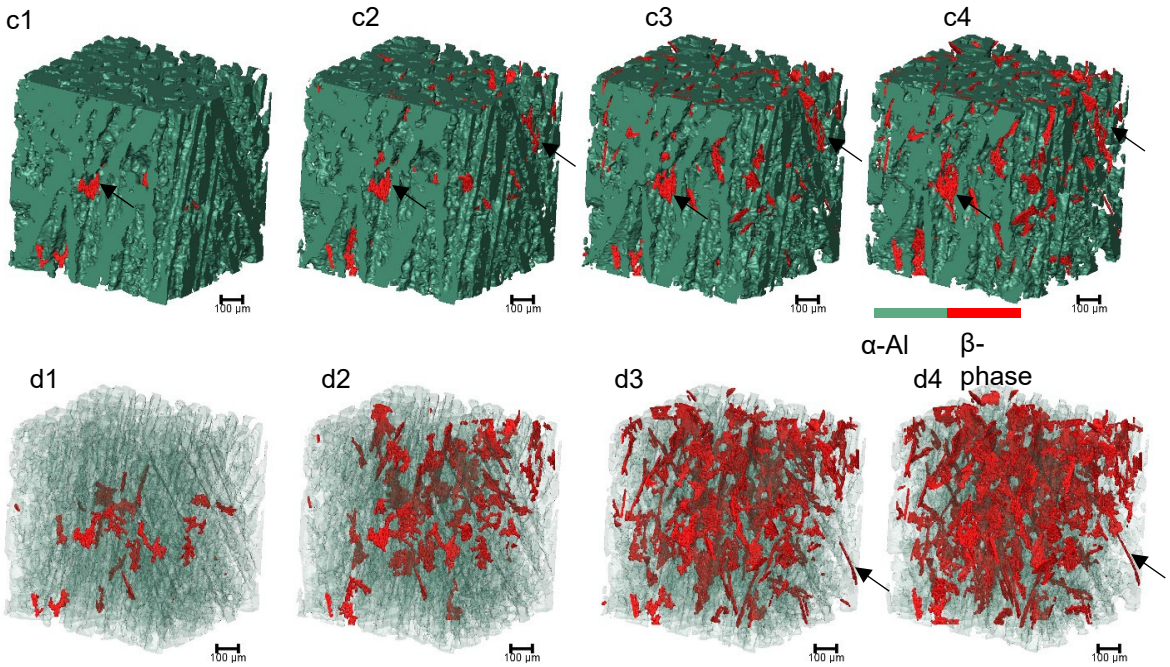

Figure 6.8 (c) 3D volumes (d) 3D volume with transparent α-Al phase.

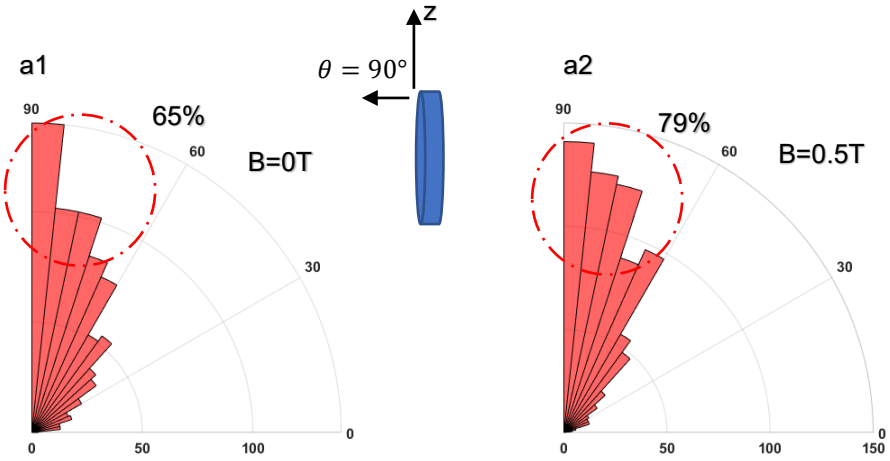

Figure 6.9 (a) Growth orientations of β-phase (a1) without magnetic field at ta1+96s; (a2) with magnetic field at tb1+96s.

The growth orientation of IMCs was quantified based on the principal component analysis [13]. The angle θ was defined as the difference between the through-thickness direction of the plate-let intermetallics and the vertical direction of the sample (schematic diagram is shown in Figure 6.9-a, the z-axis is the vertical direction of the sample). Without the magnetic field, the growth orientation of β-Al_5FeSi shows a preference towards the vertical direction of the sample (65% of the IMCs grew in between 60º and 90º in Figure 6.9-a1). The preferable growth direction towards the temperature gradient can be further influenced under a higher temperature gradient of 10℃/mm in ref [13]. When the magnetic field is on, higher percentage of β-Al_5FeSi IMCs (around 79%) grew between 60º to 90º in Figure 6.9-a2. These indicate that the application of magnetic field might affect the growth orientation of IMCs.

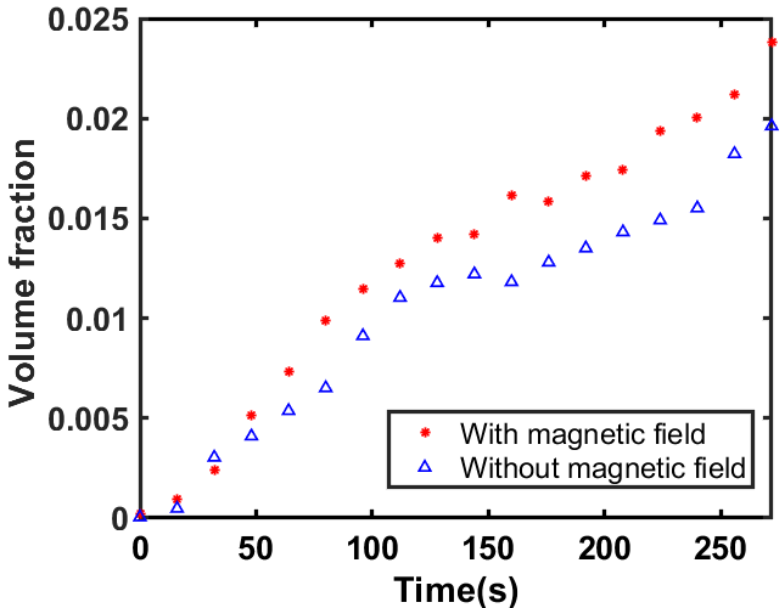

Figure 6.10 Overall volume fraction as a function of time

The volume fractions of β-phase versus time are plotted in Figure 6.10. Without the magnetic field, the volume fraction of the β-phase gradually increased during solidification, with an average growth rate of about 0.7% per second. In 272s, the volume fractions of β-phase achieved 1.9 % which is consistent with a previous study [13]. The volume fraction of IMCs during solidification with the magnetic field grew at a rate of about 0.88% per second, slightly higher than the sample solidified without a magnetic field. The volume fraction increased to 2.4% in 272s.

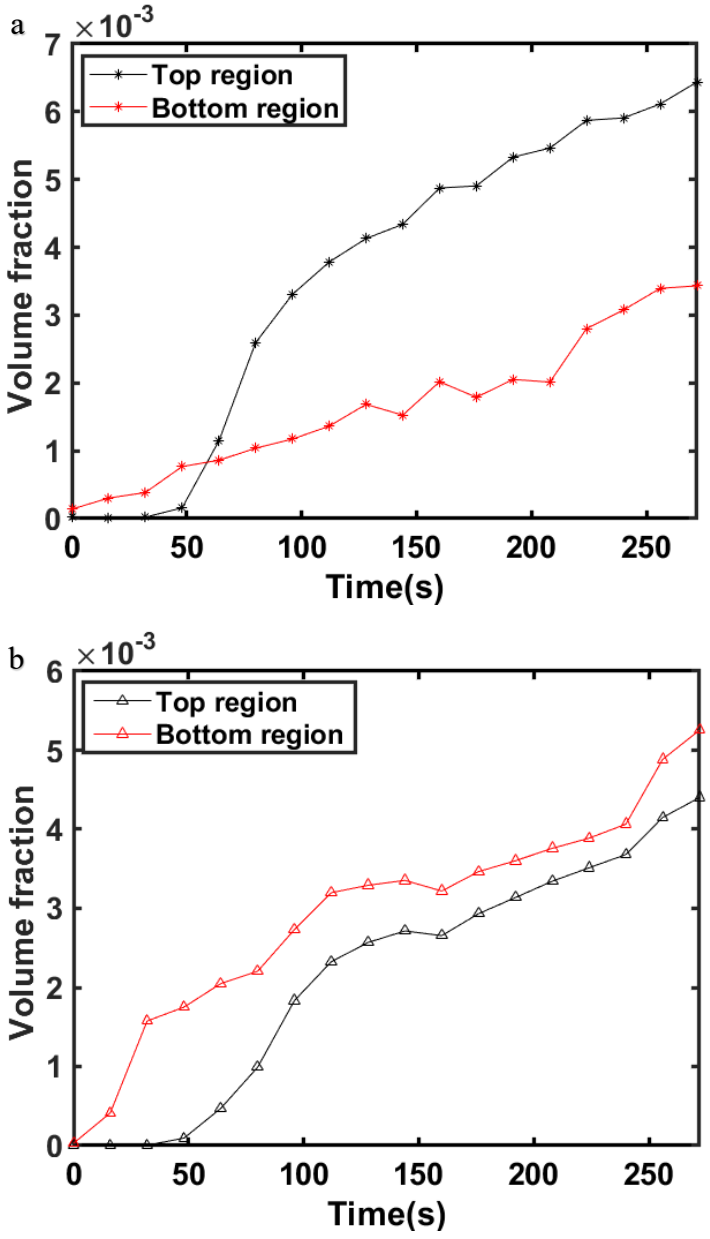

Figure 6.11 Volume fraction of β-phase at different height when (a) B=0T; (b) B=0.5T.

Under the magnetic field, we noticed, in Figure 6.5-b4, that the number of IMCs which grew at the bottom region of the FOV is lower than that at the top. We then quantified the volume fractions of the IMCs at the bottom (0-0.554mm) and the top (1.662-2.216mm) of the FOV as a function of time, as shown in Figure 6.11-a and b. Figure 6.11-a presents that the average growth rates of the IMCs of the bottom and top regions are very close (about 0.0020% per second and 0.0018% per second, respectively). However, with the application of the magnetic field, the average growth rate (the tendency of the curves) of IMCs at the bottom region is 0.0013% per second, much slower than that at the top (0.0024% per second). The top region achieved a higher volume fraction (0.64%) than the bottom one (0.34%). The gradient volume distribution of the β-phase formed along the vertical direction of the FOV, suggesting the concentration of the Fe element might be higher at the top region than at the bottom. This behaviour is different from the sample solidified without the application of the magnetic field.

6.3.3 Permeability estimation

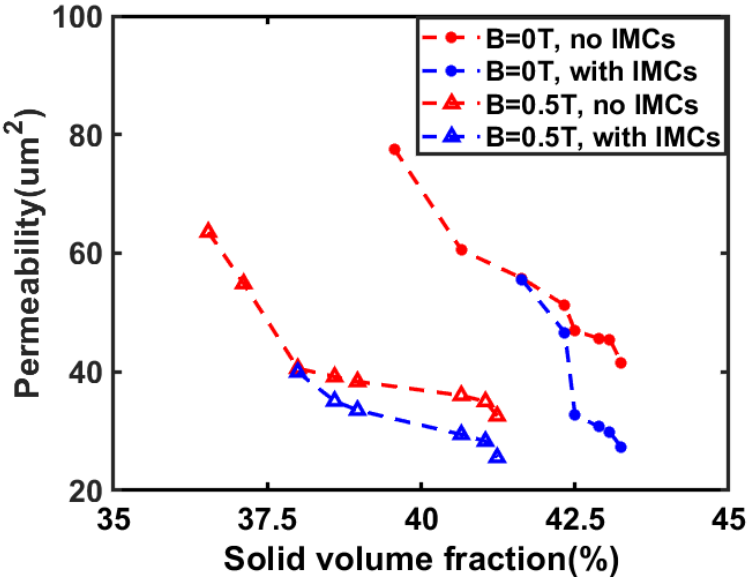

Figure 6.12 Simulated absolute permeability as a function of the solid volume fraction.

Figure 6.12 presents the simulated absolute permeabilities of the semi-solid W319 alloys during solidification without and with the magnetic field, based on solving the Stokes equations. Without the magnetic field, the solid volume fraction of α-Al dendrites increased from 39.6% to 41.6% within the chosen 8 tomographic scans. The absolute permeabilities reduced from 77.6 μm^2 to 41.6 μm^2. The permeability decreased monotonically with the increase of solid volume fraction of α-Al dendrites as expected. The permeabilities are significantly lower in the presence of intermetallics. At a solid volume fraction of α-Al dendrites of 41.6%, the absolute permeability was reduced by 34% from 41.6 μm^2 to 27.3μm^2 by the intermetallics. As the intermetallics nucleate and grow at the inter-dendritic spacing [13,30,263], they can block the liquid flow through the channels.

Under the magnetic field, the permeability shows the same tendency. It was decreased from 63.6μm^2 to 32.5μm^2 while the solid volume fraction increased from 36.5% to 41.2%. Permeabilities loss due to the presence of intermetallics also occurred. At a solid volume fraction of α-Al dendrites of 41.2%, the absolute permeability due to IMCs was reduced from 32.5 μm^2 to 25.6 μm^2.

However, at the same solid volume fraction of α-Al phase around 40.6% without and with magnetic field, the permeability has decreased from 60.5 μm^2 to 36.0 μm^2. The permeability is not only monotonically related to volume fraction but can also be influenced by the inter-dendrite-arm spacing. Under the magnetic field, much finer dendrites were formed, resulting in narrower liquid channels. This can block melt to flow through the solidified structures, leading to poorer absolute permeability. Under the magnetic field, the fine dendritic structure of the α-Al phase has a higher negative impact than the blocking effect from the intermetallics, on the reduction of the absolute permeability.

6.3.4 Discussion

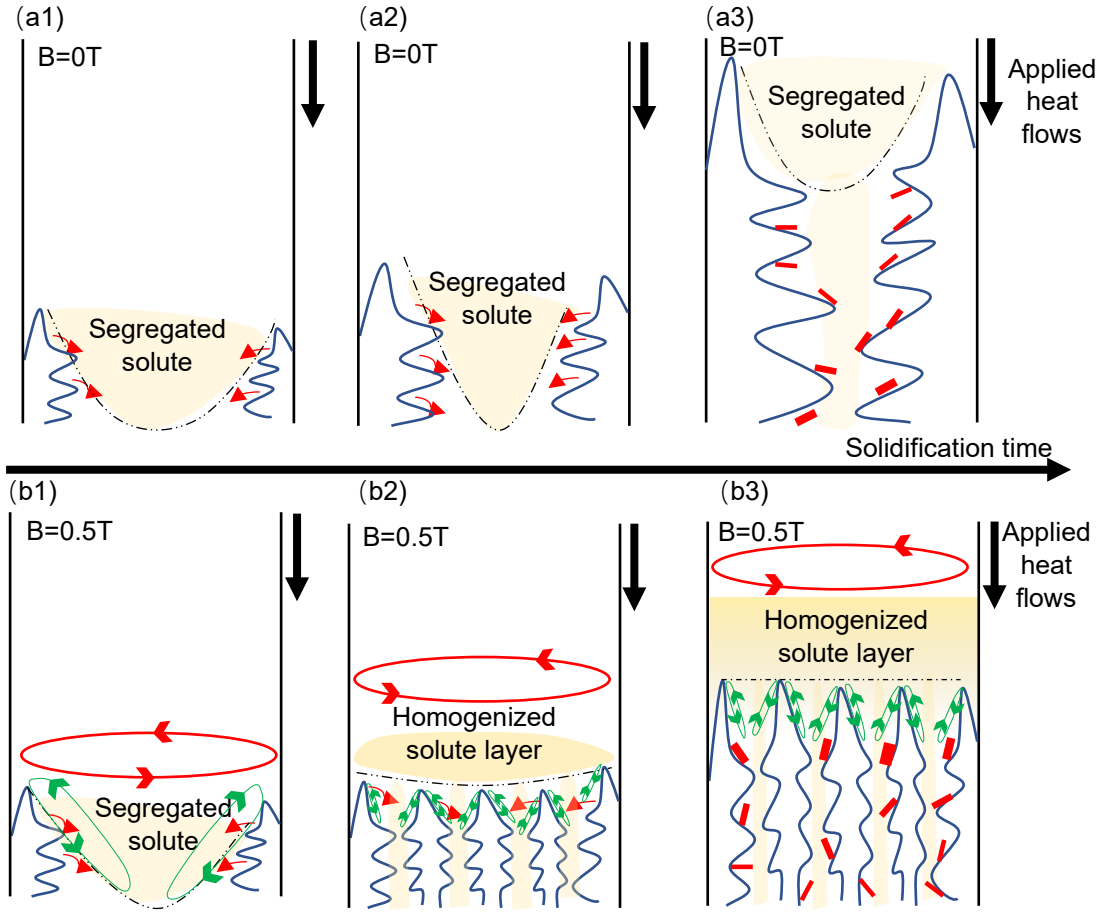

Figure 6.13 Schematic diagram of the solidification process (a) without a transverse magnetic field; (b) under a transverse magnetic field while the sample was rotating.

Figure 6.13 shows the schematic diagram of the solidification process under both conditions without and with the magnetic field. The presence of a magnetic field has changed the morphologies of the primary α-Al phase from coarse to fine dendritic structures. The distribution of the β-Al_5FeSi IMCs was also altered.

Under solidification condition I without the magnetic field, initially, the primary α-Al was formed near the surface of the sample (Figure 6.13-a1). Solute elements such as Cu, Fe and Si were ejected into the melt. Due to the gravity effect, heavy elements such as Cu and Fe settled down to the bottom of the FOV, forming a macro-segregation zone, which retards the upwards growth of the primary α-Al into this region. Therefore, a concavely

curved solid/liquid interface was formed. The curved interface due to solute accumulation has been observed in Al-Cu alloys [264] by examining the solidified sample. In-situ X-ray radiography has been used by A. Bogno et al. [265] to reveal the initial transient of the solid/liquid interface due to solute segregation. The primary dendrite arms continued to grow upwards, while the secondary arms branched into the central region during cooling. The macro-segregation became more serious, which is because more Cu and Fe were ejected and accumulated into this region during solidification. The solid/liquid interface becomes more concave in Figure 6.13-a2. As the solidification process proceeded, the secondary β-IMCs started to nucleate and grew at the inter-dendritic spacing of the primary α-Al dendrites in Figure 6.13-a3. The size of the secondary β-IMCs is constrained by the available spacing [13]. Its growth orientation is strongly controlled by the temperature gradient.

Under the magnetic field, initially, during solidification, the segregated heavy elements of Cu and Fe also accumulated at the centre region of the sample to form a curved solid/liquid interface in Figure 6.4-a2 and schematically shown in Figure 6.13-b1. A rotating magnetic field can induce a strong azimuthal flow that came from the convection damping effect [111,266]). Similarly, the sample is rotating under a transverse magnetic field. During solidification, the liquid flow was impeded due to the convection damping effect, while the solid α-Al dendrites are still rotating at angular velocity of π/s. Due to the speed difference between the liquid and solid part (α-Al dendrite), a rotational flow can be generated (in the red circle) in the mushy zone (Figure 6.13-b1) in the direction of rotation.

Furthermore, due to the different electrical conductivities of the primary α-Al phase and the melt, current loops at the solid/liquid interface can be generated as shown in Figure

6.13-b1 (in green), which is known as the Seebeck effect [198,199,253]. The interaction between the Seebeck current loops and the rotating magnetic field can induce Lorenz forces acting on both dendrites and the melt in the mushy zone. This can produce meridional flow ahead of the solid/liquid interface [267]. The changed interface from tilted to flat in Al-Cu alloys under a transverse magnetic field was observed by Wang et al.[268] by using in-situ radiography, and a corresponding 3D simulation was also performed to confirm the changed interface was attributed to the induced thermoelectric magnetohydrodynamic flows(TEMHD) [269]. In their work, the sample was static, TEMHD alone was attributed to being the main mechanism for changing the solid/liquid interface. In our experiment, the sample was rotating. The combination of these two forces from the convection damping effect and TEMHD might homogenise the temperature distribution via mixing of the solute [201] and ease the macro-segregation, which allows more primary dendrites to grow into this region (Figure 6.13-b2). The solid/liquid interface transformed from curved to flat during solidification.

As a result of these combined magnetohydrodynamic effects, the number of dendrites was increased, and PDAS was reduced. Smaller PDAS led to narrower liquid channels, which can reduce the absolute permeability [134]. The refined primary dendrites led to the growth orientation of the IMCs towards the vertical direction of the sample. Finally, segregated solute was pushed above the solidified structures in Figure 6.13-b3. This leads to a higher solute concentration at the top region of the sample, which promotes more β-Al_5FeSi IMCs to form at the top region, resulting in a gradient volume distribution of IMCs [267]. This study demonstrates that applying a static magnetic field to a rotating sample can not only successfully reduce the PDAS but also alter the distribution of the Al_5FeSi IMCs. It provides a cost-effective method for controlling or eliminating the iron-

rich intermetallic in recycled aluminium alloys and thus improving mechanical properties and corrosion resistance.

6.4 Summary

High-speed synchrotron X-ray tomography has been used to reveal the growth dynamic of both the primary α-Al phase and secondary β-Al_5FeSi IMCs in W319 alloys directionally solidified without and with a magnetic field. This work reveals that the application of a transverse magnetic field during solidification processes can effectively change the morphology of the primary α-Al phase and subsequently alter the distribution of the secondary β-Al_5FeSi IMCs. The following conclusions can be drawn from this study:

1. Without the magnetic field, a high concentration of heavy elements such as Cu and Fe at the periphery of the sample was revealed by mapping the solute distribution. Under the magnetic field, the peripheral macro-segregation was removed. Concavely curved solid/liquid interfaces were observed in the initial stage of solidification under both conditions. However, it was transferred from a curved to flat solid/liquid interface when the magnetic field is on.
2. Without the magnetic field, the primary α-Al phase has coarse and well-developed dendritic structures with large primary dendritic arm spacing of 434.9 μm. Under the magnetic field, the primary α-Al phase becomes fine dendritic structures with smaller dendritic arm spacing of 140.2 μm.
3. Absolute permeabilities were simulated based on tomographic data. It shows the presence of β-Al_5FeSi IMCs can reduce the absolute permeability of the semi-solid structure by blocking flows in both solidification conditions. However,

under the magnetic field, fine dendritic structures have a negative influence on reducing the permeability due to narrower liquid channels.

4. Without a magnetic field, the volume fraction and growth rate of β-Al_5FeSi IMCs have almost the same values in different regions of the sample. However, under the magnetic field, at the top region of the sample, the β-Al_5FeSi IMCs have higher growth rates and volume fractions than the bottom.

Chapter 7: Conclusions and future work

7.1 Conclusions

In-situ synchrotron X-ray tomography has been used to investigate the growth dynamics and mechanisms of intermetallic compounds in four types of aluminium alloys (Al-5wt%Fe, Al-45wt%Cu, Al-10wt%Ni and W319 alloys) under various solidification conditions. The investigation can be summarized as follows:

1. The growth dynamics of faceted $Al_{13}Fe_4$ intermetallic compounds were revealed, which grew into various morphology including plate-like, hexagonal tabular, stair-like and V-shaped under a slow cooling rate of 0.1℃/min. Crystal structure and twinning of the particle can cause variation in morphologies. The growth velocities and volume changes of each representative morphology were quantified, which provide experimental data to verify the simulation results of faceted IMCs. Oriented particle attachment was proposed to be a potential hypothesis, to describe the faceted growth of $Al_{13}Fe_4$ IMCs and its internal defect formation.

2. Under slow cooling rates, Al_2Cu IMCs are identified including basic units and faceted dendrites. The basic units include various IMCs that are elongated with different cross-section shapes such as L-shaped, U-shaped, or even hollow-rectangular. The growth process of the basic units was revealed from the 4D tomographic results. The morphologies of the basic units were related to their solidification time. For example, L-shaped and U-shaped IMCs were the intermediate stage, while the hollow-rectangular was the final stage. Layer-by-layer growth mode was proposed to be the main growth mechanism of the faceted dendrite structure. Imposition of the magnetic field of 0.5T

while the sample was rotating, fine and regulated IMCs were observed, which is much smaller than the sample without the magnetic field. A rotational stirring flow that was induced by the magnetic field can regulate and homogenize the temperature and solute distribution.

3. Four samples of Al-10wt%Ni were solidified under different cooling rates from $0.5℃/min$ up to $24℃/min$. Under slowing cooling rates of $0.5℃/min$ and $3℃/min$, V-shaped, hollow-rhomboid and faceted dendrites were observed. Zigzag-layered structures were observed under a high cooling rate of $12℃/min$ and $24℃/min$. Faceted dendritic patterns Al_3Ni IMCs include different shapes in the cross-section area (V-shaped and hollow- rhomboid). The V-shaped and hollow rhomboid structures are the intermediate stage of the faceted Al_3Ni IMCs, which can continue to grow into faceted dendritic structures. The anisotropic growth rates in the direction <010> and <101> can be the cause of central holes in hollow-rhomboid or faceted dendrites. The Layer-by-layer growth mechanism is still applicable to the faceted Al_3Ni dendrites with a preferable growth direction of <010> and bounding planes of $\{101\}$. The zigzag-layered branching growth mechanism was proposed to be the growth of a zigzag-layered structure of Al_3Ni IMCs at high cooling rates of $12℃/min$ and $24℃/min$. By increasing the cooling rate from $0.5℃/min$ to $24℃/min$, the morphology of the IMCs has been changed from faceted dendrite to zigzag-layered structures while the specific surface area has been increased from 0.0478 $\mu m^{-1}$to 0.187 μm^{-1}.

4. In W319 alloys, without the magnetic field, a high concentration of heavy elements such as Cu and Fe at the periphery of the sample was revealed by mapping the solute distribution. Under the magnetic field, the peripheral macro-segregation was removed. Concavely curved solid/liquid interfaces were observed in the initial stage of

solidification under both conditions. However, it was transferred from a curved to flat solid/liquid interface when the magnetic field is on. Without the magnetic field, the primary α-Al phase has coarse and well-developed dendritic structures with large primary dendritic arm spacing of 434.9 μm. Under the magnetic field, the primary α-Al phase becomes fine dendritic structures with smaller dendritic arm spacing of 140.2 μm. Absolute permeabilities were simulated based on tomographic data. It shows the presence of β-Al_5FeSi IMCs can reduce the absolute permeability of the semi-solid structure by blocking flows in both solidification conditions. However, under the magnetic field, fine dendritic structures have a negative influence on reducing permeability due to narrower liquid channels. Without a magnetic field, the volume fraction and growth rate of β-Al_5FeSi IMCs have almost the same values in different regions of the sample. However, under the magnetic field, at the top region of the sample, the β-Al_5FeSi IMCs have higher growth rates and volume fractions than the bottom.

5. Under slow cooling rates, two categories of both Al_2Cu and Al_3Ni IMCs are identified including basic units and faceted dendrites. The basic units of Al_2Cu IMCs include various IMCs that are elongated with different cross-section shapes such as L-shaped, U-shaped, or even hollow-rectangular. The transition process from L-shape to U-shape, and finally to a hollow-rectangular shape was observed. The Al_3Ni IMCs have V-shaped or hollow rhomboid cross-sections. The transition from V-shaped to hollow-rhomboid shape was observed. Due to the difference in crystal structure and preferable growth orientation of Al_2Cu and Al_3Ni IMCs, its basic units have different cross-section shapes.

6. Faceted dendritic patterns of Al_2Cu and Al_3Ni IMCs include different shapes in the cross-section area (hollow-rectangular for Al_2Cu and hollow-rhombus for Al_3Ni

IMCs). The 4D visualization of the formation of both types of faceted dendrites suggests that the self-repeated layer-by-layer stacking of faceted basic units (such as L-shaped in Al_2Cu IMCs or V-shaped in Al_3Ni IMCs) is the growth mechanism.

7. When rotating the solidifying sample in a transversal 0.5 T magnetic field in both Al-45wt% alloys and W319 (Al-Si-Cu based alloys), fine and regulated crystals were observed. The combination of two forces from the convection damping effect and induced thermoelectric magnetohydrodynamic flows (TEMHD) might homogenise the temperature and solute distribution via mixing of the melt.

7.2 Future work

In this PhD project, the growth dynamics, and mechanisms of four types of IMCs are quantified and revealed by using in-situ synchrotron X-ray tomography under different cooling conditions. Experimental studies of the influence of magnetic field in solidification in terms of their morphologies, primary dendrite arm spacing and solute distribution in the melt were also performed. However, further investigations are recommended as follows:

1. In-situ X-ray nanotomography [270] or transmission electron microscopy (TEM) [78,81,271,272] is recommended to investigate the formation process of faceted intermetallic compounds, aiming to discover the evidence of the non-classical crystal growth such as oriented particle attachment and to acquire its process on a nanoscale.
2. To further investigate how the magnetic field influences the fluid flows during solidification, it is recommended to perform in-situ radiography experiments to reveal the high resolution of solute distribution during magnetic field-assisted solidification. 3D numerical simulations from COMSOL Multiphysics are recommended to reveal the magnetic field-induced convection in the melt [22,104].
3. It is suggested to extend the applications of the magnetic fields from directional solidification to welding and additive manufacturing. For instance, the magnetic fields can be coupled with the welding process [273], to study the influence of the magnetic field on the morphologies of IMCs at the bonding interface and correlate to its mechanical properties. It can also combine additive manufacturing with in-situ X-ray radiography or tomography [274,275] to study how the melting pool is altered during additive manufacturing by the use of the magnetic field.

References:

[1] J. Campbell, Casting alloys, Butterworth-Heinemann, 2011. https://doi.org/10.1016/B978-1-85617-809-9.10006-4.

[2] M.S. Pham, B. Dovgyy, P.A. Hooper, C.M. Gourlay, A. Piglione, The role of side-branching in microstructure development in laser powder-bed fusion, Nat. Commun. 11 (2020) 1–12. https://doi.org/10.1038/s41467-020-14453-3.

[3] M. Sokoluk, C. Cao, S. Pan, X. Li, Nanoparticle-enabled phase control for arc welding of unweldable aluminum alloy 7075, Nat. Commun. 10 (2019) 1–8. https://doi.org/10.1038/s41467-018-07989-y.

[4] W. Kurz, D.J. Fisher, Fundamentals of Solidification, 4th rev. e, 1992.

[5] J. Warren, Rule of thumb breaks down, Nat. Mater. 5 (2006) 595–596. https://doi.org/10.1038/nmat1702.

[6] H. Yasuda, Y. Yamamoto, N. Nakatsuka, M. Yoshiya, T. Nagira, A. Sugiyama, I. Ohnaka, K. Uesugi, K. Umetani, In situ observation of solidification phenomena in Al-Cu and Fe-Si-Al alloys, Int. J. Cast Met. Res. 22 (2009) 15–21. https://doi.org/10.1179/136404609X368118.

[7] B. Cai, J. Wang, A. Kao, K. Pericleous, A.B. Phillion, R.C. Atwood, P.D. Lee, 4D synchrotron X-ray tomographic quantification of the transition from cellular to dendrite growth during directional solidification, Acta Mater. 117 (2016) 160–169. https://doi.org/10.1016/j.actamat.2016.07.002.

[8] N. Limodin, L. Salvo, E. Boller, M. Suéry, M. Felberbaum, S. Gailliègue, K.

Madi, In situ and real-time 3-D microtomography investigation of dendritic solidification in an Al-10 wt.% Cu alloy, Acta Mater. 57 (2009) 2300–2310. https://doi.org/10.1016/j.actamat.2009.01.035.

[9] H.B. Dong, P.D. Lee, Simulation of the columnar-to-equiaxed transition in directionally solidified Al-Cu alloys, Acta Mater. 53 (2005) 659–668. https://doi.org/10.1016/j.actamat.2004.10.019.

[10] S. Feng, Y. Cui, E. Liotti, A. Lui, C.M. Gourlay, P.S. Grant, In-situ X-ray radiography of twinned crystal growth of primary Al13Fe4, Scr. Mater. 184 (2020) 57–62. https://doi.org/10.1016/j.scriptamat.2020.04.010.

[11] S. Feng, E. Liotti, A. Lui, M.D. Wilson, T. Connolley, R.H. Mathiesen, P.S. Grant, In-situ X-ray radiography of primary Fe-rich intermetallic compound formation, Acta Mater. 196 (2020) 759–769. https://doi.org/10.1016/j.actamat.2020.06.045.

[12] K. Gao, S. Song, S. Li, H. Fu, Characterization of microstructures and growth orientation deviating of Al2Cu phase dendrite at different directional solidification rates, J. Alloys Compd. 660 (2016) 73–79. https://doi.org/10.1016/j.jallcom.2015.11.093.

[13] B. Cai, A. Kao, P.D. Lee, E. Boller, H. Basevi, A.B. Phillion, A. Leonardis, K. Pericieous, Growth of β intermetallic in an Al-Cu-Si alloy during directional solidification via machine learned 4D quantification, Scr. Mater. 165 (2019) 29–33. https://doi.org/10.1016/j.scriptamat.2019.02.007.

[14] S.Y. Sun, Q.D. Hu, W.Q. Lu, Z.Y. Ding, M.Q. Xu, M.X. Xia, J.G. Li, In situ

Study on the Growth Behavior of Primary Al3Ni Phase in Solidifying Al–Ni Alloy by Synchrotron Radiography, Acta Metall. Sin. (English Lett. 31 (2018) 668–672. https://doi.org/10.1007/s40195-017-0684-2.

[15] W.R. Osório, P.R. Goulart, G.A. Santos, C.M. Neto, A. Garcia, Effect of dendritic arm spacing on mechanical properties and corrosion resistance of Al 9 wt pct Si and Zn 27 wt pct Al alloys, Metall. Mater. Trans. A Phys. Metall. Mater. Sci. 37 (2006) 2525–2538. https://doi.org/10.1007/BF02586225.

[16] G.A. Santos, C. de Moura Neto, W.R. Osório, A. Garcia, Design of mechanical properties of a Zn27Al alloy based on microstructure dendritic array spacing, Mater. Des. 28 (2007) 2425–2430. https://doi.org/10.1016/j.matdes.2006.09.009.

[17] H.A. CHEDZEY, D.. T.. J. HURLE, Avoidance of Growth-striae in Semiconductor and Metal Crystals grown by Zone-melting Techniques, Nature. 210 (1966) 933–934. https://doi.org/10.1038/210934a0.

[18] F. Hecht, B.K. McCaw, D. Peakman, A. Robinson, Texturing of magnetic materials at high temperature by solidification in a magnetic field, Nature. 255 (1975) 243–244. https://doi.org/10.1038/255243a0.

[19] L. Zhang, S. Wang, A. Dong, J. Gao, L.N.W. Damoah, Application of Electromagnetic (EM) Separation Technology to Metal Refining Processes: A Review, Metall. Mater. Trans. B Process Metall. Mater. Process. Sci. 45 (2014) 2153–2185. https://doi.org/10.1007/s11663-014-0123-y.

[20] X.U. Zhenming, L.I. Tianxiao, Z. Yaohe, Elimination of Fe in Al-Si cast alloy scrap, J. Mater. Sci. 8 (2003) 4557–4565.

[21] D.A. Shu, B. Sun, J.U.N. Wang, T. Li, Z. Xu, Y. Zhou, Numerical Calculation of the Electromagnetic Expulsive Force upon Nonmetallic Inclusions in an Aluminum Melt : Part I . Spherical Particles, Metall. Mater. Trans. B. 31 (2000).

[22] J. Wang, S. Yue, Y. Fautrelle, P.D. Lee, X. Li, Y. Zhong, Z. Ren, Refinement and growth enhancement of Al2Cu phase during magnetic field assisting directional solidification of hypereutectic Al-Cu alloy, Sci. Rep. 6 (2016) 1–6. https://doi.org/10.1038/srep24585.

[23] S. Nafisi, D. Emadi, M.T. Shehata, R. Ghomashchi, Effects of electromagnetic stirring and superheat on the microstructural characteristics of Al-Si-Fe alloy, Mater. Sci. Eng. A. 432 (2006) 71–83. https://doi.org/10.1016/j.msea.2006.05.076.

[24] M. Hainke, J. Friedrich, D. Vizman, G. Müller, MHD Effects in Semiconductor Crystal Growth and Alloy Solidification, Int. Sci. Colloq. Model. Electromagn. Process. (2003) 24–26.

[25] D. Vizman, K. Dadzis, J. Friedrich, Numerical parameter studies of 3D melt flow and interface shape for directional solidification of silicon in a traveling magnetic field, J. Cryst. Growth. 381 (2013) 169–178. https://doi.org/10.1016/j.jcrysgro.2013.06.023.

[26] K. Dadzis, D. Vizman, J. Friedrich, Unsteady coupled 3D calculations of melt flow, interface shape, and species transport for directional solidification of silicon in a traveling magnetic field, J. Cryst. Growth. 367 (2013) 77–87. https://doi.org/10.1016/j.jcrysgro.2012.12.135.

[27] C. Puncreobutr, A.B. Phillion, J.L. Fife, P. Rockett, A.P. Horsfield, P.D. Lee, In situ quantification of the nucleation and growth of Fe-rich intermetallics during Al alloy solidification, Acta Mater. 79 (2014) 292–303. https://doi.org/10.1016/j.actamat.2014.07.018.

[28] C. Puncreobutr, P.D. Lee, K.M. Kareh, T. Connolley, J.L. Fife, A.B. Phillion, Influence of Fe-rich intermetallics on solidification defects in Al-Si-Cu alloys, Acta Mater. 68 (2014) 42–51. https://doi.org/10.1016/j.actamat.2014.01.007.

[29] J. Wang, P.D. Lee, R.W. Hamilton, M. Li, J. Allison, The kinetics of Fe-rich intermetallic formation in aluminium alloys: In situ observation, Scr. Mater. 60 (2009) 516–519. https://doi.org/10.1016/j.scriptamat.2008.11.048.

[30] S. Terzi, J.A. Taylor, Y.H. Cho, L. Salvo, M. Suéry, E. Boller, A.K. Dahle, In situ study of nucleation and growth of the irregular α-Al/β-Al5FeSi eutectic by 3-D synchrotron X-ray microtomography, Acta Mater. 58 (2010) 5370–5380. https://doi.org/10.1016/j.actamat.2010.06.012.

[31] A. Bjurenstedt, D. Casari, S. Seifeddine, R.H. Mathiesen, A.K. Dahle, In-situ study of morphology and growth of primary α-Al(FeMnCr)Si intermetallics in an Al-Si alloy, Acta Mater. 130 (2017) 1–9. https://doi.org/10.1016/j.actamat.2017.03.026.

[32] Y. Zhao, W. Du, B. Koe, T. Connolley, S. Irvine, P.K. Allan, C.M. Schlepütz, W. Zhang, F. Wang, D.G. Eskin, J. Mi, 3D characterisation of the Fe-rich intermetallic phases in recycled Al alloys by synchrotron X-ray microtomography and skeletonisation, Scr. Mater. 146 (2018) 321–326.

https://doi.org/10.1016/j.scriptamat.2017.12.010.

[33] E. Guo, A.B. Phillion, B. Cai, S. Shuai, D. Kazantsev, T. Jing, P.D. Lee, Dendritic evolution during coarsening of Mg-Zn alloys via 4D synchrotron tomography, Acta Mater. 123 (2017) 373–382. https://doi.org/10.1016/j.actamat.2016.10.022.

[34] Shyamprasad Karagadde, C.L.A. Leung, Peter D. Lee, Progress on In Situ and Operando X-ray Imaging of Solidification Processes, Materials (Basel). 14 (2021). https://doi.org/https://doi.org/ 10.3390/ma14092374 Academic.

[35] J.D. Robson, Modelling the overlap of nucleation, growth and coarsening during precipitation, Acta Mater. 52 (2004) 4669–4676. https://doi.org/10.1016/j.actamat.2004.06.024.

[36] G. Madras, B.J. McCoy, Nucleation, growth, and coarsening for two- and three-dimensional phase transitions, J. Cryst. Growth. 279 (2005) 466–476. https://doi.org/10.1016/j.jcrysgro.2005.02.029.

[37] M.C. Flemings, Coarsening in solidification processing, Mater. Trans. 46 (2005) 895–900. https://doi.org/10.2320/matertrans.46.895.

[38] J.A. Dantzig, M. Rappaz, Solidification, First edit, EPFL Press, Lausanne, 2009.

[39] F. Wang, D. Eskin, J. Mi, T. Connolley, J. Lindsay, M. Mounib, A refining mechanism of primary Al3Ti intermetallic particles by ultrasonic treatment in the liquid state, Acta Mater. 116 (2016) 354–363. https://doi.org/10.1016/j.actamat.2016.06.056.

[40] J. Røyset, N. Ryum, Scandium in aluminium alloys, Int. Mater. Rev. 50 (2005) 19–44. https://doi.org/10.1179/174328005X14311.

[41] A. Jiang, X. Wang, Dendritic and Seaweed Growth of Proeutectic Scandium Tri-Aluminide in Hypereutectic Al-Sc Undercooled Melt, Acta Mater. (2020). https://doi.org/10.1016/j.actamat.2020.08.078.

[42] W.J. Boettinger, D.K. Banerjee, Solidification, in: Phys. Metall. Fifth Ed., 2014: pp. 639–850. https://doi.org/10.1016/B978-0-444-53770-6.00007-1.

[43] D. Eskin, Q. Du, D. Ruvalcaba, L. Katgerman, Experimental study of structure formation in binary Al-Cu alloys at different cooling rates, Mater. Sci. Eng. A. 405 (2005) 1–10. https://doi.org/10.1016/j.msea.2005.05.105.

[44] F. Wang, D. Eskin, T. Connolley, J. Mi, Effect of ultrasonic melt treatment on the refinement of primary Al3Ti intermetallic in an Al-0.4Ti alloy, J. Cryst. Growth. 435 (2016) 24–30. https://doi.org/10.1016/j.jcrysgro.2015.11.034.

[45] V.K. Ivanov, P.P. Fedorov, A.Y. Baranchikov, V. V Osiko, Oriented attachment of particles: 100 years of investigations of non-classical crystal growth, Russ. Chem. Rev. 1204 (2014) 127–131. https://doi.org/10.1016/b978-0-08-012210-6.50078-8.

[46] J.W. Xian, S.A. Belyakov, M. Ollivier, K. Nogita, H. Yasuda, C.M. Gourlay, Cu6Sn5 crystal growth mechanisms during solidification of electronic interconnections, Acta Mater. 126 (2017) 540–551. https://doi.org/10.1016/j.actamat.2016.12.043.

[47] H. Kang, T. Wang, Y. Lu, J. Jie, X. Li, Y. Su, J. Guo, Controllable 3D morphology and growth mechanism of quasicrystalline phase in directionally solidified Al-Mn-Be alloy, J. Mater. Res. 29 (2014) 2547–2555. https://doi.org/10.1557/jmr.2014.287.

[48] A. Jiang, X. Wang, Dendritic and seaweed growth of proeutectic scandium tri-aluminide in hypereutectic Al-Sc undercooled melt, Acta Mater. 200 (2020) 56–65. https://doi.org/10.1016/j.actamat.2020.08.078.

[49] Z. Ding, Q. Hu, F. Yang, L. Yu, T. Yang, N. Zhang, W. Lu, Unveiling the Growth Mechanism of Faceted Primary - Al2Cu with Complex Morphologies During Solidification, Acta Metall. Sin. (English Lett. (2021). https://doi.org/10.1007/s40195-021-01327-w.

[50] W. Kurz, M. Rappaz, R. Trivedi, Progress in modelling solidification microstructures in metals and alloys. Part II: dendrites from 2001 to 2018, Int. Mater. Rev. 0 (2020) 1–47. https://doi.org/10.1080/09506608.2020.1757894.

[51] N. Limodin, L. Salvo, M. Suéry, M. DiMichiel, In situ investigation by X-ray tomography of the overall and local microstructural changes occurring during partial remelting of an Al-15.8 wt.% Cu alloy, Acta Mater. 55 (2007) 3177–3191. https://doi.org/10.1016/j.actamat.2007.01.027.

[52] J.W. Gibbs, K.A. Mohan, E.B. Gulsoy, A.J. Shahani, X. Xiao, C.A. Bouman, M. De Graef, P.W. Voorhees, The Three-Dimensional Morphology of Growing Dendrites, Sci. Rep. 5 (2015) 1–9. https://doi.org/10.1038/srep11824.

[53] B. Cai, J. Wang, A. Kao, K. Pericleous, A.B. Phillion, R.C. Atwood, P.D. Lee,

4D synchrotron X-ray tomographic quantification of the transition from cellular to dendrite growth during directional solidification, Acta Mater. 117 (2016) 160–169. https://doi.org/10.1016/j.actamat.2016.07.002.

[54] S. Shuai, E. Guo, A.B. Phillion, M.D. Callaghan, T. Jing, P.D. Lee, Fast synchrotron X-ray tomographic quantification of dendrite evolution during the solidification of Mg-Sn alloys, Acta Mater. 118 (2016) 260–269. https://doi.org/10.1016/j.actamat.2016.07.047.

[55] M.P. Quispe, Single crystal growth and structural characterization of intermetallic phases for thermoelectric applications, Ludwig Maximilian University of Munich, 2020.

[56] H.H.W. Physical, N.F. Communicated, The growth of crystals and the equilibrium structure of their surfaces, Philos. Trans. R. Soc. London. Ser. A, Math. Phys. Sci. 243 (1951) 299–358. https://doi.org/10.1098/rsta.1951.0006.

[57] D.P. Woodruff, How does your crystal grow? A commentary on Burton, Cabrera and Frank (1951) "The growth of crystals and the equilibrium structure of their surfaces," Philos. Trans. R. Soc. A Math. Phys. Eng. Sci. 373 (2015). https://doi.org/10.1098/rsta.2014.0230.

[58] W.K. BURTON, N. CABRERA, F.C. FRANK, Role of Dislocations in Crystal Growth, Nature. 163 (1949) 1992.

[59] L.J. Griffin, Observation of unimolecular growth steps on crystal surfaces, London, Edinburgh, Dublin Philos. Mag. J. Sci. 41 (1950) 196–199. https://doi.org/10.1080/14786445008521781.

[60] A.R. Verma, CI. Observations on carborundum of growth spirals originating from screw dislocations, London, Edinburgh, Dublin Philos. Mag. J. Sci. 42:332 (1951) 1005–1013. https://doi.org/10.1080/14786445108561345.

[61] K.A.JACKSON, D.R.UHLMANN, J.D.HUNT, On the nature of crystal growth from the melt, J. Cryst. Growth. (1967). https://doi.org/10.3726/978-3-653-04732-5/13.

[62] K.A. Jackson, Current concepts in crystal growth from the melt, Prog. Solid State Chem. 4 (1967). https://doi.org/10.1016/0079-6786(67)90005-2.

[63] N. Zhang, Q. Hu, Z. Ding, W. Lu, F. Yang, J. Li, 3D morphological evolution and growth mechanism of proeutectic FeAl3 phases formed at Al/Fe interface under different cooling rates, J. Mater. Sci. Technol. 116 (2022) 83–93. https://doi.org/10.1016/j.jmst.2021.11.036.

[64] C.M.L. Adam, L.M. Hogan, Crystallography of the Al-Al3Fe eutectic, Acta Metall. 23 (1975) 345–354. https://doi.org/10.1016/0001-6160(75)90127-3.

[65] A.J. McLeod, L.M. Hogan, C.M. Adam, D.C. Jenkinson, Growth mode of the aluminum phase in Al-Si and Al-Al3Fe eutectics, J. Cryst. Growth. 19 (1973) 301–309. https://doi.org/10.1016/0022-0248(73)90054-7.

[66] X. Yang, K. Fujiwara, K. Maeda, J. Nozawa, H. Koizumi, S. Uda, Dependence of Si faceted dendrite growth velocity on undercooling, Appl. Phys. Lett. 98 (2011) 1–4. https://doi.org/10.1063/1.3543623.

[67] K. Fujiwara, K. Maeda, N. Usami, K. Nakajima, Growth mechanism of Si-

faceted dendrites, Phys. Rev. Lett. 101 (2008) 1–4. https://doi.org/10.1103/PhysRevLett.101.055503.

[68] A. Hellawell, The growth and structure of eutectics with silicon and germanium, Prog. Mater. Sci. 15 (1970) 3–78. https://doi.org/10.1016/0079-6425(70)90001-0.

[69] D.R. Hamilton, R.G. Seidensticker, Propagation mechanism of germanium dendrites, J. Appl. Phys. 31 (1960) 1165–1168. https://doi.org/10.1063/1.1735796.

[70] W. Losert, B.Q. Shi, H.Z. Cummins, Evolution of dendritic patterns during alloy solidification: Onset of the initial instability, Proc. Natl. Acad. Sci. U. S. A. 95 (1998) 431–438. https://doi.org/10.1073/pnas.95.2.431.

[71] J.W. Rutter, B. Chalmers, a Prismatic Substructure Formed During Solidification of Metals, Can. J. Phys. 31 (1953) 15–39. https://doi.org/10.1139/p53-003.

[72] W.A. Tiller, K.A. Jackson, J.W. Rutter, B. Chalmers, The redistribution of solute atoms during the solidification of metals, Acta Metall. 1 (1953) 428–437. https://doi.org/10.1016/0001-6160(53)90126-6.

[73] A.P.Alivisatos, Scaling Law for Structural Metastability in Semiconductor Nanocrystals, Ber. Bunsenges Phys. Chem. 11 (1997) 1573–1577.

[74] R.L. Penn, J.F. Banfield, Morphology development and crystal growth in nanocrystalline aggregates under hydrothermal conditions: Insights from titania, Geochim. Cosmochim. Acta. 63 (1999) 1549–1557. https://doi.org/10.1016/S0016-7037(99)00037-X.

[75] D. Li, M.H.M.H. Nielsen, J.R.I.J.R.I. Lee, C. Frandsen, J.F. Banfield, J.J. De Yoreo, Direction-Specific Interactions Control Crystal Growth by Oriented Attachment, Science (80-.). 336 (2012) 1014–1018. https://doi.org/10.1126/science.1219643.

[76] R.L. Penn, J.F. Banfield, Imperfect oriented attachment: Dislocation generation in defect-free nanocrystals, Science (80-.). 281 (1998) 969–971. https://doi.org/10.1126/science.281.5379.969.

[77] J.F. Banfield, S.A. Welch, H. Zhang, T.T. Ebert, R.L. Penn, Aggregation-based crystal growth and microstructure development in natural iron oxyhydroxide biomineralization products, Science (80-.). 289 (2000) 751–754. https://doi.org/10.1126/science.289.5480.751.

[78] J.J. De Yoreo, P.U.P.A. Gilbert, N.A.J.M. Sommerdijk, R.L. Penn, S. Whitelam, D. Joester, H. Zhang, J.D. Rimer, A. Navrotsky, J.F. Banfield, A.F. Wallace, F.M. Michel, F.C. Meldrum, H. Cölfen, P.M. Dove, Crystallization by particle attachment in synthetic, biogenic, and geologic environments, Science (80-.). 349 (2015) aaa6760. https://doi.org/10.1126/science.aaa6760.

[79] N. Gehrke, H. Cölfen, N. Pinna, M. Antonietti, N. Nassif, Superstructures of calcium carbonate crystals by oriented attachment, Cryst. Growth Des. 5 (2005) 1317–1319. https://doi.org/10.1021/cg050051d.

[80] M.H. Nielsen, S. Aloni, J.J. De Yoreo, In situ TEM imaging of CaCO3 nucleation reveals coexistence of direct and indirect pathways, Science (80-.). 345 (2014) 1158–1162. https://doi.org/10.1126/science.1254051.

[81] G. Mirabello, A. Ianiro, P.H.H. Bomans, T. Yoda, A. Arakaki, H. Friedrich, G. de With, N.A.J.M. Sommerdijk, Crystallization by particle attachment is a colloidal assembly process, Nat. Mater. 19 (2019) 391–396. https://doi.org/10.1038/s41563-019-0511-4.

[82] A.I. Lupulescu, J.D. Rimer, In situ imaging of silicalite-1 surface growth reveals the mechanism of crystallization, Science (80-.). 344 (2014) 729–732. https://doi.org/10.1126/science.1250984.

[83] D. Li, F. Soberanis, J. Fu, W. Hou, J. Wu, D. Kisailus, Growth mechanism of highly branched titanium dioxide nanowires via oriented attachment, Cryst. Growth Des. 13 (2013) 422–428. https://doi.org/10.1021/cg301388e.

[84] H. Liang, H. Zhao, D. Rossouw, W. Wang, H. Xu, G.A. Botton, D. Ma, Silver Nanorice Structures: Oriented Attachment-Dominated Growth, High Environmental Sensitivity, and Real-Space Visualization of Multipolar Resonances, Chem. Mater. 24 (2012) 2339–2346. https://doi.org/10.1021/cm3006875.

[85] A. Halder, N. Ravishankar, Ultrafine single-crystalline gold nanowire arrays by oriented attachment, Adv. Mater. 19 (2007) 1854–1858. https://doi.org/10.1002/adma.200602325.

[86] A.A. Tzavaras, H.D. Brody, Electromagnetic Stirring and Continuous Casting - Achievements, Problems, and Goals., J. Met. 36 (1984) 31–37.

[87] W. Poppmeier, B. Tarmann, O. Schaaber, Application of alternating electromagnetic fields in the continuous casting of steel, Jom. 18 (1966) 1109–

1114. https://doi.org/10.1007/bf03378503.

[88] B.A. Sivak, V.G. Grachev, V.M. Parshin, A.D. Chertov, S. V. Zarubin, V.G. Fisenko, A.A. Solov'Ev, MHD processes in the electromagnetic stirring of liquid metal in continuous section and bloom casters, Metallurgist. 53 (2009) 469–481. https://doi.org/10.1007/s11015-009-9209-1.

[89] D.G. Eskin, J. Mi, Solidication Processing of Metallic Alloys Under External fields, Springer, Cham, Switzerland, 2018. https://doi.org/https://doi.org/10.1007/978-3-319-94842-3.

[90] P.A. Davidson, MAGNETOHYDRODYNAMICS IN MATERIALS PROCESSING, Annu. Rev. Fluid Mech. 31 (1999) 273–300.

[91] H. Yasuda, A. Nakahira, I. Ohnaka, Y. Yamamoto, K. Kishio, Formation of crystallography aligned grains during coarsening in a magnetic field, Mater. Trans. 44 (2003) 2555–2562. https://doi.org/10.2320/matertrans.44.2555.

[92] Y. Han, C. Ban, S. Guo, X. Liu, Q. Ba, J. Cui, Alignment behavior of primary Al3Fe phase in Al-Fe alloy under a high magnetic field, Mater. Lett. 61 (2007) 983–986. https://doi.org/10.1016/j.matlet.2006.06.027.

[93] W. Zhu, Z. Ren, W. Ren, Y. Zhong, K. Deng, Effects of high magnetic field on the unidirectionally solidified Al-Al2Cu eutectic crystal orientations and the induced microstructures, Mater. Sci. Eng. A. 441 (2006) 181–186. https://doi.org/10.1016/j.msea.2006.08.081.

[94] X. Li, Y. Fautrelle, Z. Ren, Influence of a high magnetic field on columnar

dendrite growth during directional solidification, Acta Mater. 55 (2007) 5333–5347. https://doi.org/10.1016/j.actamat.2007.05.036.

[95] M. Shimotomai, K. Maruta, K. Mine, M. Matsui, Formation of aligned two-phase microstructures by applying a magnetic field during the austenite to ferrite transformation in steels, Acta Mater. 51 (2003) 2921–2932. https://doi.org/10.1016/S1359-6454(03)00106-X.

[96] P. Gillon, Uses of intense d.c. magnetic fields in materials processing, Mater. Sci. Eng. A. 287 (2000) 146–152. https://doi.org/10.1016/s0921-5093(00)00767-x.

[97] H.B. Callen, The application of onsager's reciprocal relations to thermoelectric, thermomagnetic, and galvanomagnetic effects, Phys. Rev. 73 (1948) 1349–1358. https://doi.org/10.1103/PhysRev.73.1349.

[98] P. Lehmann, R. Moreau, D. Camel, R. Bolcato, Modification of interdendritic convection in directional solidification by a uniform magnetic field, Acta Mater. 46 (1998) 4067–4079. https://doi.org/10.1016/S1359-6454(98)00064-0.

[99] D.T.J. Hurle, Temperature oscillations in molten metals and their relationship to growth striae in melt-grown crystals, Philos. Mag. 13 (1966) 305–310. https://doi.org/10.1080/14786436608212608.

[100] H.P. Utech, M.C. Flemings, Elimination of solute banding in indium antimonide crystals by growth in a magnetic field, J. Appl. Phys. 37 (1966) 2021–2024. https://doi.org/10.1063/1.1708664.

[101] W. V. YOUDEL, R.C. DORWA, DIRECTIONAL SOLIDIFICATION OF

ALUMINIUM-COPPER ALLOYS IN A MAGNETIC FIELD, Can. J. Phys. 44 (1966) 139–150.

[102] L. Zhu, C. Han, L. Hou, A. Gagnoud, Y. Fautrelle, Z. Ren, X. Li, Influence of a static magnetic field on the distribution of solute Cu and interdendritic constitutional undercooling in directionally solidified Al-4.5wt.%Cu alloy, Mater. Lett. 248 (2019) 73–77. https://doi.org/10.1016/j.matlet.2019.03.142.

[103] X. Li, Z. Ren, A. Gagnoud, O. Budebkova, Y. Fautrelle, Effects of thermoelectric magnetic convection on the solidification structure during directional solidification under lower transverse magnetic field, Metall. Mater. Trans. A Phys. Metall. Mater. Sci. 42 (2011) 3459–3471. https://doi.org/10.1007/s11661-011-0741-9.

[104] X. Li, Z. Lu, Y. Fautrelle, A. Gagnoud, R. Moreau, Z. Ren, Effect of a weak transverse magnetic field on the microstructure in directionally solidified peritectic alloys, Sci. Rep. 6 (2016) 1–15. https://doi.org/10.1038/srep37872.

[105] P. Lehmann, R. Moreau, D. Camel, R. Bolcato, A simple analysis of the effect of convection on the structure of the mushy zone in the case of horizontal Bridgman solidification comparison with experimental results, J. Cryst. Growth. 183 (1998) 690–704. https://doi.org/10.1016/S0022-0248(97)00468-5.

[106] X. Li, Y. Fautrelle, A. Gagnoud, R. Moreau, D. Du, Z. Ren, X. Lu, EBSD Study on the Effect of a Strong Axial Magnetic Field on the Microstructure and Crystallography of Al-Ni Alloys During Solidification, Metall. Mater. Trans. A Phys. Metall. Mater. Sci. 47 (2016) 1180–1197. https://doi.org/10.1007/s11661-

015-3279-4.

[107] L. Li, Y. Zhang, C. Esling, K. Qin, Z. Zhao, Y. Zuo, J. Cui, A microstructural and crystallographic investigation of the precipitation behaviour of a primary Al3Zr phase under a high magnetic field, J. Appl. Crystallogr. 46 (2013) 421–429. https://doi.org/10.1107/S0021889813001258.

[108] X. Li, J. Wang, L. Hou, A. Gagnoud, Y. Fautrelle, Studying on the morphology of primary phase by 3D-CT technology and controlling eutectic growth by tailoring the primary phase, J. Alloys Compd. 821 (2020). https://doi.org/10.1016/j.jallcom.2019.153457.

[109] X. Li, Z.M. Ren, Y. Fautrelle, Effect of a vertical magnetic field on the dendrite morphology during Bridgman crystal growth of Al-4.5 wt% Cu, J. Cryst. Growth. 290 (2006) 571–575. https://doi.org/10.1016/j.jcrysgro.2006.02.017.

[110] X. Li, Y. Fautrelle, Z. Ren, R. Moreau, Formation mechanism of axial macrosegregation of primary phases induced by a static magnetic field during directional solidification, Sci. Rep. 7 (2017) 1–13. https://doi.org/10.1038/srep45834.

[111] P. Mikolajczak, L. Ratke, Effect of stirring induced by rotating magnetic field on β-Al5FeSi intermetallic phases during directional solidification in AlSi alloys, Int. J. Cast Met. Res. 26 (2013) 339–353. https://doi.org/10.1179/1743133613Y.0000000069.

[112] Z. Yan, M. Chen, Y. Teng, J. Yang, L. Yang, H. Gao, Forced Flow and Solidification Process of Sn-3.5%Pb Melt in Hollow Billet Under Rotating

Magnetic Field, J. Mater. Eng. Perform. 24 (2015) 1059–1064. https://doi.org/10.1007/s11665-014-1303-2.

[113] J.K. Roplekar, J.A. Dantzig, A study of solidification with a rotating magnetic field, Int. J. Cast Met. Res. 14 (2001) 79–95. https://doi.org/10.1080/13640461.2001.11819428.

[114] G. Zimmermann, V.T. Vitusevych, L. Sturz, Microstructure formation in AlSi6Cu4 alloy with forced melt flow induced by a rotating magnetic field, Mater. Sci. Forum. 649 (2010) 249–254. https://doi.org/10.4028/www.scientific.net/MSF.649.249.

[115] William D. Coolidge, VACUUM TUBE, 1916. https://patents.google.com/patent/US1203495A/en.

[116] M. Drakopoulos, T. Connolley, C. Reinhard, R. Atwood, O. Magdysyuk, N. Vo, M. Hart, L. Connor, B. Humphreys, G. Howell, S. Davies, T. Hill, G. Wilkin, U. Pedersen, A. Foster, N. De Maio, M. Basham, F. Yuan, K. Wanelik, a, J. Synchrotron Radiat. 22 (2015) 828–838. https://doi.org/10.1107/S1600577515003513.

[117] A. Haibel, SYNCHROTRON X-RAY ABSORPTION TOMOGRAPHY, in: J. Banhart (Ed.), Adv. Tomogr. Methods Mater. Res. Eng., OXFORD SCHOLARSHIP ONLINE, 2008: pp. 583–605. https://doi.org/DOI:10.1093/acprof:oso/9780199213245.003.0005.

[118] R.C. Atwood, A.J. Bodey, S.W.T. Price, M. Basham, M. Drakopoulos, A high-throughput system for high-quality tomographic reconstruction of large datasets

at Diamond Light Source, Philos. Trans. R. Soc. A Math. Phys. Eng. Sci. (2015). https://doi.org/10.1098/rsta.2014.0398.

[119] B. Cai, P.D. Lee, S. Karagadde, T.J. Marrow, T. Connolley, Time-resolved synchrotron tomographic quantification of deformation during indentation of an equiaxed semi-solid granular alloy, Acta Mater. 105 (2016) 338–346. https://doi.org/10.1016/j.actamat.2015.11.028.

[120] M. Drakopoulos, Engineering Science at the I12 Beamline at Diamond Light Source, Synchrotron Radiat. News. 30 (2017) 41–47. https://doi.org/10.1080/08940886.2017.1316131.

[121] H. Nguyen-Thi, L. Salvo, R.H. Mathiesen, L. Arnberg, B. Billia, M. Suery, G. Reinhart, On the interest of synchrotron X-ray imaging for the study of solidification in metallic alloys, Comptes Rendus Phys. 13 (2012) 237–245. https://doi.org/10.1016/j.crhy.2011.11.010.

[122] F. García-Moreno, P.H. Kamm, T.R. Neu, F. Bülk, M.A. Noack, M. Wegener, N. von der Eltz, C.M. Schlepütz, M. Stampanoni, J. Banhart, Tomoscopy: Time-Resolved Tomography for Dynamic Processes in Materials, Adv. Mater. 33 (2021). https://doi.org/10.1002/adma.202104659.

[123] S. Feng, I. Han, A. Lui, R. Vincent, G. Ring, P.S. Grant, E. Liotti, Investigating Metal Solidification with X-ray Imaging, Metals (Basel). 12 (2022) 395. https://doi.org/10.3390/met12030395.

[124] J. Hirsch, Recent development in aluminium for automotive applications, Trans. Nonferrous Met. Soc. China (English Ed. 24 (2014) 1995–2002.

https://doi.org/10.1016/S1003-6326(14)63305-7.

[125] S.K. Das, J.A.S. Green, J.G. Kaufman, The development of recycle-friendly automotive aluminum alloys, Jom. 59 (2007) 47–51. https://doi.org/10.1007/s11837-007-0140-2.

[126] J. Cui, H.J. Roven, Recycling of automotive aluminum, Trans. Nonferrous Met. Soc. China (English Ed. 20 (2010) 2057–2063. https://doi.org/10.1016/S1003-6326(09)60417-9.

[127] T.O. Mbuya, B.O. Odera, S.P. Ng'ang'a, Influence of iron on castability and properties of aluminium silicon alloys: Literature review, Int. J. Cast Met. Res. 16 (2003) 451–465. https://doi.org/10.1080/13640461.2003.11819622.

[128] L. Zhang, J. Gao, L.N.W. Damoah, D.G. Robertson, Removal of iron from aluminum: A review, Miner. Process. Extr. Metall. Rev. 33 (2012) 99–157. https://doi.org/10.1080/08827508.2010.542211.

[129] Y. Zedan, F.H. Samuel, A.M. Samuel, H.W. Doty, Effects of Fe intermetallics on the machinability of heat-treated Al-(7-11)% Si alloys, J. Mater. Process. Technol. 210 (2010) 245–257. https://doi.org/10.1016/j.jmatprotec.2009.09.007.

[130] E. Taghaddos, M.M. Hejazi, R. Taghiabadi, S.G. Shabestari, Effect of iron-intermetallics on the fluidity of 413 aluminum alloy, J. Alloys Compd. 468 (2009) 539–545. https://doi.org/10.1016/j.jallcom.2008.01.079.

[131] S. Shankar, D. Apelian, Die soldering: Mechanism of the interface reaction between molten aluminum alloy and tool steel, Metall. Mater. Trans. B Process

Metall. Mater. Process. Sci. 33 (2002) 465–476. https://doi.org/10.1007/s11663-002-0057-7.

[132] Z. Ma, A.M. Samuel, F.H. Samuel, H.W. Doty, S. Valtierra, A study of tensile properties in Al-Si-Cu and Al-Si-Mg alloys: Effect of β-iron intermetallics and porosity, Mater. Sci. Eng. A. 490 (2008) 36–51. https://doi.org/10.1016/j.msea.2008.01.028.

[133] R. Taghiabadi, H.M. Ghasemi, S.G. Shabestari, Effect of iron-rich intermetallics on the sliding wear behavior of Al-Si alloys, Mater. Sci. Eng. A. 490 (2008) 162–170. https://doi.org/10.1016/j.msea.2008.01.001.

[134] C. Puncreobutr, A.B. Phillion, J.L. Fife, P.D. Lee, Coupling in situ synchrotron X-ray tomographic microscopy and numerical simulation to quantify the influence of intermetallic formation on permeability in aluminium–silicon–copper alloys, Acta Mater. 64 (2014) 316–325. https://doi.org/10.1016/j.actamat.2013.10.044.

[135] R. Daudin, S. Terzi, P. Lhuissier, J. Tamayo, M. Scheel, N.H. Babu, D.G. Eskin, L. Salvo, Particle-induced morphological modification of Al alloy equiaxed dendrites revealed by sub-second in situ microtomography, Acta Mater. 125 (2017) 303–310. https://doi.org/10.1016/j.actamat.2016.12.005.

[136] Y. Zhao, W. Zhang, B. Koe, W. Du, M. Wang, W. Wang, E. Boller, A. Rack, Z. Sun, D. Shu, B. Sun, J. Mi, Multiscale characterization of the nucleation and 3D structure of Al3Sc phases using electron microscopy and synchrotron X-ray tomography, Mater. Charact. 164 (2020) 110353.

https://doi.org/10.1016/j.matchar.2020.110353.

[137] L. Yu, Q. Hu, Z. Ding, F. Yang, W. Lu, N. Zhang, S. Cao, J. Li, Effect of cooling rate on the 3D morphology of the proeutectic Al3Ni intermetallic compound formed at the Al/Ni interface after solidification, J. Mater. Sci. Technol. 69 (2021) 60–68. https://doi.org/10.1016/j.jmst.2020.08.005.

[138] J. Wang, Y. Fautrelle, Z.M. Ren, X. Li, H. Nguyen-Thi, N. Mangelinck-Noel, G. Salloum Abou Jaoude, Y.B. Zhong, I. Kaldre, A. Bojarevics, L. Buligins, Thermoelectric magnetic force acting on the solid during directional solidification under a static magnetic field, Appl. Phys. Lett. 101 (2012). https://doi.org/10.1063/1.4772510.

[139] X. Li, Y. Fautrelle, A. Gagnoud, D. Du, J. Wang, Z. Ren, H. Nguyen-Thi, N. Mangelinck-Noel, Effect of a weak transverse magnetic field on solidification structure during directional solidification, Acta Mater. 64 (2014) 367–381. https://doi.org/10.1016/j.actamat.2013.10.050.

[140] C.Y. Ban, X. Zhang, P. Qian, Y. Han, J.Z. Cui, Study on the Solidification Structures of Al-Fe-Si Alloy under DC and AC Magnetic Fields, Adv. Mater. Res. 189–193 (2011) 4477–4482. https://doi.org/10.4028/www.scientific.net/AMR.189-193.4477.

[141] S. Hu, Y. Dai, A. Gagnoud, Y. Fautrelle, R. Moreau, Z. Ren, K. Deng, C. Li, X. Li, Effect of a magnetic field on macro segregation of the primary silicon phase in hypereutectic Al-Si alloy during directional solidification, J. Alloys Compd. 722 (2017) 108–115. https://doi.org/10.1016/j.jallcom.2017.06.084.

[142] S. Shuai, X. Lin, Y. Dong, L. Hou, H. Liao, J. Wang, Z. Ren, Three dimensional dendritic morphology and orientation transition induced by high static magnetic field in directionally solidified Al-10 wt.%Zn alloy, J. Mater. Sci. Technol. 35 (2019) 1587–1592. https://doi.org/10.1016/j.jmst.2019.03.029.

[143] P. Mikolajczak, Effect of Rotating Magnetic Field on Microstructure in AlCuSi alloys, Metals (Basel). 11 (2021). https://doi.org/https://doi.org/10.3390/met11111804.

[144] A. Kao, N. Shevchenko, S. He, P.D. Lee, S. Eckert, K. Pericleous, Magnetic Effects on Microstructure and Solute Plume Dynamics of Directionally Solidifying Ga-In Alloy, Jom. (2020). https://doi.org/10.1007/s11837-020-04305-2.

[145] T. Wang, P. Zhou, F. Cao, H. Kang, Z. Chen, Y. Fu, T. Xiao, W. Huang, Q. Yuan, Growth behavior of Cu6Sn5 in Sn-6.5 Cu solders under DC considering trace Al: In situ observation, Intermetallics. 58 (2015) 84–90. https://doi.org/10.1016/j.intermet.2014.11.010.

[146] S.-H. Kim, H. Kim, N.J. Kim, Brittle intermetallic compound makes ultrastrong low-density steel with large ductility, Nature. 518 (2015) 77–79. https://doi.org/10.1038/nature14144.

[147] K. Tran, Z.W. Ulissi, Active learning across intermetallics to guide discovery of electrocatalysts for CO2 reduction and H2 evolution, Nat. Catal. 1 (2018) 696–703. https://doi.org/10.1038/s41929-018-0142-1.

[148] Y. Liu, W. Liu, Y. Ma, C. Liang, C. Liu, C. Zhang, Q. Cai, Microstructure and

wear resistance of compositionally graded Ti–Al intermetallic coating on Ti6Al4V alloy fabricated by laser powder deposition, Surf. Coatings Technol. 353 (2018) 32–40. https://doi.org/10.1016/j.surfcoat.2018.08.067.

[149] K. Gschneidner, A. Russell, A. Pecharsky, J. Morris, Z. Zhang, T. Lograsso, D. Hsu, C.H.C. Lo, Y. Ye, A. Slager, D. Kesse, A family of ductile intermetallic compounds, Nat. Mater. 2 (2003) 587–590. https://doi.org/10.1038/nmat958.

[150] A.J. Shahani, X. Xiao, K. Skinner, M. Peters, P.W. Voorhees, Ostwald ripening of faceted Si particles in an Al-Si-Cu melt, Mater. Sci. Eng. A. 673 (2016) 307–320. https://doi.org/10.1016/j.msea.2016.06.077.

[151] M.R.J. Scherer, P.M.S. Cunha, U. Steiner, Labyrinth-induced faceted electrochemical growth, Adv. Mater. 26 (2014) 2403–2407. https://doi.org/10.1002/adma.201305074.

[152] K.G. Libbrecht, Physical Dynamics of Ice Crystal Growth, Annu. Rev. Mater. Res. 47 (2017) 271–295. https://doi.org/10.1146/annurev-matsci-070616-124135.

[153] J.W. Barrett, H. Garcke, R. Nürnberg, Numerical computations of faceted pattern formation in snow crystal growth, Phys. Rev. E - Stat. Nonlinear, Soft Matter Phys. 86 (2012) 4–8. https://doi.org/10.1103/PhysRevE.86.011604.

[154] M. Polacci, F. Arzilli, G. La Spina, N. Le Gall, B. Cai, M.E. Hartley, D. Di Genova, N.T. Vo, S. Nonni, R.C. Atwood, E.W. Llewellin, P.D. Lee, M.R. Burton, Crystallisation in basaltic magmas revealed via in situ 4D synchrotron X-ray microtomography, Sci. Rep. 8 (2018) 1–13. https://doi.org/10.1038/s41598-018-26644-6.

[155] D. Liang, H. Jones, Morphologies of primary Al3Fe in Bridgman solidification and TIG weld traversing of hypereutectic AlFe alloys, Mater. Sci. Eng. A. 173 (1993) 109–114. https://doi.org/10.1016/0921-5093(93)90197-M.

[156] H. Kang, T. Wang, X. Li, Y. Su, J. Guo, H. Fu, Faceted-nonfaceted growth transition and 3-D morphological evolution of primary Al6Mn microcrystals in directionally solidified Al-3 at.% Mn alloy, J. Mater. Res. 29 (2014) 1256–1263. https://doi.org/10.1557/jmr.2014.111.

[157] S. Hu, A. Gagnoud, Y. Fautrelle, R. Moreau, X. Li, Fabrication of aluminum alloy functionally graded material using directional solidification under an axial static magnetic field, Sci. Rep. 8 (2018) 1–13. https://doi.org/10.1038/s41598-018-26297-5.

[158] S.G. Shabestari, E. Parshizfard, Effect of semi-solid forming on the microstructure and mechanical properties of the iron containing Al-Si alloys, J. Alloys Compd. 509 (2011) 7973–7978. https://doi.org/10.1016/j.jallcom.2011.05.052.

[159] J. Hirsch, T. Al-Samman, Superior light metals by texture engineering: Optimized aluminum and magnesium alloys for automotive applications, Acta Mater. 61 (2013) 818–843. https://doi.org/10.1016/j.actamat.2012.10.044.

[160] X. Wu, H. Zhang, F. Zhang, Z. Ma, L. Jia, B. Yang, T. Tao, H. Zhang, Effect of cooling rate and Co content on the formation of Fe-rich intermetallics in hypoeutectic Al7Si0.3Mg alloy with 0.5%Fe, Mater. Charact. 139 (2018) 116–124. https://doi.org/10.1016/j.matchar.2018.02.029.

[161] Y. Han, C. Ban, H. Zhang, H. Nagaumi, Q. Ba, J. Cui, Investigations on the Solidification Behavior of Al-Fe-Si Alloy in an Alternating Magnetic Field, Mater. Trans. 47 (2006) 2092–2098. https://doi.org/10.2320/matertrans.47.2092.

[162] L. Li, Y. Zhang, C. Esling, H. Jiang, Z. Zhao, Y. Zuo, J. Cui, Crystallographic features of the primary Al3Fe phase in as-cast Al-3.31wt% Fe alloy, J. Appl. Crystallogr. 43 (2010) 1108–1112. https://doi.org/10.1107/S0021889810029493.

[163] P. Skjerpe, An electron microscopy study of the phase Al3Fe, J. Microsc. 148 (1987) 33–50. https://doi.org/10.1111/j.1365-2818.1987.tb02853.x.

[164] G. Zeng, J.W. Xian, C.M. Gourlay, Nucleation and growth crystallography of Al8Mn5 on B2-Al(Mn,Fe) in AZ91 magnesium alloys, Acta Mater. 153 (2018) 364–376. https://doi.org/10.1016/j.actamat.2018.04.032.

[165] B. Kim, S. Lee, H. Yasuda, Morphological Variation of Fe/Cr-Rich Intermetallic Phase in Recycled Al-Si Alloy as a Function of Solidification Rate: Time-Resolved Radiography, Mater. Sci. Forum - MATER SCI FORUM. 654 (2010) 974–977. https://doi.org/10.4028/www.scientific.net/MSF.654-656.974.

[166] T. Nelson, B. Cai, N. Warnken, P.D. Lee, E. Boller, O. V. Magdysyuk, N.R. Green, Gravity effect on thermal-solutal convection during solidification revealed by four-dimensional synchrotron imaging with compositional mapping, Scr. Mater. 180 (2020) 29–33. https://doi.org/10.1016/j.scriptamat.2019.12.026.

[167] J.M. Yu, N. Wanderka, A. Rack, R. Daudin, E. Boller, H. Markötter, A. Manzoni, F. Vogel, T. Arlt, I. Manke, J. Banhart, Formation of intermetallic δ phase in Al-10Si-0.3Fe alloy investigated by in-situ 4D X-ray synchrotron

tomography, Acta Mater. 129 (2017) 194–202. https://doi.org/10.1016/j.actamat.2017.02.048.

[168] A.J. Shahani, E.B. Gulsoy, S.O. Poulsen, X. Xiao, P.W. Voorhees, Twin-mediated crystal growth: An enigma resolved, Sci. Rep. 6 (2016) 1–11. https://doi.org/10.1038/srep28651.

[169] J.W. Gibbs, P.W. Voorhees, Segmentation of four-dimensional, X-ray computed tomography data, Integr. Mater. Manuf. Innov. 3 (2014) 73–84. https://doi.org/10.1186/2193-9772-3-6.

[170] M. Wang, W. Xu, Q. Han, Study of Refinement and Morphology Change of AlFeSi Phase in A380 Alloy due to Addition of Ca, Sr/ Ca, Mn and Mn, Sr, Mater. Trans. 57 (2016) 1509–1513. https://doi.org/10.2320/matertrans.m2015329.

[171] K. Yamagiwa, Y. Watanabe, Y. Fukui, P. Kapranos, Novel Recycling System of Aluminum and Iron Wastes- in-situ Al-Al 3 Fe Functionally Graded Material Manufactured by a Centrifugal Method-, Mater. Trans. 44 (2003) 2461–2467.

[172] K. Yamagiwa, Y. Watanabe, K. Matsuda, Y. Fukui, P. Kapranos, Characteristics of a near-net-shape formed Al-Al3Fe eco-functionally graded material produced over its eutectic melting temperature, Mater. Sci. Eng. A. 416 (2006) 80–91. https://doi.org/10.1016/j.msea.2005.10.031.

[173] F. Marone, M. Stampanoni, Regridding reconstruction algorithm for real-time tomographic imaging, J. Synchrotron Radiat. 19 (2012) 1029–1037. https://doi.org/10.1107/S0909049512032864.

[174] S. Yue, P.D. Lee, G. Poologasundarampillai, J.R. Jones, Evaluation of 3-D bioactive glass scaffolds dissolution in a perfusion flow system with X-ray microtomography, Acta Biomater. 7 (2011) 2637–2643. https://doi.org/10.1016/j.actbio.2011.02.009.

[175] V.A. Blatov, A.P. Shevchenko, D.M. Proserpio, Applied topological analysis of crystal structures with the program package topospro, Cryst. Growth Des. 14 (2014) 3576–3586. https://doi.org/10.1021/cg500498k.

[176] W. Khalifa, F.H. Samuel, J.E. Gruzleski, H.W. Doty, S. Valtierra, Nucleation of Fe-intermetallic phases in the Al-Si-Fe alloys, Metall. Mater. Trans. A Phys. Metall. Mater. Sci. 36 (2005) 1017–1032. https://doi.org/10.1007/s11661-005-0295-9.

[177] Z. Fan, F. Gao, L. Zhou, S.Z. Lu, A new concept for growth restriction during solidification, Acta Mater. 152 (2018) 248–257. https://doi.org/10.1016/j.actamat.2018.04.045.

[178] P.J. Black, The structure of $FeAl_3$. I, Acta Crystallogr. 8 (1955) 43–48. https://doi.org/10.1107/S0365110X5500011X.

[179] G. Sha, K.A.Q. O'Reilly, B. Cantor, Characterization of fe-rich intermetallic phases in a 6xxx series al alloy, Mater. Sci. Forum. 519–521 (2006) 1721–1726. https://doi.org/10.4028/www.scientific.net/msf.519-521.1721.

[180] M.E. und U. Burkhardt, Zur Bildung von Drehmehrlingen mit pentagonaler Pseudosymmetrie beim Erstarrungsvorgang des Fe4A11, J. Alloys Compd. 198 (1993) 91–100.

[181] A.J. Shahani, X. Xiao, P.W. Voorhees, The mechanism of eutectic growth in highly anisotropic materials, Nat. Commun. 7 (2016) 1–7. https://doi.org/10.1038/ncomms12953.

[182] K.S. Eom, J.Y. Kwon, M.J. Kim, H.S. Kwon, Design of Al-Fe alloys for fast on-board hydrogen production from hydrolysis, J. Mater. Chem. 21 (2011) 13047–13051. https://doi.org/10.1039/c1jm11329a.

[183] K. Gao, S. Li, L. Xu, H. Fu, Effect of sample size on intermetallic Al2Cu microstructure and orientation evolution during directional solidification, J. Cryst. Growth. 394 (2014) 89–96. https://doi.org/10.1016/j.jcrysgro.2014.02.023.

[184] R. Kumar, J. Villanova, P. Lhuissier, L. Salvo, In situ nanotomography study of creep cavities in Al-3.6-Cu alloy, Acta Mater. 166 (2019) 18–27. https://doi.org/10.1016/j.actamat.2018.12.020.

[185] T. Haxhimali, A. Karma, F. Gonzales, M. Rappaz, Orientation selection in dendritic evolution, Nat. Mater. 5 (2006) 660–664. https://doi.org/10.1038/nmat1693.

[186] D.J. Fisher, W. Kurz, A theory of branching limited growth of irregular eutectics, Acta Metall. 28 (1980) 777–794. https://doi.org/10.1016/0001-6160(80)90155-8.

[187] A.J. Clarke, D. Tourret, Y. Song, S.D. Imhoff, P.J. Gibbs, J.W. Gibbs, K. Fezzaa, A. Karma, Microstructure selection in thin-sample directional solidification of an Al-Cu alloy: In situ X-ray imaging and phase-field simulations, Acta Mater. 129 (2017) 203–216. https://doi.org/10.1016/j.actamat.2017.02.047.

[188] B. Cai, S. Karagadde, D. Rowley, T.J. Marrow, T. Connolley, P.D. Lee, Time-resolved synchrotron tomographic quantification of deformation-induced flow in a semi-solid equiaxed dendritic Al-Cu alloy, Scr. Mater. 103 (2015) 69–72. https://doi.org/10.1016/j.scriptamat.2015.03.011.

[189] W.J. Boettinger, J.A. Warren, C. Beckermann, A. Karma, Phase-field simulation of solidification, Annu. Rev. Mater. Sci. 32 (2002) 163–194. https://doi.org/10.1146/annurev.matsci.32.101901.155803.

[190] Z. Song, O. Magdysyuk, L. Tang, T. Sparks, B. Cai, Growth dynamics of Faceted Al13Fe4 Intermetallic Revealed by High-Speed Synchrotron X-Ray Quantification, J. Alloys Compd. 861 (2021) 1–15. https://doi.org/https://doi.org/10.1016/j.jallcom.2021.158604.

[191] Z. Ding, Q. Hu, W. Lu, N. Zhang, X. Ge, S. Cao, T. Yang, M. Xia, J. Li, Continuous Morphological Transition and Its Mechanism of Al3Ni Phase at the Liquid–Solid Interface During Solidification, Metall. Mater. Trans. A Phys. Metall. Mater. Sci. 50 (2019) 556–561. https://doi.org/10.1007/s11661-018-5059-4.

[192] X. Li, Z. Ren, Y. Fautrelle, Y. Zhang, C. Esling, Morphological instabilities and alignment of lamellar eutectics during directional solidification under a strong magnetic field, Acta Mater. 58 (2010) 1403–1417. https://doi.org/10.1016/j.actamat.2009.10.048.

[193] P. Jarry, M. Rappaz, Recent advances in the metallurgy of aluminium alloys. Part I: Solidification and casting, Comptes Rendus Phys. 19 (2018) 672–687.

https://doi.org/10.1016/j.crhy.2018.09.003.

[194] H. Shi, E.H. Han, F. Liu, T. Wei, Z. Zhu, D. Xu, Study of corrosion inhibition of coupled Al2Cu-Al and Al3Fe-Al by cerium cinnamate using scanning vibrating electrode technique and scanning ion-selective electrode technique, Corros. Sci. 98 (2015) 150–162. https://doi.org/10.1016/j.corsci.2015.05.019.

[195] R. Bonnet, M. Loubradou, Crystalline defects in a B.C.T. Al2Cu(θ) single crystal obtained by unidirectional solidification along [001], Phys. Status Solidi Appl. Res. 194 (2002) 173–191. https://doi.org/10.1002/1521-396X(200211)194:1<173::AID-PSSA173>3.0.CO;2-P.

[196] K. Gao, Y. Xu, W. Song, L. Guan, M. Li, K. Li, X. Guo, R. Zhang, Preparation and growth characterization of Al2Cu phase crystal with the single orientation under directional solidification, Mater. Res. 21 (2018). https://doi.org/10.1590/1980-5373-MR-2018-0381.

[197] R. Hamar, C. Lemaignan, Facetting behaviour of Al2Cu during solidification, J. Cryst. Growth. 53 (1981) 586–590. https://doi.org/10.1016/0022-0248(81)90143-3.

[198] A. Kao, B. Cai, P.D. Lee, K. Pericleous, The effects of Thermoelectric Magnetohydrodynamics in directional solidification under a transverse magnetic field, J. Cryst. Growth. 457 (2017) 270–274. https://doi.org/10.1016/j.jcrysgro.2016.07.003.

[199] J.A. Shercliff, Thermoelectric magnetohydrodynamics, Phys. Fluids. 22 (1979) 635–640. https://doi.org/10.1063/1.862646.

[200] Z. Yan, X. Li, Z. Cao, X. Zhang, T. Li, Grain refinement of horizontal continuous casting of the CuNi10Fe1Mn alloy hollow billets by rotating magnetic field (RMF), Mater. Lett. 62 (2008) 4389–4392. https://doi.org/10.1016/j.matlet.2008.07.010.

[201] B. Cai, A. Kao, E. Boller, O. V. Magdysyuk, R.C. Atwood, N.T. Vo, K. Pericleous, P.D. Lee, Revealing the mechanisms by which magneto-hydrodynamics disrupts solidification microstructures, Acta Mater. 196 (2020) 200–209. https://doi.org/10.1016/j.actamat.2020.06.041.

[202] X. Li, Z. Ren, Y. Fautrelle, Effect of a high axial magnetic field on the microstructure in a directionally solidified Al-Al2Cu eutectic alloy, Acta Mater. 54 (2006) 5349–5360. https://doi.org/10.1016/j.actamat.2006.06.051.

[203] J.L. Fife, J.W. Gibbs, E.B. Gulsoy, C.L. Park, K. Thornton, P.W. Voorhees, The dynamics of interfaces during coarsening in solid-liquid systems, Acta Mater. 70 (2014) 66–78. https://doi.org/10.1016/j.actamat.2014.01.024.

[204] A.J. Shahani, E.B. Gulsoy, V.J. Roussochatzakis, J.W. Gibbs, J.L. Fife, P.W. Voorhees, The dynamics of coarsening in highly anisotropic systems: Si particles in Al-Si liquids, Acta Mater. 97 (2015) 325–337. https://doi.org/10.1016/j.actamat.2015.06.064.

[205] N. Wadeson, M. Basham, Savu: A Python-based, MPI Framework for Simultaneous Processing of Multiple, N-dimensional, Large Tomography Datasets, (2016). http://arxiv.org/abs/1610.08015.

[206] Nobuyuki Otsu, A Threshold Selection Method from Gray-Level Histograms,

IEEE Trans. Syst. Man Cybern. 9 (1979) 62–66.

[207] M.A. Tschopp, J.D. Miller, A.L. Oppedal, K.N. Solanki, Characterizing the local primary dendrite arm spacing in directionally solidified dendritic microstructures, Metall. Mater. Trans. A Phys. Metall. Mater. Sci. 45 (2014) 426–437. https://doi.org/10.1007/s11661-013-1985-3.

[208] F.P. Vidal, J.M. Létang, G. Peix, P. Cloetens, Investigation of artefact sources in synchrotron microtomography via virtual X-ray imaging, Nucl. Instruments Methods Phys. Res. Sect. B Beam Interact. with Mater. Atoms. 234 (2005) 333–348. https://doi.org/10.1016/j.nimb.2005.02.003.

[209] H.Z. Wang, D.Y.C. Leung, M.K.H. Leung, M. Ni, A review on hydrogen production using aluminum and aluminum alloys, Renew. Sustain. Energy Rev. 13 (2009) 845–853. https://doi.org/10.1016/j.rser.2008.02.009.

[210] H.J. Scheel, Accelerated crucible rotation: a novel stirring technique in high-temperature solution growth, J. Cryst. Growth. 13/14 (1972) 560–565.

[211] W. Kurz, C. Bezençon, M. Gäumann, Columnar to equiaxed transition in solidification processing, Sci. Technol. Adv. Mater. 2 (2001) 185–191. https://doi.org/10.1016/S1468-6996(01)00047-X.

[212] A. Baldan, Progress in Ostwald ripening theories and their applications in nickel-base super alloys, J. Mater. Sci. 37 (2002) 2171– 2202.

[213] Jackson K.A., The interface kinetics of crystal growth processes, Interface Sci. 10 (2002) 159–169.

[214] H. Zhang, J.F. Banfield, Energy calculations predict nanoparticle attachment orientations and asymmetric crystal formation, J. Phys. Chem. Lett. 3 (2012) 2882–2886. https://doi.org/10.1021/jz301161j.

[215] Y. Grin, F.R. Wagner, M. Armbrüster, M. Kohout, A. Leithe-Jasper, U. Schwarz, U. Wedig, H. Georg von Schnering, CuAl2 revisited: Composition, crystal structure, chemical bonding, compressibility and Raman spectroscopy, J. Solid State Chem. 179 (2006) 1707–1719. https://doi.org/10.1016/j.jssc.2006.03.006.

[216] D.L. Miao Song, Gang Zhou, Ning Lu, Jaewon Lee1, Elias Nakouzi1, Hao Wang, Oriented attachment induces fivefold twins by forming and decomposing high-energy grain boundaries, Science (80-.). 367 (2020) 40–45. https://doi.org/10.1017/cbo9781316389508.016.

[217] L. Liu, D. Ren, F. Liu, A review of dissimilar welding techniques for magnesium alloys to aluminum alloys, Materials (Basel). 7 (2014) 3735–3757. https://doi.org/10.3390/ma7053735.

[218] J. Zhang, G. Luo, Q. Shen, L. Zhang, Diffusion mechanism and kinetics of diffusion bonded Mg/Ni/Al joint, Key Eng. Mater. 616 (2014) 286–290. https://doi.org/10.4028/www.scientific.net/KEM.616.286.

[219] F. Yin, C. Liu, Y. Zhang, Y. Qin, N. Liu, Effect of Ni interlayer on characteristics of diffusion bonded Mg/Al joints, Mater. Sci. Technol. 34 (2018) 1104–1111. https://doi.org/10.1080/02670836.2018.1424382.

[220] J. Zhang, G. Luo, Y. Wang, Q. Shen, L. Zhang, An investigation on diffusion bonding of aluminum and magnesium using a Ni interlayer, Mater. Lett. 83

(2012) 189–191. https://doi.org/10.1016/j.matlet.2012.06.014.

[221] M. Sun, S.T. Niknejad, G. Zhang, M.K. Lee, L. Wu, Y. Zhou, Microstructure and mechanical properties of resistance spot welded AZ31/AA5754 using a nickel interlayer, Mater. Des. 87 (2015) 905–913. https://doi.org/10.1016/j.matdes.2015.08.097.

[222] P. Penner, L. Liu, A. Gerlich, Y. Zhou, Feasibility study of resistance spot welding of dissimilar Al/Mg combinations with Ni based interlayers, Sci. Technol. Weld. Join. 18 (2013) 541–550. https://doi.org/10.1179/1362171813Y.0000000129.

[223] W.S. Chang, S.R. Rajesh, C.K. Chun, H.J. Kim, Microstructure and Mechanical Properties of Hybrid Laser-Friction Stir Welding between AA6061-T6 Al Alloy and AZ31 Mg Alloy, J. Mater. Sci. Technol. 27 (2011) 199–204. https://doi.org/10.1016/S1005-0302(11)60049-2.

[224] H. Wang, L. Liu, F. Liu, The characterization investigation of laser-arc-adhesive hybrid welding of Mg to Al joint using Ni interlayer, Mater. Des. 50 (2013) 463–466. https://doi.org/10.1016/j.matdes.2013.02.085.

[225] Z. Ding, Q. Hu, W. Lu, F. Yang, Y. Zhou, N. Zhang, S. Cao, L. Yu, J. Li, Intergrowth mechanism and morphology prediction of faceted Al3Ni formed during solidification by a spatial geometric model, J. Mater. Sci. Technol. 54 (2020) 40–47. https://doi.org/10.1016/j.jmst.2020.02.078.

[226] Z. DING, Q. HU, F. YANG, W. LU, T. YANG, S. CAO, J. LI, A New Sight of the Growth Characteristics of Solidified Al3Ni at the Liquid–Solid Interface by

Synchrotron Radiography and 3D Tomography, Metall. Mater. Trans. A. 51 (2020) 2689–2696. https://doi.org/10.1007/s11661-020-05729-w.

[227] Z. Ding, Q. Hu, W. Lu, N. Zhang, X. Ge, S. Cao, T. Yang, M. Xia, J. Li, Continuous Morphological Transition and Its Mechanism of Al3Ni Phase at the Liquid–Solid Interface During Solidification, Metall. Mater. Trans. A. 50 (2019) 556–561. https://doi.org/10.1007/s11661-018-5059-4.

[228] Z. Song, O. V Magdysyuk, T. Sparks, Y. Chiu, B. Cai, Revealing growth mechanisms of faceted Al2Cu intermetallic compounds via high-speed Synchrotron X-ray tomography, Acta Mater. 231 (2022) 117903. https://doi.org/10.1016/j.actamat.2022.117903.

[229] N.D. Broom, G.J. Davies, Fracture behaviour of crystalline Al3Ni intermetallic fibres, Philos. Mag. 28 (1973) 685–702. https://doi.org/10.1080/14786437308221012.

[230] D. Jaffrey, G.A. Chadwick, The nucleation, growth morphology, and thermal stability of Sn-Zn and Al-Al3Ni eutectic alloys, Metall. Trans. 1 (1970) 3389–3396. https://doi.org/10.1007/BF03037869.

[231] X. Li, Z. Ren, Y. Fautrelle, Alignment behavior of the primary Al3Ni phase in Al-Ni alloy under a high magnetic field, J. Cryst. Growth. 310 (2008) 3488–3497. https://doi.org/10.1016/j.jcrysgro.2008.04.038.

[232] C. Wang, Q. Wang, Z. Wang, H. Li, K. Nakajima, J. He, Phase alignment and crystal orientation of Al3Ni in Al-Ni alloy by imposition of a uniform high magnetic field, J. Cryst. Growth. 310 (2008) 1256–1263.

https://doi.org/10.1016/j.jcrysgro.2007.12.045.

[233] F. Meng, S.A. Morin, S. Jin, Growth of nanomaterials by screw dislocation, Springer Handb. Nanomater. 46 (2013) 639–664. https://doi.org/10.1007/978-3-642-20595-8_17.

[234] S.A. Morin, M.J. Bierman, J. Tong, S. Jin, Mechanism and kinetics of spontaneous nanotube growth driven by screw dislocations, Science (80-.). 328 (2010) 476–480. https://doi.org/10.1126/science.1182977.

[235] A.J. Shahani, X. Xiao, P.W. Voorhees, The mechanism of eutectic growth in highly anisotropic materials, Nat. Commun. 7 (2016) 1–7. https://doi.org/10.1038/ncomms12953.

[236] Y. Wang, J. Gao, W. Sun, A.J. Shahani, In situ observation of faceted growth and morphological instability of a complex-regular eutectic in Zn−Mg−Al system, Scr. Mater. 206 (2022) 114224. https://doi.org/10.1016/j.scriptamat.2021.114224.

[237] Z. Song, O. V Magdysyuk, T. Sparks, Y. Chiu, B. Cai, Revealing growth mechanisms of faceted Al2Cu intermetallic compounds via high-speed Synchrotron X-ray tomography, Acta Mater. (2022) 117903. https://doi.org/10.1016/j.actamat.2022.117903.

[238] X.H. Wang, H.W. Wang, C.M. Zou, Z.J. Wei, Y. Uwatoko, J. Gouchi, D. Nishio-Hamane, H. Gotou, The effects of high pressure and superheating on the planar growth of Al3Ni phase in hypo-peritectic Al-30wt%Ni alloy, J. Alloys Compd. 772 (2019) 1052–1060. https://doi.org/10.1016/j.jallcom.2018.09.079.

[239] J. Guo, M.D. Seo, C. Bin Shi, J.W. Cho, S.H. Kim, Control of Crystal Morphology for Mold Flux During High-Aluminum AHSS Continuous Casting Process, Metall. Mater. Trans. B Process Metall. Mater. Process. Sci. 47 (2016) 2211–2221. https://doi.org/10.1007/s11663-016-0697-7.

[240] L. Bacherud, Solidification Characteristics of Aluminium Alloys, Skanaluminium, Oslo, 1986.

[241] H. Fredriksson, U. Åkerlind, Faceted and Dendritic Solidification Structures, Solidif. Cryst. Process. Met. Alloy. (2012) 475–586. https://doi.org/10.1002/9781119975540.ch9.

[242] K.B. Hyde, A.F. Norman, P.B. Prangnell, The effect of cooling rate on the morphology of primary Al3Sc intermetallic particles in Al-Sc alloys, Acta Mater. 49 (2001) 1327–1337. https://doi.org/10.1016/S1359-6454(01)00050-7.

[243] M. Uwaha, Growth Kinetics: Basics of Crystal Growth Mechanisms, Second Edi, Elsevier B.V., 2015. https://doi.org/10.1016/B978-0-444-56369-9.00008-3.

[244] S.K. Das, W. Yin, The worldwide aluminum economy: The current state of the industry, Jom. 59 (2007) 57–63. https://doi.org/10.1007/s11837-007-0142-0.

[245] D. Wang, X. Zhang, H. Nagaumi, X. Li, H. Zhang, 3D morphology and growth mechanism of cubic a -Al (FeMnCr) Si intermetallic in an Al-Si cast alloy, Mater. Lett. 277 (2020) 128384. https://doi.org/10.1016/j.matlet.2020.128384.

[246] J.A. Taylor, Iron-Containing Intermetallic Phases in Al-Si Based Casting Alloys, Procedia Mater. Sci. 1 (2012) 19–33.

https://doi.org/10.1016/j.mspro.2012.06.004.

[247] Y. Zhao, W. Zhang, D. Song, B. Lin, F. Shen, D. Zheng, C.X. Xie, Z. Sun, Y. Fu, R. Li, Nucleation and growth of Fe-rich phases in Al-5Ti-1B modified Al-Fe alloys investigated using synchrotron X-ray imaging and electron microscopy, J. Mater. Sci. Technol. 80 (2021) 84–99. https://doi.org/10.1016/j.jmst.2020.12.011.

[248] L. Zhang, W. Jing, Y. Yang, H. Yang, Y. Guo, H. Sun, J. Zhao, J. Yao, The investigation of permeability calculation using digital core simulation technology, Energies. 12 (2019) 1–9. https://doi.org/10.3390/en12173273.

[249] S. Ji, W. Yang, F. Gao, D. Watson, Z. Fan, Effect of iron on the microstructure and mechanical property of Al-Mg-Si-Mn and Al-Mg-Si diecast alloys, Mater. Sci. Eng. A. 564 (2013) 130–139. https://doi.org/10.1016/j.msea.2012.11.095.

[250] F. Wang, D. Eskin, J. Mi, C. Wang, B. Koe, A. King, C. Reinhard, T. Connolley, A synchrotron X-radiography study of the fragmentation and refinement of primary intermetallic particles in an Al-35 Cu alloy induced by ultrasonic melt processing, Acta Mater. 141 (2017) 142–153. https://doi.org/10.1016/j.actamat.2017.09.010.

[251] T. Manuwong, W. Zhang, P.L. Kazinczi, A.J. Bodey, C. Rau, J. Mi, Solidification of Al Alloys Under Electromagnetic Pulses and Characterization of the 3D Microstructures Using Synchrotron X-ray Tomography, Metall. Mater. Trans. A Phys. Metall. Mater. Sci. 46 (2015) 2908–2915. https://doi.org/10.1007/s11661-015-2874-8.

[252] Z. Zhang, C. Wang, B. Koe, C.M. Schlepütz, S. Irvine, J. Mi, Synchrotron X-ray imaging and ultrafast tomography in situ study of the fragmentation and growth dynamics of dendritic microstructures in solidification under ultrasound, Acta Mater. (2021) 116796. https://doi.org/10.1016/j.actamat.2021.116796.

[253] J. Cao, S. Shuai, C. Huang, T. Hu, C. Chen, J. Wang, Z. Ren, 4D synchrotron X-ray tomographic study of the influence of transverse magnetic field on iron intermetallic compounds precipitation behavior during solidification of Al–Si–Fe alloy, Intermetallics. 143 (2022) 107471. https://doi.org/10.1016/j.intermet.2022.107471.

[254] S. Hu, L. Hou, K. Wang, Z. Liao, Y. Fautrelle, W. Li, X. Li, Formation mechanism of gradient structure of aluminum matrix composite under static magnetic field during directional solidification, J. Mater. Res. Technol. 9 (2020) 4459–4468. https://doi.org/10.1016/j.jmrt.2020.02.072.

[255] N. Shevchenko, O. Roshchupkina, O. Sokolova, S. Eckert, The effect of natural and forced melt convection on dendritic solidification in Ga-In alloys, J. Cryst. Growth. 417 (2015) 1–8. https://doi.org/10.1016/j.jcrysgro.2014.11.043.

[256] F. Cao, F. Yang, H. Kang, C. Zou, T. Xiao, W. Huang, T. Wang, Effect of traveling magnetic field on solute distribution and dendritic growth in unidirectionally solidifying Sn–50 wt%Pb alloy: An in situ observation, J. Cryst. Growth. 450 (2016) 91–95. https://doi.org/10.1016/j.jcrysgro.2016.06.034.

[257] W. Ren, Z. Ren, K. Deng, Y. Zhong, Z. Lei, X. Li, Progress in research on solidification in a strong static magnetic field, Steel Res. Int. 78 (2007) 373–378.

https://doi.org/10.1002/srin.200705906.

[258] W.L. Ren, Y.F. Fan, J.W. Feng, Y.B. Zhong, J.B. Yu, Z.M. Ren, P.K. Liaw, Non-monotonic changes in critical solidification rates for stability of liquid-solid interfaces with static magnetic fields, Sci. Rep. 6 (2016) 2–11. https://doi.org/10.1038/srep20598.

[259] S. Agrawal, A.K. Ghose, I. Chakrabarty, Effect of rotary electromagnetic stirring during solidification of In-situ Al-TiB2 composites, Mater. Des. 113 (2017) 195–206. https://doi.org/10.1016/j.matdes.2016.10.007.

[260] X. Li, Y. Fautrelle, Z. Ren, Influence of thermoelectric effects on the solid–liquid interface shape and cellular morphology in the mushy zone during the directional solidification of Al–Cu alloys under a magnetic field, Acta Mater. 55 (2007) 3803–3813. https://doi.org/10.1016/j.actamat.2007.02.031.

[261] M. Javidani, D. Larouche, Application of cast Al-Si alloys in internal combustion engine components, Int. Mater. Rev. 59 (2014) 132–158. https://doi.org/10.1179/1743280413Y.0000000027.

[262] R. March, XXIX. An experimental investigation of the circumstances which determine whether the motion of water shall be direct or sinuous, and of the law of resistance in parallel channels, Philos. Trans. R. Soc. London. 174 (1883) 935–982. https://doi.org/10.1098/rstl.1883.0029.

[263] J.S. Wang, P.D. Lee, In-situ Observation and Mathematical Modelling of the Nucleation and Growth of Intermetallics and Micropores During the Solidification of Aluminium Alloys, Dep. Mater. PhD (2009).

[264] M.H. Burden, D.J. Hebditch, J.D. Hunt, Macroscopic stability of a planar, cellular or dendritic interface during directional freezing, J. Cryst. Growth. 20 (1973) 121–124. https://doi.org/10.1016/0022-0248(73)90125-5.

[265] A. Bogno, H. Nguyen-Thi, A. Buffet, G. Reinhart, B. Billia, N. Mangelinck-Noël, N. Bergeon, J. Baruchel, T. Schenk, Analysis by synchrotron X-ray radiography of convection effects on the dynamic evolution of the solid-liquid interface and on solute distribution during the initial transient of solidification, Acta Mater. 59 (2011) 4356–4365. https://doi.org/10.1016/j.actamat.2011.03.059.

[266] H. Zhang, M. Wu, Z. Zhang, A. Ludwig, A. Kharicha, A. Rónaföldi, A. Roósz, Z. Veres, M. Svéda, Experimental Evaluation of MHD Modeling of EMS During Continuous Casting, Metall. Mater. Trans. B. (2022). https://doi.org/10.1007/s11663-022-02516-3.

[267] H. Zhang, M. Wu, C.M.G. Rodrigues, A. Ludwig, A. Kharicha, Directional Solidification of AlSi7Fe1 Alloy Under Forced Flow Conditions: Effect of Intermetallic Phase Precipitation and Dendrite Coarsening, Metall. Mater. Trans. A Phys. Metall. Mater. Sci. 52 (2021) 3007–3022. https://doi.org/10.1007/s11661-021-06295-5.

[268] J. Wang, Y. Fautrelle, Z.M. Ren, H. Nguyen-Thi, G. Salloum Abou Jaoude, G. Reinhart, N. Mangelinck-Noël, X. Li, I. Kaldre, Thermoelectric magnetic flows in melt during directional solidification, Appl. Phys. Lett. 104 (2014). https://doi.org/10.1063/1.4870099.

[269] J. Wang, Y. Fautrelle, H. Nguyen-Thi, G. Reinhart, H. Liao, X. Li, Y. Zhong, Z. Ren, Thermoelectric Magnetohydrodynamic Flows and Their Induced Change of Solid–Liquid Interface Shape in Static Magnetic Field-Assisted Directional Solidification, Metall. Mater. Trans. A Phys. Metall. Mater. Sci. 47 (2016) 1169–1179. https://doi.org/10.1007/s11661-015-3277-6.

[270] J. Scharf, M. Chouchane, D.P. Finegan, B. Lu, C. Redquest, M. cheol Kim, W. Yao, A.A. Franco, D. Gostovic, Z. Liu, M. Riccio, F. Zelenka, J.M. Doux, Y.S. Meng, Bridging nano- and microscale X-ray tomography for battery research by leveraging artificial intelligence, Nat. Nanotechnol. 17 (2022) 446–459. https://doi.org/10.1038/s41565-022-01081-9.

[271] L. Liu, E. Nakouzi, M.L. Sushko, G.K. Schenter, C.J. Mundy, J. Chun, J.J. De Yoreo, Connecting energetics to dynamics in particle growth by oriented attachment using real-time observations, Nat. Commun. 11 (2020) 1–11. https://doi.org/10.1038/s41467-020-14719-w.

[272] D. Zhang, Y. Wang, J. Deng, X. Wang, G. Guo, Microfluidics revealing formation mechanism of intermetallic nanocrystals, Nano Energy. 70 (2020) 104565. https://doi.org/10.1016/j.nanoen.2020.104565.

[273] Y. Hu, S. Wu, Y. Guo, Z. Shen, A.M. Korsunsky, Y. Yu, X. Zhang, Y. Fu, Z. Che, T. Xiao, S. Lozano-Perez, Q. Yuan, X. Zhong, X. Zeng, G. Kang, P.J. Withers, Inhibiting weld cracking in high-strength aluminium alloys, Nat. Commun. 13 (2022) 5816. https://doi.org/10.1038/s41467-022-33188-x.

[274] M. Towrie, R.C. Atwood, C.L.A. Leung, P.D. Lee, S. Marussi, P.J. Withers, In

situ X-ray imaging of defect and molten pool dynamics in laser additive manufacturing, Nat. Commun. 9 (2018) 1–9. https://doi.org/10.1038/s41467-018-03734-7.

[275] Y. Huang, T.G. Fleming, S.J. Clark, S. Marussi, K. Fezzaa, J. Thiyagalingam, C.L.A. Leung, P.D. Lee, Keyhole fluctuation and pore formation mechanisms during laser powder bed fusion additive manufacturing, Nat. Commun. 13 (2022) 1170. https://doi.org/10.1038/s41467-022-28694-x.